DISS. ETH NO.: 27263

Fluxes and pathways of carbon export associated with Himalayan erosion

A thesis submitted to attain the degree of

DOCTOR OF SCIENCES of ETH ZURICH

(Dr. sc. ETH Zurich)

presented by

Lena Märki

Master of Science (MSc) in Geology,
Geneva and Lausanne Universities

born on 13.02.1991

citizen of Unterbözberg, Switzerland

accepted on the recommendation of:

Prof. T. Eglinton, examiner

Dr. M. Lupker, co-examiner

Dr. M. Galvez, co-examiner

Dr. C. France-Lanord, co-examiner

Prof. J. West, external-examiner

2021

All my life through, the new sights of Nature
made me rejoice like a child.

Marie Curie

Summary

The evolution of the global climate is controlled through the cycling of carbon between its reservoirs on multiple timescales. The erosion and weathering of mountain ranges are major actors in the carbon cycle contributing significantly to the global carbon fluxes between the Earth's surface and the Earth's crust on timescales of millions of years. Different mechanisms acting as carbon sources or sinks to the Earth's surface add up to a complex system controlling the erosional carbon budget of a mountain range. Enhanced soil erosion in rapidly eroding mountain ranges plays additionally a crucial role in climatic fluctuations on timescales of millennials and is important for the sustainability of agricultural soils.

In this thesis, I address different aspects of the carbon fluxes associated with the erosion and weathering of the Central Himalaya. This tectonically active mountain range is characterized by high erosion rates and the large amounts of riverine sediments and solutes annually exported by rivers from the Nepalese Himalaya are of global importance.

In the first part, I define the net carbon budget of the Central Himalayan erosion and evaluate the impact of a major earthquake on this budget. On a sample set of daily suspended sediment samples from a large Himalayan river, I quantify the export of biospheric Organic Carbon (OC) using radiocarbon signatures and total OC concentrations. Chemical weathering rates in the catchment are constrained by measurements of major ion concentrations on daily water samples from the same river. We find that the Central Himalayan erosion acts as a net carbon sink from the Earth's surface and that coseismic landslides of the 2015 Gorkha earthquake (Mw 7.8) did not significantly influence the carbon fluxes.

In the second part, I explore the application of brGDGTs (branched Glycerol Dialkyl Glycerol Tetraethers), a soil biomarker, as a tracer of the elevation at which soil OC is preferentially mobilized at the scale of large Himalayan catchments. Our results of brGDGT distributions in soils and river sediments show that soil organic matter entrained in fluvial sediments mostly reflects the mean elevation of the soil-covered catchments. Inverse modelling of the brGDGT dataset suggests that riverine soil OC export in the Himalaya occurs pervasively and is insensitive to anthropogenic perturbations at the catchment scale.

Further, I investigate the structural diversity and main source region of petrogenic OC exported in Himalayan river sediments. The characterization of petrogenic OC by Raman spectroscopy reveals a large diversity of structural ordering, highlighting the importance of a systematic study of petrogenic OC material in river sediments. I show that petrogenic OC in suspended sediments of the Central Himalaya is mostly sourced from the upstream region's metasedimentary units and that in-river oxidation is likely negligible.

Finally, the partitioning of chemical weathering pathways in 28 catchments across the Nepalese Himalaya is studied. I test the use of radiogenic and stable carbon isotopic compositions of dissolved inorganic carbon, sulfur isotopic signatures of dissolved sulfate, and major ion concentrations of river water samples for tracing chemical weathering reactions. Inverse modeling results suggest a strong lithological control on the weathering pathways and reveal the importance of sulfuric acid-driven weathering of both carbonates and silicates.

In summary, this thesis shows that the Himalaya's highly erosive environment acts as a carbon sink to the Earth's surface. This carbon budget is not significantly impacted by extreme events such as major earthquakes. While the mobilization of soil organic matter happens mostly uniformly across the wide-spanning elevations of the Himalaya, petrogenic OC exported in river sediments is mostly sourced from upstream metasedimentary units. The chemical weathering regime of the Central Himalaya is mainly controlled by the bedrock lithology, revealing local changes in the relative contribution of different chemical weathering pathways.

Zusammenfassung

Das globale Klima ist durch den Austausch von Kohlenstoff zwischen seinen verschiedenen Speichern über mehrere Zeitskalen beeinflusst. Die Erosion und die Verwitterung von Bergketten bilden essentielle Teile des Kohlenstoffzyklus, da sie auf einer Zeitskala von Millionen von Jahren erheblich zu den globalen Kohlenstoffflüssen zwischen der Erdoberfläche und der Erdkruste beitragen. Verschiedene Mechanismen dienen als Kohlenstoffquellen oder –senken und summieren sich zu einem komplexen System, welches das erosive Kohlenstoffbudget einer Bergkette kontrolliert. Erhöhte Bodenerosion in schnell erodierenden Gebirgszügen spielt zudem eine wichtige Rolle für klimatische Schwankungen auf einer Zeitskala von tausend Jahren und ist wichtig Aufrechterhaltung landwirtschaftilcher Böden.

In dieser Doktorarbeit beschäftige ich mich mit verschiedenen Aspekten der Kohlenstoffflüsse, die durch die Erosion und die Verwitterung des Zentralhimalayas angetrieben werden. Diese tektonisch aktive Bergkette ist durch hohe Erosionsraten charakterisiert und die grossen Mengen an Flusssedimenten und gelösten Stoffen, die jährlich von nepalesischen Flüssen exportiert werden, sind von globaler Bedeutung. Im ersten Teil dieser Arbeit definiere ich das Kohlenstoffbudget der Erosion des Zentralhimlayas und evaluiere die Auswirkungen eines starken Erdbebens auf dieses Budget. Mit einem Set täglicher Proben von suspendiertem Sediment aus einem grossen Fluss des Himalayas quantifiziere ich den Export von organischem Kohlenstoff durch Radiokohlenstoffdatierung und durch die Ermittlung der totalen Konzentration an organischem Kohlenstoff. Mithilfe der Ionenkonzentrationen in täglichen Wasserproben vom gleichen Fluss berechne ich chemische Verwitterungsraten. Ich zeige, dass die Erosion des Zentralhimalayas als Kohlenstoffsenke dient und dass die Kohlenstoffflüsse nicht signifikant von co-seismischen Erdrutschen des Erdbebens Gorkha im Jahr 2015 (7.8 auf der Momenten-Magnituden-Skala) beeinflusst wurden.

Im zweiten Teil studiere ich die Anwendung von brGDGTs (branched Glycerol Dialkyl Glycerol Tetraethers), ein Biomarker aus Böden, als Indikator der Höhe, auf welcher organischer Kohlenstoff aus Böden auf einer Skala von weitläufigen Einzugsgebieten im Himalaya mobilisiert wird. Unsere Resultate von brGDGTs in Böden und Flusssedimenten zeigen, dass die organische Substanz aus Böden, welche in Flusssedimenten transportiert wird, vorwiegend die durchschnittliche Höhe der bodenbedeckten Einzugsgebiete reflektiert. Die Resultate einer inversen Modellierung des Datensets suggerieren, dass fluvialer Export von organischer Substanz aus Böden übergreifend auf allen Höhen des Zentralhimalayas geschieht und dass dieser Export nicht durch anthropogene Eingriffe beeinflusst wird.

Weiter untersuche ich die strukturelle Diversität und die Hauptquelle von petrogenem organischen Kohlenstoff in Flusssedimenten des Himalayas. Die Charakterisierung von petrogenem organischen Kohlenstoff durch Raman Spektroskopie ergibt eine breite Diversität der strukturellen Ordnung dieses Materials. Dies hebt die Wichtigkeit einer systematischen Studie von petrogenem organischen Material in Flusssedimenten hervor. Ich zeige, dass petrogener organischer Kohlenstoff in suspendierten Sedimenten des Zentralhimalayas vorwiegend aus einer flussaufwärts gelegenen Sequenz von Metasedimenten stammt und dass die Oxidierung dieses Materials im Fluss vernachlässigbar ist.

Im letzten Kapitel wird die Verteilung von chemischer Verwitterung in ihre verschiedenen Prozesse in 28 Einzugsgebieten Nepals studiert. Ich teste die Anwendung von radiogenen und stabilen Kohlenstoffisotopen an gelöstem inorganischen Kohlenstoff, sowie Schwefelisotope an Sulfaten und Ionenkonzentrationen in Flusswasserproben für die Nachverflogung von Prozessen der chemischen Verwitterung. Eine inverse Modellierung der Daten weist auf einen starken lithologischen Einfluss und auf die Wichtigkeit der Verwitterung von Karbonaten und Silikaten durch Schwefelsäure hin.

Zusammenfassend zeigt diese Doktorarbeit, dass der stark erodierende Himalaya als Kohlenstoffsenke relativ zu Erdoberfläche wirkt. Dieses Kohlenstoffbudget wurde durch ein grosses Erdbeben nicht signifikant beeinträchtigt. Während die Mobilisierung von organischem Kohlenstoff in Böden auf allen Höhen des Zentralhimalayas verteilt geschieht, scheint der petrogene organische Kohlenstoff vor allem aus einer flussaufwärts gelegenen metasedimentären Schicht zu kommen. Die chemische Verwitterung im Zentralhimalaya ist vorwiegend über die Lithologie kontrolliert und zeigt lokale Heterogenitäten in der relativen Kontribution von verschiedenen Prozessen der chemischen Verwitterung.

Table of contents

1

Introduction

Motivation for this work

While Earth's climate is currently deregulated through anthropogenic activities, the complex interplay of mechanisms controlling the natural climatic balance still remains with many open questions.

Relative to their surface area, rapidly eroding mountain ranges contribute disproportionally to the natural carbon fluxes between the Earth's surface and its crust, and therefore play a key role for the long-term evolution of the global climate (e.g., Galy *et al.*, 2015; Hilton *et al.*, 2014; Hilton and West, 2020; Larsen *et al.*, 2014; Torres *et al.*, 2016). The erosional carbon budget of a mountain range reflects the co-existence of multiple carbon sources and sinks. While the net erosional carbon budget of some environments have been defined (Horan *et al.*, 2019; Hilton and West, 2020), the carbon fluxes and pathways associated with erosion remain difficult to understand. One question arises from the difficulty of integrating calculated carbon fluxes on longer timescales. In some environments, the long-term carbon budget seems to be dominated by the occurrence of extreme events, such as earthquakes, complicating the time-integration of carbon fluxes (Wang *et al.*, 2016; Frith *et al.*, 2018).

Highly erosive mountain environments are particularly vulnerable to soil erosion (e.g., Alewell *et al.*, 2008). The mobilization and riverine export of soil organic matter impacts the global climate on different timescales (decades to millennia and millions of years) (Ludwig *et al.*, 1996; Jacinthe and Lal, 2001; Berhe *et al.*, 2012) and influences the productivity of soils for agricultural use. Despite its importance, only few methods are available to constrain soil organic matter mobilization processes at the catchment scale.

The oxidation of petrogenic organic carbon is one of the less understood parts of the long-term carbon cycle as associated carbon fluxes remain difficult to measure. Oxidation rates of petrogenic organic carbon depend not only on the local climate and erosion rates (Hilton *et al.*, 2014), but also on inherent properties of the petrogenic organic carbon material (Galvez *et al.*, 2020), complicating estimations of the related CO_2 release.

Carbon fluxes associated with chemical weathering have traditionally been defined with dissolved ion concentrations of river water (Gaillardet *et al.*, 1999; Galy and France-Lanord, 1999). However, the need to distinguish between the two major acids (carbonic and sulfuric acids) involved in chemical weathering reactions and to constrain the source of dissolved sulfate, call for new methods. Recently, Blattmann *et al.* (2019) proposed a novel approach for defining chemical weathering pathways by inverse modelling of the radiocarbon composition of dissolved inorganic carbon coupled to major ion concentrations.

In this thesis, we address different aspects of erosional carbon fluxes and pathways using the example of the Central Himalaya. We define the net carbon budget of the Central Himalaya and test the impact of the 2015 Gorkha earthquake (Mw 7.8) and associated landsliding on the erosional carbon fluxes. Using brGDGTs (branched Glycerol Dialkyl Glycerol Tetraethers), a soil biomarker, we trace the origin of soil organic carbon exported in river sediments, which allows us to define the preferential locations of soil organic matter mobilization in the Central Himalaya. Further, we characterize the structural diversity of petrogenic organic carbon entrained in suspended sediments aiming to better understand oxidation rates of petrogenic organic carbon in the Central Himalaya. Finally, we test the application of radiocarbon

signatures of dissolved inorganic carbon for constraining chemical weathering pathways across the Nepalese Himalaya.

The geological carbon cycle

The concentration of carbon dioxide (CO_2) in the atmosphere is an important regulator of the global climate. On timescales of millions of years the atmospheric CO_2 concentration is modulated by the fluxes between the carbon reservoirs of the Earth's surface and the Earth's crust. Different carbon sources and sinks to and from the Earth's surface maintain the complex and slowly changing balance of the carbon cycle and thus of the global climate. Acting as the main carbon sources, volcanic activity and metamorphic degassing release around 155-185 megatons (Mt) of carbon (C) per year to the Earth's surface (Kerrick and Caldeira, 1998; Becker *et al.*, 2008; Plank and Manning, 2019). These important fluxes require the presence of efficient mechanisms of carbon drawdown to counterbalance the carbon sources to the Earth's surface and maintain a relatively stable atmospheric CO_2 concentration.

Two pathways, an organic and an inorganic one, have been identified as main carbon sinks from the Earth's surface. For the first mechanism, biospheric organic carbon (OC_{bio}, Table 1, reaction 1) produced in the oceans or on the continents is considered. Continental OC_{bio} is mostly derived from soil organic matter and is transferred through erosion and riverine transport to continental margins. While most of the OC_{bio} is respired during transport or in the ocean, a small part escapes oxidation and is buried in marine sediments (Berner, 1982; France-Lanord and Derry, 1994, 1997; Burdige, 2005; Galy *et al.*, 2007). Burial and subsequent diagenesis locks the OC_{bio} in the lithospheric carbon reservoir for millions of years (Table 1, reaction 2).

The inorganic carbon drawdown acts through the weathering of silicate minerals with carbonic acid (Table 1, reaction 4). The ions and alkalinity produced through this reaction are exported in rivers. In the oceans they can precipitate as carbonate minerals and thus transfer carbon to the Earth's crust (Ebelmen, 1845; Walker *et al.*, 1981; Berner and Canfield, 1989) (Table 1, reaction 6). Silicate weathering has been estimated to drawdown between 130-380 Mt carbon annually (Gaillardet *et al.*, 1999; Moon *et al.*, 2014), while around 170 Mt biospheric OC is buried in marine sediments annually (Hedges and Keil, 1995; Burdige, 2007). However, these fluxes as well as the relative importance of the organic and the inorganic carbon sinks remain unclear (e.g., Hilton and West, 2020).

Erosion and chemical weathering not only promote the drawdown of carbon, but also include mechanisms that add to the carbon sources to the Earth's surface. The oxidative weathering of petrogenic, or rock-derived, organic carbon (OC_{petro}) releases CO_2 to the atmosphere (Berner and Canfield, 1989; Petsch, 2014; Galvez *et al.*, 2020) (Table 1, reaction 3). The oxidation of OC_{petro} can likely take place through abiotic and biotic weathering on hillslopes or in floodplains (Petsch *et al.*, 2000, 2001; Galy *et al.*, 2008a; Hemingway *et al.*, 2018). Additionally, oxidation rates are to a large part controlled by the inherent structural and

reactive diversity of the OC_{petro} material mostly depending on the degree of metamorphism the host rock underwent (Galvez *et al.*, 2020).

(1) Organic carbon formation through photosynthesis

$$CO_2 + H_2O + \text{light} \rightarrow CH_2O + O_2$$

(2) First diagenetic transformation of OC through burial

$$CH_2O \rightarrow + CO_2 + H_2O + \text{kerogen}$$

(3) Oxidation of petrogenic OC

$$OC_{petro} + O_2 \rightarrow CO_2$$

(4) Silicate weathering with carbonic acid

$$CaSiO_3 + 2CO_2 + H_2O \rightarrow Ca^{2+} + 2HCO_3^- + SiO_2$$

(5) Carbonate weathering with sulfuric acid

$$CaCO_3 + 0.5\ H_2SO_4 \rightarrow Ca^{2+} + HCO_3^- + 0.5\ SO_4^{2-}$$

(6) Carbonate precipitation in oceans

$$Ca^{2+} + 2HCO_3^- \rightarrow CaCO_3 + CO_2 + H_2O$$

Table 1: *Major reactions involved in the long-term carbon cycle.*

On the other hand, the chemical weathering of carbonate minerals with sulfuric acid also acts as a carbon source to the atmosphere (Calmels *et al.*, 2007; Torres *et al.*, 2014; Burke *et al.*, 2018) (Table 1, reaction 5). Sulfuric acid is the weathering product of sulfide minerals, such as pyrite. The dissolution of carbonates by sulfuric acid leads to a CO_2 release during subsequent carbonate precipitation in the ocean (Calmels *et al.*, 2007; Torres *et al.*, 2014) (Table 1, reaction 6). On timescales shorter than the residence time of sulfur in the ocean (5-10 Myrs), this reaction acts as a carbon source to the Earth's surface (Burke *et al.*, 2018).

The fluxes and relative importance of these different processes modulating the carbon cycle depend on various factors such as the lithology of an environment, its erosion rates and climate. This complex interplay of the different carbon fluxes as well as the controls on the different processes remain with many open questions.

The role of erosion in the carbon cycle

Erosion, the geological process of removing and transporting rocks and soils on the Earth's surface, is a main driver for most of the processes influencing the carbon cycle. Relative to their surface area, steep and wet mountain ranges characterized by high erosion rates contribute disproportionally to the global carbon fluxes (e.g., Galy *et al*., 2015; Hilton *et al.*, 2014; Hilton and West, 2020; Larsen *et al*., 2014; Torres *et al.*, 2016). As such, the concentration of OC in riverine sediments has been shown to positively correlate to the sediment yield of a river (Galy *et al.*, 2015), revealing that the export of OC is at least partly controlled by physical erosion. In active mountain ranges, landslides play an important role in landscape denudation, and thus sediment production (Hovius *et al.*, 1997; Hilton *et al.*, 2012). Together with surface runoff on steep hillslopes (Hilton *et al.*, 2008a) these processes constitute the main drivers for OC export (Hovius *et al.*, 2011). This enhanced production and export of OC-rich sediments not only favors the burial of OC_{bio} (Galy *et al.*, 2015), but also enhances the oxidation rates of OC_{petro} (Hilton *et al.*, 2014).

At the same time, chemical weathering rates are generally enhanced in highly erosive environments through the constant supply of fresh minerals prone to weathering (Gaillardet *et al.*, 1999; West, 2012; Larsen *et al.*, 2014). Fresh landslide scars favor chemical weathering through carbonic and sulfuric acid by exposing pristine bedrock surfaces (Emberson *et al.*, 2016, 2018).

Extreme events, such as floods or earthquakes can significantly increase local erosion rates and are likely to dominate the erosional budget of some environments (e.g., Hilton *et al.*, 2008b; Howarth *et al.*, 2012; Wang *et al.*, 2015, 2020). This raises the question if such extreme events govern the local long-term carbon budgets. Enhanced landsliding rates linked to earthquakes have recently been suggested to significantly influence the carbon fluxes in some environments (Wang *et al.*, 2016; Frith *et al.*, 2018).

Highly erosive environments are also particularly vulnerable to soil erosion processes (e.g., Alewell *et al.*, 2008). Besides representing an important mechanism for the geological carbon cycle, the erosion of soils impacts the cycling of carbon between its different reservoirs on the Earth's surface (the atmosphere, the biosphere and the oceans) on timescales of decades to millennia (e.g., Doetterl *et al*., 2016; Yue *et al.*, 2016). The overall carbon budget of soil erosion on the atmospheric CO_2 concentration remains a subject of debate (Stockmann *et al.*, 2013). It may act either as a carbon source to the atmosphere due to soil organic matter degradation (Schlesinger, 1995; Jacinthe and Lal, 2001) or as a carbon sink through OC sequestration and stabilization (Stallard, 1998; Smith *et al.*, 2001; Berhe *et al.*, 2012).

Rivers as conveyers of terrestrial carbon fluxes to the oceans

Rivers efficiently integrate erosional and chemical weathering processes in their catchments (Niemi *et al.*, 2005; Viers *et al.*, 2009) and represent the main transport vectors for translocation of terrestrial carbon from the continents to the oceans.

Organic carbon can be transported in its dissolved form (dissolved organic carbon - DOC) or as particulate organic carbon (POC) where POC is generally the most important form in highly erosive environments (Lloret *et al.*, 2011). While the burial rate of DOC in the oceans is probably minimal (Bauer and Bianchi, 2012), around 20-45% of the terrestrial POC is buried in marine sediments (Burdige, 2005). Similarly, rivers transport ions and alkalinity produced by chemical weathering on the continents to the ocean (e.g., Gaillardet *et al.*, 1999; Galy and France-Lanord, 1999).

While mountainous rivers transport sediments and solutes without major modifications, large rivers and floodplains can serve as reactors for silicate weathering (Lupker *et al.*, 2012) and for the replacement and oxidation of biospheric OC (Galy *et al.*, 2008b; Freymond *et al.*, 2018). Further, it has also been suggested that floodplains are the major driver for the oxidation of petrogenic OC (Galy *et al.*, 2008a; Bouchez *et al.*, 2014).

The Central Himalaya

General

The Himalaya, the highest mountain range on Earth, serves as an ideal natural laboratory for studying erosional carbon fluxes. The central part of the Himalaya is situated between Nepal and Tibet (Figure 1). The steep valleys of the Central Himalaya are characterized by high erosion rates (Gabet *et al.*, 2008) and the relatively warm climate allows the formation of soils up to high altitudes. Mass wasting processes are the major agents of erosion in the Central Himalaya (Morin *et al.*, 2018; Marc *et al.*, 2019) resulting in the annual export of around 240 Mt of river sediments to the Gangetic floodplain (Andermann *et al.*, 2012). River sediments from the Central Himalaya are transferred through the Gangetic floodplain to the Bay of Bengal (Figure 1b). The latter is characterized by OC burial rates of around 100% and accounts for ~ 15 % of the modern total burial flux of terrestrial OC (France-Lanord and Derry, 1994; Galy *et al.*, 2007), implying that the Ganga-Brahmaputra fluvial system is of global significance for the modern carbon cycle (France-Lanord *et al.*, 1994; Galy and Eglinton, 2011). The transit of Himalayan sediments through the Gangetic floodplain has been proposed to serve as major driver of oxidation of Himalayan OC_{petro} material (Galy *et al.*, 2008a).

Chemical weathering rates in the Central Himalaya are dominated by carbonate dissolution (e.g., Bickle *et al.*, 2015; Galy and France-Lanord, 1999; Tipper *et al.*, 2006). The high abundance of sulfate in large Himalayan rivers suggests that sulfuric acid-mediated weathering of carbonates could be an important pathway of chemical weathering in this region (Tipper *et al.*, 2006; Bickle *et al.*, 2015).

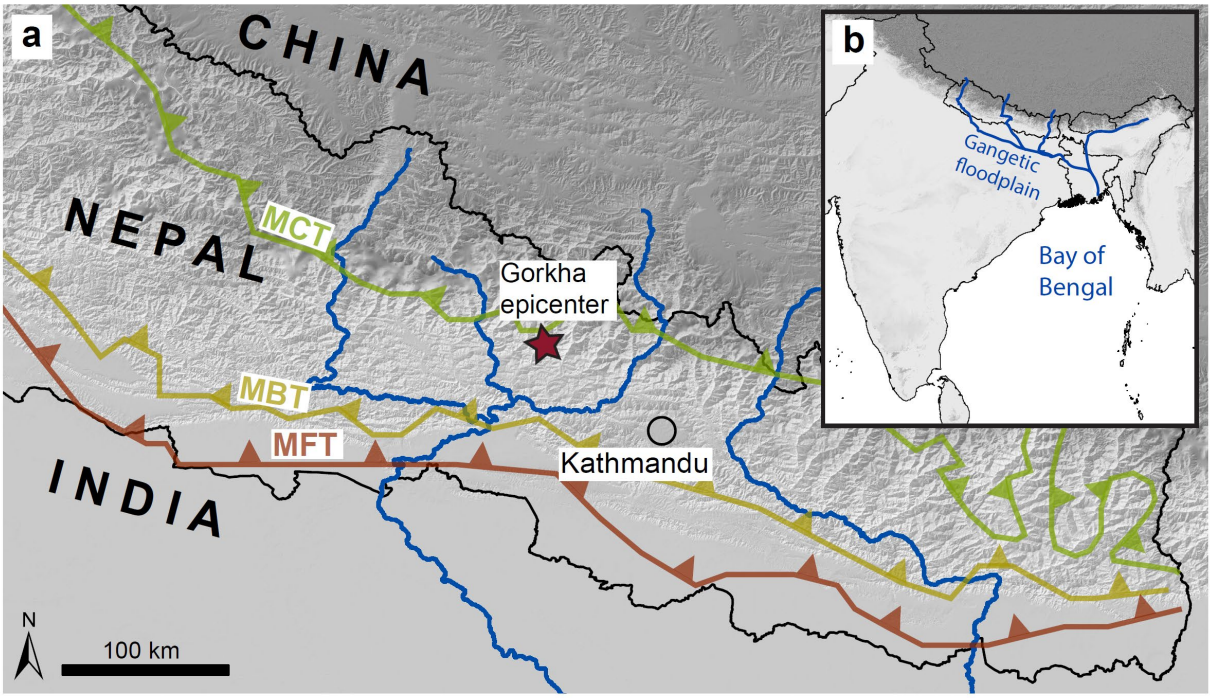

Figure 1: a. *Map of the Central Himalaya. The epicenter of the 2015 Gorkha earthquake and major rivers are shown. Colored lines correspond to the locations of the MFT (main frontal thrust), MBT (main boundary thrust) and the MCT (main central thrust) after Prajapati et al. (2017).* ***b.*** *Overview of the Himalaya, the Gangetic floodplain and the Bay of Bengal.*

Climate

The climate of the Central Himalaya ranges from subtropical in the Himalayan foreland to alpine at high elevations creating large temperature differences over the mountain range. Overall, the climate on the southern flank of the Himalaya is heavily influenced by the Indian summer monsoon. During the summer months of June to September, humid air from the Indian Ocean moves towards the warm landmasses of the Himalaya and creates heavy rainfall. In contrast, in the colder months of the year, dry air from the continent moves to the warmer Indian Ocean leading to a dry Himalayan winter. The monsoonal precipitation is distributed over the Central Himalaya by a strong N-S gradient leading to a humid southern flank and an all-year dry climate on the Tibetan Plateau (Figure 2) (Burbank *et al.*, 2003).

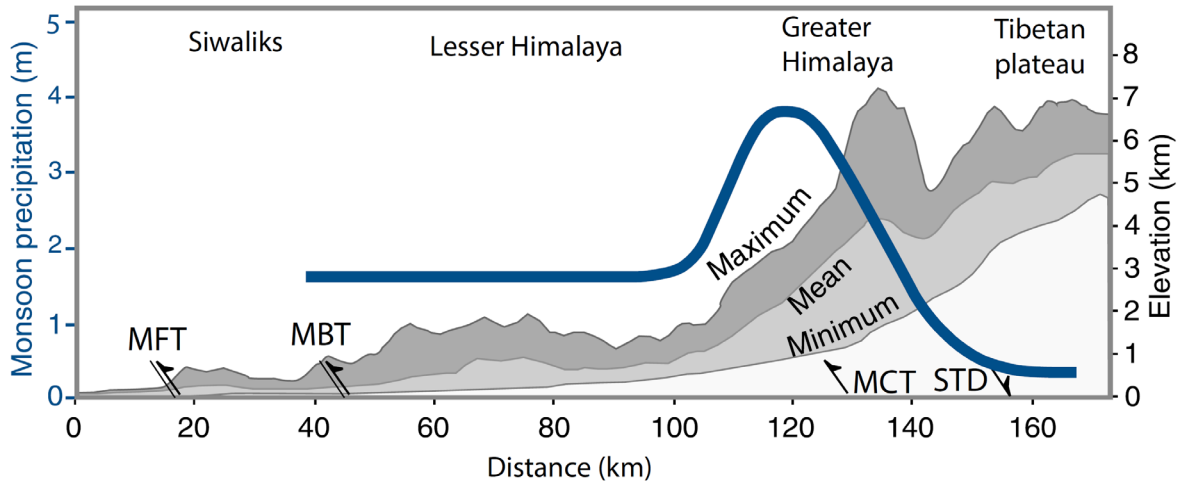

Figure 2: *Topographic profile through the Central Himalaya with maximum, mean and minimum elevations. The total monsoonal precipitation gradient is shown in blue. The locations of the MFT (main frontal thrust), MBT (main boundary thrust), MCT (main central thrust) and the STD (south Tibetan detachment) are schematically indicated. Figure modified from Burbank et al. (2003).*

Geology

The Himalayan mountain range is the result of the collision between the two continental plates of Eurasia and India. The orogeny started about 55 Myrs ago when the northwards moving Indian plate reached Eurasia (Powell and Conaghan, 1973). The resulting subduction and crustal shortening created the 2500 km long Himalayan arc.

A cross section through the central Himalaya shows four main tectonic units (e.g., Le Fort, 1975) (Figure 3): The Siwaliks form the Central Himalayan foothills and are composed of molassic sediments from the erosion of the Himalaya. They are the tectonically most active part in the current Himalayan system with uplift rates of 1.5 cm/yr at the Main Frontal Thrust (MFT) which separates them from the Indo-Gangetic plain (Lavé and Avouac, 2000). The Siwaliks are thrusted under the Lesser Himalaya (LH) by the Main Boundary Thrust (MBT). The LH compromises a series of late Precambrian to early Paleozoic metasediments locally cut by granitic and volcanic intrusions (Stöcklin, 1980). Following an inverted metamorphic gradient, the LH range from low-grade metasedimentary rocks in the south to mid-grade metasediments in the north (e.g., Le Fort, 1975; Gansser, 1964). The Main Central Thrust (MCT) separates the LH from the High Himalayan Crystallines (HHC). The HHC consist of a 30 km thick sequence of highly metamorphosed Precambrian metasediments frequently intruded by leucogranites (Le Fort, 1975). The inverted metamorphic gradient continues in the HHC, with increasing metamorphic peak temperatures stratigraphically upwards (Gansser, 1964; Le Fort, 1975). The South Tibetan Detachment (STD) system thrusted the Tibetan Sedimentary Series (TSS) over these high-grade metamorphic rocks. The TSS are a sequence of metasediments from the Cambrian to Eocene evolution of the Neo-Tethys ocean (Le Fort, 1975; Garzanti, 1999). They range from thick carbonates and pelites at the bottom of the sequence overlain by sand-and mudstones to marly limestones and shales near the top (Garzanti, 1999). The TSS

have undergone a low- to mid-grade metamorphism during the Himalayan orogeny (Le Fort, 1975). The Indus Suture Zone to the north of the TSS defines the zone of collision between the Indian plate and the Ladakh batholith. The three major north dipping thrusts (MFT, MBT and MCT) form the Main Himalayan Thrust (MHT) at depths of around 7 km and are the result of the northward under-thrusting of the Indian plate.

A topographic N-S profile through the Central Himalaya (Figure 2) highlights the contrasted landscape that characterizes this region: the elevation increases abruptly from the Gangetic floodplain at around 0 m asl to the peaks of the High Himalaya which host the highest point on Earth (8848 m asl). In the north of the High Himalayan peaks, the Tibetan Plateau constitutes a flat and vast region at elevations of around 5000 m asl.

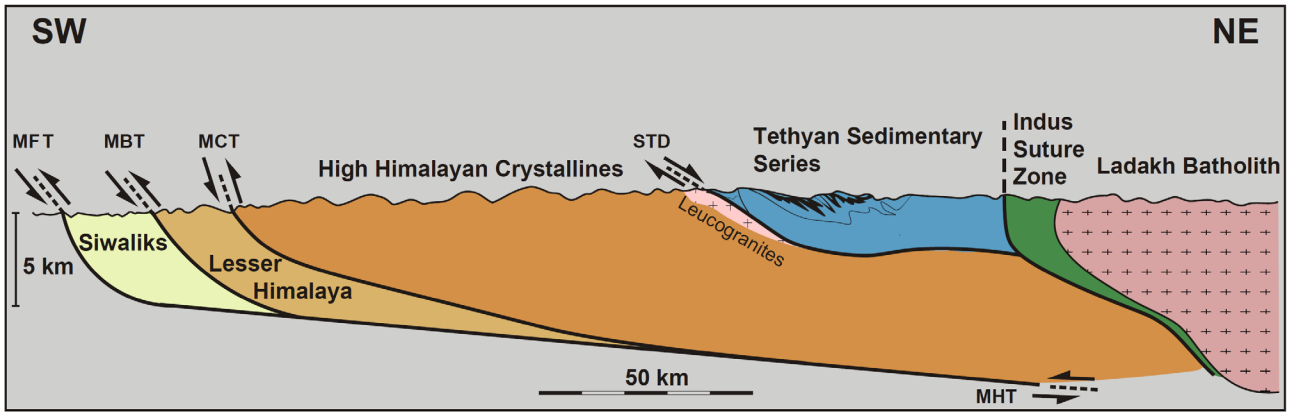

Figure 3: *Cross section through the Central Himalaya with main tectonic units and main thrusts shown. Figure modified from Dèzes (1999).*

The 2015 Gorkha earthquake

On the 25th April 2015 Nepal was hit by the Gorkha earthquake with a moment magnitude Mw 7.8. The epicenter was located near the village of Gorkha, about 80 km northwest of Kathmandu (Figure 1a). The earthquake was followed by a series of large aftershocks including a Mw 7.2 event (Avouac *et al.*, 2015). The shaking was the result of a rupture in the Main Himalayan Thrust, which propagated around 140 km eastward (Avouac *et al.*, 2015). The earthquake killed 8964 people, injured many more and caused massive damage to infrastructure. During the Gorkha earthquake, more than 25'000 landslides were triggered in the steep valleys of the Himalaya (Roback *et al.*, 2018).

Thesis outline

This thesis is divided in the following four chapters presenting the main results of this work.

In **chapter 2**, we define the organic and inorganic carbon fluxes of erosion in the catchment of the Narayani River, a major outlet of the Nepalese Himalaya. Furthermore, we address the influence of a major earthquake on this erosional carbon budget of the Central Himalaya.

Chapter 3 aims to trace the origin of soil organic carbon entrained in riverine sediments of the Central Himalaya. Signatures of brGDGTs (branched Glycerol Dialkyl Glycerol Tetraethers), a soil biomarker, in Himalayan soils are used to trace the altitudinal origin of brGDGTs in river suspended sediments.

The structural diversity of petrogenic organic carbon exported in rivers of the Central Himalaya is characterized in **chapter 4**. With Raman spectroscopy, we define the degree of structural ordering of riverine petrogenic organic carbon which allows us to trace its main source region and study its fate during transport in a trans-Himalayan river.

Chapter 5 presents results of an inverse model of isotopic measurements on dissolved inorganic carbon and sulfate aiming to trace chemical weathering pathways in the Central Himalaya. We show that radiocarbon signature of dissolved inorganic carbon is a useful tracer of chemical weathering processes and discuss the main controls on weathering pathways across the Central Himalaya.

The conclusions of this thesis are outlined in **chapter 6**, together with an outlook for future studies.

References

Alewell, C., Meusburger, K., Brodbeck, M. & Bänninger, D. (2008). Methods to describe and predict soil erosion in mountain regions. *Landscape and Urban Planning* **88**, 46–53.

Andermann, C., Crave, A., Gloaguen, R. & Davy, P. (2012). Connecting source and transport : Suspended sediments in the Nepal Himalayas. *Earth and Planetary Science Letters* **352**, 158–170.

Avouac, J.-P., Meng, L., Wei, S., Wang, T. & Ampuero, J.-P. (2015). Lower edge of locked Main Himalayan Thrust unzipped by the 2015 Gorkha earthquake. *Nature Geoscience* **8**, 708–711.

Bauer, J. E. & Bianchi, T. S. (2012). *Dissolved Organic Carbon Cycling and Transformation*. *Treatise on Estuarine and Coastal Science*. Elsevier Inc.

Becker, J. A., Bickle, M. J., Galy, A. & Holland, T. J. B. (2008). Himalayan metamorphic CO2 fluxes: Quantitative constraints from hydrothermal springs. *Earth and Planetary Science Letters*. Elsevier B.V. **265**, 616–629.

Berhe, A. A., Harden, J. W., Torn, M. S., Kleber, M., Burton, S. D. & Harte, J. (2012). Persistence of soil organic matter in eroding versus depositional landform positions. *Journal of Geophysical Research: Biogeosciences* **117**, 1–16.

Berner, R. A. (1982). Burial of organic carbon and pyrite sulfur in the modern ocean: its geochemical and environmental significance. *American Journal of Science* **282**, 451–473.

Berner, R. A. & Canfield, D. E. (1989). A new model for atmospheric oxygen over Phanerozoic time. *American Journal of Science*, 333–361.

Bickle, M. J., Tipper, E., Galy, A., Chapman, H. & Harris, N. (2015). On discrimination between carbonate and silicate inputs to Himalayan rivers. *American Journal of Science* **315**, 120–166.

Bouchez, J., Galy, V., Hilton, R. G., Gaillardet, J., Moreira-Turcq, P., Perez, M. A., France-Lanord, C. & Maurice, L. (2014). Source , transport and fluxes of Amazon River particulate organic carbon : Insights from river sediment depth-profiles. *Geochimica et Cosmochimica Acta* **133**, 280–298.

Burbank, D. W., Blythe, A. E., Putkonen, J. L., Pratt-Situala, B. A., Gabet, E. J., Oskin, M. E., Barros, A. P. & Ohja, T. P. (2003). Decoupling of erosion and climate in the Himalaya. *Nature* **426**, 652–655.

Burdige, D. J. (2005). Burial of terrestrial organic matter in marine sediments: A re-assessment. *Global Biogeochemical Cycles* **19**, 1–7.

Burdige, D. J. (2007). Preservation of organic matter in marine sediments: Controls, mechanisms, and an imbalance in sediment organic carbon budgets? *Chemical Reviews* **107**, 467–485.

Burke, A. *et al.* (2018). Sulfur isotopes in rivers : Insights into global weathering budgets, pyrite oxidation, and the modern sulfur cycle. *Earth and Planetary Science Letters*. Elsevier B.V. **496**, 168–177.

Calmels, D., Gaillardet, J., Brenot, A. & France-Lanord, C. (2007). Sustained sulfide oxidation by physical erosion processes in the Mackenzie River basin: Climatic perspectives. *Geology* **35**, 1003–1006.

Dèzes, P. (1999). *Tectonic and Metamorphic evolution of the Central Himalayan domain in southeast Zanskar*. *zanskar.geoheritage.ch*.

Doetterl, S., Berhe, A. A., Nadeu, E., Wang, Z., Sommer, M. & Fiener, P. (2016). Erosion, deposition and soil carbon: A review of process-level controls, experimental tools and models to address C cycling in dynamic landscapes. *Earth-Science Reviews*. Elsevier B.V. **154**, 102–122.

Ebelmen, J. (1845). Sur les produits de la décomposition des especes minérales de la famille des silicates. *Annal des Mines* **7**, 3–66.

Emberson, R., Galy, A. & Hovius, N. (2018). Weathering of Reactive Mineral Phases in Landslides Acts as a Source of Carbon Dioxide in Mountain Belts. *Journal of Geophysical Research: Earth Surface* **123**, 2695–2713.

Emberson, R., Hovius, N., Galy, A. & Marc, O. (2016). Chemical weathering in active mountain belts controlled by stochastic bedrock landsliding. *Nature Geoscience* **9**, 42–45.

France-Lanord, C. & Derry, L. A. (1994). δ13C of organic carbon in the Bengal Fan: Source evolution and transport of C3 and C4 plant carbon to marine sediments. *Geochimica et Cosmochimica Acta* **58**, 4809–4814.

France-Lanord, C. & Derry, L. A. (1997). Organic carbon burial forcing of the carbon cycle from Himalayan erosion. *Nature* **390**, 65–67.

Freymond, C. V. *et al.* (2018). Evolution of biomolecular loadings along a major river system. *Geochimica et Cosmochimica Acta* **223**, 389–404.

Frith, N. V *et al.* (2018). Carbon export from mountain forests enhanced by earthquake-triggered landslides over

millennia. *Nature Geoscience* **11**, 772–776.
Gabet, E. J., Burbank, D. W., Pratt-Sitaula, B., Putkonen, J. & Bookhagen, B. (2008). Modern erosion rates in the High Himalayas of Nepal. *Earth and Planetary Science Letters* **267**, 482–494.
Gaillardet, J., Dupré, B., Louvat, P. & Allègre, C. J. (1999). Global silicate weathering and CO2 consumption rates deduced from the chemistry of large rivers. *Chemical Geology* **159**, 3–30.
Galvez, M. E., Fischer, W. W., Jaccard, S. L. & Eglinton, T. I. (2020). Materials and pathways of the organic carbon cycle through time. *Nature Geoscience*. Springer US **13**, 535–546.
Galy, A. & France-Lanord, C. (1999). Weathering processes in the Ganges-Brahmaputra basin and the riverine alkalinity budget. *Chemical Geology* **159**, 31–60.
Galy, V., Beyssac, O., France-Lanord, C. & Eglinton, T. (2008a). Recycling of graphite during Himalayan erosion: a geological stabilization of carbon in the crust. *Science* **322**, 943–945.
Galy, V. & Eglinton, T. (2011). Protracted storage of biospheric carbon in the Ganges–Brahmaputra basin. *Nature Geoscience*. Nature Publishing Group **4**, 843–847.
Galy, V., France-Lanord, C., Beyssac, O., Faure, P., Kudrass, H. & Palhol, F. (2007). Efficient organic carbon burial in the Bengal fan sustained by the Himalayan erosional system. *Natural Hazards and Earth System Science* 407–411.
Galy, V., France-Lanord, C. & Lartiges, B. (2008b). Loading and fate of particulate organic carbon from the Himalaya to the Ganga-Brahmaputra delta. *Geochimica et Cosmochimica Acta* **72**, 1767–1787.
Galy, V., Peucker-Ehrenbrink, B. & Eglinton, T. (2015). Global carbon export from the terrestrial biosphere controlled by erosion. *Nature* **521**, 204–207.
Gansser, A. (1964). Geology of the Himalayas. *Interscience*.
Garzanti, E. (1999). Stratigraphy and sedimentary history of the Nepal Tethys Himalaya passive margin. *Journal of Asian Earth Sciences* **17**, 805–827.
Hedges, J. I. & Keil, R. G. (1995). Sedimentary organic matter preservation: an assessment and speculative synthesis. *Marine Chemistry* **49**, 81–115.
Hemingway, J. D., Hilton, R. G., Hovius, N., Eglinton, T. I., Haghipour, N., Wacker, L., Chen, M. & Galy, V. V (2018). Microbial oxidation of lithospheric organic carbon in rapidly eroding tropical mountain soils. *Science* **360**, 209–212.
Hilton, R. G., Gaillardet, J., Calmels, D. & Birck, J. L. (2014). Geological respiration of a mountain belt revealed by the trace element rhenium. *Earth and Planetary Science Letters*. Elsevier B.V. **403**, 27–36.
Hilton, R. G., Galy, A. & Hovius, N. (2008a). Riverine particulate organic carbon from an active mountain belt: Importance of landslides. *Global Biogeochemical Cycles* **22**, 1–12.
Hilton, R. G., Galy, A., Hovius, N., Chen, M.-C., Horng, M.-J. & Chen, H. (2008b). Tropical-cyclone-driven erosion of the terrestrial biosphere from mountains. *Nature Geoscience* **1**, 759–762.
Hilton, R. G., Galy, A., Hovius, N., Kao, S. J., Horng, M. J. & Chen, H. (2012). Climatic and geomorphic controls on the erosion of terrestrial biomass from subtropical mountain forest. *Global Biogeochemical Cycles* **26**, 1–12.
Hilton, R. G. & West, A. J. (2020). Mountains, erosion and the carbon cycle. *Nature Reviews Earth & Environment*. Springer US **1**, 284–299.
Horan, K. *et al.* (2019). Carbon dioxide emissions by rock organic carbon oxidation and the net geochemical carbon budget of the Mackenzie River Basin. *American Journal of Science* **319**, 473–499.
Hovius, N., Galy, A., Hilton, R. G., Sparkes, R., Smith, J., Shuh-Ji, K., Hongey, C., In-Tian, L. & Joshua West, A. (2011). Erosion-driven drawdown of atmospheric carbon dioxide: The organic pathway. *Applied Geochemistry*. Elsevier Ltd **26**, S285–S287.
Hovius, N., Stark, C. P. & Allen, P. A. (1997). Sediment flux from a mountain belt derived by landslide mapping. *Geology* **25**, 231–234.
Howarth, J. D., Fitzsimons, S. J., Norris, R. J. & Jacobsen, G. E. (2012). Lake sediments record cycles of sediment flux driven by large earthquakes on the Alpine fault , New Zealand. *Geology* **40**, 1091–1094.
Jacinthe, P. A. & Lal, R. (2001). A mass balance approach to assess carbon dioxide evolution during erosional events. *Land Degradation and Development* **12**, 329–339.
Kerrick, D. M. & Caldeira, K. (1998). Metamorphic CO2 degassing from orogenic belts. *Chemical Geology* **145**, 213–232.
Larsen, I. J., Montgomery, D. R. & Greenberg, H. M. (2014). The contribution of mountains to global denudation. *Geology* **42**, 527–530.

Lavé, J. & Avouac, J.-P. (2000). Active folding of fluvial terraces across the Siwaliks Hills , Himalayas of central Nepal Precambrian. *Journal of Geophysical Research* **105**, 5735–5770.

Le Fort, P. (1975). Himalayas: the collided range. Present knowledge of the continental arc. *American Journal of Science*, 1–44.

Lloret, E., Dessert, C., Gaillardet, J., Albéric, P., Crispi, O., Chaduteau, C. & Benedetti, M. F. (2011). Comparison of dissolved inorganic and organic carbon yields and fl uxes in the watersheds of tropical volcanic islands , examples from Guadeloupe (French West Indies). *Chemical Geology*. Elsevier B.V. **280**, 65–78.

Ludwig, W., Probst, J. L. & Kempe, S. (1996). Predicting the oceanic input of organic carbon by continental erosion. *Global Biogeochemical Cycles* **10**, 23–41.

Lupker, M. *et al.* (2012). Predominant floodplain over mountain weathering of Himalayan sediments (Ganga basin). *Geochimica et Cosmochimica Acta* **84**, 410–432.

Marc, O., Behling, R., Andermann, C., Turowski, J. M., Illien, L., Roessner, S. & Hovius, N. (2019). Long-term erosion of the Nepal Himalayas by bedrock landsliding: The role of monsoons, earthquakes and giant landslides. *Earth Surface Dynamics* **7**, 107–128.

Moon, S., Chamberlain, C. P. & Hilley, G. E. (2014). New estimates of silicate weathering rates and their uncertainties in global rivers. *Geochimica et Cosmochimica Acta*. Elsevier Ltd **134**, 257–274.

Morin, G. P., Lavé, J., France-Lanord, C., Rigaudier, T., Gajurel, A. P. & Sinha, R. (2018). Annual Sediment Transport Dynamics in the Narayani Basin, Central Nepal: Assessing the Impacts of Erosion Processes in the Annual Sediment Budget. *Journal of Geophysical Research: Earth Surface* **123**, 2341–2376.

Niemi, N. A., Oskin, M., Burbank, D. W., Heimsath, A. M. & Gabet, E. J. (2005). Effects of bedrock landslides on cosmogenically determined erosion rates. *Earth and Planetary Science Letters* **237**, 480–498.

Petsch, S. T. (2014). Weathering of organic carbon. *Treatise on Geochemistry* **12**, 217–238.

Petsch, S. T., Berner, R. A. & Eglinton, T. I. (2000). A field study of the chemical weathering of ancient sedimentary organic matter. *Organic Geochemistry* **31**, 475–487.

Petsch, S. T., Eglinton, T. I. & Edwards, K. J. (2001). 14C-dead living biomass: Evidence for microbial assimilation of ancient organic carbon during shale weathering. *Science* **292**, 1127–1131.

Plank, T. & Manning, C. E. (2019). Subducting carbon. *Nature*. Springer US **574**, 343–352.

Powell, C. M. & Conaghan, P. J. (1973). Plate tectonics and the Himalayas. *Earth and Planetary Science Letters* **20**, 1–12.

Prajapati, S. K., Dadhich, H. K. & Chopra, S. (2017). Isoseismal map of the 2015 Nepal earthquake and its relationships with ground-motion parameters, distance and magnitude. *Journal of Asian Earth Sciences*. Elsevier Ltd **133**, 24–37.

Roback, K., Clark, M. K., West, A. J., Zekkos, D., Li, G., Gallen, S. F., Chamlagain, D. & Godt, J. W. (2018). The size, distribution, and mobility of landslides caused by the 2015 Mw7.8 Gorkha earthquake, Nepal. *Geomorphology*. The Authors **301**, 121–138.

Schlesinger, W. H. (1995). Soil respiration and changes in soil carbon stocks. *Biotic feedbacks in the global climatic system: will the warming feed the warming, Oxford Univ. Press* 159–168.

Smith, S. V., Renwick, W. H., Buddemeier, R. W. & Crossland, C. J. (2001). Budgets of soil erosion and deposition for sediments and sedimentary organic carbon across the posited across the United States. *Global Biogeochemical Cycles* **15**, 697–707.

Stallard, R. F. (1998). Terrestrial sedimentation and the carbon cycle : Coupling weathering and erosion to carbon burial. *Water Resources* **12**, 231–257.

Stöcklin, J. (1980). Geology of Nepal and its regional frame. *Journal of Geological Society London* **137**, 1–34.

Stockmann, U. *et al.* (2013). The knowns, known unknowns and unknowns of sequestration of soil organic carbon. *Agriculture, Ecosystems and Environment*. Elsevier B.V. **164**, 80–99.

Tipper, E. T., Bickle, M. J., Galy, A., West, A. J., Pomiès, C. & Chapman, H. J. (2006). The short term climatic sensitivity of carbonate and silicate weathering fluxes: Insight from seasonal variations in river chemistry. *Geochimica et Cosmochimica Acta* **70**, 2737–2754.

Torres, M. A., West, A. J., Clark, K. E., Paris, G., Bouchez, J., Ponton, C., Feakins, S. J., Galy, V. & Adkins, J. F. (2016). The acid and alkalinity budgets of weathering in the Andes–Amazon system: Insights into the erosional control of global biogeochemical cycles. *Earth and Planetary Science Letters*. Elsevier B.V. **450**, 381–391.

Torres, M. A., West, A. J. & Li, G. (2014). Sulphide oxidation and carbonate dissolution as a source of CO2 over geological timescales. *Nature*. Nature Publishing Group **507**, 346–349.

Viers, J., Dupré, B. & Gaillardet, J. (2009). Chemical composition of suspended sediments in World Rivers: New insights from a new database. *Science of the Total Environment*. Elsevier B.V. **407**, 853–868.

Walker, J. C. G., Hays, P. B. & Kasting, J. F. (1981). A negative feedback mechanism for the long-term stabilization of Earth's surface temperature. *Journal of Geophysical Research: Oceans* **86**, 9776–9782.

Wang, J. *et al.* (2020). Long-term patterns of hillslope erosion by earthquake-induced landslides shape mountain landscapes. *Science Advances* **6**, 1–10.

Wang, J., Jin, Z., Hilton, R. G., Zhang, F., Densmore, A. L., Li, G. & Joshua West, A. (2015). Controls on fluvial evacuation of sediment from earthquake-triggered landslides. *Geology*. Geological Society of America **43**, 115–118.

Wang, J., Jin, Z., Hilton, R. G., Zhang, F., Li, G., Densmore, A. L., Gröcke, D. R., Xu, X. & Joshua West, A. (2016). Earthquake-triggered increase in biospheric carbon export from a mountain belt. *Geology* **44**, 471–474.

West, A. J. (2012). Thickness of the chemical weathering zone and implications for erosional and climatic drivers of weathering and for carbon-cycle feedbacks. *Geology* **40**, 811–814.

Yue, Y. *et al.* (2016). Lateral transport of soil carbon and land-atmosphere CO2 flux induced by water erosion in China. *Proceedings of the National Academy of Sciences of the United States of America* **113**, 6617–6622.

2

An unshakable carbon budget for the Himalaya

Lena Märki[1], Maarten Lupker[1], Christian France-Lanord[2], Jérôme Lavé[2], Sean Gallen[3], Ananta P. Gajurel[4], Negar Haghipour[1,5], Fanny Leuenberger-West[1], Timothy Eglinton[1]

[1] Geological Institute, ETH Zürich, Switzerland
[2] CRPG, CNRS – Université de Lorraine, France
[3] Department of Geosciences, Colorado State University, USA
[4] Department of Geology, Tribhuvan University, Nepal
[5] Ion Beam Physics, ETH Zürich, Switzerland

In Review in *Nature Geoscience*

The erosion and weathering of mountain ranges exert a key control on the long-term (10^5-10^6 yr) cycling of carbon between the Earth's surface and the crust. The net carbon budget of a mountain range reflects the co-existence of multiple carbon sources and sinks with corresponding fluxes remaining difficult to quantify. Uncertain responses of these carbon fluxes to the stochastic nature of erosional processes further complicates the extrapolation of short-term observations to longer, climatically relevant timescales. Here, we quantify the evolution of the organic and inorganic carbon fluxes in response to the 2015 Gorkha earthquake (Mw 7.8) in the Central Himalaya. We find that the Himalayan erosion acts as a net carbon sink due to the dominance of silicate weathering and biospheric organic carbon export. Our high-resolution time-series encompassing four monsoon seasons before and after the Gorkha earthquake reveal that coseismic landslides did not significantly perturb large-scale Himalayan sediment and carbon fluxes. This muted response of the Central Himalaya to a geologically-frequent perturbation such as the Gorkha earthquake further suggests that our estimates are representative on timescales of at least interglacials.

Mountain building and associated erosion are major actors in the cycling of carbon between the reservoirs of the Earth's surface and the crust, controlling the long-term evolution of the global climate. The weathering of silicate minerals coupled to carbonate precipitation in the oceans, as well as the erosion, riverine transport and burial of biospheric Organic Carbon (OC) on continental margins represent major carbon sinks with respect to the Earth's surface[1,2]. While both mechanisms are enhanced in highly erosive environments such as the Himalaya[3–5], their relative importance remains unclear. Enhanced silicate weathering rates associated with the uplift of the Himalaya were initially suggested as the main driver of the global Cenozoic cooling[6], but more recent work shows the importance of the organic pathway in the Himalayan carbon budget[7,8].

Globally, these carbon sinks are counterbalanced by CO_2 emissions from volcanic activity and metamorphic reactions, the latter constituting an important carbon source in the Central Himalaya[9]. While these carbon sources are not directly related to erosion, other, yet poorly constrained, mechanisms of carbon release during erosion have been identified. The oxidation of rock-derived organic carbon[1,10] and sulfuric acid-mediated weathering of carbonate rocks[11] have the potential to offset the previously mentioned carbon sinks[5]. Chemical weathering in the Central Himalaya is dominated by the dissolution of carbonates[12], and it has been shown that the sulfide oxidation coupled to carbonate weathering is likely an important carbon source in this environment[12,13]. Defining the carbon budget of Himalayan erosion, therefore, requires quantification and comparison of all of the above-mentioned sources and sinks.

While the carbon fluxes associated with the erosion of various mountain ranges have been estimated[5,14], their integration over longer timescales remains challenging due to the stochastic nature of erosional processes dominating sediment and solute fluxes in most mountainous landscapes. This is especially

important regarding the proposition that extreme events such as earthquakes or floods could dominate the long-term budget of erosional carbon fluxes[15–17]. Large earthquakes, coupled with coseismic landsliding, in particular, have been shown to increase the riverine OC export[18,19], and fresh landslide scars can serve as loci for enhanced chemical weathering rates of silicates and sulfide oxidation[20,21].

In the tectonically active Central Himalaya, major earthquakes are geologically-frequent events with return times of 250-500 years[22]. As these events are still rare on an observational timescale, their impact on the carbon budget of the Himalaya is unknown. In April 2015, the Central Nepalese Himalaya was hit by the Mw 7.8 Gorkha earthquake and several strong to major aftershocks[23]. The fault rupture propagated from the epicenter eastward and caused > 25,000 coseismic landslides in the steep valleys of the Upper Himalaya[24] (Fig. 1).

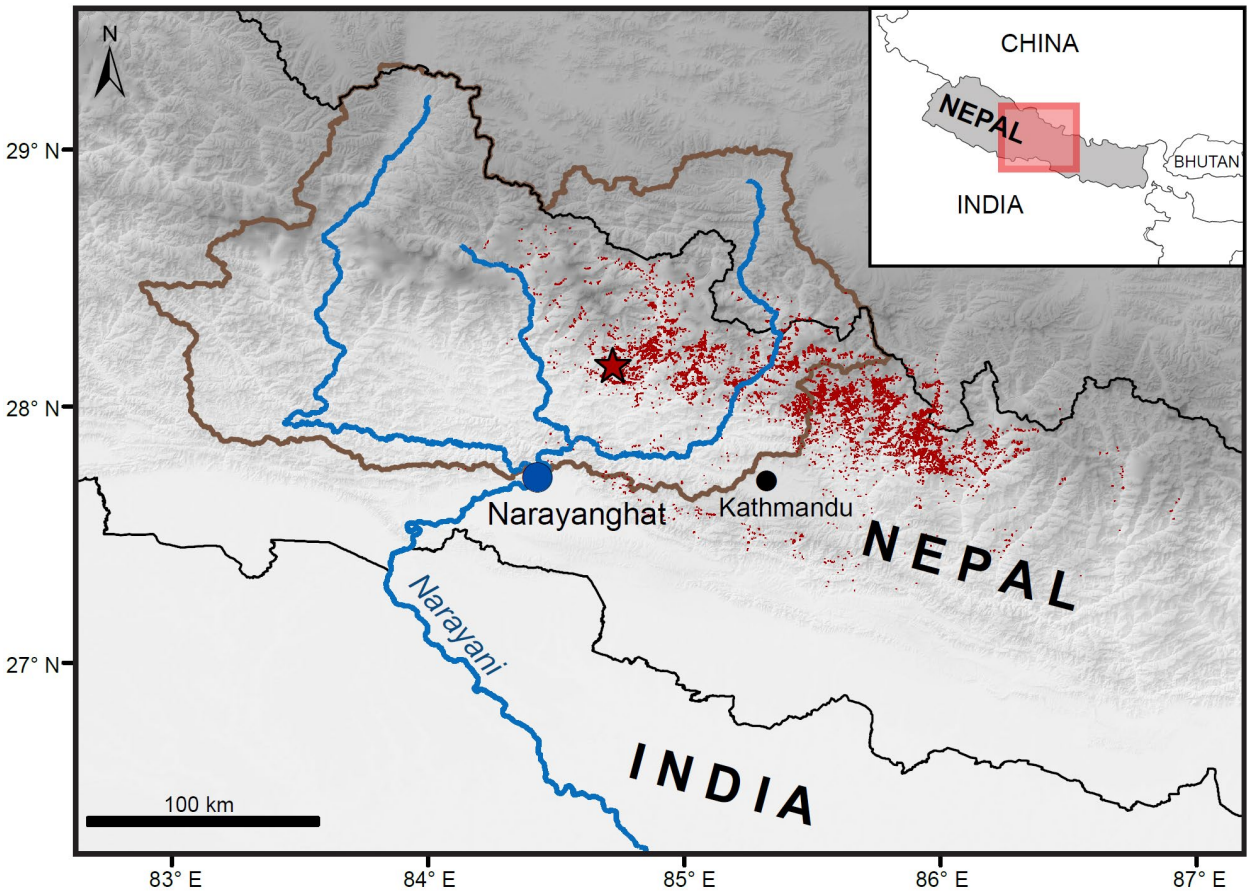

Fig. 1: Map of the Central Himalaya and location of the studied drainage basin. *The Narayani catchment (brown outline) and the sampling station in Narayanghat are displayed. The epicenter of the 2015 Gorkha earthquake is shown by the star, and red dots illustrate the mapped cosesimic landslides[24].*

In this study, we assess the net carbon budget (organic and inorganic sources and sinks) of erosion in the Narayani catchment in the Central Himalaya. Our set of daily suspended sediment and water samples of the Narayani River during the monsoon seasons of a pre-earthquake year (2010) and three years following the Gorkha earthquake (2015-2017) provides a unique opportunity to evaluate the influence of such an extreme event on the carbon budget of a large portion of the Himalaya. It also allows us to refine the carbon budget of Himalayan erosion by evaluating the magnitude of the main carbon sinks and sources associated with the erosion of the Himalaya.

High-resolution record of organic carbon export and chemical weathering rates

With a catchment area of 32,000 km^2, the Narayani river basin covers around a third of the Nepalese Himalaya (Fig. 1). Our sampling station lies at the Himalayan front, near Narayanghat, shortly before the Narayani enters the Gangetic floodplain. The Indian Summer Monsoon (June-September) dominates the precipitation regime in the catchment and is responsible for around 80% of the annual water discharge. The Narayani River annually exports around 100 Mt of sediments to the Gangetic floodplain (equivalent to ca. 1.6 mm/yr of erosion), around 95% of which is transported during the monsoon season[25,26]. The Gorkha earthquake, whose epicenter was located in the Narayani basin, heavily affected the eastern part of the catchment with coseismic landslides, while the western part was mostly spared (Fig. 1). Coseismic landslides mobilized a total of ca. 0.2 km^3 material in the Narayani catchment, which is around four times the interseismic annual volume of sediment export of the Narayani, and equivalent to an average surface lowering over the entire catchment of ca. 6.3 mm (Methods). The Narayani provides an ideal catchment area for studying the effect of such an extreme event at a scale large enough to be of global importance.

With our daily suspended sediment and water samples we calculate the sediment yield and the carbon fluxes linked to erosion of successive monsoon seasons. Records of total discharge and sediment yield ([26]; Department of Hydrology and Meteorology of Nepal (DHM); this study) of the Narayani from 8 years before the earthquake, reveal that the monsoon in 2015, which started shortly after the Gorkha earthquake, was particularly weak (Fig. 2). Despite the active coseismic landsliding in the catchment[24], the total sediment yield of the Narayani does not reveal a detectable earthquake signal and falls within the observed trends before 2015. Sediment fluxes (relative to monsoon discharge), however, peaked a year later. This peak in sediment yield is likely attributable to a delayed response to the Gorkha earthquake and the reactivation or mobilization of landslide material that had not previously connected to the fluvial network[24]. However, this anomalously high sediment yield disappears in 2017 despite an equally intense monsoon. As landslide rates have been shown to decay to background values in 1-4 years after a large earthquake[27], we interpret that the Gorkha earthquake signal dissipated by 2017.

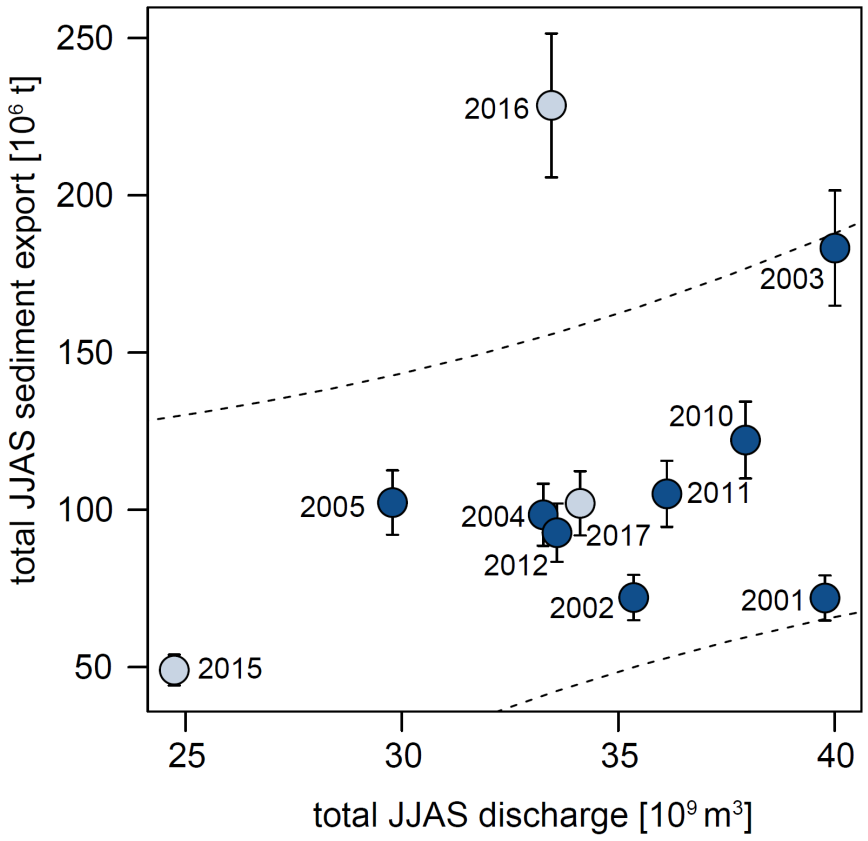

Fig. 2: Total discharge and sediment yields of the Narayani River during different monsoon seasons. *Total discharge as a function of the sediment yield of the monsoon months June-July-August-September (JJAS) of the Narayani in Narayanghat (discharge data and sediment loads from 2001-2012 from the DHM and ref.[26]). Dashed lines illustrate the 0.997 confidence interval of the linear regression between discharge and sediment yield. Grey points show records after the April 2015 Gorkha earthquake.*

To constrain the fluxes of biospheric OC (OC_{bio}, fresh OC derived from soils and plant debris) export, we measured the total organic carbon content (TOC) and the radiogenic (^{14}C) isotopic compositions of OC in riverine suspended sediment samples (Methods). The TOC of the suspended sediments from the Narayani varies between 0.04 and 0.99 % and the fraction modern (Fm) of the OC spans a large range, varying between 0.27 and 0.91 (Supplementary Fig. 2). Our high-resolution time-series (with measurements up to every second day) reveal a large variability in TOC concentrations and ^{14}C signatures of suspended sediments. This variability is not directly linked to the river discharge, highlighting the need for time-series sampling approaches. For disentangling the OC_{bio} and petrogenic OC (OC_{petro}, rock-derived OC) inputs, we employ a binary mixing model using the TOC and the radiocarbon signatures of the bulk samples as well as a biospheric and a petrogenic endmember (Methods and Supplementary Fig. 2). Soil samples from the Narayani catchment mostly reflect a recent biospheric endmember (Fm 1.1 – 0.9), whereas the petrogenic end-member was assigned an Fm value of 0. Hydrodynamic processes do not significantly affect OC concentrations within the water column in large and turbulent Himalayan river systems[28], including the Narayani (Supplementary Information). We can, therefore, confidently assume that suspended sediment

samples collected from surface waters are representative of the OC_{bio} content in the whole water column. Using the measured daily sediment load and discharge data from the DHM, we are able to estimate the total amount of OC_{bio} exported by the Narayani River during a monsoon season and upscale it to a whole year (Methods).

Major ion concentrations measured in filtered river water (every day for the monsoon 2010; every second day for monsoons 2015-2017) provide estimates for silicate and carbonate weathering rates by carbonic and sulfuric acid, respectively. We calculate the relative amounts of silicate and carbonate weathering using a forward Monte Carlo approach with known elemental ratios of the weathering products of the main lithologies of the Central Himalaya[12,13] (Methods). We consider the CO_2 removal over timescales >10^4 yr for which one mole of carbon is removed from the Earth's surface through carbonate precipitation per mole of Ca and Mg derived from silicate weathering by carbonic acid[2] (Ca_{sil} and Mg_{sil}). The carbon source through carbonate weathering by sulfuric acid is calculated using the SO_4^{2-} concentration and the known ratio of carbonate to silicate weathering (Methods). In Himalayan rivers, the proportion of SO_4^{2-} derived from sulfide oxidation has been estimated to 70-100% ([12]). Per mole of carbonates weathered by sulfuric acid, half a mole of carbon is released to the atmosphere on timescales of 10^5-10^7 yr ([11]).

To complement our analysis of the carbon budget of Himalayan erosion, we estimate the OC_{petro} oxidation rate in the Narayani basin with Re data from the literature. Dissolved Re concentrations are a proxy to trace the fluxes of carbon released through rock-derived carbon oxidation[10,29]. Compiling Re concentrations of Himalayan rivers and sediments[29–32] allows us to provide a first-order estimate of the carbon flux released through OC_{petro} oxidation in the Central Himalaya (Methods). It should, however, be noted that these estimates do not allow us to derive annually resolved OC_{petro} oxidation fluxes estimates since Re was not directly measured in our samples.

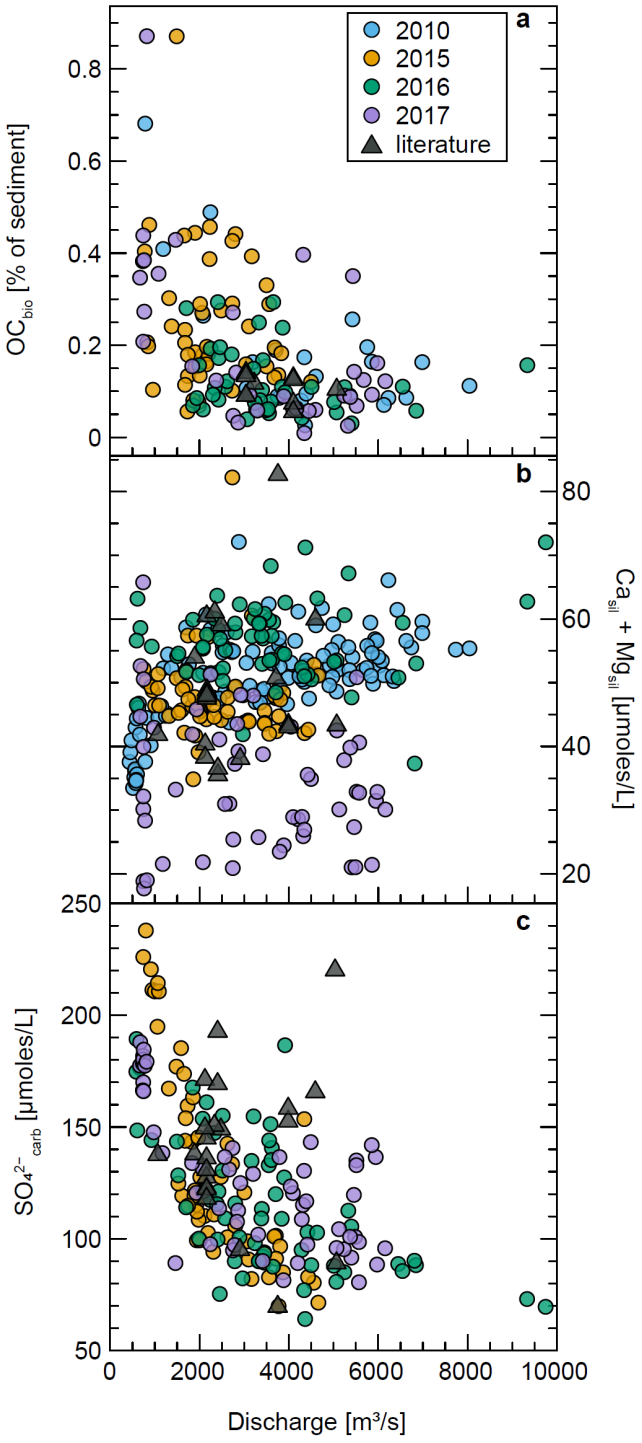

Fig. 3: OC_{bio}, Ca_{sil}+Mg_{sil} and $SO_4^{2-}{}_{carb}$ as a function of the discharge of the Narayani River. a. *OC_{bio} in percentage of the total suspended sediment. Literature data are from ref.[8] (pre-earthquake).* ***b.*** *Concentrations of Ca and Mg derived from silicate weathering through carbonic acid (Ca_{sil}+Mg_{sil}). Literature data are from refs.[12,33,34] (pre-earthquake) and ref.[13] (post-earthquake).* ***c.*** *Concentration of the fraction of SO_4^{2-} associated with carbonate weathering ($SO_4^{2-}{}_{carb}$). Literature data are from refs.[12,33,34] (pre-earthquake) and ref.[13] (post-earthquake). Panels a, b and c are plotted against the daily discharge of the Narayani River in Narayanghat.*

Carbon fluxes over four monsoon seasons

The fraction of OC_{bio} in the total sediment load of the Narayani is diluted by increasing runoff (Fig. 3a), which has been proposed to result from a lower degree of soil erosion relative to mass wasting during the monsoon[26]. At higher discharge the concentration of OC_{bio} remains constant with changing runoff, which suggests that the OC_{bio} is supply-limited, similar to the total sediment load in the Narayani[25,26]. The slightly higher concentrations of OC_{bio} in the year 2015 could be associated with material evacuated from coseismic landslides or could alternatively be linked to the lower sediment load during this weak monsoon season. The unusually large sediment yield observed in 2016 (Fig. 4a) is accompanied by a substantially higher OC_{bio} export compared to the other years on record (Fig. 4b). This ca. 85% increase in OC_{bio} export combined with a ca. 130% higher than expected sediment yield (from the linear relationship between the total discharge and the monsoonal sediment yield, Fig. 2) is likely a consequence of the coseismic landslides associated with the Gorkha earthquake. However, this earthquake signal in the total sediment and the OC_{bio} export 2016 of the Narayani remains minor as it disappears a year later, suggesting that significant portions of the landslide sediments are either not or only very slowly evacuated.

As reported in previous studies, our results show that chemical weathering in the Central Himalaya is dominated by carbonates, with around 10% of the cations being derived from silicate weathering[12,33,34]. The calculated Ca_{sil} and Mg_{sil} concentrations do not significantly vary between the different years (Fig. 3b). The lower concentrations in 2017 can likely be attributed to an anthropogenic Cl source (Supplementary Information), which does not have a major impact on the total carbon budget calculation (Fig. 4c). The concentration of SO_4^{2-} coupled with carbonate weathering displays a typical dilution pattern that has been described for anion concentrations in the Himalaya[12,34] (Fig. 3d). When summing up these carbon fluxes per monsoon season (Fig. 4c and 4d), we observe that the carbon source through sulfuric acid weathering is ~2.5 times higher than the carbon sink through silicate weathering. Both of these carbon fluxes did not significantly increase after the Gorkha earthquake at the scale of the Narayani basin.

Following page:

Fig. 4: Total carbon fluxes of the Narayani basin during 4 monsoon seasons and its mean net erosional carbon budget. *Total export during four different monsoon seasons of* ***a.*** *suspended sediments (error bars indicate 10% error due to the depth correction of the surface sediment load[26]);* ***b.*** *OC_{bio} (error bars include uncertainty in the total sediment yield and the standard deviation of the OC_{bio} calculation from total OC);* ***c.*** *Ca_{sil} + Mg_{sil} (errors of the elemental ratios defining Ca_{sil} and Mg_{sil} are propagated); and* ***d.*** *$SO_4^{2-}{}_{carb}$ (error bars indicate the range of 100-70% of SO_4^{2-} which is derived from sulfide oxidation ([12])). Round symbols illustrate the Gorkha earthquake that happened shortly before the monsoon 2015.* ***e.*** *Mean carbon fluxes from the four studied years of erosion in the Narayani basin in t of C/(km^{2}yr) and in moles of C/(km^{2}yr). Total fluxes in tC/(km^{2}yr) and in tC/yr are indicated in square brackets. Error bars are calculated by the mean of the above-described errors, and for the OC_{petro} oxidation, the error of the oxidation rate calculation is propagated. Red bar illustrates the sum of the carbon fluxes, and its error bar is propagated with a Monte Carlo simulation.*

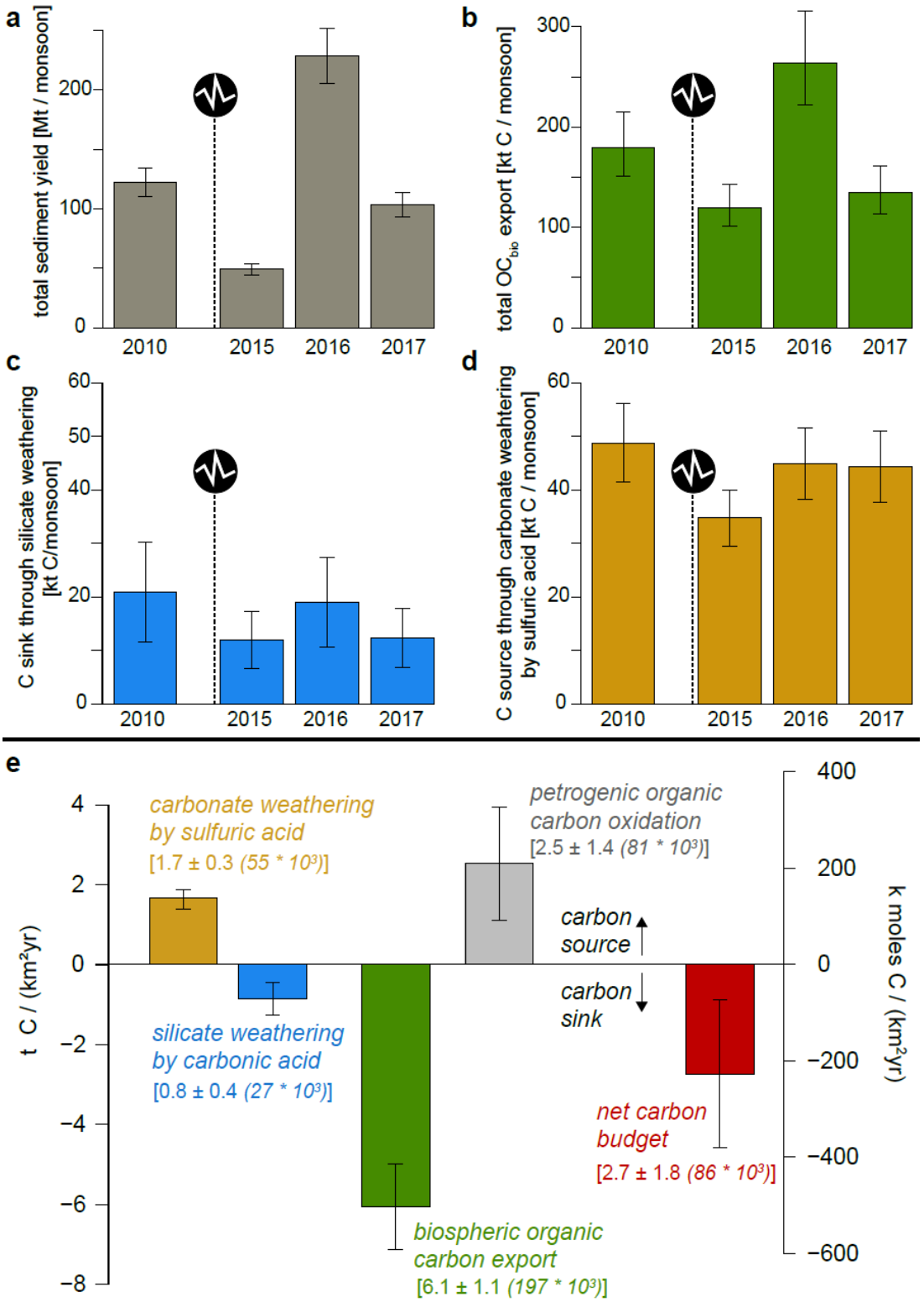
a
total sediment yield [Mt / monsoon]
0
100
200
2010
2015
2016
2017
b
total OC_{bio} export [kt C / monsoon]
0
100
200
300
2010
2015
2016
2017
c
C sink through silicate weathering [kt C/monsoon]
0
20
40
50
60
2010
2015
2016
2017
d
C source through carbonate weahtering by sulfuric acid [kt C / monsoon]
0
20
40
60
2010
2015
2016
2017
e
t C / (km²yr)
4
2
0
−2
−4
−6
−8
k moles C / (km²yr)
400
200
0
−200
−400
−600
carbonate weathering by sulfuric acid
[1.7 ± 0.3 (55 * 10³)]
silicate weathering by carbonic acid
[0.8 ± 0.4 (27 * 10³)]
petrogenic organic carbon oxidation
[2.5 ± 1.4 (81 * 10³)]
biospheric organic carbon export
[6.1 ± 1.1 (197 * 10³)]
carbon source
carbon sink
net carbon budget
[2.7 ± 1.8 (86 * 10³)]

Minor impact of the Gorkha earthquake on the Himalayan carbon budget

Our data suggest that, in contrast to other seismically impacted systems, the Central Himalaya had a muted response to the Gorkha earthquake. The Mw 7.9 earthquake that struck Wenchuan in 2008 resulted in widespread coseismic landsliding[35], increased riverine sediment fluxes[36] and doubled OC_{bio} export over four years after the earthquake[18]. Similarly, sediment cores from a mountain lake in the Southern Alps of New Zealand revealed that over the last ~1000 yr large earthquakes were responsible for 27% of the sediment flux[37] and 43% of the OC_{bio} export[19] in its catchment. As the Narayani catchment area is three orders of magnitude larger than the example from New Zealand, the different responses could partly be linked to the system size and the related capacity to buffer sedimentary signals through intermittent storage and lack of connectivity to the channel[38]. The catchment studied after the Wenchuan earthquake[18,36] is, however, only seven times smaller than the Narayani catchment.

Moreover, both basins were only partly affected by coseismic landslides, suggesting that factors other than the catchment size control the sediment and biogeochemical export fluxes following a major perturbation.

Despite similar moment magnitudes, the coseismic landslides after Wenchuan earthquake mobilized a substantially larger volume of material (~2.3 km^3 ([35])) than the total landsliding associated with the Gorkha earthquake (~0.8 km^3 ([24])). In addition, the landslide density in the Central Himalaya during the year 2015 was only 4-6 times higher relative to that during interseismic periods[39]. This increase in landslide density following the Gorkha earthquake was significantly lower than the 22 times higher landslide density in the year after an earthquake of similar strength in 1999 in Taiwan[27]. While the relatively weak earthquake impact on landsliding rates in the Central Himalaya can partly be linked to the seismic rupture characteristics[40], the short major earthquake recurrence[22] and high density of interseismic landsliding[39] result in a landscape that is in quasi-equilibrium with frequent mass wasting. The addition of coseismic landslide material equivalent to around four years of interseismic erosion in the Narayani catchment was therefore likely not sufficient to significantly perturb the geochemical fluxes in this highly erosive system. The magnitude of a perturbation relative to background conditions exerts thus an important influence on the system's response.

Earthquakes with a larger moment magnitude than the Mw 7.8 Gorkha earthquake trigger more landslides[35] but the long recurrence-time of great (Mw >9) earthquakes in the Himalaya, which is on the order of millenia[41], means that they do not dominate the long-term erosion budget[39]. We similarly assume that long-term carbon fluxes associated with erosion processes in the Central Himalaya would not be significantly impacted by larger and less frequent earthquakes compared to Gorkha.

The net carbon budget of the Central Himalayan erosion

Integrating the mean carbon fluxes constrained for four years reveals that the Central Himalayan erosion acts as a net carbon sink with respect to the Earth's surface (Fig. 4e). Due to relatively low interannual variability and stability with respect to seismic perturbations, we propose that these Himalayan carbon fluxes are representative of long-term periods with relatively stable climatic conditions, such as interglacials. The magnitude of carbon removal through OC_{bio} export (and subsequent burial) is around ten times larger than the sink resulting from silicate weathering (and subsequent carbonate precipitation). This finding further underlines the predominant role of the organic carbon cycle in the Himalaya[7,8]. Moreover, our results demonstrate that the relative contribution of OC_{bio} export versus silicate weathering to the carbon sink at the outlet of the Himalaya is higher than previously found in Neogene sediments of the Bay of Bengal[7,42]. As highlighted for other mountain ranges[5], the oxidative weathering of OC_{petro} and sulfuric acid weathering of carbonates are important carbon sources that must be included in the net carbon budget of the Himalayan erosion. These carbon sources considerably reduce the magnitude of carbon sequestration associated with erosional processes. The comparison of the OC_{petro} oxidation flux with the calculated riverine export of OC_{petro} suggests that ca. 37% of the total OC in the bedrock is lost to oxidation within the catchment (Supplementary Information). This oxidation rate remains lower than that previously calculated for Taiwan[43].

If the flux of metamorphic CO_2 degassing in the Narayani basin (ca. 150 kt C/year ([9])) is added to the orogenic carbon budget, the balance between sources and sinks shifts to positive carbon emission values. However, since there is no direct feedback between metamorphic emissions and erosion processes, it is unlikely that these fluxes play a role in the regulation of Earth's long-term climate by Earth surface processes.

Overall, these results shed new light on the erosional carbon budget of a tectonically active and highly erosive mountain range. We emphasize that carbon fluxes were calculated for the outlet of the Himalayan front, from where the solutes and sediments transit through the Gangetic floodplain before being discharged in the Bay of Bengal. As the concentration of OC_{bio} in suspended sediments is not significantly affected by the floodplain transit[8] and due to the high burial efficiency in the Bay of Bengal[42], we can assume that ca. 100% of the exported OC_{bio} by the Narayani is buried in marine sediments. In contrast, chemical weathering rates have been shown to double from the Himalayan front to the Indian Ocean[13,44]. Further weathering of carbonates by sulfuric acid during floodplain transfer is probably small given that sulfides oxidize readily upon exposure at the surface in the upland areas[45] and are not detected in the sediment load downstream in the Gangetic floodplain[46]. At the same time, oxidation rates of rock-derived OC are likely to increase in the Ganges by 50-70% ([47]). Hence, while some of the carbon fluxes likely increase during the transport through the Gangetic floodplain, the overall carbon budget from the Central Himalaya is unlikely to be significantly shifted in one direction.

This unique time-series dataset from before and after the 2015 Gorkha earthquake allows us to evaluate the impact of an extreme event on the carbon fluxes of the Central Himalayan erosion. Unlike previously studied systems[18,19], Himalayan carbon fluxes were not significantly perturbed by a major earthquake. This budget reveals that the erosion of a large Himalayan catchment acts as a net carbon sink; this sink is however smaller than previously thought[6–8] and reflects the complex interplay of processes that must be considered in developing net erosional carbon budgets. Due to relatively low interannual variability, Himalayan carbon fluxes can be integrated on timescales of at least interglacials. While the export and burial rates of OC_{bio}, as well as chemical weathering rates in the Ganges-Brahmaputra basin, both fluctuate on glacial-interglacial timescales[48,49], it has recently been shown that erosion rates in this basin remained relatively stable during the late Cenozoic[50]. As erosion exerts a primary control on carbon fluxes[5], we speculate that our carbon budget for the Central Himalaya may be relevant on late Cenozoic timescales.

Acknowledgments

We thank K. B. Adhikari from the hydrological station in Narayanghat for the daily sampling. E. Tipper is thanked for kindly providing the confluence samples.

Author contributions

L.M. and M.L. designed the study. M.L., C. F.-L., J.L., A.G. and S.G. organized and maintained daily sampling in Narayanghat. J.L. provided the depth profile samples and L.M., M.L., C.F-L., J.L. and S.G. conducted the soil sampling. L.M., N.H. and F.W.-L. prepared the samples and preformed the measurements. S.G. conducted the landslide volume calculation. L.M., M.L. and T.E. made the carbon flux calculations. All authors contributed to the interpretation of the data and the redaction of the manuscript.

References

1. Berner, R. A. & Canfield, D. E. A new model for atmospheric oxygen over Phanerozoic time. *American Journal of Science* vol. 289 333–361 (1989).

2. Walker, J. C. G., Hays, P. B. & Kasting, J. F. A negative feedback mechanism for the long-term stabilization of Earth's surface temperature. *J. Geophys. Res. Ocean.* **86**, 9776–9782 (1981).

3. West, A. J. Thickness of the chemical weathering zone and implications for erosional and climatic drivers of weathering and for carbon-cycle feedbacks. *Geology* **40**, 811–814 (2012).

4. Galy, V., Peucker-Ehrenbrink, B. & Eglinton, T. Global carbon export from the terrestrial biosphere controlled by erosion. *Nature* **521**, 204–207 (2015).

5. Hilton, R. G. & West, A. J. Mountains, erosion and the carbon cycle. *Nat. Rev. Earth Environ.* **1**, 284–299 (2020).

6. Raymo, M. E. & Ruddiman, W. F. Tectonic forcing of late Cenozoic climate. *Nature* **357**, 57–59 (1992).

7. France-Lanord, C. & Derry, L. A. Organic carbon burial forcing of the carbon cycle from Himalayan erosion. *Nature* **390**, 65–67 (1997).

8. Galy, V., France-Lanord, C. & Lartiges, B. Loading and fate of particulate organic carbon from the Himalaya to the Ganga-Brahmaputra delta. *Geochim. Cosmochim. Acta* **72**, 1767–1787 (2008).

9. Evans, M. J., Derry, L. A. & France-Lanord, C. Degassing of metamorphic carbon dioxide from the Nepal Himalaya. *Geochemistry, Geophys. Geosystems* **9**, (2008).

10. Hilton, R. G., Gaillardet, J., Calmels, D. & Birck, J. L. Geological respiration of a mountain belt revealed by the trace element rhenium. *Earth Planet. Sci. Lett.* **403**, 27–36 (2014).

11. Calmels, D., Gaillardet, J., Brenot, A. & France-Lanord, C. Sustained sulfide oxidation by physical erosion processes in the Mackenzie River basin: Climatic perspectives. *Geology* **35**, 1003–1006 (2007).

12. Galy, A. & France-Lanord, C. Weathering processes in the Ganges-Brahmaputra basin and the riverine alkalinity budget. *Chem. Geol.* **159**, 31–60 (1999).

13. Bickle, M. J. *et al.* Chemical weathering outputs from the flood plain of the Ganga. *Geochim. Cosmochim. Acta* **225**, 146–175 (2018).

14. Horan, K. *et al.* Carbon dioxide emissions by rock organic carbon oxidation and the net geochemical carbon budget of the Mackenzie River Basin. *Am. J. Sci.* **319**, 473–499 (2019).

15. Hilton, R. G. *et al.* Tropical-cyclone-driven erosion of the terrestrial biosphere from mountains. *Nat. Geosci.* **1**, 759–762 (2008).

16. Wang, J. *et al.* Long-term patterns of hillslope erosion by earthquake-induced landslides shape mountain landscapes. *Sci. Adv.* **6**, 1–10 (2020).

17. Rathburn, S. . *et al.* The fate of sediment, wood, and organic carbon eroded during an extreme flood, Colorado Front Range, USA. *Geology* **45**, 1–14 (2017).

18. Wang, J. *et al.* Earthquake-triggered increase in biospheric carbon export from a mountain belt. *Geology* **44**, 471–474 (2016).

19. Frith, N. V *et al.* Carbon export from mountain forests enhanced by earthquake-triggered landslides over millennia. *Nat. Geosci.* **11**, 772–776 (2018).

20. Emberson, R., Hovius, N., Galy, A. & Marc, O. Chemical weathering in active mountain belts controlled by

stochastic bedrock landsliding. *Nat. Geosci.* **9**, 42–45 (2016).

21. Emberson, R., Galy, A. & Hovius, N. Weathering of Reactive Mineral Phases in Landslides Acts as a Source of Carbon Dioxide in Mountain Belts. *J. Geophys. Res. Earth Surf.* **123**, 2695–2713 (2018).

22. Avouac, J. P., Bollinger, L., Lave, J., Cattin, R. & Flouzat, M. Seismic cycle in the Himalayas. *Comptes Rendus l'Academie Sci. - Ser. IIa Sci. la Terre des Planetes* **333**, 513–529 (2001).

23. Avouac, J.-P., Meng, L., Wei, S., Wang, T. & Ampuero, J.-P. Lower edge of locked Main Himalayan Thrust unzipped by the 2015 Gorkha earthquake. *Nat. Geosci.* **8**, 708–711 (2015).

24. Roback, K. *et al.* The size, distribution, and mobility of landslides caused by the 2015 Mw7.8 Gorkha earthquake, Nepal. *Geomorphology* **301**, 121–138 (2018).

25. Andermann, C., Crave, A., Gloaguen, R. & Davy, P. Connecting source and transport : Suspended sediments in the Nepal Himalayas. *Earth Planet. Sci. Lett.* **352**, 158–170 (2012).

26. Morin, G. P. *et al.* Annual Sediment Transport Dynamics in the Narayani Basin, Central Nepal: Assessing the Impacts of Erosion Processes in the Annual Sediment Budget. *J. Geophys. Res. Earth Surf.* **123**, 2341–2376 (2018).

27. Marc, O., Hovius, N., Meunier, P., Uchida, T. & Hayashi, S. Transient changes of landslide rates after earthquakes. *Geology* **43**, 883–886 (2015).

28. Menges, J. *et al.* Variations in organic carbon sourcing along a trans-Himalayan river determined by a Bayesian mixing approach. *Geochim. Cosmochim. Acta* **286**, 159–176 (2020).

29. Dalai, T. K., Singh, S. K., Trivedi, J. R. & Krishnaswami, S. Dissolved rhenium in the Yamuna River System and the Ganga in the Himalaya: Role of black shale weathering on the budgets of Re, Os, and U in rivers and CO2 in the atmosphere. *Geochim. Cosmochim. Acta* **66**, 29–43 (2002).

30. Rahaman, W., Singh, S. K. & Shukla, A. D. Rhenium in Indian rivers: Sources, fluxes, and contribution to oceanic budget. *Geochemistry, Geophys. Geosystems* **13**, (2012).

31. Paul, M. (Université de L. Etude des isotopes de l'osmium dans les eaux souterraines du Bangladesh et les sédiments himalayens: implications et rôle de l'érosion himalayenne sur le budget océanique de l'osmium. (2018).

32. Pierson-Wickmann, A. C., Reisberg, L. & France-Lanord, C. The Os isotopic composition of Himalayan river bedloads and bedrocks: Importance of black shales. *Earth Planet. Sci. Lett.* **176**, 203–218 (2000).

33. France-Lanord, C., Evans, M., Hurtrez, J. E. & Riotte, J. Annual dissolved fluxes from Central Nepal rivers: Budget of chemical erosion in the Himalayas. *Comptes Rendus - Geosci.* **335**, 1131–1140 (2003).

34. Bhatt, M. P., Hartmann, J. & Acevedo, M. F. Seasonal variations of biogeochemical matter export along the Langtang-Narayani river system in central Himalaya. *Geochim. Cosmochim. Acta* **238**, 208–234 (2018).

35. Marc, O., Hovius, N., Meunier, P., Gorum, T. & Uchida, T. A seismologically consistent expression for the total area and volume of earthquake-triggered landsliding. *J. Geophys. Res. Earth Surf.* 640–663 (2016) doi:10.1002/2015JF003732.

36. Wang, J. *et al.* Controls on fluvial evacuation of sediment from earthquake-triggered landslides. *Geology* **43**, 115–118 (2015).

37. Howarth, J. D., Fitzsimons, S. J., Norris, R. J. & Jacobsen, G. E. Lake sediments record cycles of sediment flux driven by large earthquakes on the Alpine fault , New Zealand. *Geology* **40**, 1091–1094 (2012).

38. Wohl, E. *et al.* Connectivity as an emergent property of geomorphic systems. *Earth Surf. Process. Landforms* **44**, 4–26 (2019).

39. Marc, O. *et al.* Long-term erosion of the Nepal Himalayas by bedrock landsliding: The role of monsoons, earthquakes and giant landslides. *Earth Surf. Dyn.* **7**, 107–128 (2019).

40. Xu, C. *et al.* Two Comparable Earthquakes Produced Greatly Different Coseismic Landslides : The 2015 Gorkha , Nepal and. *J. Earth Sci.* **27**, 1008–1015 (2016).

41. Stevens, V. L. & Avouac, J. P. Millenary Mw > 9.0 earthquakes required by geodetic strain in the Himalaya. *Geophys. Res. Lett.* **43**, 1118–1123 (2016).

42. Galy, V. *et al.* Efficient organic carbon burial in the Bengal fan sustained by the Himalayan erosional system. *Nat. Hazards Earth Syst. Sci.* 407–411 (2007) doi:10.1038/nature06273.

43. Hemingway, J. D. *et al.* Microbial oxidation of lithospheric organic carbon in rapidly eroding tropical mountain soils. *Science (80-.).* **360**, 209–212 (2018).

44. Lupker, M. *et al.* Predominant floodplain over mountain weathering of Himalayan sediments (Ganga basin). *Geochim. Cosmochim. Acta* **84**, 410–432 (2012).

45. Torres, M. A. *et al.* The acid and alkalinity budgets of weathering in the Andes–Amazon system: Insights into the erosional control of global biogeochemical cycles. *Earth Planet. Sci. Lett.* **450**, 381–391 (2016).

46. Garzanti, E. *et al.* Mineralogical and chemical variability of fluvial sediments 2 . Suspended-load silt (Ganga-Brahmaputra, Bangladesh). *Earth Planet. Sci. Lett.* **302**, 107–120 (2011).

47. Galy, V., Beyssac, O., France-Lanord, C. & Eglinton, T. Recycling of graphite during Himalayan erosion: a geological stabilization of carbon in the crust. *Science (80-.).* **322**, 943–945 (2008).

48. Lupker, M., France-Lanord, C., Galy, V., Lavé, J. & Kudrass, H. Increasing chemical weathering in the Himalayan system since the Last Glacial Maximum. *Earth Planet. Sci. Lett.* **365**, 243–252 (2013).

49. Hein, C. J. *et al.* Post-glacial climate forcing of surface processes in the Ganges – Brahmaputra river basin and implications for carbon sequestration. *Earth Planet. Sci. Lett.* **478**, 89–101 (2017).

50. Lenard, S. J. P. *et al.* Steady erosion rates in the Himalayas through late Cenozoic climatic changes. *Nat. Geosci.* **13**, 448–452 (2020).

51. Larsen, I. J., Montgomery, D. R. & Korup, O. Landslide erosion controlled by hillslope material. *Nat. Geosci.* **3**, 247–251 (2010).

52. Märki, L. *et al.* Molecular tracing of riverine soil organic matter from the Central Himalaya. *Geophys. Res. Lett.* (2020) doi:10.1029/2020GL087403.

53. Eckhardt, K. How to construct recursive digital filters for baseflow separation. *Hydrol. Process.* **19**, 507–515 (2005).

54. McIntyre, C. P. *et al.* Online 13C and 14C Gas Measurements by EA-IRMS–AMS at ETH Zürich. *Radiocarbon* **59**, 893–903 (2017).

55. Wolff-Boenisch, D., Gabet, E. J., Burbank, D. W., Langner, H. & Putkonen, J. Spatial variations in chemical weathering and CO2 consumption in Nepalese High Himalayan catchments during the monsoon season. *Geochim. Cosmochim. Acta* **73**, 3148–3170 (2009).

56. Tipper, E. T. *et al.* The short term climatic sensitivity of carbonate and silicate weathering fluxes: Insight from seasonal variations in river chemistry. *Geochim. Cosmochim. Acta* **70**, 2737–2754 (2006).

57. Burke, A. *et al.* Sulfur isotopes in rivers : Insights into global weathering budgets, pyrite oxidation, and the modern sulfur cycle. *Earth Planet. Sci. Lett.* **496**, 168–177 (2018).

58. Lupker, M., France-Lanord, C. & Lartiges, B. Impact of sediment-seawater cation exchange on Himalayan

chemical weathering fluxes. *Earth Surf. Dyn.* **4**, 675–684 (2016).

59. Horan, K. *et al.* Mountain glaciation drives rapid oxidation of rock-bound organic carbon. *Sci. Adv.* **3**, 1–9 (2017).

60. Pierson-Wickmann, A. C., Reisberg, L. & France-Lanord, C. Behavior of Re and Os during low-temperature alteration: Results from Himalayan soils and altered black shales. *Geochim. Cosmochim. Acta* **66**, 1539–1548 (2002).

Methods

Calculation of coseismic landslide volume and lowering rates

The total volume of coseismic landslide material in the Narayani catchment was calculated using the earthquake-triggered landslide inventory from ref.[24] and the area-volume scaling parameters from ref.[51] (Supplementary Table 1). We here used the global parameters from ref.[51]. The uncertainties were propagated with a Monte Carlo approach (n = 10^4). The mean landscape surface lowering rate was obtained by dividing the landslide volume within the catchment by the Narayani catchment surface area (32,000 km^2).

Sampling

Surface suspended sediments were taken in the middle of the Narayani river during the monsoon seasons (June-September) 2010 and 2015-2017 (Supplementary Table 2). The sampling in 2010 is described in more detail in ref.[26] and is similar to the sampling during the other years. For samples in 2015-2017, 3L of surface water was taken at the sampling station in Narayanghat (27.73° N; 84.43° E). The water was immediately filtered with a pressure filtration unit through 0.2 µm polyethersulfone (PES) membranes, and the sediment sample was stored in a dark and cool place until return to the laboratory. 250 ml of the filtered river water was collected for measurements of major ions.

Sediment sampling of four depth profiles (Supplementary Table 3) within the water column was performed in 2011 in Narayanghat and is further described in ref.[26]. At the sampling location, the Narayani channel is around 15-20 m deep. Samples of both tributaries shortly before the confluence, which is situated around 2 km upstream of the sampling station and samples from both sides of the Narayani river, were taken during different field campaigns between 2015 and 2017 (Supplementary Table 4). For the samples NEQ-17204 - NEQ-172-39, 10-20L of surface water was filtered as described above and stored in a cool place. Samples NEP-15-02 – NEP-17-43 were taken with a bucket or a sediment sampler from the surface water and filtered through a pressure filtration unit similar as described above.

Soil samples (Supplementary Table 5) cover a variety of conditions such as elevation and annual precipitation within the Narayani catchment and were collected between 2009 and 2017. The samples are further described in ref.[52]. The samples integrate the surface soil layer of a depth of up to 15 cm. The uppermost few cm of the soils were removed so as not to include vegetation and litter in the surface soil samples.

Determination of the total sediment yield of a monsoon season

For estimating the sediment load of days without measurement, we applied the method described in ref.[26]. Briefly, a digital filter[53] was used to separate the total discharge of the Narayani in the baseflow and the direct discharge[25] with the parameters used in ref.[26] (Supplementary Fig. 1). The missing sediment load was subsequently calculated with the linear relationship between the direct discharge and the sediment load data.

TOC, $\delta^{13}C$ and radiocarbon measurement of suspended sediments

Sediment and soil samples were frozen upon arrival at ETH Zürich and subsequently freeze-dried. Sediments were weighed for calculating the surface sediment load and carefully removed from the filters. Soil samples were sieved at < 2 mm. An aliquot of the sediments and soils was milled in a Retsch zirconium ball mill. ~50 mg of the milled samples were weighed into combusted silver capsules. Samples were fumigated in HCl vapor for removal of inorganic carbon (3 days at 60 °C), and neutralized with NaOH (4 days at 60 °C). The capsules were subsequently wrapped in tin boats, and TOC and its isotopic compositions were measured on a coupled online elemental analyzer-isotope ratio mass spectrometer-accelerator mass spectrometer (EA-IRMS-AMS) system[54] at the Ion Beam Physics Institute of the ETH Zürich. $^{13}C/^{12}C$ ratios are reported in $\delta^{13}C$ notation relative to the Vienna Pee Dee Belemnite (VPDB) standard and the ^{14}C content is reported as fraction modern (Fm).

In addition to routine standard measurements by AMS[54], an internal standard consisting of a suspended sediment sample was measured eight times in different batches (including different fumigation batches). The standard deviation of the results is used as typical uncertainty on the measurements (TOC: mean 0.24% ± 0.01; Fm: mean 0.51 ± 0.03; $\delta^{13}C$: mean -24.02 ‰ ± 0.17).

Determination of OC_{bio} yield

A binary mixing model was applied to disentangle the concentrations of OC_{bio} and OC_{petro} in the total OC of the suspended sediment (Supplementary Fig. 2). With the following assumptions similar to the method applied in ref.[43] we are able calculate the concentrations (%) of OC_{bio} and OC_{petro} in the total sediment:

$$OC_{tot} = OC_{bio} + OC_{petro} \quad (1)$$

$$Fm_{tot} * OC_{tot} = Fm_{bio} * OC_{bio} + Fm_{petro} * OC_{petro} \quad (2)$$

The rock-derived OC_{petro} is characterized by $Fm_{petro} = 0$ because its age exceeds the ^{14}C half-life by more than an order of magnitude. We can therefore rewrite equations 1 and 2:

$$Fm_{tot} * OC_{tot} = Fm_{bio} * OC_{bio} \quad (3)$$

$$OC_{bio} = OC_{tot} – OC_{petro} \quad (4)$$

If we combine the equations we obtain:

$$Fm_{tot} * OC_{tot} = Fm_{bio} * (OC_{tot} - OC_{petro}) \quad (5)$$

From where we can calculate OC_{petro}

$$OC_{petro} = OC_{tot} – (Fm_{tot} * OC_{tot}) / Fm_{bio} \quad (6)$$

And OC_{bio}

$$OC_{bio} = OC_{tot} - OC_{petro} \quad (7)$$

The radiocarbon signature of 15 surface soils from the Narayani basin (Supplementary Table 5) was used to define the Fm of the OC_{bio} endmember (Fm_{bio} = 1.1- 0.9). OC_{tot} and Fm_{tot} are the measured values, and standard deviations are derived from the internal standard as described above. A Monte Carlo simulation ($n=10^5$) was used to randomly sample within the Fm_{bio} endmember and the standard deviation of OC_{tot} and Fm_{tot}. Errors of the model were defined by the standard deviation of the model results. This approach for determining OC_{bio} is not as sensitive to possible autocorrelation biases[47]. The two methods, however, give broadly similar results.

In order to calculate the total sediment yield, the surface sediment load was corrected for increasing concentrations with the depth of the water column. For this purpose, we use the method proposed by ref.[26] (equation 3.2), which integrates the surface sediment concentration for depth and water velocity in the Narayani river. The daily discharge data of the Narayani river was provided by the Department of Hydrology and Meteorology of Nepal (DHM), enabling calculation of daily sediment yield of the Narayani during the four studied monsoon seasons. With these data we were able to calculate the total amount of OC_{bio} exported by the Narayani in a given day for which TOC and Fm measurements are available. We observe a high daily variability in our TOC and Fm data without any significant correlation to the runoff, the sediment load or the season at the time of sampling. We upscale the estimate to the entire monsoon and hence interpolate across days without TOC and Fm measurements as follows:

ΣOC_{bio}(measured) * Σdaily sediment yield (all) / Σdaily sediment yield (with Fm and TOC measurement)

The concentration of TOC and its radiocarbon signature of surface sediments is taken to be representative of the whole water column (Supplementary Information and Supplementary Fig. 3). Suspended sediment samples from upstream the major confluence close to the sampling station confirm that incomplete mixing of the sediments from this confluence does not have a major influence on the TOC and radiocarbon concentration in Narayanghat (Supplementary Information and Supplementary Fig. 4).

Chemical weathering rates calculated by major ion chemistry

The concentrations of major cations in water samples from 2010 were determined with an Inductively Coupled Plasma Optical Emission Spectroscopy (ICP-OES) at the CRPG Nancy. Major cations and anions of samples from 2015-2017 were measured by Ion Chromatography (IC) at ETH Zürich. All results are reported in Supplementary Table 2. Ion concentrations were corrected for atmospheric input, as suggested by ref.[12] and using ion concentrations of rainwater from ref.[55]. Concentrations of Cl and SO_4 for the year 2010 were estimated by correlating the concentrations of the measured years to river discharge (Supplementary Information and Supplementary Fig. 5 and 6).

Concentrations of Ca and Mg derived from silicate weathering through carbonic acid (Ca_{sil} and Mg_{sil}) were calculated using elemental ratios of silicates and carbonates in the Central Himalaya from refs.[12,13]. A Monte Carlo simulation ($n=10^5$) sampled randomly within a normal distribution with the following standard deviation.

$Mg_{sil} = K * x$; x=0.5 with standard deviation of 0.25 (ref.[12]) (8)

$Ca_{sil} = (Na\text{-}Cl) * y$; y=0.4 with standard deviation of 0.15 (ref.[13]) (9)

The proportion of silicate weathering relative to carbonate weathering (x_{sil}) was calculated:

$X_{sil} = (1.8 * (Na – Cl) + 2* K) / (Na + K + 2*Mg + 2* Ca)$ (modified from ref.[12]) (10)

All the concentrations in equations 8-12 have been corrected for atmospheric input.

Secondary calcite precipitation along the Narayani and its tributary might slightly bias x_{sil} ([13,56]), but at the scale of the whole catchment, we assume that its effect is minor. For the years 2015-2017, where every second day was measured, the days without measurement had to be interpolated for the calculation of total fluxes per monsoon. Interpolation was done by taking the average of the measurements from the day before and after. This method takes into account previously reported seasonal changes of weathering rates and dilution effects in the beginning of the monsoon season[12,56]. Using the daily discharge data from the DHM we are able to calculate the total flux of Ca_{sil} and Mg_{sil} per monsoon.

For calculating the long-term carbon sink through silicate weathering, we subtract the amount of Ca_{sil} and Mg_{sil} derived from sulfuric acid weathering as the latter does not involve any carbon uptake. Assuming that sulfuric acid reacts with carbonates and silicates in the same relative proportions as carbonic acid[57], we can use x_{sil}:

$SO_{4,sil} = SO_{4,tot} * x_{sil}$ (11)

We define the proportion of Mg and Ca in the total ions derived from silicate weathering:

$(Mg_{sil} + Ca_{sil})_{SO4} = SO_{4,sil} * ((Ca_{sil} + Mg_{sil}) / (Ca_{sil} + Mg_{sil} + K/2 + (Na\text{-}Cl) /2)$ (12)

where Na-Cl is the total Na derived from silicate weathering[12]. We then calculate the Mg_{sil} and Ca_{sil} that has been weathered through carbonic acid.

$$(Mg_{sil} + Ca_{sil})_{HCO3} = (Mg_{sil} + Ca_{sil})_{tot} - (Mg_{sil} + Ca_{sil})_{SO4} \quad (13)$$

Finally, one mole of carbon per mole of $Ca_{sil,HCO3}$ or $Mg_{sil,HCO3}$ can be removed from the Earth's surface through carbonate precipitation and is thus considered as a long-term (>10^5 yr) carbon sink. As cation exchange between sediments and seawater is negligible[58] we do not take into account K and Na for the long-term carbon removal through silicate weathering.

For determining the proportion of carbonates weathered by sulfuric acid we can modify equation 11:

$$SO_{4,carb} = SO_{4,tot} * (1-x_{sil}) \quad (14)$$

The main uncertainty of the sulfuric acid weathering rate calculation derives from the unknown proportion of SO_4^- derived from evaporites. The latter produces SO_4^- during weathering but does not produce sulfuric acid which could act as a weathering agent. Previous studies estimate the evaporitic input in the Narayani basin as negligible to up to 30% of the total SO_4^- ([12]). We, therefore, use error bars between 100 – 70% for the calculated values. For calculating total fluxes per monsoon, we use the same interpolation as described above for silicate weathering.

OC_{petro} oxidation calculation with dissolved Re

The release of carbon through OC_{petro} oxidation in the Narayani catchment was estimated using Re as a tracer for the weathering of OC_{petro} [10,29,59]. We compiled dissolved Re concentration data from Himalayan rivers[29,30] and used the linear relationship between the sum of cations and Re (r^2 = 0.83) for estimating the Re concentrations in the Narayani (Supplementary Fig. 7). We calculated the mean flux of dissolved Re (Re_{flux}, 40.7 kg/monsoon) over the four studied monsoon seasons. Data of Re concentrations in bulk suspended sediments from the Narayani from refs.[31,32] (Re_{sd}; 2.7-4.8 * 10^{-10} pg/g) are used together with the mean OC_{petro} concentration of samples from this study (OC_{sd}). The OC_{petro} oxidation rate is finally calculated as described in ref.[59] with a Monte Carlo simulation (n=10^5):

$$C_{released} = Re_{flux} * (OC_{sd}/Re_{sd}) * f_C - f_{graphite} \quad (15)$$

Where f_c is the factor correcting for Re from inorganic phases and for the ratio of Re dissolved during OC_{petro} oxidation in soils ($0.5 < f_c < 1$; [10,59,60] and $f_{graphite}$ corrects for the fraction of crystalline graphite that is less prone to oxidation ($0.3 < f_{graphite} < 0.5$; estimated from data from ref.[47]).

Upscaling from a monsoonal to an annual carbon budget

The erosion as well as the carbon fluxes in the Central Himalaya, are mostly driven by the monsoonal precipitation. In order to render our carbon flux calculations comparable to other studies, we up-scale the monsoonal carbon budget to annual values based on the following assumptions. For the total OC_{bio} export we considered that ~95% of the annually suspended sediments of the Narayani are discharged during the monsoon[25] and that the relative importance of soil erosion increases during the dry season[26]. We, therefore, assume that the OC_{bio} discharged during the monsoon represents 90% of the annual OC_{bio} export. The monsoonal OC_{petro} export is assumed to follow the total sediment flux constituting 95% of the annual flux. For the silicate weathering budget, we follow ref.[56] who showed that in the Central Himalaya, ~60% of the annual silicate weathering flux is occurring during the monsoon. As the monsoon accounts for ~80% of the total water discharge of the Narayani River[25], we assume this same proportion for carbonate weathering by sulfuric acid and OC_{petro} oxidation. This calculation is conservative, as the fraction of sulfuric acid relative to carbonic acid is likely decreasing during the monsoon in the headwaters of the Narayani[56].

References Methods

51. Larsen, I. J., Montgomery, D. R. & Korup, O. Landslide erosion controlled by hillslope material. *Nat. Geosci.* **3**, 247–251 (2010).

52. Märki, L. *et al.* Molecular tracing of riverine soil organic matter from the Central Himalaya. *Geophys. Res. Lett.* (2020) doi:10.1029/2020GL087403.

53. Eckhardt, K. How to construct recursive digital filters for baseflow separation. *Hydrol. Process.* **19**, 507–515 (2005).

54. McIntyre, C. P. *et al.* Online 13C and 14C Gas Measurements by EA-IRMS–AMS at ETH Zürich. *Radiocarbon* **59**, 893–903 (2017).

55. Wolff-Boenisch, D., Gabet, E. J., Burbank, D. W., Langner, H. & Putkonen, J. Spatial variations in chemical weathering and CO2 consumption in Nepalese High Himalayan catchments during the monsoon season. *Geochim. Cosmochim. Acta* **73**, 3148–3170 (2009).

56. Tipper, E. T. *et al.* The short term climatic sensitivity of carbonate and silicate weathering fluxes: Insight from seasonal variations in river chemistry. *Geochim. Cosmochim. Acta* **70**, 2737–2754 (2006).

57. Burke, A. *et al.* Sulfur isotopes in rivers : Insights into global weathering budgets, pyrite oxidation, and the modern sulfur cycle. *Earth Planet. Sci. Lett.* **496**, 168–177 (2018).

58. Lupker, M., France-Lanord, C. & Lartiges, B. Impact of sediment-seawater cation exchange on Himalayan chemical weathering fluxes. *Earth Surf. Dyn.* **4**, 675–684 (2016).

59. Horan, K. *et al.* Mountain glaciation drives rapid oxidation of rock-bound organic carbon. *Sci. Adv.* **3**, 1–9 (2017).

60. Pierson-Wickmann, A. C., Reisberg, L. & France-Lanord, C. Behavior of Re and Os during low-temperature alteration: Results from Himalayan soils and altered black shales. *Geochim. Cosmochim. Acta* **66**, 1539–1548 (2002).

51. Larsen, I. J., Montgomery, D. R. & Korup, O. Landslide erosion controlled by hillslope material. *Nat. Geosci.* **3**, 247–251 (2010).

52. Märki, L. *et al.* Molecular tracing of riverine soil organic matter from the Central Himalaya. *Geophys. Res. Lett.* (2020) doi:10.1029/2020GL087403.

53. Eckhardt, K. How to construct recursive digital filters for baseflow separation. *Hydrol. Process.* **19**, 507–515 (2005).

54. McIntyre, C. P. *et al.* Online 13C and 14C Gas Measurements by EA-IRMS–AMS at ETH Zürich. *Radiocarbon* **59**, 893–903 (2017).

55. Wolff-Boenisch, D., Gabet, E. J., Burbank, D. W., Langner, H. & Putkonen, J. Spatial variations in chemical weathering and CO2 consumption in Nepalese High Himalayan catchments during the monsoon season. *Geochim. Cosmochim. Acta* **73**, 3148–3170 (2009).

56. Tipper, E. T. *et al.* The short term climatic sensitivity of carbonate and silicate weathering fluxes: Insight from seasonal variations in river chemistry. *Geochim. Cosmochim. Acta* **70**, 2737–2754 (2006).

57. Burke, A. *et al.* Sulfur isotopes in rivers : Insights into global weathering budgets, pyrite oxidation, and the modern sulfur cycle. *Earth Planet. Sci. Lett.* **496**, 168–177 (2018).

58. Lupker, M., France-Lanord, C. & Lartiges, B. Impact of sediment-seawater cation exchange on Himalayan chemical weathering fluxes. *Earth Surf. Dyn.* **4**, 675–684 (2016).

59. Horan, K. *et al.* Mountain glaciation drives rapid oxidation of rock-bound organic carbon. *Sci. Adv.* **3**, 1–9 (2017).

60. Pierson-Wickmann, A. C., Reisberg, L. & France-Lanord, C. Behavior of Re and Os during low-temperature alteration: Results from Himalayan soils and altered black shales. *Geochim. Cosmochim. Acta* **66**, 1539–1548 (2002).

Supplementary Information for: An unshakable carbon budget for the Himalaya

Depth profiles and samples upstream of the confluence close to Narayanghat

We test whether TOC, $\delta^{13}C$ and radiocarbon signatures of surface samples from the Narayani are representative of those of the entire water column using four sediment depth profiles (Supplementary Table 3). While sediment load increases with depth in the water column[26], the radiocarbon signature does not show any systematic variation with depth and TOC concentrations slightly decrease. We calculate the proportions of OC_{bio} and OC_{petro} as explained in the Methods, for each sample in the depth profile. Using the water velocity estimated from velocity profiles in the Narayani[26], we are able to estimate the amount of OC_{bio} and OC_{petro} exported per day at a certain depth. As expected from previous studies in the Himalaya[28], we do not find any systematic change of OC_{bio} and OC_{petro} export with water depth (Supplementary Fig. 3) and therefore assume that surface sediments are representative of the whole water column with respect to OC_{bio} fluxes.

The time-series sampling station in Narayanghat lies around 2 km downstream of the confluence of two major rivers (Trisuli and Khali Gandaki). We evaluate whether our data variability reflects the possible incomplete mixing of sediments from this confluence. For this purpose, sediment samples from the two tributaries just upstream the confluence are compared to suspended sediments from the Narayanghat sampling station and from a bridge 4 km further downstream. Supplementary Figure 4 shows that the TOC content and the radiocarbon signature of samples from the two rivers are similar; and that the geochemical signature of sediments from the Narayani integrates the signal of the two rivers. A set of samples taken from the left side, the middle, and the right side of the Narayani confirm a complete mixing of the suspended sediments (Supplementary Table 5). We thus argue that the daily changes in TOC and radiocarbon signature in sediments from the Narayani are unlikely to be driven solely by incomplete mixing of the two major tributaries. The high variability instead reflects temporal changes in the sources of the exported OC and the proportion of OC_{bio} and OC_{petro}.

Estimation of anion concentrations for 2010 samples

Concentrations of Cl and SO_4 of the 2010 samples were not measured and estimated by correlating the concentrations from the measured years to river discharge (Q) with a power law (Supplementary Fig. 5):

$$Cl = e^{9.57} * Q^{-0.79} \ (r^2=0.73) \quad (1)$$

$$SO_4 = e^{7.45} * Q^{-0.31} \ (r^2=0.51) \quad (2)$$

For the Cl estimation, the year 2017 was not taken into account (see also next paragraph). As we do not observe any major difference of any cation concentration as a function of the river discharge between

2010 and the post-seismic years, we assume that the anion concentration in 2010 followed the same patterns as in the years 2015-2017.

Cl concentrations in 2017 samples

The Cl concentrations of the year 2017 differ from the other measured years, and most of the 2017 samples do not show a linear relationship between the Na and Cl concentrations (Supplementary Fig. 6) which makes a natural source of the excess Cl improbable. The samples have been measured twice with different standards to exclude any measurement bias. We assume that the elevated Cl concentrations in 2017 are associated to anthropogenic Cl inputs to the Narayani. As we use the Cl to calculate the Ca_{sil} (Methods), the Ca_{sil}+Mg_{sil} concentrations of the year 2017 (Fig. 3) and with it the potential carbon sink linked to silicate weathering in 2017 (Fig. 4c) are probably slightly underestimated, but this potential bias does not affect our conclusions.

OC_{petro} oxidation versus riverine export

By comparing the estimated flux of OC_{petro} oxidation (81 kt C/yr) within the Narayani catchment with the exported OC_{petro} in riverine sediments (138 kt C/yr), we find that ca. 37% of the OC initially present in the bedrock is oxidized. This is a lower fraction of oxidized OC_{petro} than that found in Taiwan (67% ([43])), which can be attributed to the lower initial concentration of OC_{petro} in the Himalayan bedrock or different climatic conditions.

Differences in riverine OC_{petro} export rates between the Narayani and smaller Himalayan catchments in the upstream region can be linked OC_{petro} concentration in the bedrock. As such, the OC_{petro} export in the Narayani (4.6 t/km^{2}yr) is lower than in an upstream catchment in draining the Tibetan Sedimentary Series (7.7 t/km^{2}yr), and an order of magnitude higher than a High Himalayan upstream segment of a major confluent of the Narayani (0.8 t/km^{2}yr)[28].

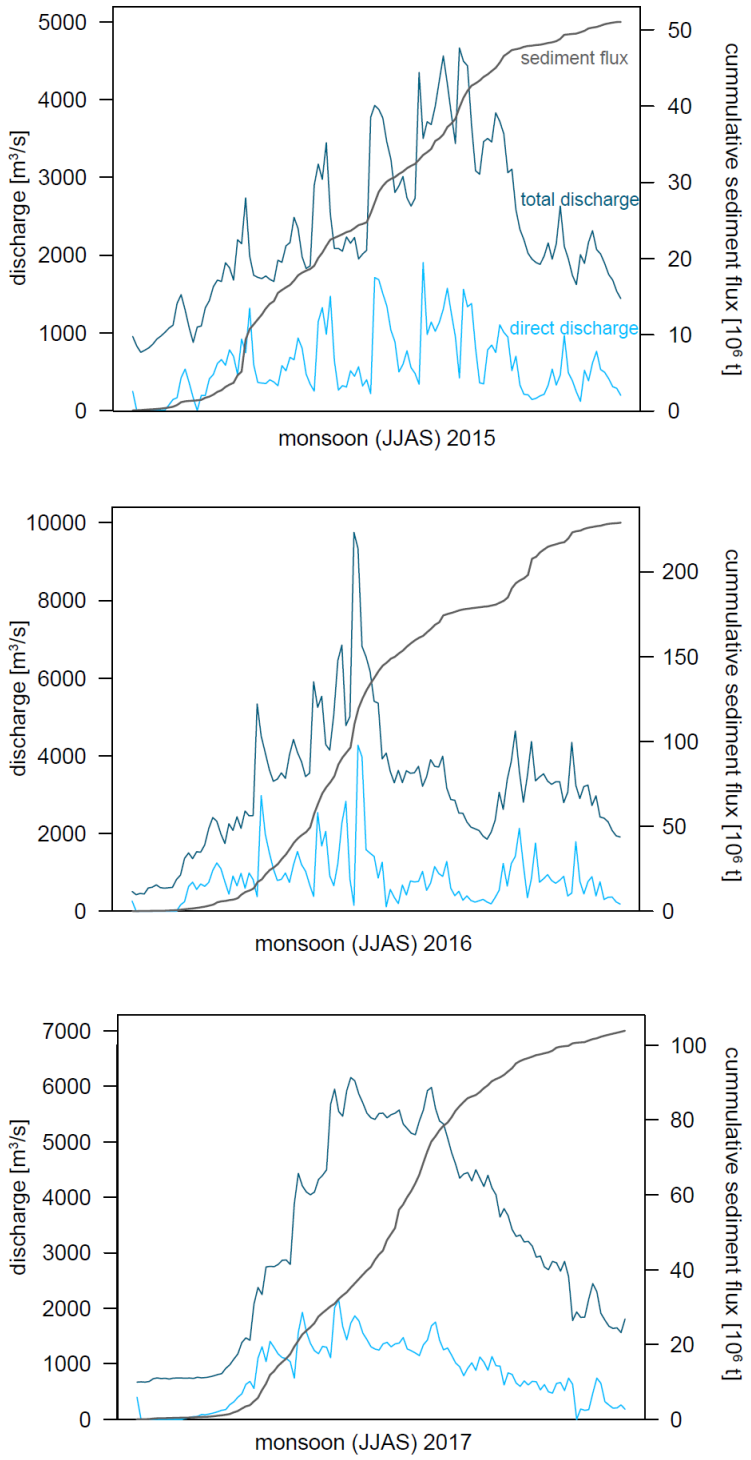

Supplementary Fig. 1: *Daily discharge (dark blue; from the DHM) and calculated direct discharge (light blue; calculated with a digital filter[53] as described in ref.[26]) for the monsoon months (JJAS – June, July, August, September) of the years 2015, 2016 and 2017. The cumulative sediment flux is shown in grey.*

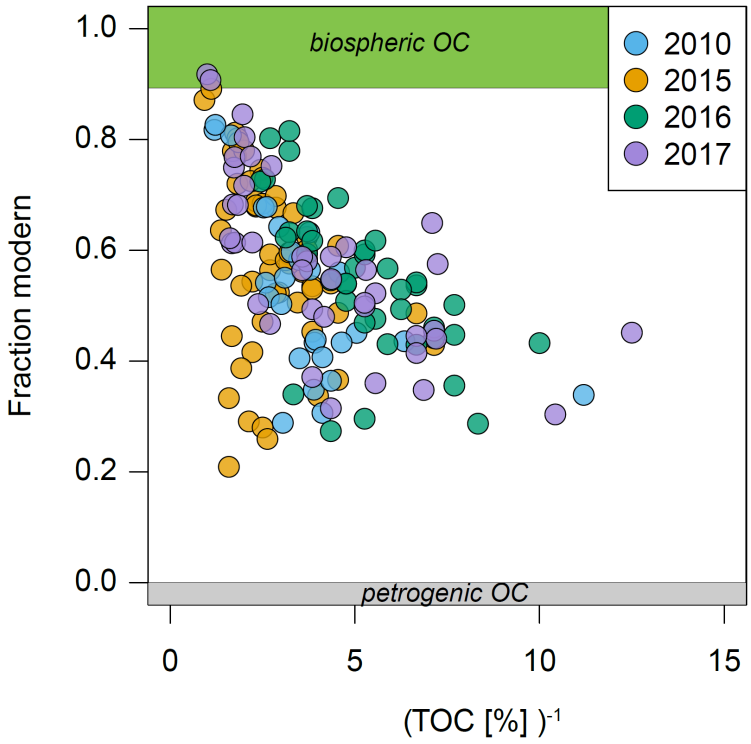

Supplementary Fig. 2: *TOC^{-1} plotted against the fraction modern of the bulk suspended sediment colored as a function of the sampling year. The biospheric and petrogenic endmembers used in the mixing model for disentangling OC_{bio} and OC_{petro} inputs are schematically shown.*

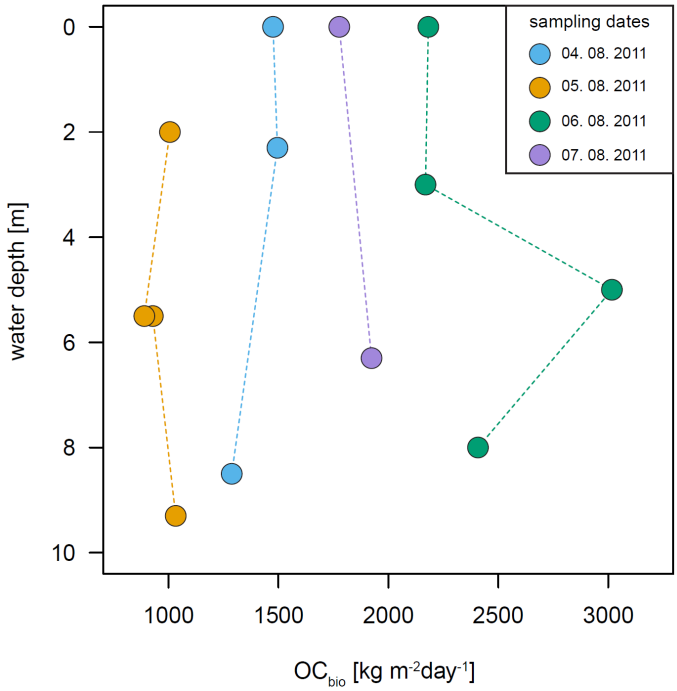

Supplementary Fig. 3: *OC_{bio} export per day [kg*m^{-2}day^{-1}] at different depths in the Narayani River calculated with depth profile samples and water velocity data*[26].

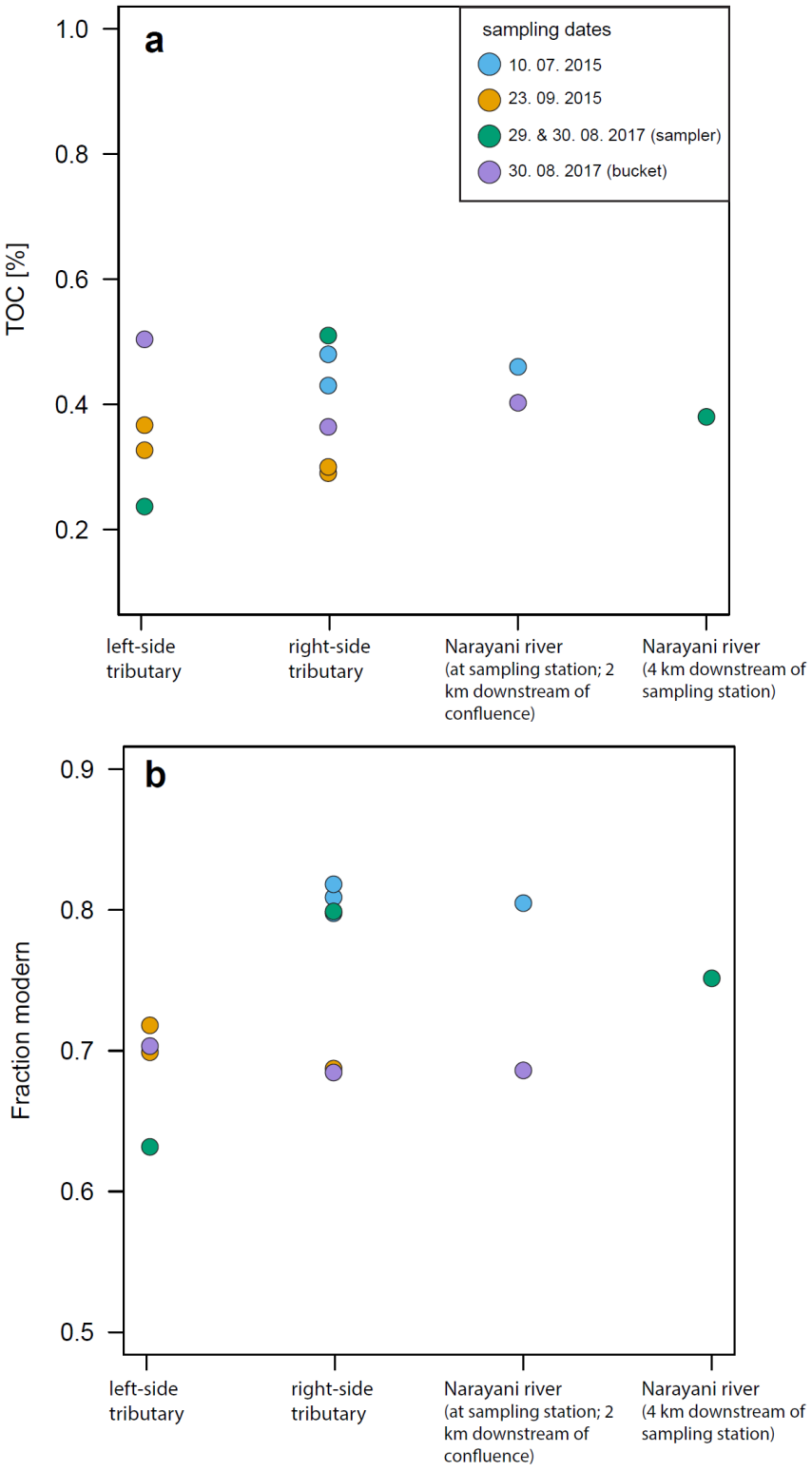

Supplementary Fig. 4: (a) *TOC concentration and* ***(b)*** *fraction modern in suspended sediments of the two tributaries shortly upstream the confluence and of two stations in the Narayani river colored as a function of the sampling date.*

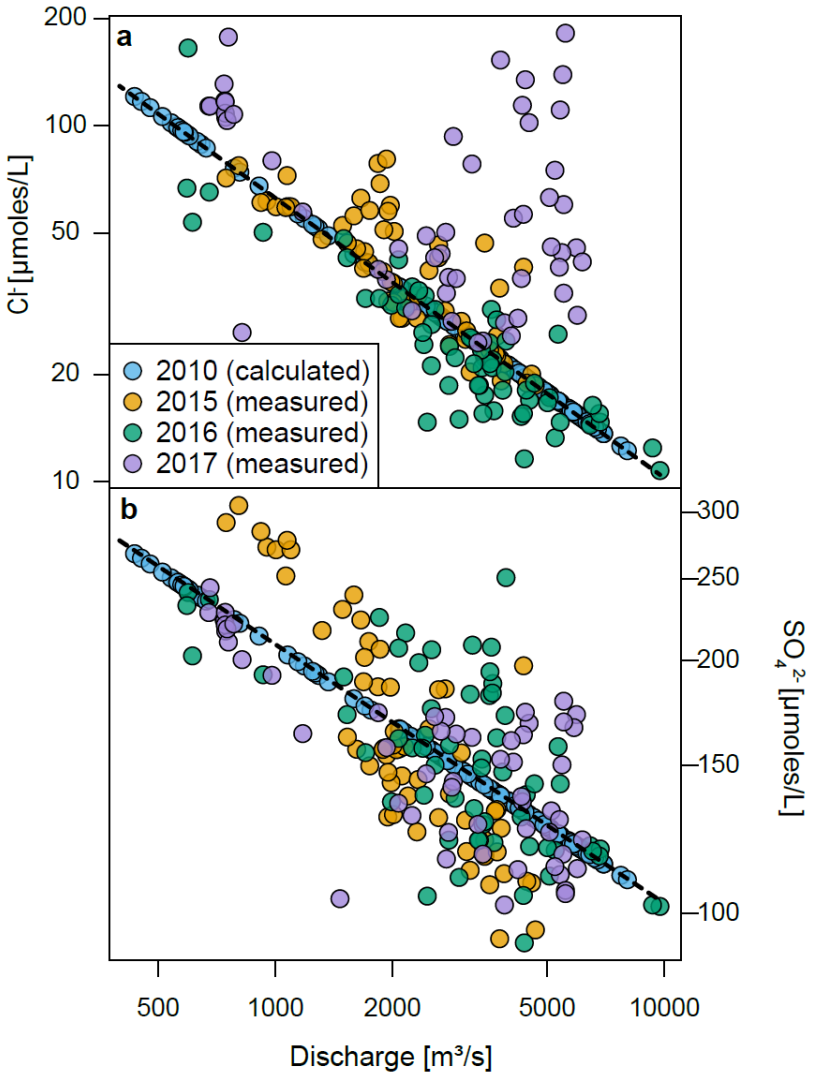

Supplementary Fig. 5: (a) *Cl^- and* ***(b)*** *SO_4^{2-} concentrations as a function of the river discharge in Narayanghat. The anion concentrations of the samples 2015-2017 were measured. Exponential functions (dashed lines) through the measured values were used to determine the concentrations of the 2010 samples with the river discharge (Q): $[Cl] = e^{9.57} * Q^{-0.79}$ (r^2=0.73); $[SO_4] = e^{7.45} * Q^{-0.3}$ (r^2=0.51). For Cl, the 2017 concentrations were not taken into account (see text).*

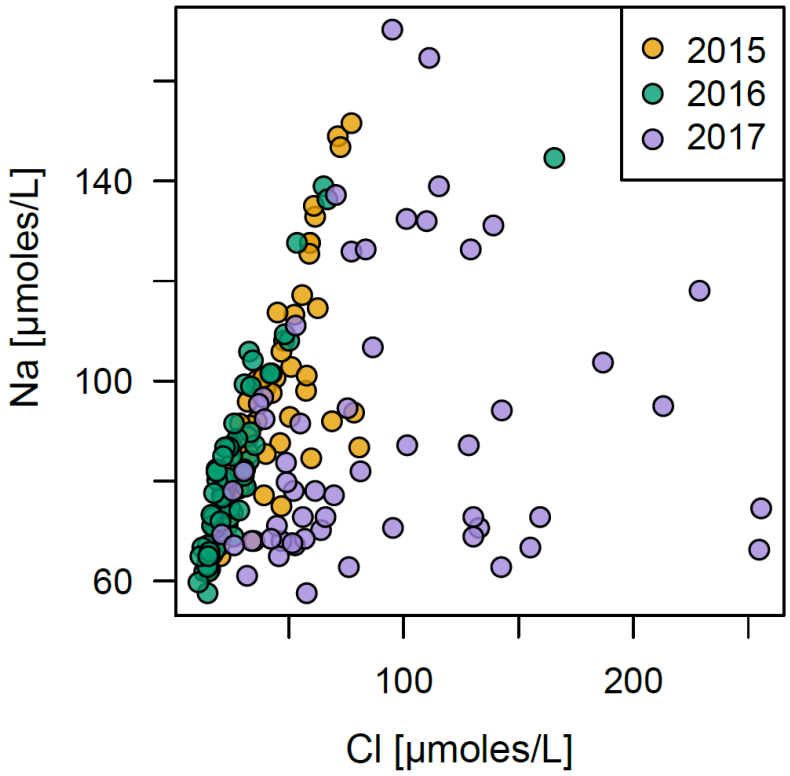

Supplementary Fig. 6: *Cl versus Na concentrations (corrected for atmospheric input) of the measured monsoon seasons.*

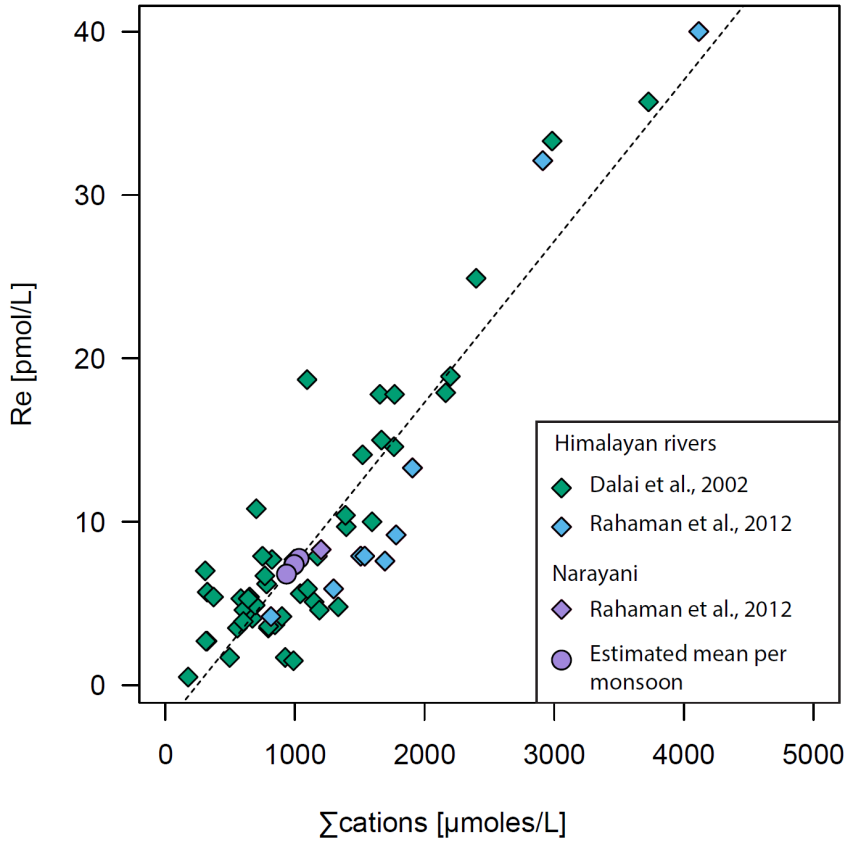

Supplementary Fig. 7: *Sum of cations as a function of the Re concentration in Himalayan rivers from refs.*[29,30] *(diamonds) and mean sum of cations in the Narayani per monsoon season as a function of the estimated Re concentration (circles). Dashed line shows linear regression between the measured sum of cations and Re concentrations (r^2 = 0.83).*

Narayani catchment Gorkha earthquake-triggered landslide volumes and lowering rates*

	mean volume (km^3)	± 1 std (km^3)	mean lowering (mm)	± 1 std (mm)
full area, global	0.201	0.013	6.279	0.413
scar area, global, soil	0.011	0.001	0.337	0.031
scar area, global, bedrock	0.043	0.010	1.331	0.311
full area, Himalaya, mixed	0.506	0.149	15.822	4.648
full area, Himalaya, bedrock	0.486	0.064	15.191	2.014
full area, Himalaya, soil	0.220	0.081	6.888	2.544

*calculations convert landslide area to volume using the scaling schemes in ref.[51]

Supplementary Table 1: *Volume of coseismic landslides of the 2015 Gorkha earthquake in the Narayani catchment and associated lowering rates.*

date	Q (m3/s)	sediment load (g/L)	date	Q (m3/s)	sediment load (g/L)	date	Q (m3/s)	sediment load (g/L)
2010			14.07.2010	2725	3.23	27.08.2010	4451	2.59
01.06.2010	435	0.20	15.07.2010	2880	7.99	28.08.2010	6627	3.60
02.06.2010	453	NA	16.07.2010	2610	5.79	29.08.2010	5740	3.21
03.06.2010	477	NA	17.07.2010	2755	3.10	30.08.2010	5999	3.22
04.06.2010	568	0.25	18.07.2010	2575	3.52	31.08.2010	6352	2.44
05.06.2010	645	NA	19.07.2010	3780	3.62	01.09.2010	6126	2.13
06.06.2010	630	NA	20.07.2010	5884	3.57	02.09.2010	5964	3.36
07.06.2010	595	NA	21.07.2010	4210	5.25	03.09.2010	5353	2.62
08.06.2010	557	0.34	22.07.2010	5106	3.98	04.09.2010	6323	1.90
09.06.2010	540	NA	23.07.2010	4270	4.58	05.09.2010	5361	1.66
10.06.2010	513	NA	24.07.2010	4045	2.47	06.09.2010	4632	1.38
11.06.2010	562	NA	25.07.2010	5062	5.67	07.09.2010	5823	5.43
12.06.2010	575	0.49	26.07.2010	4614	3.24	08.09.2010	5753	2.42
13.06.2010	602	NA	27.07.2010	5422	4.65	09.09.2010	4320	2.06
14.06.2010	585	NA	28.07.2010	5066	2.17	10.09.2010	3795	2.51
15.06.2010	582	NA	29.07.2010	3985	3.01	11.09.2010	3548	5.68
16.06.2010	665	0.52	30.07.2010	6987	4.08	12.09.2010	4973	2.01
17.06.2010	785	0.82	31.07.2010	6227	8.04	13.09.2010	4604	3.72
18.06.2010	909	1.75	01.08.2010	4961	4.12	14.09.2010	4739	2.41
19.06.2010	811	1.48	02.08.2010	4505	1.69	15.09.2010	4991	2.22
20.06.2010	1188	3.08	03.08.2010	5089	2.48	16.09.2010	6427	2.85
21.06.2010	1293	3.69	04.08.2010	4362	2.03	17.09.2010	5331	1.03
22.06.2010	1267	2.02	05.08.2010	6030	1.75	18.09.2010	5857	1.55
23.06.2010	1077	1.55	06.08.2010	4915	2.14	19.09.2010	5839	2.04
24.06.2010	1144	2.19	07.08.2010	4140	3.04	20.09.2010	4906	1.03
25.06.2010	1247	1.58	08.08.2010	3705	1.38	21.09.2010	4295	1.03
26.06.2010	1370	1.58	09.08.2010	3560	1.18	22.09.2010	3795	0.90
27.06.2010	1593	1.73	10.08.2010	3370	1.43	23.09.2010	4390	0.55
28.06.2010	2244	4.30	11.08.2010	3625	3.23	24.09.2010	4235	0.49
29.06.2010	1763	2.26	12.08.2010	3745	1.93	25.09.2010	3445	0.54
30.06.2010	1700	2.65	13.08.2010	3255	2.17	26.09.2010	3125	0.51
01.07.2010	2146	3.94	14.08.2010	3355	2.23	27.09.2010	2775	0.45
02.07.2010	2083	3.76	15.08.2010	3780	6.03	28.09.2010	2445	0.38
03.07.2010	2520	4.10	16.08.2010	4345	3.07	29.09.2010	2227	0.45
04.07.2010	2515	3.30	17.08.2010	4250	3.74	30.09.2010	2097	0.26
05.07.2010	2685	3.47	18.08.2010	4400	3.47			
06.07.2010	3615	2.88	19.08.2010	4773	5.07			
07.07.2010	3190	2.29	20.08.2010	6984	3.62			
08.07.2010	2665	1.46	21.08.2010	5927	3.54			
09.07.2010	2292	2.06	22.08.2010	6739	2.79			
10.07.2010	2970	2.13	23.08.2010	7735	2.81			
11.07.2010	5849	3.45	24.08.2010	8041	4.09			
12.07.2010	3960	2.01	25.08.2010	6081	6.84			
13.07.2010	3050	1.94	26.08.2010	5662	3.96			

Supplementary Table 2.1: *Daily water discharge in Narayanghat from the Department of Hydrology and Meteorology of Nepal (DHM) and sediment load (data of 2010 from ref.[26])*

date	Q (m3/s)	sediment load (g/L)	date	Q (m3/s)	sediment load (g/L)	date	Q (m3/s)	sediment load (g/L)
2015			14.07.2015	1827	1.54	27.08.2015	3460	1.49
01.06.2015	952	0.78	15.07.2015	1860	1.22	28.08.2015	3500	0.97
02.06.2015	830	0.26	16.07.2015	2898	1.56	29.08.2015	3455	1.33
03.06.2015	748	0.37	17.07.2015	3170	3.36	30.08.2015	3830	1.17
04.06.2015	775	0.60	18.07.2015	2975	2.45	31.08.2015	3720	1.91
05.06.2015	806	0.54	19.07.2015	3445	NA	01.09.2015	3560	2.54
06.06.2015	853	0.34	20.07.2015	2528	NA	02.09.2015	3060	1.26
07.06.2015	919	0.43	21.07.2015	2085	1.18	03.09.2015	3105	1.39
08.06.2015	958	0.57	22.07.2015	2085	1.19	04.09.2015	2585	0.42
09.06.2015	1005	0.63	23.07.2015	2050	1.27	05.09.2015	2330	0.55
10.06.2015	1060	0.84	24.07.2015	2233	1.29	06.09.2015	2195	0.97
11.06.2015	1097	0.97	25.07.2015	2152	0.80	07.09.2015	2023	0.56
12.06.2015	1377	1.72	26.07.2015	2226	1.74	08.09.2015	1947	0.25
13.06.2015	1490	2.66	27.07.2015	1950	NA	09.09.2015	1903	0.41
14.06.2015	1293	0.96	28.07.2015	2013	0.80	10.09.2015	1880	0.26
15.06.2015	1065	0.49	29.07.2015	2061	1.10	11.09.2015	1987	0.58
16.06.2015	876	0.41	30.07.2015	3775	3.26	12.09.2015	2155	0.60
17.06.2015	1073	0.44	31.07.2015	3925	NA	13.09.2015	1947	0.48
18.06.2015	1087	0.66	01.08.2015	3875	3.81	14.09.2015	2143	0.71
19.06.2015	1320	2.16	02.08.2015	3765	2.13	15.09.2015	2630	1.20
20.06.2015	1413	1.15	03.08.2015	3455	1.78	16.09.2015	2112	NA
21.06.2015	1593	1.77	04.08.2015	3235	1.09	17.09.2015	1950	0.30
22.06.2015	1677	2.29	05.08.2015	2805	0.89	18.09.2015	1740	0.35
23.06.2015	1660	1.35	06.08.2015	2890	1.49	19.09.2015	1620	0.28
24.06.2015	1900	2.43	07.08.2015	3010	1.10	20.09.2015	2005	0.93
25.06.2015	1837	1.74	08.08.2015	2735	1.71	21.09.2015	1893	1.05
26.06.2015	1677	1.54	09.08.2015	2630	1.24	22.09.2015	2164	1.55
27.06.2015	2196	4.71	10.08.2015	2730	0.99	23.09.2015	2314	0.49
28.06.2015	2147	2.42	11.08.2015	4350	1.34	24.09.2015	2071	0.42
29.06.2015	2735	16.19	12.08.2015	3500	1.83	25.09.2015	2013	0.89
30.06.2015	1987	7.28	13.08.2015	3715	1.02	26.09.2015	1893	1.08
01.07.2015	1740	3.76	14.08.2015	3680	1.23	27.09.2015	1750	0.66
02.07.2015	1713	4.02	15.08.2015	3915	NA	28.09.2015	1677	0.66
03.07.2015	1697	3.96	16.08.2015	4240	0.82	29.09.2015	1533	0.46
04.07.2015	1730	4.91	17.08.2015	4562	1.18	30.09.2015	1440	0.15
05.07.2015	1687	3.88	18.08.2015	4205	2.41			
06.07.2015	1660	2.21	19.08.2015	3810	1.27			
07.07.2015	1933	5.95	20.08.2015	3435	1.92			
08.07.2015	1907	2.12	21.08.2015	4665	3.28			
09.07.2015	2118	1.73	22.08.2015	4495	2.96			
10.07.2015	2161	1.53	23.08.2015	4435	2.17			
11.07.2015	2485	2.46	24.08.2015	3675	1.91			
12.07.2015	2341	3.07	25.08.2015	3085	1.03			
13.07.2015	1977	1.89	26.08.2015	3040	1.25			

date	Q (m3/s)	sediment load (g/L)	date	Q (m3/s)	sediment load (g/L)	date	Q (m3/s)	sediment load (g/L)
2016			14.07.2016	3465	5.03	27.08.2016	1933	1.92
01.06.2016	508	NA	15.07.2016	3555	8.05	28.08.2016	1853	1.01
02.06.2016	425	NA	16.07.2016	5906	14.16	29.08.2016	2033	2.79
03.06.2016	458	NA	17.07.2016	5246	12.16	30.08.2016	2340	2.33
04.06.2016	443	0.58	18.07.2016	5530	10.73	31.08.2016	3060	3.90
05.06.2016	597	0.68	19.07.2016	4290	9.04	01.09.2016	2620	4.50
06.06.2016	618	0.60	20.07.2016	4145	7.34	02.09.2016	3390	6.16
07.06.2016	677	0.45	21.07.2016	5068	7.34	03.09.2016	3860	14.60
08.06.2016	607	0.47	22.07.2016	6452	11.04	04.09.2016	4637	6.75
09.06.2016	593	0.66	23.07.2016	6849	6.09	05.09.2016	3600	4.64
10.06.2016	603	1.96	24.07.2016	4778	6.52	06.09.2016	2805	4.65
11.06.2016	613	1.70	25.07.2016	5012	6.15	07.09.2016	3490	5.99
12.06.2016	816	1.53	26.07.2016	9750	14.69	08.09.2016	4369	22.78
13.06.2016	931	3.18	27.07.2016	9335	10.06	09.09.2016	3355	3.48
14.06.2016	1360	2.23	28.07.2016	6815	8.78	10.09.2016	3455	8.05
15.06.2016	1500	1.65	29.07.2016	6547	7.66	11.09.2016	3535	5.18
16.06.2016	1353	1.80	30.07.2016	6170	6.67	12.09.2016	3350	4.98
17.06.2016	1530	2.28	31.07.2016	5403	6.78	13.09.2016	3265	2.49
18.06.2016	1520	2.59	01.08.2016	5354	7.36	14.09.2016	3330	2.13
19.06.2016	1707	2.47	02.08.2016	3920	8.16	15.09.2016	3330	2.32
20.06.2016	2127	2.77	03.08.2016	4070	4.61	16.09.2016	2795	1.67
21.06.2016	2411	2.64	04.08.2016	3595	6.60	17.09.2016	3065	7.53
22.06.2016	2315	6.18	05.08.2016	3305	3.54	18.09.2016	4346	8.67
23.06.2016	1990	3.00	06.08.2016	3625	5.78	19.09.2016	3240	2.07
24.06.2016	1743	1.48	07.08.2016	3310	5.38	20.09.2016	2900	1.37
25.06.2016	2250	2.30	08.08.2016	3615	6.79	21.09.2016	3210	3.55
26.06.2016	2081	1.62	09.08.2016	3550	5.77	22.09.2016	3245	2.01
27.06.2016	2430	3.22	10.08.2016	3565	5.21	23.09.2016	2720	1.66
28.06.2016	2133	11.05	11.08.2016	3730	4.04	24.09.2016	2970	1.65
29.06.2016	2578	6.37	12.08.2016	3215	3.67	25.09.2016	2425	1.15
30.06.2016	2455	3.40	13.08.2016	3460	6.62	26.09.2016	2395	2.94
01.07.2016	2460	5.33	14.08.2016	3900	5.43	27.09.2016	2300	2.13
02.07.2016	5335	7.41	15.08.2016	3730	6.65	28.09.2016	2077	1.18
03.07.2016	4507	3.42	16.08.2016	3710	3.98	29.09.2016	1940	0.82
04.07.2016	4080	7.99	17.08.2016	3990	10.53	30.09.2016	1910	NA
05.07.2016	3650	7.02	18.08.2016	3170	2.71			
06.07.2016	3345	4.71	19.08.2016	2875	2.37			
07.07.2016	3400	6.20	20.08.2016	2855	2.71			
08.07.2016	3560	9.05	21.08.2016	2525	3.55			
09.07.2016	3420	7.89	22.08.2016	2520	2.18			
10.07.2016	4020	9.00	23.08.2016	2295	1.56			
11.07.2016	4420	8.37	24.08.2016	2164	1.66			
12.07.2016	4085	6.59	25.08.2016	2121	1.43			
13.07.2016	3845	5.28	26.08.2016	2077	1.38			

date	Q (m3/s)	sediment load (g/L)	date	Q (m3/s)	sediment load (g/L)	date	Q (m3/s)	sediment load (g/L)
2017			15.07.2017	4095	2.78	29.08.2017	4045	1.46
01.06.2017	670	0.15	16.07.2017	4320	4.26	30.08.2017	3645	1.33
02.06.2017	675	0.22	17.07.2017	4395	2.29	31.08.2017	3795	1.78
03.06.2017	670	0.25	18.07.2017	4495	2.04	01.09.2017	3670	2.62
04.06.2017	680	0.30	19.07.2017	5674	1.66	02.09.2017	3420	2.68
05.06.2017	730	1.90	20.07.2017	5949	1.16	03.09.2017	3295	4.15
06.06.2017	746	1.20	21.07.2017	5547	2.36	04.09.2017	3320	1.96
07.06.2017	733	0.30	22.07.2017	5460	1.80	05.09.2017	3195	1.52
08.06.2017	739	0.29	23.07.2017	5921	1.47	06.09.2017	3205	1.08
09.06.2017	725	0.38	24.07.2017	6158	2.07	07.09.2017	3120	1.28
10.06.2017	742	0.62	25.07.2017	6098	1.93	08.09.2017	2920	1.50
11.06.2017	744	0.42	26.07.2017	5860	2.04	09.09.2017	2940	0.74
12.06.2017	744	0.39	27.07.2017	5698	2.15	10.09.2017	2745	1.07
13.06.2017	740	0.34	28.07.2017	5516	2.12	11.09.2017	2695	0.99
14.06.2017	744	0.29	29.07.2017	5432	1.80	12.09.2017	2845	1.62
15.06.2017	736	0.48	30.07.2017	5403	3.58	13.09.2017	2820	3.01
16.06.2017	758	1.14	31.07.2017	5510	2.75	14.09.2017	2670	1.07
17.06.2017	746	0.68	01.08.2017	5516	2.00	15.09.2017	2845	0.44
18.06.2017	752	0.43	02.08.2017	5432	5.31	16.09.2017	2570	0.48
19.06.2017	764	0.58	03.08.2017	5488	3.05	17.09.2017	1780	3.87
20.06.2017	782	1.47	04.08.2017	5516	3.04	18.09.2017	1933	0.93
21.06.2017	806	1.90	05.08.2017	5573	9.14	19.09.2017	1837	0.50
22.06.2017	822	1.43	06.08.2017	5321	2.66	20.09.2017	1840	0.40
23.06.2017	917	1.77	07.08.2017	5237	3.93	21.09.2017	2168	2.11
24.06.2017	981	2.08	08.08.2017	5154	3.24	22.09.2017	2445	1.63
25.06.2017	1083	4.40	09.08.2017	5127	4.09	23.09.2017	2300	0.99
26.06.2017	1177	3.24	10.08.2017	5375	4.46	24.09.2017	1910	NA
27.06.2017	1383	4.99	11.08.2017	5573	5.93	25.09.2017	1787	NA
28.06.2017	1467	4.35	12.08.2017	5922	5.38	26.09.2017	1677	NA
29.06.2017	1423	2.23	13.08.2017	5979	4.56	27.09.2017	1637	NA
30.06.2017	2076	5.21	14.08.2017	5601	2.57	28.09.2017	1647	NA
01.07.2017	2375	4.12	15.08.2017	5375	3.12	29.09.2017	1563	NA
02.07.2017	2247	9.70	16.08.2017	5320	2.38	30.09.2017	1807	NA
03.07.2017	2745	6.60	17.08.2017	5072	1.66			
04.07.2017	2755	9.03	18.08.2017	4804	3.12			
05.07.2017	2750	3.84	19.08.2017	4595	3.97			
06.07.2017	2790	5.36	20.08.2017	4345	2.97			
07.07.2017	2865	3.64	21.08.2017	4420	2.64			
08.07.2017	2870	3.46	22.08.2017	4445	2.35			
09.07.2017	2790	4.46	23.08.2017	4295	1.12			
10.07.2017	3885	5.33	24.08.2017	4496	0.87			
11.07.2017	4430	3.77	25.08.2017	4345	1.94			
12.07.2017	4205	4.14	26.08.2017	4195	2.55			
13.07.2017	4095	2.62	27.08.2017	4395	1.86			
14.07.2017	4045	2.36	28.08.2017	4170	2.72			

date	Fraction modern	TOC (%)	$\delta^{13}C$ (‰)	OCbio (%)	OCpetro (%)	OC export (t/day)	OCbio export (t/day)	OCpetro export (t/day)
2010								
17.06.2010	0.82	0.84	-24.20	0.69	0.15	500.62	410.47	90.14
20.06.2010	0.68	0.60	NA	0.41	0.19	2059.14	1412.96	646.18
28.06.2010	0.81	0.61	-24.39	0.49	0.12	5560.28	4503.89	1056.39
02.07.2010	0.68	0.40	-23.86	0.27	0.13	2922.68	1985.45	937.23
07.07.2010	0.58	0.29	-24.73	0.17	0.12	1995.54	1165.87	829.67
13.07.2010	0.43	0.26	-24.38	0.11	0.14	1440.81	625.76	815.05
19.07.2010	0.35	0.26	-25.11	0.09	0.17	3371.05	1177.48	2193.56
23.07.2010	0.36	0.23	NA	0.08	0.15	4313.90	1576.77	2737.12
27.07.2010	0.68	0.38	NA	0.26	0.12	9306.06	6333.37	2972.69
31.07.2010	0.45	0.20	-24.73	0.09	0.11	9597.28	4338.90	5258.38
04.08.2010	0.34	0.09	-26.19	0.03	0.06	756.76	257.21	499.55
08.08.2010	0.52	0.37	-25.29	0.19	0.18	1825.83	943.65	882.18
12.08.2010	0.43	0.22	-25.08	0.09	0.12	1487.84	646.98	840.86
16.08.2010	0.55	0.32	-25.10	0.18	0.14	4123.30	2276.87	1846.43
20.08.2010	0.50	0.33	-24.45	0.17	0.16	8135.65	4104.22	4031.43
24.08.2010	0.40	0.29	-24.94	0.12	0.17	9143.97	3713.64	5430.33
28.08.2010	0.44	0.21	-24.98	0.09	0.12	4757.42	2086.08	2671.34
01.09.2010	0.31	0.24	-24.31	0.07	0.17	3056.68	939.55	2117.13
05.09.2010	0.29	0.33	-25.17	0.09	0.23	2815.37	814.55	2000.82
08.09.2010	0.62	0.32	-24.85	0.20	0.12	4322.40	2687.07	1635.33
13.09.2010	0.56	0.24	-25.73	0.14	0.11	3974.02	2242.13	1731.90
18.09.2010	0.63	0.27	-25.15	0.17	0.10	2334.22	1480.00	854.22
23.09.2010	0.41	0.24	-24.84	0.10	0.14	566.28	231.23	335.05
2015								
02.06.2015	0.33	0.63	-24.80	0.21	0.42	126.76	42.34	84.42
04.06.2015	0.57	0.72	-23.60	0.41	0.31	310.12	175.77	134.35
06.06.2015	0.39	0.52	-24.40	0.20	0.32	141.64	55.00	86.64
08.06.2015	0.49	0.22	-23.70	0.11	0.11	112.69	55.07	57.62
12.06.2015	0.54	0.45	-24.25	0.25	0.20	999.56	544.97	454.59
13.06.2015	0.88	0.99	-24.95	0.87	0.12	3680.29	3252.09	428.20
16.06.2015	0.64	0.73	-25.60	0.47	0.26	245.40	156.57	88.84
19.06.2015	0.75	0.41	-25.50	0.31	0.10	1096.63	819.74	276.89
22.06.2015	0.68	0.35	-25.70	0.24	0.11	1266.62	860.19	406.43
24.06.2015	0.79	0.57	-25.05	0.45	0.12	2458.25	1950.45	507.81
26.06.2015	0.56	0.37	-24.90	0.21	0.16	901.60	510.22	391.38
28.06.2015	0.62	0.27	-24.70	0.17	0.10	1324.39	829.20	495.19
29.06.2015	0.68	0.43	-24.05	0.29	0.14	18091.66	12406.55	5685.11

Supplementary Table 2.2: *Measured Fraction modern, TOC and $\delta^{13}C$ on suspended sediments and calculated proportions of OC_{bio} and OC_{petro} and total OC export per day.*

date	Fraction modern	TOC (%)	$\delta^{13}C$ (‰)	OCbio (%)	OCpetro (%)	OC export (t/day)	OCbio export (t/day)	OCpetro export (t/day)
30.06.2015	0.49	0.15	-24.00	0.07	0.08	2048.51	998.87	1049.63
01.07.2015	0.29	0.47	-24.20	0.14	0.33	2895.20	845.21	2049.98
04.07.2015	0.43	0.14	-23.80	0.06	0.08	1118.54	481.22	637.32
06.07.2015	0.80	0.55	NA	0.44	0.11	1902.57	1530.67	371.91
08.07.2015	0.56	0.28	-25.50	0.16	0.12	1070.38	602.45	467.93
11.07.2015	0.54	0.52	NA	0.28	0.24	3013.43	1620.21	1393.22
13.07.2015	0.37	0.22	-24.30	0.08	0.14	777.30	285.38	491.92
15.07.2015	0.34	0.25	-24.60	0.08	0.17	534.56	180.66	353.89
17.07.2015	0.72	0.55	-26.20	0.40	0.15	5580.48	4030.54	1549.93
21.07.2015	0.59	0.31	-25.90	0.18	0.13	719.58	427.33	292.25
24.07.2015	0.78	0.59	-24.50	0.46	0.13	1612.98	1260.18	352.79
26.07.2015	0.78	0.50	-24.50	0.39	0.11	1828.20	1430.70	397.50
29.07.2015	0.68	0.40	-26.20	0.27	0.13	855.61	587.00	268.61
02.08.2015	0.54	0.26	-25.30	0.14	0.12	1994.77	1070.86	923.91
05.08.2015	0.67	0.66	-25.60	0.45	0.21	1567.80	1058.65	509.15
08.08.2015	0.80	0.54	NA	0.43	0.11	2395.06	1910.14	484.92
10.08.2015	0.27	0.39	-24.50	0.11	0.28	1002.80	271.20	731.60
12.08.2015	0.73	0.46	-25.60	0.33	0.13	2814.14	2046.69	767.45
14.08.2015	0.58	0.34	NA	0.20	0.14	1468.66	860.61	608.06
22.08.2015	0.54	0.23	-24.60	0.12	0.11	2935.15	1590.05	1345.10
24.08.2015	0.61	0.22	-25.00	0.13	0.09	1473.09	898.28	574.81
26.08.2015	0.60	0.27	-26.10	0.16	0.11	974.44	587.46	386.99
28.08.2015	0.58	0.27	-25.40	0.16	0.11	878.31	514.62	363.69
30.08.2015	0.58	0.32	-25.70	0.19	0.13	1373.25	801.82	571.43
01.09.2015	0.73	0.40	NA	0.29	0.11	3452.28	2531.72	920.56
03.09.2015	0.70	0.35	-26.20	0.25	0.10	1441.82	1009.66	432.17
06.09.2015	0.60	0.31	-25.80	0.19	0.12	626.56	374.52	252.04
09.09.2015	0.47	0.40	-25.50	0.19	0.21	296.92	140.27	156.64
12.09.2015	0.51	0.32	NA	0.16	0.15	386.50	199.55	186.95
18.09.2015	0.52	0.35	-26.40	0.18	0.17	201.88	105.73	96.14
20.09.2015	0.53	0.26	-25.50	0.14	0.12	457.59	243.26	214.32
22.09.2015	0.67	0.30	-26.20	0.20	0.10	951.81	636.76	315.05
25.09.2015	0.68	0.43	-26.80	0.29	0.14	731.36	499.61	231.75
28.09.2015	0.45	0.26	-25.40	0.12	0.14	271.05	123.22	147.84
2016								
19.06.2016	0.73	0.39	-24.93	0.28	0.11	1544.80	1128.03	416.78
21.06.2016	0.72	0.41	-24.67	0.30	0.11	2472.88	1795.96	676.92
23.06.2016	0.59	0.27	-24.28	0.16	0.11	1521.55	905.90	615.65

date	Fraction modern	TOC (%)	$\delta^{13}C$ (‰)	OCbio (%)	OCpetro (%)	OC export (t/day)	OCbio export (t/day)	OCpetro export (t/day)
25.06.2016	0.63	0.31	-25.01	0.20	0.11	1514.99	961.39	553.59
27.06.2016	0.68	0.26	-26.07	0.18	0.08	1927.97	1307.46	620.51
29.06.2016	0.57	0.20	NA	0.11	0.09	3113.52	1775.64	1337.88
01.07.2016	0.62	0.32	-24.78	0.20	0.12	3977.48	2485.71	1491.78
03.07.2016	0.54	0.21	-24.73	0.11	0.10	3103.24	1678.21	1425.03
05.07.2016	0.80	0.37	-25.83	0.30	0.07	9053.82	7287.55	1766.27
07.07.2016	0.51	0.21	-23.97	0.11	0.10	4220.18	2152.57	2067.61
09.07.2016	0.63	0.27	-25.48	0.17	0.10	6948.63	4420.54	2528.09
11.07.2016	0.42	NA	-24.96	NA	NA	NA	NA	NA
13.07.2016	0.54	0.21	-24.51	0.11	0.10	4079.80	2210.27	1869.53
15.07.2016	0.30	0.19	-23.40	0.06	0.13	5193.45	1541.51	3651.94
17.07.2016	0.59	0.19	-25.19	0.11	0.08	11676.06	6939.03	4737.03
19.07.2016	0.36	0.13	-25.06	0.05	0.08	4833.62	1724.43	3109.18
21.07.2016	0.45	0.13	-24.84	0.06	0.07	4652.83	2087.10	2565.74
23.07.2016	0.44	0.14	-24.44	0.06	0.08	5655.96	2503.74	3152.22
25.07.2016	0.54	0.15	-25.97	0.08	0.07	4445.15	2392.73	2052.42
27.07.2016	0.62	0.26	NA	0.16	0.10	23842.80	14756.24	9086.56
29.07.2016	0.60	0.19	-25.35	0.11	0.08	9223.25	5549.43	3673.82
31.07.2016	0.29	0.12	-25.66	0.03	0.09	4238.68	1219.91	3018.77
02.08.2016	0.34	0.30	-24.49	0.10	0.20	9184.91	3131.21	6053.70
26.08.2016	0.43	0.15	NA	0.06	0.09	406.25	175.02	231.23
28.08.2016	0.43	0.17	-24.45	0.07	0.10	298.49	128.87	169.62
30.08.2016	0.62	0.18	-24.90	0.11	0.07	927.47	574.52	352.95
01.09.2016	0.55	0.23	-24.95	0.13	0.10	2571.15	1407.65	1163.50
03.09.2016	0.78	0.31	-26.36	0.24	0.07	16716.09	13067.07	3649.03
05.09.2016	0.54	0.15	NA	0.08	0.07	2393.93	1301.68	1092.26
07.09.2016	0.27	0.23	-25.26	0.06	0.17	4587.24	1258.13	3329.10
09.09.2016	0.53	0.16	-26.22	0.08	0.08	1782.22	945.71	836.51
11.09.2016	0.50	0.13	-26.18	0.07	0.06	2270.90	1142.11	1128.79
13.09.2016	0.46	0.14	-25.65	0.06	0.08	1085.26	501.34	583.93
15.09.2016	0.82	0.31	-25.44	0.25	0.06	2284.36	1868.27	416.10
17.09.2016	0.43	0.10	-26.85	0.04	0.06	2194.93	952.36	1242.58
19.09.2016	0.49	0.16	-26.79	0.08	0.08	1022.89	506.35	516.54
21.09.2016	0.69	0.22	-25.41	0.15	0.07	2386.27	1662.06	724.21
23.09.2016	0.68	0.27	-25.68	0.18	0.09	1154.50	787.66	366.84
25.09.2016	0.48	0.18	-25.83	0.09	0.09	475.69	227.19	248.50
27.09.2016	0.57	0.17	-25.42	0.10	0.07	788.29	448.52	339.77
29.09.2016	0.47	0.19	-25.81	0.09	0.10	283.54	133.52	150.02

date	Fraction modern	TOC (%)	$\delta^{13}C$ (‰)	OCbio (%)	OCpetro (%)	OC export (t/day)	OCbio export (t/day)	OCpetro export (t/day)
2017								
01.06.2017	0.61	0.57	NA	0.35	0.22	53.14	32.71	20.43
07.06.2017	0.62	0.62	-25.03	0.39	0.23	127.32	79.41	47.91
10.06.2017	0.77	0.57	-22.43	0.44	0.13	246.67	190.09	56.58
13.06.2017	0.50	0.42	-22.90	0.21	0.21	99.06	49.97	49.09
16.06.2017	0.68	0.57	-23.53	0.39	0.18	454.97	311.42	143.55
19.06.2017	0.61	0.45	-23.31	0.28	0.17	184.39	113.57	70.82
22.06.2017	0.91	0.96	-24.41	0.88	0.08	1049.60	958.88	90.72
25.06.2017	0.72	0.50	NA	0.36	0.14	2222.90	1597.88	625.02
28.06.2017	0.85	0.51	-23.33	0.43	0.08	3061.51	2596.78	464.73
01.07.2017	0.61	0.21	-23.51	0.13	0.08	1946.29	1181.98	764.31
04.07.2017	0.35	0.15	-26.59	0.05	0.09	3444.92	1201.87	2243.05
07.07.2017	0.45	0.08	NA	0.04	0.04	794.47	359.60	434.86
10.07.2017	0.57	0.16	NA	0.09	0.07	3236.82	1850.48	1386.34
13.07.2017	0.36	0.18	-23.70	0.06	0.11	1851.42	668.51	1182.91
16.07.2017	0.80	0.50	NA	0.40	0.10	8775.04	7078.30	1696.74
19.07.2017	0.49	0.26	-24.01	0.13	0.13	2361.32	1169.14	1192.18
22.07.2017	0.58	0.25	NA	0.15	0.10	2372.48	1390.99	981.50
24.07.2017	0.55	0.23	NA	0.13	0.10	2828.76	1554.93	1273.83
26.07.2017	0.37	0.26	-22.81	0.10	0.16	2997.44	1115.51	1881.93
29.07.2017	0.77	0.46	-24.27	0.35	0.10	4318.72	3332.62	986.10
01.08.2017	0.31	0.23	-24.10	0.07	0.16	2452.77	774.47	1678.30
07.08.2017	0.51	0.19	-24.17	0.09	0.09	3665.84	1876.71	1789.13
10.08.2017	0.65	0.14	-24.59	0.09	0.05	3261.60	2124.17	1137.43
13.08.2017	0.59	0.28	-25.64	0.17	0.11	7382.95	4357.20	3025.75
16.08.2017	0.30	0.10	-24.16	0.03	0.07	1170.17	356.45	813.72
19.08.2017	0.45	0.14	-24.53	0.06	0.08	2454.51	1119.28	1335.22
22.08.2017	0.44	0.14	NA	0.06	0.08	1390.64	614.09	776.55
25.08.2017	0.33	0.04	NA	0.01	0.03	322.83	107.45	215.39
28.08.2017	0.45	0.15	NA	0.07	0.08	1627.68	727.28	900.40
03.09.2017	0.41	0.15	NA	0.06	0.09	1955.21	812.94	1142.27
07.09.2017	0.51	0.19	-25.29	0.10	0.09	723.45	366.57	356.87
10.09.2017	0.75	0.36	-25.92	0.28	0.09	1020.39	769.91	250.47
13.09.2017	0.47	0.31	-23.93	0.14	0.16	2460.42	1168.50	1291.92
19.09.2017	0.56	0.28	-24.75	0.16	0.12	242.04	136.88	105.16

Following pages:

Supplementary Table 2.3: *Measured concentrations of major ions in µmoles/L (cations of 2010 are from ref.[26]). Calculated xsil, Ca_{sil}, Mg_{sil} and SO_4^- associated with carbonate weathering (the last three in µmoles/L).*

date	Ca	Mg	K	NH_4	Na	SO_4	Cl	F	NO_3	HCO_3	xsil	Casil	Mgsil	SO_4 + carbonates
2010														
01.06.2010	703	306	54	NA	169	NA	NA	NA	NA	NA	0.07	13	24	NA
02.06.2010	703	306	54	NA	169	NA	NA	NA	NA	NA	0.07	14	24	NA
03.06.2010	703	306	54	NA	169	NA	NA	NA	NA	NA	0.08	16	24	NA
04.06.2010	758	320	53	NA	161	NA	NA	NA	NA	NA	0.08	20	23	NA
05.06.2010	758	320	53	NA	161	NA	NA	NA	NA	NA	0.09	24	23	NA
06.06.2010	758	320	53	NA	161	NA	NA	NA	NA	NA	0.08	23	23	NA
07.06.2010	758	320	53	NA	161	NA	NA	NA	NA	NA	0.08	21	23	NA
08.06.2010	704	291	55	NA	143	NA	NA	NA	NA	NA	0.07	12	24	NA
09.06.2010	704	291	55	NA	143	NA	NA	NA	NA	NA	0.07	10	24	NA
10.06.2010	704	291	55	NA	143	NA	NA	NA	NA	NA	0.06	9	24	NA
11.06.2010	704	291	55	NA	143	NA	NA	NA	NA	NA	0.07	12	24	NA
12.06.2010	714	288	52	NA	139	NA	NA	NA	NA	NA	0.07	11	23	NA
13.06.2010	714	288	52	NA	139	NA	NA	NA	NA	NA	0.07	13	23	NA
14.06.2010	714	288	52	NA	139	NA	NA	NA	NA	NA	0.07	12	23	NA
15.06.2010	714	288	52	NA	139	NA	NA	NA	NA	NA	0.07	12	23	NA
16.06.2010	726	288	54	NA	145	NA	NA	NA	NA	NA	0.08	18	24	NA
17.06.2010	734	264	54	NA	125	NA	NA	NA	NA	NA	0.07	15	24	NA
18.06.2010	734	268	60	NA	114	NA	NA	NA	NA	NA	0.08	14	27	NA
19.06.2010	779	304	65	NA	126	NA	NA	NA	NA	NA	0.08	16	29	NA
20.06.2010	837	283	73	NA	116	NA	NA	NA	NA	NA	0.09	20	33	NA
21.06.2010	800	273	82	NA	106	NA	NA	NA	NA	NA	0.10	17	38	NA
22.06.2010	691	236	69	NA	100	NA	NA	NA	NA	NA	0.10	15	31	NA
23.06.2010	699	247	63	NA	113	NA	NA	NA	NA	NA	0.09	17	28	NA
24.06.2010	703	243	69	NA	108	NA	NA	NA	NA	NA	0.10	16	31	NA
25.06.2010	677	245	64	NA	107	NA	NA	NA	NA	NA	0.10	17	29	NA
26.06.2010	738	264	70	NA	114	NA	NA	NA	NA	NA	0.10	22	32	NA
27.06.2010	694	234	69	NA	106	NA	NA	NA	NA	NA	0.11	21	31	NA
28.06.2010	766	230	85	NA	95	NA	NA	NA	NA	NA	0.12	20	39	NA
29.06.2010	670	222	75	NA	100	NA	NA	NA	NA	NA	0.12	19	35	NA
30.06.2010	722	233	82	NA	107	NA	NA	NA	NA	NA	0.12	22	38	NA
01.07.2010	720	239	81	NA	106	NA	NA	NA	NA	NA	0.13	24	37	NA
02.07.2010	700	220	77	NA	89	NA	NA	NA	NA	NA	0.11	17	35	NA
03.07.2010	664	185	80	NA	92	NA	NA	NA	NA	NA	0.13	20	37	NA
04.07.2010	643	178	84	NA	84	NA	NA	NA	NA	NA	0.13	17	39	NA
05.07.2010	691	181	86	NA	80	NA	NA	NA	NA	NA	0.12	16	40	NA
06.07.2010	580	178	82	NA	78	NA	NA	NA	NA	NA	0.14	18	38	NA
07.07.2010	581	183	83	NA	80	NA	NA	NA	NA	NA	0.14	17	39	NA
08.07.2010	571	199	66	NA	78	NA	NA	NA	NA	NA	0.11	15	30	NA
09.07.2010	637	210	70	NA	86	NA	NA	NA	NA	NA	0.11	17	32	NA
10.07.2010	583	201	72	NA	78	NA	NA	NA	NA	NA	0.12	16	33	NA
11.07.2010	681	188	79	NA	78	NA	NA	NA	NA	NA	0.13	20	36	NA
12.07.2010	594	195	67	NA	76	NA	NA	NA	NA	NA	0.12	18	30	NA
13.07.2010	658	223	76	NA	85	NA	NA	NA	NA	NA	0.12	19	35	NA
14.07.2010	699	231	82	NA	84	NA	NA	NA	NA	NA	0.12	18	38	NA
15.07.2010	799	254	119	NA	80	NA	NA	NA	NA	NA	0.13	17	57	NA
16.07.2010	671	237	100	NA	70	NA	NA	NA	NA	NA	0.12	12	47	NA
17.07.2010	659	252	84	NA	81	NA	NA	NA	NA	NA	0.12	17	39	NA
18.07.2010	604	229	80	NA	73	NA	NA	NA	NA	NA	0.12	13	37	NA
19.07.2010	677	252	84	NA	78	NA	NA	NA	NA	NA	0.12	18	39	NA
20.07.2010	595	215	73	NA	70	NA	NA	NA	NA	NA	0.12	17	33	NA

date	Ca	Mg	K	NH_4	Na	SO_4	Cl	F	NO_3	HCO_3	xsil	Casil	Mgsil	SO_4 + carbonates
21.07.2010	603	210	98	NA	72	NA	NA	NA	NA	NA	0.15	16	46	NA
22.07.2010	633	221	83	NA	76	NA	NA	NA	NA	NA	0.13	19	38	NA
23.07.2010	585	230	79	NA	70	NA	NA	NA	NA	NA	0.12	16	36	NA
24.07.2010	621	255	74	NA	83	NA	NA	NA	NA	NA	0.12	20	34	NA
25.07.2010	558	194	77	NA	74	NA	NA	NA	NA	NA	0.14	18	35	NA
26.07.2010	578	231	74	NA	76	NA	NA	NA	NA	NA	0.13	18	34	NA
27.07.2010	586	231	75	NA	80	NA	NA	NA	NA	NA	0.13	21	34	NA
28.07.2010	572	231	61	NA	84	NA	NA	NA	NA	NA	0.12	22	27	NA
29.07.2010	582	220	68	NA	84	NA	NA	NA	NA	NA	0.13	21	31	NA
30.07.2010	593	211	82	NA	81	NA	NA	NA	NA	NA	0.15	22	38	NA
31.07.2010	654	194	96	NA	82	NA	NA	NA	NA	NA	0.15	22	45	NA
01.08.2010	588	214	80	NA	77	NA	NA	NA	NA	NA	0.14	19	37	NA
02.08.2010	614	239	66	NA	85	NA	NA	NA	NA	NA	0.12	22	30	NA
03.08.2010	605	235	67	NA	85	NA	NA	NA	NA	NA	0.12	23	30	NA
04.08.2010	622	235	67	NA	88	NA	NA	NA	NA	NA	0.12	23	31	NA
05.08.2010	589	235	63	NA	90	NA	NA	NA	NA	NA	0.13	25	28	NA
06.08.2010	610	234	65	NA	89	NA	NA	NA	NA	NA	0.13	24	30	NA
07.08.2010	670	251	77	NA	87	NA	NA	NA	NA	NA	0.12	22	35	NA
08.08.2010	614	241	61	NA	88	NA	NA	NA	NA	NA	0.11	22	27	NA
09.08.2010	619	239	64	NA	84	NA	NA	NA	NA	NA	0.11	20	29	NA
10.08.2010	597	234	62	NA	90	NA	NA	NA	NA	NA	0.12	22	28	NA
11.08.2010	581	203	77	NA	81	NA	NA	NA	NA	NA	0.13	19	35	NA
12.08.2010	615	227	68	NA	80	NA	NA	NA	NA	NA	0.12	19	31	NA
13.08.2010	588	220	69	NA	77	NA	NA	NA	NA	NA	0.12	17	31	NA
14.08.2010	601	230	68	NA	78	NA	NA	NA	NA	NA	0.11	17	31	NA
15.08.2010	695	268	86	NA	79	NA	NA	NA	NA	NA	0.12	18	40	NA
16.08.2010	633	284	69	NA	80	NA	NA	NA	NA	NA	0.11	20	31	NA
17.08.2010	607	252	71	NA	81	NA	NA	NA	NA	NA	0.12	20	32	NA
18.08.2010	602	285	73	NA	83	NA	NA	NA	NA	NA	0.12	21	33	NA
19.08.2010	610	253	83	NA	72	NA	NA	NA	NA	NA	0.12	17	38	NA
20.08.2010	614	288	79	NA	81	NA	NA	NA	NA	NA	0.13	22	36	NA
21.08.2010	654	313	75	NA	85	NA	NA	NA	NA	NA	0.12	23	35	NA
22.08.2010	626	301	69	NA	88	NA	NA	NA	NA	NA	0.12	25	31	NA
23.08.2010	614	286	71	NA	83	NA	NA	NA	NA	NA	0.12	23	33	NA
24.08.2010	619	275	77	NA	76	NA	NA	NA	NA	NA	0.12	21	35	NA
25.08.2010	617	282	71	NA	81	NA	NA	NA	NA	NA	0.12	22	32	NA
26.08.2010	670	253	72	NA	77	NA	NA	NA	NA	NA	0.11	20	33	NA
27.08.2010	592	258	66	NA	77	NA	NA	NA	NA	NA	0.11	19	30	NA
28.08.2010	630	268	77	NA	81	NA	NA	NA	NA	NA	0.13	22	35	NA
29.08.2010	614	273	68	NA	83	NA	NA	NA	NA	NA	0.12	22	31	NA
30.08.2010	626	266	73	NA	81	NA	NA	NA	NA	NA	0.12	22	33	NA
31.08.2010	638	296	64	NA	81	NA	NA	NA	NA	NA	0.11	22	29	NA
01.09.2010	651	306	63	NA	86	NA	NA	NA	NA	NA	0.11	24	28	NA
02.09.2010	641	275	77	NA	82	NA	NA	NA	NA	NA	0.12	22	35	NA
03.09.2010	614	252	71	NA	80	NA	NA	NA	NA	NA	0.12	21	32	NA
04.09.2010	589	278	65	NA	83	NA	NA	NA	NA	NA	0.12	23	29	NA
05.09.2010	598	290	62	NA	87	NA	NA	NA	NA	NA	0.12	24	28	NA
06.09.2010	611	295	63	NA	89	NA	NA	NA	NA	NA	0.11	24	28	NA
07.09.2010	632	256	85	NA	80	NA	NA	NA	NA	NA	0.13	21	39	NA
08.09.2010	612	265	77	NA	80	NA	NA	NA	NA	NA	0.13	21	36	NA
09.09.2010	580	253	70	NA	83	NA	NA	NA	NA	NA	0.12	21	32	NA

date	Ca	Mg	K	NH_4	Na	SO_4	Cl	F	NO_3	HCO_3	xsil	Casil	Mgsil	SO_4 + carbonates
10.09.2010	595	236	78	NA	77	NA	NA	NA	NA	NA	0.13	18	36	NA
11.09.2010	605	225	102	NA	73	NA	NA	NA	NA	NA	0.15	16	48	NA
12.09.2010	581	292	72	NA	77	NA	NA	NA	NA	NA	0.12	19	33	NA
13.09.2010	586	274	88	NA	77	NA	NA	NA	NA	NA	0.13	19	41	NA
14.09.2010	609	262	91	NA	81	NA	NA	NA	NA	NA	0.14	20	42	NA
15.09.2010	630	280	83	NA	84	NA	NA	NA	NA	NA	0.13	22	38	NA
16.09.2010	684	284	83	NA	86	NA	NA	NA	NA	NA	0.13	24	38	NA
17.09.2010	677	320	65	NA	96	NA	NA	NA	NA	NA	0.11	27	29	NA
18.09.2010	635	301	68	NA	88	NA	NA	NA	NA	NA	0.12	25	31	NA
19.09.2010	595	265	72	NA	75	NA	NA	NA	NA	NA	0.12	19	33	NA
20.09.2010	611	299	62	NA	86	NA	NA	NA	NA	NA	0.11	23	28	NA
21.09.2010	622	305	62	NA	90	NA	NA	NA	NA	NA	0.11	23	28	NA
22.09.2010	637	314	59	NA	93	NA	NA	NA	NA	NA	0.11	24	26	NA
23.09.2010	649	329	58	NA	97	NA	NA	NA	NA	NA	0.11	26	26	NA
24.09.2010	639	327	55	NA	100	NA	NA	NA	NA	NA	0.11	28	24	NA
25.09.2010	636	331	54	NA	100	NA	NA	NA	NA	NA	0.10	26	24	NA
26.09.2010	639	334	54	NA	103	NA	NA	NA	NA	NA	0.10	27	24	NA
27.09.2010	641	338	54	NA	105	NA	NA	NA	NA	NA	0.10	26	24	NA
28.09.2010	645	338	53	NA	106	NA	NA	NA	NA	NA	0.10	25	23	NA
29.09.2010	651	336	53	NA	107	NA	NA	NA	NA	NA	0.10	25	23	NA
30.09.2010	662	344	51	NA	110	NA	NA	NA	NA	NA	0.10	26	22	NA
2015														
01.06.2015	790	315	45	0	146	279	71	5	0	1767	0.09	29	19	216
03.06.2015	845	332	47	0	162	298	81	5	0	1882	0.09	32	20	231
05.06.2015	849	339	46	0	165	312	87	5	0	1870	0.08	31	20	243
07.06.2015	805	316	44	0	148	291	71	6	0	1776	0.09	31	19	225
09.06.2015	802	302	43	0	141	277	69	4	0	1764	0.09	28	18	216
11.06.2015	802	302	43	0	141	277	69	4	0	1764	0.09	28	18	216
13.06.2015	802	270	58	0	127	236	62	3	0	1791	0.09	25	26	182
15.06.2015	792	295	50	0	139	258	69	4	0	1773	0.09	27	22	200
17.06.2015	783	324	48	0	160	284	82	5	0	1767	0.09	31	21	219
19.06.2015	692	269	46	0	121	223	58	4	0	1582	0.09	25	20	172
21.06.2015	747	286	47	0	130	246	66	2	0	1684	0.09	25	20	190
23.06.2015	735	261	48	0	128	230	72	5	0	1631	0.08	22	21	179
25.06.2015	710	248	85	0	107	192	88	5	0	1629	0.09	7	39	149
27.06.2015	703	200	78	0	96	144	41	6	0	1644	0.12	21	36	108
29.06.2015	824	218	130	0	93	191	40	4	0	1881	0.15	21	62	138
01.07.2015	778	262	72	0	114	217	51	5	0	1778	0.11	25	33	164
03.07.2015	750	264	63	0	114	208	54	4	0	1732	0.10	23	29	159
05.07.2015	717	245	57	0	112	195	50	4	0	1649	0.10	24	25	149
07.07.2015	675	217	115	0	100	161	91	5	0	1582	0.12	3	54	120
09.07.2015	652	212	57	0	95	152	39	4	0	1534	0.11	22	25	115
11.07.2015	719	218	63	0	90	172	49	4	0	1631	0.09	16	28	133
13.07.2015	730	244	63	0	98	192	70	4	0	1652	0.08	11	28	151
15.07.2015	753	261	56	0	105	213	79	5	0	1681	0.07	10	25	169
17.07.2015	625	211	90	0	78	119	30	3	0	1571	0.14	19	42	87
21.07.2015	681	239	52	0	98	163	39	3	0	1622	0.10	23	23	125
23.07.2015	661	238	53	0	102	163	42	4	0	1582	0.10	23	24	124
25.07.2015	725	258	51	0	99	164	43	3	0	1741	0.09	22	22	127
28.07.2015	682	255	51	0	105	165	46	4	0	1650	0.10	23	22	127
30.07.2015	564	185	68	0	81	100	45	4	0	1400	0.12	14	31	75

date	Ca	Mg	K	NH_4	Na	SO_4	Cl	F	NO_3	HCO_3	xsil	Casil	Mgsil	SO_4 + carbonates
01.08.2015	719	226	63	0	83	118	31	4	0	1767	0.10	20	28	90
03.08.2015	710	259	53	0	89	129	32	3	0	1787	0.09	22	24	99
05.08.2015	707	253	60	0	92	145	34	4	0	1743	0.10	23	27	111
07.08.2015	791	258	52	0	92	162	38	3	0	1878	0.08	21	23	126
09.08.2015	766	275	67	0	101	191	56	4	0	1807	0.09	17	30	148
11.08.2015	749	272	53	0	99	203	50	3	0	1732	0.08	19	23	159
13.08.2015	672	261	59	0	87	139	32	4	0	1697	0.10	21	26	106
14.08.2015	704	242	59	0	88	139	33	3	0	1724	0.10	22	26	106
17.08.2015	619	190	73	0	80	115	30	3	0	1508	0.13	20	33	85
19.08.2015	742	220	58	0	84	133	29	3	0	1769	0.10	21	26	102
21.08.2015	638	216	56	0	96	102	28	3	0	1626	0.12	26	25	76
23.08.2015	594	221	49	0	83	116	29	4	0	1498	0.11	21	21	88
25.08.2015	656	250	48	0	95	135	35	4	0	1646	0.10	23	21	104
27.08.2015	670	226	52	0	87	124	32	4	0	1648	0.10	21	23	95
29.08.2015	621	236	69	0	88	123	57	3	0	1565	0.10	12	31	94
31.08.2015	673	240	51	0	87	125	36	3	0	1676	0.09	20	22	96
01.09.2015	627	230	51	0	84	115	33	4	0	1584	0.10	20	22	88
03.09.2015	657	246	50	0	94	125	36	4	0	1660	0.10	22	22	96
05.09.2015	672	271	48	0	104	151	43	3	0	1690	0.10	24	21	116
07.09.2015	769	295	64	0	106	171	60	4	0	1892	0.09	18	29	133
09.09.2015	691	246	47	0	116	164	61	4	0	1645	0.09	22	20	127
11.09.2015	635	227	46	0	114	149	46	5	0	1533	0.11	26	20	113
13.09.2015	678	224	46	0	109	137	42	4	0	1641	0.10	26	20	104
15.09.2015	785	243	52	0	111	136	52	4	0	1889	0.09	23	23	106
17.09.2015	643	246	66	0	111	154	67	4	0	1577	0.10	17	30	117
19.09.2015	664	266	48	0	127	163	55	4	0	1649	0.11	28	21	124
21.09.2015	667	257	51	0	114	163	49	4	0	1635	0.10	26	22	124
23.09.2015	605	221	48	0	105	131	39	4	0	1500	0.11	26	21	99
25.09.2015	609	225	49	0	102	137	42	4	0	1497	0.11	24	21	104
27.09.2015	683	270	65	0	114	156	68	4	0	1702	0.10	18	29	120
29.09.2015	680	280	48	0	119	168	57	4	0	1690	0.09	25	21	130
2016														
05.06.2016	668	287	99	0	158	247	175	4	0	1494	0.07	0	47	195
07.06.2016	665	278	63	0	152	243	75	4	0	1537	0.12	30	28	181
09.06.2016	678	281	62	0	150	239	77	5	0	1571	0.12	29	28	180
11.06.2016	640	255	72	0	141	209	63	6	0	1516	0.14	31	33	153
13.06.2016	666	262	70	0	121	199	60	5	0	1586	0.12	24	32	149
15.06.2016	661	253	64	0	123	197	58	5	0	1559	0.12	25	29	148
17.06.2016	639	231	67	0	115	179	52	4	0	1508	0.12	24	30	133
19.06.2016	538	214	67	0	97	162	43	0	0	1303	0.13	21	30	119
21.06.2016	563	193	83	0	86	145	34	0	0	1356	0.15	20	38	105
23.06.2016	567	197	69	0	92	142	41	0	0	1365	0.13	20	31	105
25.06.2016	606	226	66	0	100	164	45	0	0	1457	0.12	22	30	122
27.06.2016	580	240	63	0	103	169	43	0	0	1425	0.12	23	28	126
29.06.2016	540	211	74	0	94	156	40	0	0	1318	0.14	21	34	114
01.07.2016	521	205	84	0	71	111	25	0	0	1361	0.15	18	39	80
02.07.2016	575	231	105	0	82	164	36	0	0	1434	0.16	18	49	118
03.07.2016	550	192	67	0	79	126	27	0	0	1350	0.13	20	30	93
05.07.2016	582	191	86	0	76	128	26	0	0	1427	0.15	20	40	92
07.07.2016	628	209	72	0	83	159	31	3	0	1476	0.12	20	33	118
09.07.2016	552	193	79	0	78	134	25	0	0	1354	0.15	21	36	97

date	Ca	Mg	K	NH_4	Na	SO_4	Cl	F	NO_3	HCO_3	xsil	Casil	Mgsil	SO_4 + carbonates
11.07.2016	594	228	69	0	80	145	28	0	0	1475	0.12	20	31	108
13.07.2016	611	228	72	0	84	154	28	0	0	1498	0.13	22	33	114
15.07.2016	611	235	84	0	88	188	34	0	0	1454	0.14	21	39	138
17.07.2016	561	193	87	0	75	125	23	0	0	1396	0.16	20	40	90
19.07.2016	502	236	72	0	75	137	25	0	0	1324	0.14	20	33	100
21.07.2016	530	221	67	0	86	117	27	0	0	1393	0.14	23	30	86
22.07.2016	537	232	67	0	77	127	24	0	0	1404	0.13	20	30	94
23.07.2016	570	244	69	0	80	126	25	4	0	1499	0.13	22	31	93
25.07.2016	555	230	68	0	84	126	27	0	0	1443	0.13	23	31	93
26.07.2016	537	168	109	0	73	108	21	0	0	1355	0.19	20	52	74
27.07.2016	548	223	87	0	80	109	22	0	0	1469	0.16	23	40	78
28.07.2016	568	260	40	0	78	123	25	4	0	1500	0.09	21	17	95
29.07.2016	537	242	78	0	87	125	26	0	0	1445	0.15	24	36	90
31.07.2016	491	249	62	0	76	149	25	0	0	1295	0.13	20	28	110
02.08.2016	666	323	80	0	100	257	35	6	0	1604	0.12	26	37	192
04.08.2016	634	305	100	0	96	214	40	0	0	1605	0.14	22	47	156
06.08.2016	617	287	68	0	91	194	32	0	0	1547	0.12	23	31	146
08.08.2016	610	266	74	0	90	189	31	5	0	1503	0.13	23	34	140
10.08.2016	593	256	65	0	94	200	31	0	0	1425	0.12	24	29	149
12.08.2016	657	281	75	0	100	215	35	0	0	1587	0.13	26	34	160
14.08.2016	591	256	72	0	85	178	30	0	0	1465	0.13	22	33	132
16.08.2016	531	228	65	0	87	168	38	0	0	1295	0.12	19	29	125
18.08.2016	609	267	72	0	98	189	35	0	0	1509	0.13	25	33	140
21.08.2016	632	286	61	0	102	212	38	0	0	1536	0.11	25	27	160
22.08.2016	563	255	61	0	90	182	31	3	0	1390	0.12	23	27	136
24.08.2016	646	299	65	0	113	222	41	3	0	1581	0.12	28	29	166
26.08.2016	594	280	63	0	112	213	43	4	0	1450	0.12	27	28	159
28.08.2016	664	300	66	0	119	231	43	4	0	1604	0.12	30	30	172
30.08.2016	640	290	69	0	117	205	44	0	0	1593	0.13	29	31	152
02.09.2016	585	235	74	0	94	155	33	0	0	1462	0.14	24	34	114
04.09.2016	576	239	82	0	94	149	29	0	0	1480	0.15	25	38	108
06.09.2016	567	249	70	0	100	165	34	0	0	1439	0.14	26	32	121
08.09.2016	586	173	104	0	78	99	21	5	0	1477	0.18	22	49	69
10.09.2016	569	252	78	0	91	135	27	0	0	1514	0.14	25	36	98
12.09.2016	608	272	73	0	95	129	28	0	0	1641	0.13	26	33	95
15.09.2016	608	272	73	0	95	129	28	0	0	1641	0.13	26	33	95
16.09.2016	608	272	73	0	95	129	28	0	0	1641	0.13	26	33	95
18.09.2016	503	240	66	0	79	111	25	0	0	1383	0.13	21	30	82
20.09.2016	626	279	78	0	100	143	32	0	0	1667	0.13	27	36	105
22.09.2016	622	284	77	0	98	140	31	0	0	1677	0.13	26	35	103
24.09.2016	468	230	49	0	78	117	25	0	0	1264	0.12	21	21	87
26.09.2016	640	286	80	0	105	164	36	0	0	1675	0.13	27	37	120
28.09.2016	632	306	68	0	115	168	52	3	0	1668	0.12	25	31	126
2017														
02.06.2017	741	297	51	0	178	234	121	7	0	1705	0.08	22	22	182
04.06.2017	787	313	50	0	184	250	105	6	0	1802	0.09	31	22	193
06.06.2017	747	288	46	0	139	223	87	6	0	1688	0.08	20	20	175
08.06.2017	731	288	83	0	151	230	80	7	0	1664	0.12	28	38	171
10.06.2017	711	258	46	0	152	230	125	6	0	1541	0.06	10	20	184
12.06.2017	744	279	44	0	146	234	111	6	0	1641	0.06	13	19	187
14.06.2017	705	251	44	0	140	227	139	6	0	1509	0.04	0	19	186

date	Ca	Mg	K	NH_4	Na	SO_4	Cl	F	NO_3	HCO_3	xsil	Casil	Mgsil	SO_4 + carbonates
16.06.2017	717	238	42	0	117	217	197	7	0	1441	0.00	0	18	184
18.06.2017	699	245	72	0	140	224	93	6	0	1530	0.10	18	33	171
20.06.2017	760	251	44	0	145	227	120	6	0	1634	0.05	10	19	183
22.06.2017	731	252	45	0	131	207	239	6	0	1687	0.00	0	19	176
24.06.2017	682	225	44	0	124	198	63	7	0	1491	0.09	24	19	153
26.06.2017	630	193	50	0	107	170	153	7	0	1388	0.00	0	22	144
28.06.2017	571	180	73	0	80	110	165	6	0	1420	0.00	0	33	94
30.06.2017	605	173	50	0	80	142	265	6	0	1341	0.00	0	22	120
02.07.2017	650	190	69	0	83	137	31	5	0	1513	0.12	20	31	103
04.07.2017	622	195	57	0	84	122	105	6	0	1481	0.04	0	25	100
06.07.2017	667	218	68	0	80	131	63	4	0	1604	0.08	7	31	102
08.07.2017	654	222	85	0	76	150	86	4	0	1505	0.07	0	39	118
10.07.2017	589	189	54	0	71	109	68	4	0	1421	0.06	1	24	87
12.07.2017	621	198	57	0	84	119	74	5	0	1497	0.07	3	25	94
13.07.2017	666	245	53	0	82	158	67	5	0	1572	0.06	5	24	126
16.07.2017	635	204	58	0	84	142	143	4	0	1407	0.00	0	26	121
18.07.2017	646	237	76	0	86	175	169	4	0	1462	0.00	0	35	148
20.07.2017	693	245	47	0	91	179	62	0	0	1602	0.07	11	20	142
22.07.2017	652	225	46	0	91	157	71	0	0	1524	0.06	7	20	125
24.07.2017	578	196	48	0	81	129	57	4	0	1365	0.08	9	21	101
26.07.2017	647	220	49	0	86	173	140	4	0	1513	0.00	0	21	147
28.07.2017	665	229	79	0	97	185	59	5	0	1519	0.11	15	36	140
30.07.2017	929	244	49	0	144	118	149	3	0	2181	0.03	0	21	97
01.08.2017	654	244	50	0	84	175	55	4	0	1532	0.07	11	22	138
03.08.2017	586	202	49	0	82	124	140	0	0	1311	0.00	0	21	105
05.08.2017	743	192	72	0	88	113	265	4	0	1607	0.00	0	33	96
07.08.2017	585	190	82	0	76	120	152	0	0	1384	0.01	0	38	101
09.08.2017	617	217	50	0	78	139	56	4	0	1459	0.07	9	22	110
11.08.2017	606	191	63	0	74	112	42	0	0	1505	0.10	13	28	86
13.08.2017	596	246	50	0	82	119	52	3	0	1534	0.08	11	22	94
15.08.2017	692	281	55	0	105	136	65	4	0	1782	0.08	15	24	106
17.08.2017	644	221	77	0	81	131	61	4	0	1549	0.09	7	35	101
21.08.2017	577	211	49	0	81	133	44	5	0	1434	0.09	15	21	103
23.08.2017	604	214	49	0	86	144	66	0	0	1438	0.07	8	21	114
25.08.2017	650	255	53	0	90	169	80	5	0	1544	0.06	4	23	136
27.08.2017	656	270	219	0	95	180	91	4	0	1659	0.20	1	107	122
29.08.2017	655	264	49	0	91	167	36	4	0	1604	0.09	22	21	128
31.08.2017	651	261	53	0	108	159	223	0	0	1504	0.00	0	24	135
02.09.2017	590	207	50	0	80	124	36	0	0	1441	0.10	17	22	95
04.09.2017	616	231	51	0	86	134	76	4	0	1525	0.06	4	22	107
06.09.2017	673	283	102	0	100	168	138	5	0	1685	0.06	0	48	135
08.09.2017	674	284	55	0	110	170	49	4	0	1691	0.10	24	24	130
10.09.2017	676	279	48	0	100	177	111	4	0	1639	0.03	0	21	146
12.09.2017	600	250	51	0	95	148	40	4	0	1509	0.10	21	22	113
14.09.2017	665	300	52	0	108	171	85	4	0	1690	0.06	8	23	136
16.09.2017	681	301	51	0	120	178	96	4	0	1723	0.06	9	22	142
18.09.2017	652	276	50	0	109	164	47	5	0	1635	0.10	24	22	125
20.09.2017	655	274	46	0	106	180	49	4	0	1597	0.09	22	20	139
22.09.2017	651	283	62	0	93	153	59	4	0	1655	0.09	13	28	119

Supplementary Table 3:
Sediment depth profile samples of the Narayani River.

sample	date	profile nr	sampling depth (m)	Fraction modern	TOC (%)	sediment load (g/L)*	water velocity (m/s)**	OCbio (%)	OCpetro (%)	sd OCbio (%)	sd OCpetro (%)	OCtot (kg/(day m^2)	OCbio (kg/(day m^2)	OCpetro (kg/(day m^2)
CA11-117	04.08.2011	1	0	0.42	0.41	2.18	388800	0.17	0.24	0.02	0.02	3475	1476	1999
CA11-118	04.08.2011	1	2.3	0.45	0.28	3.4	345600	0.13	0.15	0.01	0.01	3290	1496	1795
CA11-119	04.08.2011	1	8.5	0.49	0.28	3.63	259200	0.14	0.14	0.01	0.01	2635	1288	1347
CA11-124	05.08.2011	2	2	0.38	0.3	2.56	345600	0.11	0.19	0.01	0.01	2654	1006	1648
CA11-122	05.08.2011	2	5.5	0.39	0.21	3.65	302400	0.08	0.13	0.01	0.01	2318	910	1408
CA11-121	05.08.2011	2	9.3	0.35	0.19	5.99	259200	0.07	0.12	0.01	0.01	2950	1033	1917
CA11-127	06.08.2011	3	0	0.43	0.36	4.05	345600	0.16	0.20	0.01	0.01	5039	2182	2857
CA11-126	06.08.2011	3	3	0.48	0.33	4.49	302400	0.16	0.17	0.01	0.01	4481	2168	2312
CA11-125	06.08.2011	3	5	0.45	0.32	5.37	388800	0.14	0.18	0.01	0.01	6681	3018	3664
CA11-128	06.08.2011	3	8	0.42	0.25	6.67	345600	0.10	0.15	0.01	0.01	5763	2407	3355
CA11-130	07.08.2011	4	0	0.49	0.35	3.97	259200	0.17	0.18	0.01	0.01	3602	1777	1825
CA11-129	07.08.2011	4	6.3	0.40	0.33	5.59	259200	0.13	0.20	0.01	0.01	4781	1924	2858

* from ref.[26]

** estimated from the velocity profile in ref.[26]

Supplementary Table 4: *Samples from the two tributaries upstream the confluence near the sampling station in Narayanghat.*

sample name	river	date	Fraction modern	TOC (%)	$\delta^{13}C$ (‰)	OCbio (%)	OCpetro (%)	sd OCbio (%)	sd OCpetro (%)
NEQ-172-04	Narayani - middle	29.06.2017	0.82	0.50	NA	0.41	0.09	0.03	0.03
NEQ-172-09	Narayani - right riverside	29.06.2017	0.80	0.53	NA	0.43	0.10	0.03	0.03
NEQ-172-13	Narayani - left riverside	29.06.2017	0.80	0.60	NA	0.48	0.12	0.03	0.03
NEQ-172-25	right side confluent (Khali Gandaki)	30.06.2017	0.70	0.51	NA	0.36	0.15	0.03	0.02
NEQ-172-29	left side confluent (Trisuli)	30.06.2017	0.68	0.36	NA	0.25	0.11	0.02	0.02
NEQ-172-33	Narayani	30.06.2017	0.69	0.40	NA	0.28	0.13	0.02	0.02
NEP-15-020A	left side confluent (Trisuli)	10.07.2015	0.80	0.43	-25.15	0.35	0.08	0.02	0.02
NEP-15-020B	left side confluent (Trisuli)	10.07.2015	0.82	0.48	-25.38	0.39	0.09	0.03	0.03
NEP-15-021	Narayani	10.07.2015	0.80	0.46	-25.08	0.37	0.09	0.03	0.02
NEP-15-141	right side confluent (Khali Gandaki)	23.09.2015	0.72	0.37	-26.11	0.27	0.10	0.02	0.02
NEP-15-142	right side confluent (Khali Gandaki)	23.09.2015	0.70	0.33	-26.20	0.23	0.10	0.02	0.02
NEP-15-144	left side confluent (Trisuli)	23.09.2015	0.69	0.29	-25.02	0.20	0.09	0.01	0.01
NEP-15-145	left side confluent (Trisuli)	23.09.2015	0.69	0.3	-25.10	0.21	0.09	0.02	0.01
NEP-17-032	Narayani - bridge	29.06.2017	0.75	0.38	-24.94	0.29	0.09	0.02	0.02
NEP-17-037	left side confluent (Trisuli)	30.06.2017	0.80	0.51	-24.91	0.41	0.10	0.03	0.03
NEP-17-043	right side confluent (Khali Gandaki)	30.06.2017	0.63	0.24	-24.30	0.15	0.09	0.01	0.01

sample	region	Lat (°N)	Long (°E)	elevation (m asl)	sampling depth (cm)	Fraction modern	TOC (%)*
CA-913A	Khudi	28.30	84.30	2210	0-15 cm	0.98	3.47
CA-924	Khudi	28.36	84.28	3200	0-10 cm	1.12	8.11
CA-927	Khudi	28.40	84.25	4000	0-10 cm	1.00	4.06
CA-929	Khudi	28.40	84.26	3930	0-5 cm	1.07	7.63
NEQ-175-01A	South Kathmandu	27.57	85.23	1711	2-15 cm	1.00	0.61
NEQ-175-02A	South Kathmandu	27.57	85.20	1300	2-15 cm	1.03	4.65
NEQ-175-03A	South Kathmandu	27.53	85.09	808	2-15 cm	0.94	0.75
NEQ-175-42A	Chame	28.55	84.24	2899	2-15 cm	1.17	20.15
NEQ-175-45A	Chame	28.53	84.22	3475	2-15 cm	1.08	11.59
NEQ-175-48A	Chame	28.55	84.23	3092	2-15 cm	1.12	15.28
NEQ-175-55A	Manang	28.65	84.02	4007	2-15 cm	1.06	16.24
NEQ-175-58	Manang	28.66	84.02	3551	2-15 cm	0.77	0.40
NEQ-175-61A	Manang	28.68	84.05	4260	2-15 cm	1.02	6.33
NEQ-175-63.2	Thorung Phedi	28.78	83.97	4455	2-15 cm	0.92	NA
CA-10-155A	Langtang	28.16	85.41	2640	0-5 cm	1.09	6.62
MO-52A	Chepe	28.30	84.64	3610	10-20 cm	0.95	2.77
MO-87A	Chepe	28.16	84.65	1750	20-25 cm	0.92	1.23

* from ref.[52]

Supplementary Table 5: *Surface soil samples with corresponding TOC and fraction modern measurements.*

	OC export (*10^3 t/yr)	OC export (t/yr km^2)	OCbio export (*10^3 t/yr)	OCbio export (t/yr km^2)	OCpetro export (*10^3 t/yr)
mean (2010; 2015-2017)	322.3 ± 32.2	10.1 ± 1.0	197 ± 34.9	6.1 ± 1.1	138.6 ± 30.3
	OCpetro export (t/yr km^2)	**Casil + Mgsil (*10^3 t/yr)**	**Casil + Mgsil (t / yr km^2)**	**SO4- carb (*10^3 t/yr)**	**SO4- carb (t / yr km^2)**
mean (2010; 2015-2017)	4.3 ± 1.0	26.8 ± 12.2	0.8 ± 0.4	53.2 ± 8.0	1.7 ± 0.3

Supplementary Table 6: *Mean carbon fluxes of the four studied years.*

3

Molecular tracing of riverine soil organic matter from the Central Himalaya

Lena Märki[1], Maarten Lupker[1], Ananta P. Gajurel[2], Hannah Gies[1], Negar Haghipour[1,3], Sean Gallen[4], Christian France-Lanord[5], Jérôme Lavé[5], Timothy Eglinton[1]

[1] Geological Institute, ETH Zürich, Switzerland
[2] Department of Geology, Tribhuvan University, Nepal
[3] Ion Beam Physics, ETH Zürich, Switzerland
[4]Department of Geosciences, Colorado State University, USA
[5] CRPG, CNRS – Université de Lorraine, France

Published in *Geophysical Research Letters,* 2020,
DOI: 10.1029/2020GL087403

Abstract

The isomer distribution of branched glycerol dialkyl glycerol tetraethers (brGDGTs) in soils has been shown to correlate to the local mean annual temperature. Here, we explore the use of brGDGT distributions as proxy for the elevation at which soil organic carbon is preferentially mobilized in the Central Himalaya. Soil BrGDGT distributions collected along an altitudinal profile, spanning elevations from 200 to 4450 m asl, are linearly correlated to elevation. We use this calibration to trace the provenance of soil organic matter in suspended sediments of rivers draining the Himalaya. BrGDGT distributions of fluvial sediments reflect the mean elevation of the soil-cover in most catchments. Inverse modelling of the brGDGT dataset suggests similar relative contribution to soil organic carbon mobilization from different land-covers within a factor two. We conclude that riverine soil organic carbon export in the Himalaya mostly occurs pervasively and is at the catchment scale insensitive to anthropogenic perturbations.

Plain Language Summary

Soil degradation influences the global climate and has direct impacts on the ability of soils to deliver economic and ecological services. Identifying the source of eroded soil-derived carbon entrained in sediments of large rivers remains challenging. In this contribution, we use the temperature-sensitive signature of soil microbe-derived organic molecules to trace the source of soil carbon exported in river sediments of the rapidly eroding Central Himalaya of Nepal. Molecular signatures of soils, sampled over a wide range of elevations, and hence temperatures, are plotted on an elevation profile. River sediments are then compared to soil signatures in order to identify elevations of preferential soil export through rivers. Our data shows that soil-derived carbon is sampled uniformly over most of the catchments, indicating that soil export by Himalayan rivers is not driven by localized human perturbations such as agriculture or deforestation.

1 Introduction

Soils represent the largest organic carbon (OC) reservoir exposed at the Earth's surface (Jobbagy and Jackson, 2000). The exchange of soil organic carbon (SOC) with other carbon reservoirs such as the atmosphere or the geosphere exerts fundamental controls on the carbon budget of the Earth's surface on time scales ranging from decades to millions of years. Nevertheless, SOC dynamics and especially the lateral mobilization of carbon associated to soil erosion, remains one of the least constrained components of the carbon cycle (Doetterl *et al.*, 2016).

On timescales of decades to millennia, soil erosion is an important process that redistributes OC across the landscape (e.g., Doetterl et al., 2016; Yue et al., 2016) and exerts a primary control on SOC stocks (Yoo *et al.*, 2006; Patton *et al.*, 2019). The overall carbon budget of soil erosion on short time-scales remains a

subject of debate (Stockmann *et al.*, 2013). It may either act as a carbon source with respect to atmospheric CO_2 due to degradation and mineralization of SOC exposed during erosion (Schlesinger, 1995; Jacinthe and Lal, 2001), or as a carbon sink through effective OC sequestration and stabilization for instance in sediment accumulating areas (Stallard, 1998; Smith *et al.*, 2001; Berhe *et al.*, 2012). These considerations are particularly relevant in light of increasing anthropogenic pressure on soil systems that have led to up to a two orders of magnitude increase in soil erosion rates (Montgomery, 2007) and represent a significant perturbation of the modern carbon cycle (Wang *et al.*, 2017).

On geological timescales (millions of years), the erosion of SOC and its transport by rivers can also act as a long-term carbon sink since a fraction of the riverine particulate organic carbon is buried on continental margins (e.g., France-Lanord & Derry, 1997; Ludwig et al., 1996).

Although SOC stocks in mountain regions account for a small, yet poorly quantified, fraction of global SOC stocks (Scharlemann *et al.*, 2014), these rapidly eroding landscapes contribute disproportionally to the total export of OC (Galy *et al.*, 2015). Mountain ecosystems are also particularly vulnerable to soil erosion and associated changes in SOC stocks through changes in land-use or climate (e.g., Alewell et al., 2008). Despite the importance of soil erosion processes in mountain landscapes for global carbon budgets, few approaches are available to quantify and fingerprint soil erosion and associated SOC export, especially at the larger catchment scale.

Soil loss induced by deforestation and agriculture, particularly in steep mountain regions such as the Himalaya, has received much attention (e.g., Eckholm, 1975; Semwal *et al.*, 2004; Wasson *et al.*, 2008). Recent studies show that traditional terracing practices probably have a minor effect on soil erosion, but that modern agricultural methods and managed forests contribute more importantly to anthropogenic soil loss (Gardner and Gerrard, 2003; Upadhayay *et al.*, 2018). Anthropogenic perturbations of soil erosion in the Himalayan region could also be overshadowed by natural active denudation processes such as frequent mass wasting in the steeper areas (West *et al.*, 2015; Hoffmann *et al.*, 2016).

In this study, we use the distributions of Branched Glycerol Dialkyl Glycerol Tetraethers (brGDGTs) in soils and river sediments from 11 nested catchments (367 - 57700 km^2) in the Central Himalaya of Nepal to constrain the dominant elevations of SOC mobilization, and hence the provenance of soils eroded from a steep mountainous environment. BrGDGTs are a suite of lipids produced by microbes that occur ubiquitously in soils (Weijers *et al.*, 2007b; Schouten *et al.*, 2013). The relative abundance of different brGDGT isomers (here referred to as brGDGT distributions) depends on environmental parameters such as Mean Annual Temperature (MAT) and soil pH (Weijers *et al.*, 2007b) which makes them useful paleo-climate proxies (e.g., Weijers *et al.*, 2007a; Sinninghe Damasté *et al.*, 2012). Despite evidence for in-situ brGDGTs production in some aqueous environments (e.g., De Jonge *et al.*, 2014b), it has recently been shown that brGDGT signatures in suspended sediments can be used for tracing SOC inputs in riverine systems (Kirkels *et al.*, 2020). Here, we use the MAT calculated from brGDGT isomer distributions as a

proxy for the elevation from which soil organic carbon is mobilized and entrained in riverine suspended sediments of the Central Himalaya.

2 Materials and Methods

2.1 Study area and sampling

Rivers draining the Central Himalaya integrate a broad diversity of environmental conditions, with elevations ranging from over 8000 m in the central part of the range to ca. 150 m upon entering the Indo-Gangetic floodplain. The precipitation regime of the Central Himalaya is strongly influenced by the Indian Summer Monsoon, and a sharp precipitation gradient from the wetter Middle Hills to the dryer Upper Himalaya characterizes the region (Burbank *et al.*, 2003). The steep valleys of the Upper Himalaya, where mass wasting is the principal agent of erosion (Marc *et al.*, 2019), are characterized by high erosion rates (0.5 - 2 mm/yr) (Gabet *et al.*, 2008). The land-cover of the Upper Himalaya consists mainly of natural forests, shrub- and bare land or glaciers, whereas the Middle Hills are mostly covered by forests or agricultural land, such as rice paddies.

Samples for this study consisted of both soil samples, used to calibrate the brGDGT calculated-MAT against elevation, and river suspended sediment samples, which are used to identify the provenance of soil organic matter eroded from their respective catchments. Sample locations are shown in Figure 1a, and full details are reported in Tables S2 and S3. Soils samples (n=38) were collected over several field campaigns from 2009 to 2017. The sampling locations cover a variety of conditions such as elevation, annual precipitation, and aspect. At each location, soil samples were taken at depth intervals below the surface, if possible, down to bedrock. River sediments (n=28) were sampled from rivers draining catchments encompassing the soil sampling locations between 2015 and 2017. These consisted of two sample types: i) river samples, sampled during monsoon in 2017, by sampling surface river water followed by pressure filtration through 0.2 µm PES membranes; and ii) integrated river sediments that represent an average composition of sediments over two-week periods (for detailed sampling description see Supporting Information). No difference was found in GDGT compositions of sediments sampled using either method. Both types of suspended sediment samples are collected from surface river water and are taken to be representative of the entire water column as previous studies did not find any systematic variation of brGDGT signals with depth (Freymond *et al.*, 2018; Kirkels *et al.*, 2020). Some samples have been taken shortly after the 2015 Gorkha earthquake which triggered a large number of landslides in parts of the Central Himalaya (Roback *et al.*, 2018).

2.2 BrGDGTs and total organic carbon measurements

Soils and river sediments were frozen and freeze-dried at ETH Zurich. Soils were sieved and the fraction < 2 mm was used for further analysis. Analytical techniques for brGDGT analyses follow Hopmans et al.

(2016) and Freymond et al. (2017) and are summarized here with a detailed description in the Supporting Information. Briefly, between 2-3 g of the soil samples and around 20 g of the river sediments were extracted with solvents in a microwave or an automated extraction system. After purification via column chromatography and pre-filtration, the GDGT distributions were analyzed by High Performance Liquid Chromatography-Mass Spectrometry (HPLC-MS) at ETH Zurich. Absolute concentrations of GDGTs were determined by the addition of an internal standard (Huguet *et al.*, 2006). The relative abundance of the different GDGT isomers was determined based on integrated peak areas of mass chromatograms. The resulting brGDGT distributions are then used to calculate the corresponding MAT following the empirical calibration established by De Jonge *et al.* (2014a) (for more details on GDGT temperature calibrations see Supplementary Information).

The Total Organic Carbon (TOC) content of all samples was measured with an Elemental Analyzer at ETH Zurich (see Supporting Information).

2.3 Climate and remote sensing datasets

In order to quantify soil cover in the studied catchments, land-cover maps from the International Centre for Integrated Mountain Development (Uddin *et al.*, 2015) and from the National Geomatics Center of China (Jun *et al.*, 2014) were used. Normalized Difference Vegetation Index (NDVI) maps (MOD13Q1v006) were derived from the NASA's MODIS project (Didan, 2015). The mean elevations of soils and of vegetated areas in a catchment were calculated with the above-mentioned datasets using standard GIS software. The MAT corresponding to land-covers and sampling points was calculated using a linear regression between elevation and MAT inferred from temperature data of local weather stations (HMG, 1995; Putkonen, 2004) (see also Supporting Information). Precipitation data are taken from NASA's GIOVANNI platform.

3 Results

3.1 BrGDGT signatures in Himalayan soils

The mean absolute concentration of brGDGTs, determined as a composite of all branched isomers, in the soil samples is 3.3 $\mu g/g_{soil}$ (range: 0.005 – 17.9 $\mu g/g_{soil}$) resulting in mean TOC-normalized brGDGT concentrations of 53.4 $\mu g/g_{TOC}$ (2 – 259 $\mu g/g_{TOC}$) (Table S2). While absolute brGDGT concentrations decrease with soil depth, a clear trend is not visible for TOC-normalized brGDGT concentrations (Figure 1b). Both absolute and normalized brGDGT concentrations do not show any significant relationship with the soil elevation, as found in previous studies (Ernst *et al.*, 2013; Deng *et al.*, 2016; Kirkels *et al.*, 2020) (Figure 1c). Environmental parameters such as the measured MAT, the total annual precipitation and the aspect of the sampling site are also unrelated to brGDGT concentrations in Himalayan soils (Figure S2).

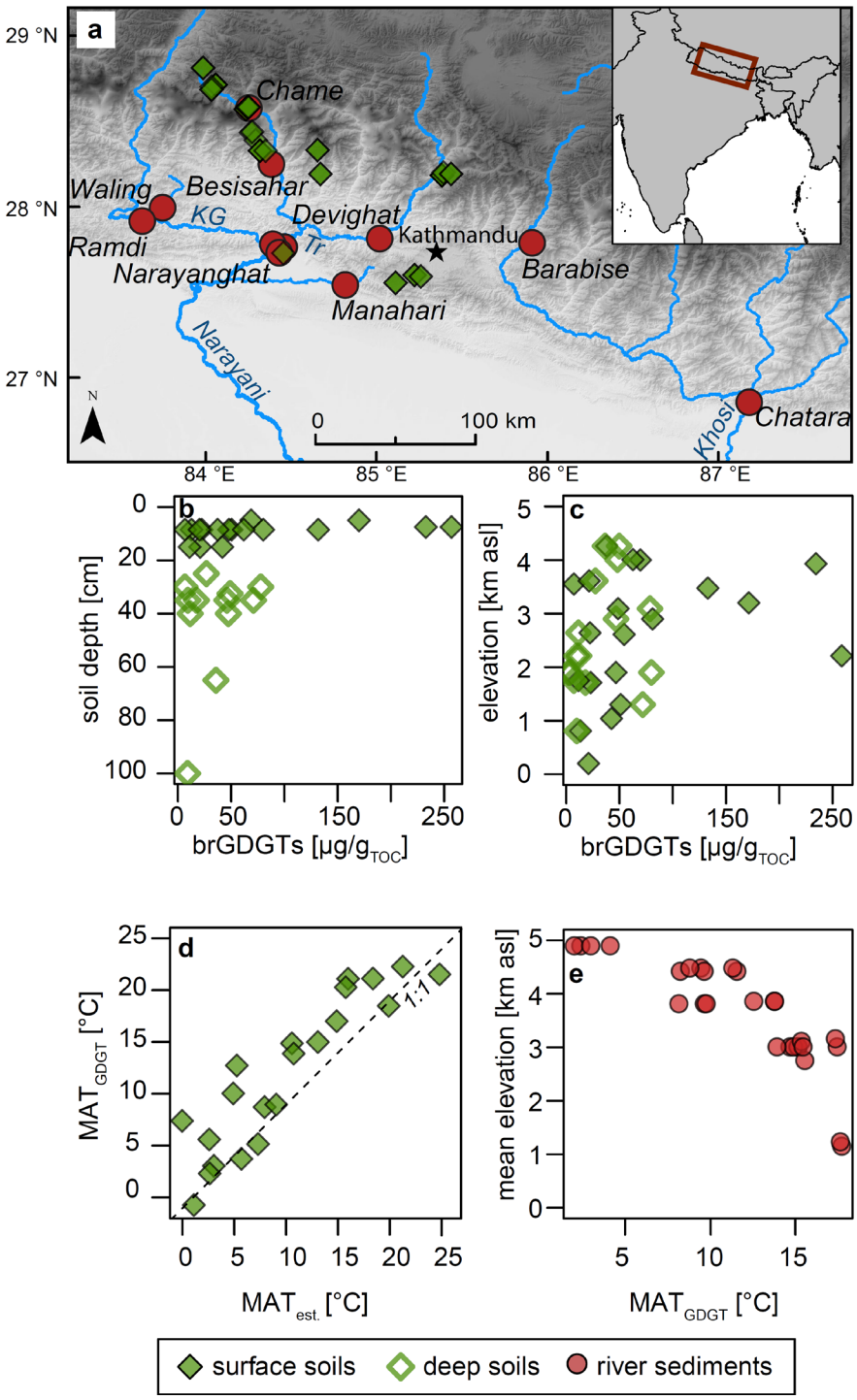

Figure 1: ***(a)*** *Map of the Central Himalaya (Nepal) displaying the soil (diamonds) and river (circles) sampling sites. Close to the station in Narayanghat, three rivers were sampled: the Khali Gandaki (KG), the Trisuli (Tr) and the Narayani.* ***(b)*** *Soil brGDGT concentrations normalized to the TOC content of soil samples as a function of the mean sampling depth.* ***(c)*** *Soil brGDGT concentrations normalized to the TOC content as a function of the elevation.* ***(d)*** *Estimated MAT values ($MAT_{est.}$) for sampling locations as a function of MAT calculated from soil brGDGTs (MAT_{GDGT}).* ***(e)*** *MAT_{GDGT} calculated with river sediment brGDGTs as a function of the mean catchment elevation.*

The MAT reconstruction calculated from brGDGT distributions of surface soils (MAT_{GDGT}) is in good agreement with the temperature estimated from climate data ($MAT_{est.}$, Figure 1d) (r^2=0.82, p<0.05, RMSE=3.0 °C). The MAT_{GDGT} values of all soils also show a robust negative linear correlation to elevation (Figure 2) (r^2= 0.81, p<0.05). There is no significant difference between the MAT_{GDGT} – elevation correlation for surface and deep soils. Our soil data agrees well with temperature estimated from nearby soils reported in Bai et al. (2018) (Figure 2).

3.2 BrGDGT signatures in suspended river sediments

TOC-normalized brGDGT concentrations of suspended river sediments lie between 0.25 and 28 $\mu g/g_{TOC}$ (mean: 8.9 $\mu g/g_{TOC}$) (Table S3). A general downstream increase in TOC-normalized brGDGT concentrations of suspended sediments can be observed despite large scatter. No systematic trend in brGDGT concentrations during the monsoon season or between sampling years is evident (Figure S3). Reconstructed MAT_{GDGT} values vary between 1.9 and 17.7 °C. Figure 1e shows that the MAT_{GDGT} correlates with the mean elevation of sampled river catchments (r^2=0.71, p<0.05).

4 Discussion

4.1 MAT reconstruction with soil brGDGTs

The calculated MAT_{GDGT} from surface soils in the Central Himalaya agree with the estimated temperatures at the sampling locations (Figure 1d). This suggests that the global calibration for temperature reconstruction with brGDGT distributions from De Jonge, Hopmans, et al. (2014) is applicable in the Himalaya. Several studies have shown that brGDGT-based indices are correlated with adiabatic temperature change along elevation profiles in different regions worldwide (e.g., Peterse *et al.*, 2009; Ernst *et al.*, 2013; Deng *et al.*, 2016; Bai *et al.*, 2018). This agrees with the calculated MAT_{GDGT} of Himalayan soils which strongly correlates with elevation (Figure 2). The obtained lapse rate (6.5 °C/km) is similar to the estimated lapse rate for the Central Himalaya (5.3 °C/km,. Soil brGDGT signals likely integrate environmental conditions over a timescale of at least decades, rendering them insensitive to seasonal or inter-annual climatic variabilities (Cao *et al.*, 2018).

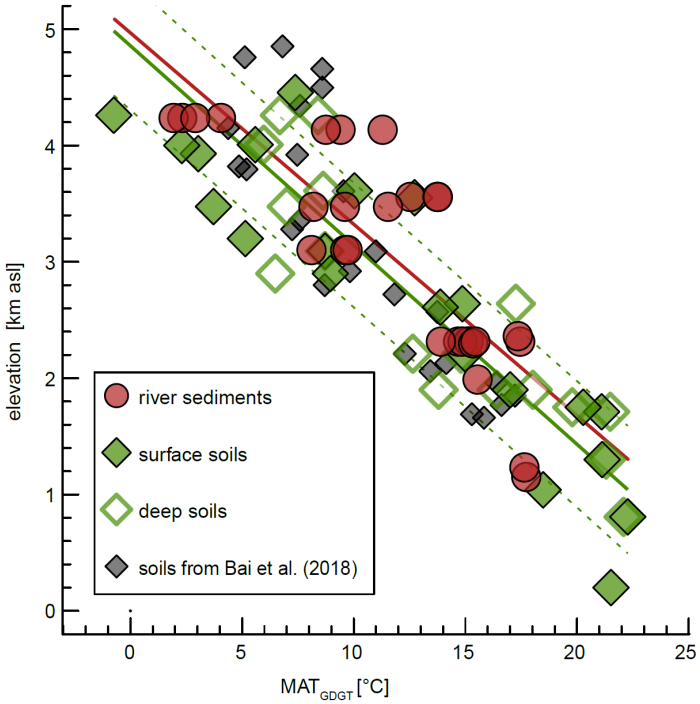

Figure 1: *MAT_{GDGT} calculated of brGDGTs in soils (green diamonds, this study; grey diamonds, nearby soil samples reported in Bai et al., 2018) and in river sediments (circles) as a function of elevation. The elevation depicted for river sediments corresponds to the mean elevation of the soil-covered areas of their respective catchments. Green lines show the linear regression (r^2=0.81) through the MAT_{GDGT} of all the soils and the one-sigma confidence interval; the red line shows the linear regression through MAT_{GDGT} of river sediments.*

4.2 Origin of the brGDGT signal in river sediments

The strong correlation between the calculated MAT_{GDGT} and soil elevation (Figure 2) provides an opportunity to trace the sources and inputs of soil organic matter exported by the fluvial system, and to refine our understanding of soil mobilization processes in rapidly eroding landscapes. Such an assessment is based on the assumptions that i) the studied proxy is distributed homogeneously across the landscape, and ii) the proxy signal is not significantly affected by transport.

As highlighted above and despite large variability, the brGDGT concentrations in soils do not vary systematically with elevation, precipitation or aspect, and TOC-normalized brGDGT concentrations and brGDGT distributions are invariant with soil depth. The MAT_{GDGT} of river sediments can, therefore, be used to directly trace soil organic matter provenance in the catchments without further correction or weighting.

We assume that in-situ production of brGDGTs in trans-Himalayan rivers is negligible given the short transit times and high turbidity of these fluvial systems. Substantial in-situ production would bias the reconstructed MAT_{GDGT} and lead to a significant increase of the isomer ratio of brGDGTs (De Jonge *et al.*,

2014a) beyond what is observed in our dataset (see Figure S2f). The lapse rate obtained from river sediment MAT_{GDGT} (5.7 °C/km, based on mean catchment elevation) agrees with the lapse rate of MAT_{GDGT} from the Himalayan soils (6.4 °C/km), further suggesting that soils are the main source of brGDGTs in river sediments.

Given that degradation of organic matter during riverine transport in a headwater system with minimal sediment storage is likely limited (Scheingross *et al.*, 2019), and that soil and river sediment-based lapse rates mentioned above are similar, this implies that brGDGTs in suspended sediments faithfully integrate upstream conditions (Kirkels *et al.*, 2020). It is therefore possible to interpret the fluvial brGDGT signal in terms of the elevational provenance of SOC mobilized in the Central Himalayan catchments. Comparison of the elevation calculated from the MAT_{GDGT} of river suspended sediments against the entire hypsometry of the upstream catchments indicates that soil organic matter is derived from below the mean elevation for most catchments. Since surfaces above 5000 - 5500 m asl are mostly covered by rocky terrain and glaciers with little to no soils, such a discrepancy is expected, and therefore the mean elevation of the soil-covered portion of a catchment serves a better representation of the likely provenance of soil-derived organic matter (difference between Figure 2 and Figure S4). As such, we use the mean soil elevation derived from land-cover maps (Jun *et al.*, 2014; Uddin *et al.*, 2015) and from vegetation-covered areas obtained from NDVI maps (Didan, 2015). Both land-cover and NDVI maps show a similar hypsometry in the different catchments (Table S3), suggesting that they provide good approximations of the mean elevation of soils in the respective catchments. The coarse resolution of these datasets compared to the elevation data likely induces a small overestimation of soil cover at elevations >5000 m asl. For the remaining analyses, we use the elevations calculated with the land-cover maps.

The elevation provenance inferred from the river-derived MAT_{GDGT} agrees well with the soil-covered average elevation of most catchments (Figure 2). We use this calibrated MAT_{GDGT}-elevation profile together with MAT_{GDGT} values of river sediments to calculate the source elevation of brGDGTs entrained in the riverine suspended load. In Figure 3, this calculated mean elevation for river sediment brGDGTs is compared to the elevation of different land-covers as well as the average slope of soil-covered portions of the catchment, binned by elevation.

In most studied catchments, the brGDGT signals in river sediments matches the mean altitude of the total soil-covered catchments (Figure 3). No specific elevation or land-cover type dominates the SOC exported by river sediments in these Central Himalayan catchments. This suggests that SOC exported by rivers as particulate organic matter represents an integrated signature of all soil-covered elevations within the catchment, and is not derived from specific elevation bands. This observation does not change between smaller drainage basins in the Upper Himalaya and larger basins integrating the Upper Himalaya and the Middle Hills. In addition, our data does not point towards any systematic temporal changes in soil provenance despite marked seasonal and inter-annual changes in the amount of total sediment and SOC export (Morin *et al.*, 2018). There is furthermore no direct evidence for changes in soil provenance linked to the 2015 Gorkha earthquake induced landslides which affected the studied catchments to different

degrees. Specifically, heavily impacted catchments such as upstream of Barabise or Devighat do not show significant differences compared to unaffected catchments such as upstream of Chame or Besisahar (Roback *et al.*, 2018).

Suspended sediments from the two rivers draining only the Middle Hills (Manahari and Walling) exhibit brGDGT signatures that would suggest that their SOC predominantly derives from an elevation above the average soil-covered elevation (Figure 3). This signal could have been affected by *in-situ* production of GDGTs or could be biased because of the saturation of the MAT_{GDGT} calibration above 22.9°C (De Jonge *et al.*, 2014a). Samples from Chatara and Barabise display brGDGT signals biased towards lower elevations than their mean soil-covered catchment elevation (Figure 3). This observation could be explained by enhanced SOC export from agricultural areas at lower elevations (see sensitivity calculation in the Supporting Information).

Soil production and erosion has been linked to landscape steepness (e.g., Heimsath *et al.*, 2012). In most of the studied catchments, hillslope angles are relatively evenly distributed with elevation (i.e. high slopes are not limited to specific elevation bands), making it difficult to identify a clear hillslope control on river brGDGT signatures (Figure 3). The catchments of Barabise and Chatara are exceptions where the highest elevation bands display significantly flatter topography from drainage portions on the Tibetan Plateau. The observed discrepancy between brGDGT signals from Chatara and Barabise and their respective mean soil-covered catchment elevation is therefore likely attributable to a limited SOC supply from the high elevation, low angled and arid Tibetan plateau, as has been suggested earlier (Hoffmann *et al.*, 2016).

4.3 Relative soil organic carbon yields of different land-covers

We use a linear inverse modelling approach in order to test the hypothesis of pervasive soil organic matter export across different land-covers in the Central Himalaya (see also Supporting Information). This model constrains the relative SOC yield from the catchment's main land-cover types (forests; shrub- and grasslands; agricultural areas) that can best explain the measured brGDGT signatures in the river sediments. For each catchment, the MAT_{GDGT} measured in river sediments is expressed as a linear function of each land-cover type's average temperature (calculated from the land-cover elevation distribution in the respective catchments), relative surface area, and the unknown SOC yield from a given land-cover type. Inverting the resulting set of equations shows that relative to shrub- and grasslands, forests contribute by a factor of ca. 0.85 (0.26 – 1.66, *q5 - q95* range) and agricultural areas by a factor ca. 1.56 (1.00 – 2.10, *q5 - q95* range) to SOC yields per unit surface-area (uncertainties are propagated from the uncertainty in the elevation – MAT_{GDGT} regression using a Monte Carlo approach). Similar results (forests: 1.99; agricultural areas: 1.30), albeit with greater uncertainty, are obtained for inversions that do not take into account the two small catchments discussed above (Manahari and Walling). The inversion is thus not sensitive to minor differences in SOC yields due to the heterogeneities between the catchments which cause relatively large errors. The inversion would however, capture orders of magnitude differences in

soil erosion rates expected in anthropogenically perturbed systems (Montgomery, 2007; Tarolli and Sofia, 2016). Our results therefore suggests that no specific land-cover type significantly dominates SOC export at the scale of the Central Himalaya, as anticipated from the results of Figure 3.

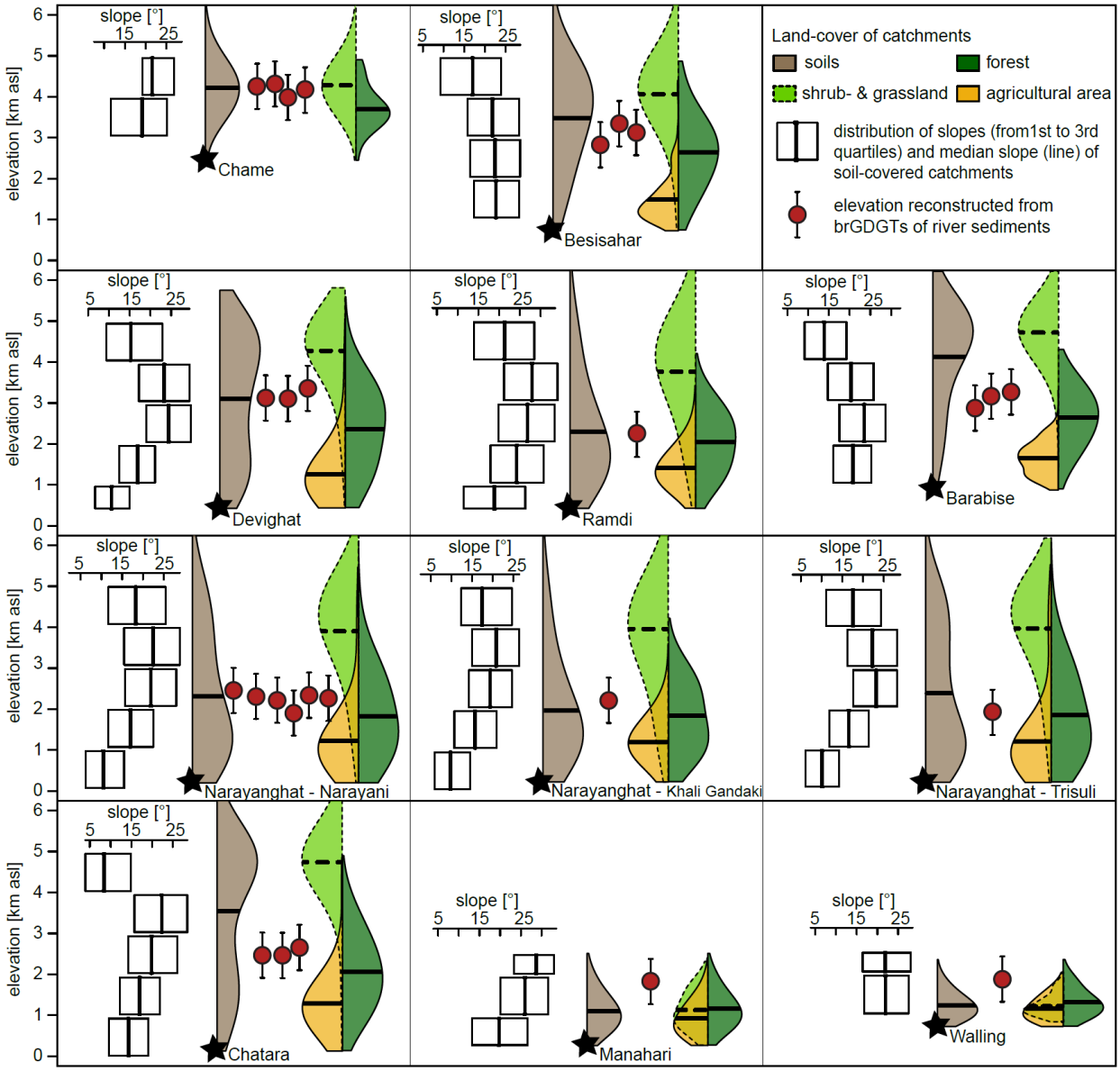

Figure 2: *Violin plots showing the elevations of the total soil-covered catchments and of different land-covers (shrub- and grassland, forest, agricultural area). Black lines indicate the mean values; stars are at the sampling site elevation. The slopes of five altitudinal portions of the soil-covered catchments are illustrated with boxplots without whiskers. Red circles show the mean elevation of SOC reflected in river suspended sediments calculated using corresponding* MAT_{GDGT} *values. Error bars correspond to the confidence interval of the* MAT_{GDGT}*-elevation calibration.*

4.4 Implications for soil organic matter carbon in the Central Himalaya

The brGDGT signals in rivers of Central Nepal show that soil organic matter entrained in their suspended load is predominantly sourced from the entire soil-mantled catchment in the Central Himalaya with a reduced SOC input from the Tibetan Plateau. The fact that brGDGT distributions in river sediments reflect the average soil-covered elevation irrespective of catchment size or mean elevation further demonstrates that brGDGTs are sourced from the entire elevation range of soil-cover in the catchment. These results therefore suggest that SOC export in Himalayan catchments is both pervasive and uniform, and is not restricted to certain elevations or land-cover types. SOC inputs due to deforestation and agriculture in the Middle Hills are therefore either negligible in comparison to overall background soil erosion processes or these erosional effects are balanced out by OC inputs through naturally enhanced soil erosion in the steeper Upper Himalaya (Montgomery, 2007; West *et al.*, 2015; Tarolli and Sofia, 2016). While mass wasting processes in the Upper Himalaya lead to high erosion rates (Marc *et al.*, 2019), bedrock landsliding probably mobilizes a relatively low proportion of soil organic matter (Morin *et al.*, 2018). This implies that even if topography, land-cover, erosion rates and annual precipitation rates are very different in the Upper Himalaya and the Nepalese Middle Hills, riverine SOC input must be fairly evenly distributed in order to not induce any significant elevation bias in brGDGT signals over the study area.

Other studies in the Himalaya have pointed at a predominant mobilization of organic matter from the southern flank of the Himalaya (Hoffmann *et al.*, 2016). The latter study focused on leaf-wax lipid biomarkers, which mainly trace vascular plant inputs. We find similar results for the catchments of Chatara and Barabise, however our data-set as a whole suggests a more widespread provenance of SOC. This possible decoupling of the brGDGT and plant-wax lipid provenance signals in river sediments may be attributed to broader altitudinal distribution of SOC compared to vascular plants OC in the Himalaya and/or to a more rapid remineralization of plant-wax lipids as it has been observed in the Andes (Feakins *et al.*, 2018; Kirkels *et al.*, 2020).

4.5 Implications for the integrative nature of brGDGTs signatures in river sediments

The signature of soil organic matter originating from all soil-covered elevations is found at the outlets of most Central Himalayan rivers. Trans-Himalayan rivers thus integrate the molecular signal from the entire soil-covered catchment, implying minimal loss of brGDGTs during transport. This is similar to observations from Andean headwaters (Kirkels *et al.*, 2020), but contrasts with studies from larger river systems as the Danube (Freymond *et al.*, 2017) or the Yangtze River (Li *et al.*, 2015). The high turbidity and short transit times of sediments and associated organic matter in mountainous rivers such as in the Central Himalaya transfer soil brGDGT signals with minimal apparent degradation. Thus, brGDGT distributions carried by suspended sediments of mountainous headwater rivers serve as reliable proxies of environmental conditions such as elevation or temperature of entire catchments. The downstream evolution of these brGDGT signals in the Gangetic floodplain remains to be studied, but long sediment transfer times and

extensive storage may cause overprinting of the headwater signals as is the case for a significant fraction of the exported organic matter (Galy *et al.*, 2008).

5 Conclusions

The MAT_{GDGT} in soils along an altitudinal transect in the Central Himalaya follow the adiabatic temperature change with altitude, and therefore correlate with the elevation of the sampling location. Due to the absence of any systematic relation between soil brGDGT concentrations and elevation, it is possible to directly use the MAT_{GDGT} of soil brGDGTs as an elevation proxy. This soil MAT_{GDGT}-elevation calibration is then used to trace the elevational provenance of SOC in suspended sediments of Central Himalayan rivers in order to identify possible zones of preferential soil organic matter mobilization.

Calculated MAT_{GDGT} values of surface soils using a global calibration closely follow the expected temperature of the sampling location. This highlights the possibility of using brGDGTs for reconstruction of paleoenvironmental conditions in the Central Himalaya.

Elevations calculated based on the MAT_{GDGT} of river sediments reflect the average elevation of the soil-cover found in most catchments. This implies that riverine SOC export is a uniform and pervasive process in the Central Himalaya, occurring over the entire range of elevations mantled by soil, whereas the SOC export efficiency on the Tibetan Plateau is probably substantially lower. Inversion of the brGDGT signals suggests no significant difference in relative SOC yield from different land-covers. Possible enhanced soil organic matter mobilization due to anthropogenic activities as agriculture or deforestation, are therefore subordinate to soil mobilization by active natural erosion processes at higher elevations.

Acknowledgments

This study was funded by grant n# 200021_166067 from the Swiss National Science Foundation. We thank D. Montluçon for lab work support and C. De Jonge for helpful discussions.

We are grateful to J. J. Baronas and an anonymous Reviewer for their insightful comments that helped to improve the manuscript. We also thank R. Cory for the efficient editorial handling.

All the data are available in the Supporting Information and are going to be uploaded to the Research Collection database of the ETH Zurich upon acceptance.

References

Alewell, C., Meusburger, K., Brodbeck, M. & Bänninger, D. (2008). Methods to describe and predict soil erosion in mountain regions. *Landscape and Urban Planning* **88**, 46–53.

Bai, Y., Chen, C., Xu, Q. & Fang, X. (2018). Paleoaltimetry Potentiality of Branched GDGTs From Southern Tibet. *Geochemistry, Geophysics, Geosystems* **19**, 551–564.

Berhe, A. A., Harden, J. W., Torn, M. S., Kleber, M., Burton, S. D. & Harte, J. (2012). Persistence of soil organic matter in eroding versus depositional landform positions. *Journal of Geophysical Research: Biogeosciences* **117**, 1–16.

Burbank, D. W., Blythe, A. E., Putkonen, J. L., Pratt-Situala, B. A., Gabet, E. J., Oskin, M. E., Barros, A. P. & Ohja, T. P. (2003). Decoupling of erosion and climate in the Himalaya. *Nature* **426**, 652–655.

Cao, M., Rueda, G., Rivas-Ruiz, P., Carmen, M., Henriksen, M., Vegas-vilarrúbia, T. & Rosell-melé, A. (2018). Organic Geochemistry Branched GDGT variability in sediments and soils from catchments with marked temperature seasonality. *Organic Geochemistry* **122**, 98–114.

De Jonge, C., Hopmans, E. C., Zell, C. I., Kim, J. H., Schouten, S. & Sinninghe Damsté, J. S. (2014a). Occurrence and abundance of 6-methyl branched glycerol dialkyl glycerol tetraethers in soils: Implications for palaeoclimate reconstruction. *Geochimica et Cosmochimica Acta* **141**, 97–112.

De Jonge, C., Stadnitskaia, A., Hopmans, E. C., Cherkashov, G., Fedotov, A. & Sinninghe Damsté, J. S. (2014b). In situ produced branched glycerol dialkyl glycerol tetraethers in suspended particulate matter from the Yenisei River, Eastern Siberia. *Geochimica et Cosmochimica Acta* **125**, 476–491.

Deng, L., Jia, G., Jin, C. & Li, S. (2016). Warm season bias of branched GDGT temperature estimates causes underestimation of altitudinal lapse rate. *Organic Geochemistry*. Elsevier Ltd **96**, 11–17.

Didan, K. (2015). MOD13Q1 MODIS/Terra Vegetation Indices 16-Day L3 Global 250m SIN Grid V006. *NASA EOSDIS LP DAAC*.

Doetterl, S., Berhe, A. A., Nadeu, E., Wang, Z., Sommer, M. & Fiener, P. (2016). Erosion, deposition and soil carbon: A review of process-level controls, experimental tools and models to address C cycling in dynamic landscapes. *Earth-Science Reviews*. Elsevier B.V. **154**, 102–122.

Eckholm, E. P. (1975). The Deterioration of Mountain Environments. *Science* **189**, 764–770.

Ernst, N., Peterse, F., Breitenbach, S. F. M., Syiemlieh, H. J. & Eglinton, T. I. (2013). Biomarkers record environmental changes along an altitudinal transect in the wettest place on Earth. *Organic Geochemistry*. Elsevier Ltd **60**, 93–99.

Feakins, S. J., Wu, M. S., Ponton, C., Galy, V. & West, A. J. (2018). Dual isotope evidence for sedimentary integration of plant wax biomarkers across an Andes-Amazon elevation transect. *Geochimica et Cosmochimica Acta*. Elsevier Ltd **242**, 64–81.

France-Lanord, C. & Derry, L. A. (1997). Organic carbon burial forcing of the carbon cycle from Himalayan erosion. *Nature* **390**, 65–67.

Freymond, C. V., Lupker, M., Peterse, F., Haghipour, N., Wacker, L., Filip, F., Giosan, L. & Eglinton, T. I. (2018). Constraining Instantaneous Fluxes and Integrated Compositions of Fluvially Discharged Organic Matter. *Geochemistry, Geophysics, Geosystems* **19**, 2453–2462.

Freymond, C. V., Peterse, F., Fischer, L. V., Filip, F., Giosan, L. & Eglinton, T. I. (2017). Branched GDGT signals in fluvial sediments of the Danube River basin: Method comparison and longitudinal evolution. *Organic Geochemistry*. Elsevier Ltd **105**, 37–38.

Fu, S., Liu, B., Liu, H. & Xu, L. (2011). The effect of slope on interrill erosion at short slopes. *Catena* **84**, 29–34.

Gabet, E. J., Burbank, D. W., Pratt-Sitaula, B., Putkonen, J. & Bookhagen, B. (2008). Modern erosion rates in the High Himalayas of Nepal. *Earth and Planetary Science Letters* **267**, 482–494.

Galy, V., France-Lanord, C. & Lartiges, B. (2008). Loading and fate of particulate organic carbon from the Himalaya to the Ganga-Brahmaputra delta. *Geochimica et Cosmochimica Acta* **72**, 1767–1787.

Galy, V., Peucker-Ehrenbrink, B. & Eglinton, T. (2015). Global carbon export from the terrestrial biosphere controlled by erosion. *Nature* **521**, 204–207.

Gardner, R. A. M. & Gerrard, A. J. (2003). Runoff and soil erosion on cultivated rainfed terraces in the Middle Hills of Nepal. *Applied Geography* **23**, 23–45.

Heimsath, A. M., DiBiase, R. A. & Whipple, K. X. (2012). Soil production limits and the transition to bedrock-dominated landscapes. *Nature Geoscience*. Nature Publishing Group **5**, 210–214.

HMG (1995). His Majesty's Government of Nepal. *Climatolgical records of Nepal 1987-1990, Dept. of Hydrol. and Meteorol.* **Kathmandu**.

Hoffmann, B., Feakins, S. J., Bookhagen, B., Olen, S. M., Adhikari, D. P., Mainali, J. & Sachse, D. (2016). Climatic and geomorphic drivers of plant organic matter transport in the Arun River, E Nepal. *Earth and Planetary Science Letters*. Elsevier B.V. **452**, 104–114.

Hopmans, E. C., Schouten, S. & Sinninghe Damsté, J. S. (2016). The effect of improved chromatography on GDGT-based palaeoproxies. *Organic Geochemistry*. Elsevier Ltd **93**, 1–6.

Huguet, C., Hopmans, E. C., Febo-Ayala, W., Thompson, D. H., Sinninghe Damsté, J. S. & Schouten, S. (2006). An improved method to determine the absolute abundance of glycerol dibiphytanyl glycerol tetraether lipids. *Organic Geochemistry* **37**, 1036–1041.

Jacinthe, P. A. & Lal, R. (2001). A mass balance approach to assess carbon dioxide evolution during erosional events. *Land Degradation and Development* **12**, 329–339.

Jobbagy, E. G. & Jackson, R. B. (2000). The vertical distribution of soil organic carbon and its relation to climate and vegetation. *Ecological Applications* **10**, 423–436.

Jun, C., Ban, Y. & Li, S. (2014). Open access to Earth land-cover map. *Nature* **514**, 434.

Kirkels, F. M. S. A., Ponton, C., Galy, V., West, A. J., Feakins, S. J. & Peterse, F. (2020). From Andes to Amazon : Assessing Branched Tetraether Lipids as Tracers for Soil Organic Carbon in the Madre de Dios River System. *Journal of Geophysical Research: Biogeosciences* **125**, 1–18.

Li, Z., Peterse, F., Wu, Y., Bao, H., Eglinton, T. I. & Zhang, J. (2015). Sources of organic matter in Changjiang (Yangtze River) bed sediments: Preliminary insights from organic geochemical proxies. *Organic Geochemistry*. Elsevier Ltd **85**, 11–21.

Ludwig, W., Probst, J. L. & Kempe, S. (1996). Predicting the oceanic input of organic carbon by continental erosion. *Global Biogeochemical Cycles* **10**, 23–41.

Marc, O., Behling, R., Andermann, C., Turowski, J. M., Illien, L., Roessner, S. & Hovius, N. (2019). Long-term erosion of the Nepal Himalayas by bedrock landsliding: The role of monsoons, earthquakes and giant landslides. *Earth Surface Dynamics* **7**, 107–128.

Montgomery, D. R. (2007). Soil erosion and agricultural sustainability. *Proceedings of the National Academy of Sciences* **104**, 13268–13272.

Morin, G. P., Lavé, J., France-Lanord, C., Rigaudier, T., Gajurel, A. P. & Sinha, R. (2018). Annual Sediment Transport Dynamics in the Narayani Basin, Central Nepal: Assessing the Impacts of Erosion Processes in the Annual

Sediment Budget. *Journal of Geophysical Research: Earth Surface* **123**, 2341–2376.

Patton, N. R., Lohse, K. A., Seyfried, M. S., Godsey, S. E. & Parsons, S. B. (2019). Topographic controls of soil organic carbon on soil-mantled landscapes. *Scientific Reports*. Springer US **9**, 1–15.

Peterse, F., Kim, J. H., Schouten, S., Kristensen, D. K., Koç, N. & Sinninghe Damsté, J. S. (2009). Constraints on the application of the MBT/CBT palaeothermometer at high latitude environments (Svalbard, Norway). *Organic Geochemistry*. Elsevier Ltd **40**, 692–699.

Putkonen, J. K. (2004). Continuous snow and rain data at 500 to 4400 m altitude near Annapurna, Nepal, 1999-2001. *Arctic, Antarctic, and Alpine Research* **36**, 244–248.

Roback, K., Clark, M. K., West, A. J., Zekkos, D., Li, G., Gallen, S. F., Chamlagain, D. & Godt, J. W. (2018). The size, distribution, and mobility of landslides caused by the 2015 Mw7.8 Gorkha earthquake, Nepal. *Geomorphology*. The Authors **301**, 121–138.

Scharlemann, J. P. W., Tanner, E. V. J., Hiederer, R., Kapos, V., Pw, J., Tanner, E. V. J., Hiederer, R. & Kapos, V. (2014). Global soil carbon : understanding and managing the largest terrestrial carbon pool Global soil carbon : understanding and managing the largest terrestrial carbon pool. *Carbon Management* **5**, 81–91.

Scheingross, J. S., Hovius, N., Dellinger, M., Hilton, R. G., Repasch, M., Sachse, D., Gröcke, D. R., Vieth-Hillebrand, A. & Turowski, J. M. (2019). Preservation of organic carbon during active fluvial transport and particle abrasion. *Geology* **47**, 958–962.

Schlesinger, W. H. (1995). Soil respiration and changes in soil carbon stocks. *Biotic feedbacks in the global climatic system: will the warming feed the warming, Oxford Univ. Press* 159–168.

Schouten, S., Hopmans, E. C. & Sinninghe Damsté, J. S. (2013). The organic geochemistry of glycerol dialkyl glycerol tetraether lipids: A review. *Organic Geochemistry*. Elsevier Ltd **54**, 19–61.

Semwal, R. L., Nautiyal, S., Sen, K. K., Rana, U., Maikhuri, R. K., Rao, K. S. & Saxena, K. G. (2004). Patterns and ecological implications of agricultural land-use changes : a case study from central Himalaya , India. *Agriculture, Ecosystems and Environment* **102**, 81–92.

Sinninghe Damasté, J. S., Ossebaar, J., Schouten, S. & Verschuren, D. (2012). Distribution of tetraether lipids in the 25-ka sedimentary record of Lake Challa : extracting reliable TEX 86 and MBT / CBT palaeotemperatures from an equatorial African lake. *Quaternary Science Reviews*. Elsevier Ltd **50**, 43–54.

Smith, S. V., Renwick, W. H., Buddemeier, R. W. & Crossland, C. J. (2001). Budgets of soil erosion and deposition for sediments and sedimentary organic carbon across the posited across the United States. *Global Biogeochemical Cycles* **15**, 697–707.

Stallard, R. F. (1998). Terrestrial sedimentation and the carbon cycle : Coupling weathering and erosion to carbon burial. *Water Resources* **12**, 231–257.

Stockmann, U. *et al.* (2013). The knowns, known unknowns and unknowns of sequestration of soil organic carbon. *Agriculture, Ecosystems and Environment*. Elsevier B.V. **164**, 80–99.

Tarolli, P. & Sofia, G. (2016). Human topographic signatures and derived geomorphic processes across landscapes. *Geomorphology* **255**, 140–161.

Uddin, K., Shrestha, H. L., Murthy, M. S. R., Bajracharya, B., Shrestha, B., Gilani, H., Pradhan, S. & Dangol, B. (2015). Development of 2010 national land cover database for the Nepal. *Journal of Environmental Management*. Elsevier Ltd **148**, 82–90.

Upadhayay, H. R., Smith, H. G., Griepentrog, M., Bodé, S., Man, R., Blake, W., Cornelis, W. & Boeckx, P. (2018). Community managed forests dominate the catchment sediment cascade in the mid-hills of Nepal : A compound-specific stable isotope analysis. *Science of the Total Environment*. Elsevier B.V. **637**–**638**, 306–317.

Wang, Z., Hoffmann, T., Six, J., Kaplan, J. O., Govers, G., Doetterl, S. & Van Oost, K. (2017). Human-induced erosion has offset one-third of carbon emissions from land cover change. *Nature Climate Change* **7**, 345–349.

Wasson, R. J., Juyal, N., Jaiswal, M., McCulloch, M., Sarin, M. M., Jain, V., Srivastava, P. & Singhvi, A. K. (2008). The mountain-lowland debate: Deforestation and sediment transport in the upper Ganga catchment. *Journal of Environmental Management* **88**, 53–61.

Weijers, J. W. H., Schefuß, E., Schouten, S. & Damsté, J. S. S. (2007a). Evolution of Tropical Africa over the Last Deglaciation. *Science* **315**, 1701–1705.

Weijers, J. W. H., Schouten, S., van den Donker, J. C., Hopmans, E. C. & Sinninghe Damsté, J. S. (2007b). Environmental controls on bacterial tetraether membrane lipid distribution in soils. *Geochimica et Cosmochimica Acta* **71**, 703–713.

West, A. J., Arnold, M., Aumaître, G., Bourlès, D. L., Keddadouche, K., Bickle, M. & Ojha, T. (2015). High natural erosion rates are the backdrop for present-day soil erosion in the agricultural Middle Hills of Nepal. *Earth Surface Dynamics* **3**, 363–387.

Yoo, K., Amundson, R., Heimsath, A. M. & Dietrich, W. E. (2006). Spatial patterns of soil organic carbon on hillslopes: Integrating geomorphic processes and the biological C cycle. *Geoderma* **130**, 47–65.

Yue, Y. *et al.* (2016). Lateral transport of soil carbon and land-atmosphere CO2 flux induced by water erosion in China. *Proceedings of the National Academy of Sciences of the United States of America* **113**, 6617–6622.

Supporting Information for:

Molecular tracing of riverine soil organic matter from the Central Himalaya

S1. Methods for brGDGTs extraction and measurement

2-3 g of freeze-dried and sieved (<2 mm) soils and ca. 20 g of freeze-dried river sediments were extracted in a microwave-assisted (CEM Corporation) or an automated extraction system (EDGE, CEM Corporation) with dichloromethane:methanol (DCM:MeOH, 9:1, v:v). For the former, extraction was performed for 25 min at 100 °C; for the latter, sequential sample extraction was performed 3 times at 110° C. After drying, sample vials were filled with a mix of ultrapure MilliQ water, NaCl and hexane (Hex) in order to extract the neutral lipid fraction. This fraction was subsequently passed through a 1 % deactivated SiO2 column first with Hex:DCM (9:1, v:v) to obtain the apolar fraction, then with DCM:MeOH (1:1, v:v) to obtain the polar fraction. The latter was dried, dissolved in hexane/isopropanol (Hex/IPA, 99:1, v:v) and 0.5 µg of an internal C_{46} GDGT standard (Huguet *et al.*, 2006) was added. The GDGT fraction was filtered (PTFE filter, 0.45 µm) before measurement.

The GDGTs dissolved in Hex:IPA (99:1, v:v) were analyzed with a High Performance Liquid Chromatograph (Agilent 1260) coupled to a quadrupole Mass Spectrometer configured for Atmospheric Pressure Chemical Ionization (HPLC-APCI-MS) at ETH Zurich. Two silica columns were used to separate the GDGTs (Hopmans *et al.*, 2016). The injection volume was 10 µL and the flow rate set to 0.2 mL/min. The detected ions were integrated from corresponding the mass chromatograms.

The relative abundances of individual brGDGTs were used to calculate the following indexes and calibrations:

MBT'_{5Me} = (Ia + Ib + Ic) / (Ia + Ib + Ic + IIa + IIb + IIc + IIIa)

$CBT' = \log_{10}[(Ic + IIa' + IIb' + IIc' + IIIa' + IIIb' + IIIc') / (Ia + IIa + IIIa)]$

pH = 7.15 + 1.59 * CBT'

MAT_{GDGT}= -8.57 + 31.45 * MBT'_{5Me} (all 4 calibrations: De Jonge *et al.*, 2014a)

The roman letters correspond to specific GDGTs (e.g., Schouten *et al.*, 2013).

S2. Measurement of total organic carbon content

For Total Organic Carbon (TOC) content, aliquots of the freeze-dried soil and river sediment samples were milled, and ~50 mg of the powder was weighed into silver capsules. Samples were fumigated in HCl vapor for removal of inorganic carbon (3 days at 60 °C), and neutralized over NaOH (4 days at 60 °C). The silver

capsules were subsequently wrapped in tin boats and TOC contents were determined with an Elemental Analyzer (EA) at ETH Zurich.

S3. Comparison of sample types

River sediment samples consist of two types: Suspended sediment from filtered surface water and integrated sediment samples over two weeks. For these later samples, a local collaborator collected 20 to 40 L of river water that was added to a 120 L opaque container and left to settle overnight before gently decanting the surface supernatant. This sampling was repeated every day for two weeks. If necessary the superior 20 to 40 L of water was removed from the container by a water tap before adding the new sample. After two weeks the resulting sediment was collected by a water tap at the bottom of the container and air-dried, providing a biweekly time series of sediment export.

In order to study the two used sampling techniques, we compare sample NEQ-D-NA1603 obtained by daily sampling and settling in large barrels to sample NEQ-NA16-d, a composite sample made by mixing daily suspended sediment samples in proportion of the measured sediment concentration, obtained from the same location over the same period and filtered immediately after collection. Both sampling methods yield similar results (concentration of brGDGTs are 0.030 and 0.038 µg/g and the MAT_{GDGT} is 14.9 and 13.9 °C for NEQ-D-NA1603 and NEQ-NA-16-d respectively). This suggests that neither the potential losses of the finer clay material that had insufficient time to settle between daily decantation of the supernatant nor eventual in-situ brGDGT production in the container significantly affected our data. The two sampling methods are therefore used in the analysis interchangeably.

S4. Mean annual temperature estimation

For estimating the MAT at the sampling locations, we used temperature data from the Department of Hydrology and Meteorology of Nepal (HMG, 1995) and Putkonen (2004). Using available data from 37 weather stations in Nepal (HMG, 1995), we calculated the mean MAT of the 4 years between 1987-1990. The measurements from 10 weather stations from Putkonen (2004) (mean of data from 1999-2001) complete our dataset at higher elevations of the Central Himalaya. We find a strong negative correlation between MAT and the elevation of a station (Figure S1, r^2=0.98, $p<0.05$). Using this correlation, we calculate the expected MAT ($MAT_{est.}$) for the soil sampling sites of this study.

S5. Soil pH measurement and reconstruction

The pH of the soil samples was measured for comparison with reconstructed pH values from brGDGT distributions. For the measurement of soil pH an aliquot of freeze-dried soil sample was mixed with KCl (1 M) to a 1:5 ratio (w:v). The mixture was put on a shaker for 10 min and then left to settle down for 2

hours. The pH was subsequently measured with a calibrated pH electrode. The measured soil pH varies over a large range, between 3.6 and 7.9. These values were compared to the pH reconstructed from brGDGT distributions according to the calibration of De Jonge *et al.* (2014a) (Figure S2e). We observe a significant correlation between measured and reconstructed pH (r^2=0.84, p<0.05, RMSE=0.36), however reconstructed pH values are systematically higher than the measured pH for all soils which indicates the need for a local CBT' - soil pH calibration. Our soil dataset suggests the following local calibration for the Central Himalaya of: 6.27 + 1.72 * CBT' = pH (r^2=0.84, p<0.05, RMSE=0.39).

S6. Isomer ratio of soil and river sediment brGDGTs

The isomer ratio (IR) was defined by De Jonge et al. (2014b) to quantify in-situ production of brGDGTs in river sediments:

IR = (IIa' + IIb' + IIc' + IIIa' + IIIb' + IIIc') / (IIa + IIb + IIc + IIIa + IIIb + IIIc + IIa'+IIb'+IIc'+IIIa'+IIIb'+IIIc')

Figure S2f shows that the IR values of soil samples vary between 0.05 and 0.9. IR values of brGDGTs in river sediments lie in a narrower range between 0.3 and 0.7. De Jonge et al. (2014b) showed that riverine in-situ production increases the IR of suspended sediments significantly. The small difference between the IR ratio of brGDGTs in Himalayan soils and river sediments does not suggest any significant in-situ production.

S7. Inverse model

We applied a linear inverse model approach to estimate relative contributions of SOC export from the three main land-cover types in the soil-mantled catchments (forests, shrub-and grasslands and agricultural areas). With 11 catchments and three unknowns this over-determined system of equations was solved as:

$$\min ||G*m - d||^2$$

Where G is the matrix containing the MAT of each land-cover calculated with the mean altitude and the elevation-MAT_{GDGT} calibration times the respective land-cover area for each of the 11 studied catchments:

$$G = area_{land\text{-}cover} * (av.\ MAT_{land\text{-}cover} \pm 3^{\circ}C) / area_{total}$$

d is the vector with the mean measured MAT_{GDGT} of river sediments at a sampling station (if they exist, multiple samples at a given station were averaged). And m the relative contribution of SOC in river sediments to be determined. All contributions were calculated relative to a shrub- and grassland contribution of 1. We applied a Monte Carlo simulation ($n = 10^5$) allowing the model to randomly sample temperature from our elevation-MAT_{GDGT} calibration and its estimated 1σ uncertainty of ± 3˚C. The 5 % best fitting inversions generated by the Monte-Carlo inversions were used to estimate the median, 5 and

95 percentiles of the land-cover contribution distributions. This inversion was performed under the statistical software R (R Studio Team, 2020) and the code is reproduced hereunder:

```
--------------------------------------------------------------------------------
#########
## Monte carlo inversions for landcover contributions to GDGT signals – R script
######### April – 2020

#clear all
rm(list = ls())
#libraries
library(limSolve)
#load data
setwd("/Users/MyUserfolder/GDGT_Inversion")
lcovers <- read.table("lcovers.txt", header = T)
lcovers[is.na(lcovers)] <- 0
sed <- read.table("sed.txt", header = T)

n=1e5    #number of Monte Carlo runs
Results <- matrix(data=NA , nrow=n , ncol=4)          #store results
temp_uncert = 3   #uncertainty around the GDGT temperature reconstruction in degrees C
cat <- nrow(lcovers)         #number of catchments

total_surface <- lcovers$agri + lcovers$grass + lcovers$forest   #normalize to surface area

for (i in 1:n){
        #fractional temperature of each landcover with randomly generated uncertainty on the GDGT-temperature
        relation
        agri_MAT_fr <- lcovers$agri * (lcovers$agri_MAT + rnorm(cat , mean = 0 , sd = temp_uncert)) /
        total_surface
        grass_MAT_fr <- lcovers$grass * (lcovers$grass_MAT + rnorm(cat , mean = 0 , sd = temp_uncert)) /
        total_surface
        forest_MAT_fr <- lcovers$forest * (lcovers$forest_MAT + rnorm(cat , mean = 0 , sd = temp_uncert)) /
        total_surface

        #Equations that have to be met exactly: shrubs & grass contribute to 1
        EE <- c(0,1,0)
        FF <- 1

        # A*x = B
        AA <- matrix(c(forest_MAT_fr , grass_MAT_fr , agri_MAT_fr) , nrow=cat , ncol=3)
        BB <- sed$MAT_GDGTs + rnorm(cat , mean = 0 , sd = temp_uncert)

        #Inequalities: all fraction must be positive numbers
        GG <- diag(nrow = 3)
        HH <- rep(0,3)

        #inversion
        INV <- lsei(AA,BB,E=EE,F=FF,G=GG,H=HH)
        Results[i,1:3] <- INV$X
        Results[i,4] <- INV$solutionNorm
}

#sort data according to best fit
keep = 0.05 * n    #keep 5% best fits
```

```
sort_fit <- order(Results[,4] , na.last = TRUE)
Results_bf <- Results[sort_fit,][1:keep,]

#stat of best fits
quant_bf <- apply(Results_bf[,1:3], 2, function(x) quantile(x , probs=c(0.05,0.5,0.95) , na.rm=T))
```

With lcovers:

location,agri,grass,forest,soil_MAT,agri_MAT,grass_MAT
Narayanghat,28.3,27.9,43.8,15.0,21.8,4.6
Chame,0.0,87.9,12.1,2.6,NA,2.1
Chatara,13.4,58.0,28.6,7.2,21.3,-0.6
Devighat,25.0,38.8,36.2,10.8,21.7,2.2
Besisahar,3.8,61.9,34.3,7.4,20.2,3.6
Barabise,5.3,72.7,22.0,3.2,19.1,-0.7
Manahari,22.2,1.7,76.1,22.4,23.6,22.2
DadiKhola,49.8,6.3,43.9,22.0,22.4,22.0
KhaliGandaki,31.5,24.0,44.5,15.6,20.9,5.7
Narayanghat-KhaliGandaki,34.2,20.7,45.1,16.9,21.7,6.0
Narayanghat-Trisuli,24.6,32.1,43.3,14.4,22.0,4.2

With sed:

location,MAT_GDGTs
Narayanghat,15.2
Chame,2.8
Chatara,13.3
Devighat,9.1
Besisahar,9.8
Barabise,9.8
Manahari,17.7
DadiKhola,17.6
KhaliGandaki,15.3
Narayanghat-KhaliGandaki,15.5
Narayanghat-Trisuli,17.3

The modelled results of the inversion using all the catchments fit the measured MAT_{GDGT} with r^2=0.7 and RMSE=4.0 °C. The mean sum of the squared residuals is 126.5.

S8. Sensitivity analysis

The inversion model presented above assumes that all studied catchments can be described by a single SOC export model. While this approach appears reasonable given the geomorphic and geographic uniformity of the studied area and takes advantage of a larger dataset; the uncertainty on the inversion results warrants further discussion. Figure S5 shows the results of a sensitivity analysis for each individual catchment and illustrates how the MAT_{GDGT} obtained from the respective river sediments would vary in

case of enhanced SOC mobilization from a single given land-cover (all else being held equal). In this sensitivity analysis, only one of the land-cover SOC yield is changing while the others are held constant providing an insight in how sensitive the GDGT signals are to changes in SOC yields from individual land-cover types. It therefore represents a maximum estimate of the model sensitivity. We observe that the brGDGT signal of river sediments is not sensitive to a small enhancement of SOC export from one land-cover and that the temporal variability of the brGDGT signal at a given sampling station can be important (e.g., Narayanghat). In general, however, the brGDGT signal of most catchments is best explained by the temperature calculated for the mean soil-covered elevations, as we expect from the inversion results. We observe that samples from Chatara and Barabise display MAT_{GDGT} that significantly exceed the temperature estimated for pervasive SOC erosion in the soil-covered catchment (brown diamond). This could be attributed to enhanced SOC yields from agricultural areas or forests (or both) but as discussed in the text is more likely related to a decrease in SOC yields from grass- and shrublands on the Tibetan Plateau (Hoffmann *et al.*, 2016). The overall climatic and topographic conditions as well as the agricultural practices in the basins of Chatara and Barabise are very similar to the other studied catchments.

The suspended sediment of the two rivers draining only the Middle Hills (Manahari and Walling) exhibit brGDGT signatures that suggest significantly colder MAT than expected from the mean soil-covered catchment elevation (Figure S5) (as anticipated from Figure 3). They cannot be simply explained by changes in SOC yields and are therefore likely related to in-situ production or the saturation of the brGDGT calibration at higher temperatures as discussed in the main text.

References Supplementary Information

Alewell, C., Meusburger, K., Brodbeck, M. & Bänninger, D. (2008). Methods to describe and predict soil erosion in mountain regions. *Landscape and Urban Planning* **88**, 46–53.

Bai, Y., Chen, C., Xu, Q. & Fang, X. (2018). Paleoaltimetry Potentiality of Branched GDGTs From Southern Tibet. *Geochemistry, Geophysics, Geosystems* **19**, 551–564.

Berhe, A. A., Harden, J. W., Torn, M. S., Kleber, M., Burton, S. D. & Harte, J. (2012). Persistence of soil organic matter in eroding versus depositional landform positions. *Journal of Geophysical Research: Biogeosciences* **117**, 1–16.

Burbank, D. W., Blythe, A. E., Putkonen, J. L., Pratt-Situala, B. A., Gabet, E. J., Oskin, M. E., Barros, A. P. & Ohja, T. P. (2003). Decoupling of erosion and climate in the Himalaya. *Nature* **426**, 652–655.

Cao, M., Rueda, G., Rivas-Ruiz, P., Carmen, M., Henriksen, M., Vegas-vilarrúbia, T. & Rosell-melé, A. (2018). Organic Geochemistry Branched GDGT variability in sediments and soils from catchments with marked temperature seasonality. *Organic Geochemistry* **122**, 98–114.

De Jonge, C., Hopmans, E. C., Zell, C. I., Kim, J. H., Schouten, S. & Sinninghe Damsté, J. S. (2014a). Occurrence and abundance of 6-methyl branched glycerol dialkyl glycerol tetraethers in soils: Implications for palaeoclimate reconstruction. *Geochimica et Cosmochimica Acta* **141**, 97–112.

De Jonge, C., Stadnitskaia, A., Hopmans, E. C., Cherkashov, G., Fedotov, A. & Sinninghe Damsté, J. S. (2014b). In situ produced branched glycerol dialkyl glycerol tetraethers in suspended particulate matter from the Yenisei

River, Eastern Siberia. *Geochimica et Cosmochimica Acta* **125**, 476–491.

Deng, L., Jia, G., Jin, C. & Li, S. (2016). Warm season bias of branched GDGT temperature estimates causes underestimation of altitudinal lapse rate. *Organic Geochemistry*. Elsevier Ltd **96**, 11–17.

Didan, K. (2015). MOD13Q1 MODIS/Terra Vegetation Indices 16-Day L3 Global 250m SIN Grid V006. *NASA EOSDIS LP DAAC*.

Doetterl, S., Berhe, A. A., Nadeu, E., Wang, Z., Sommer, M. & Fiener, P. (2016). Erosion, deposition and soil carbon: A review of process-level controls, experimental tools and models to address C cycling in dynamic landscapes. *Earth-Science Reviews*. Elsevier B.V. **154**, 102–122.

Eckholm, E. P. (1975). The Deterioration of Mountain Environments. *Science* **189**, 764–770.

Ernst, N., Peterse, F., Breitenbach, S. F. M., Syiemlieh, H. J. & Eglinton, T. I. (2013). Biomarkers record environmental changes along an altitudinal transect in the wettest place on Earth. *Organic Geochemistry*. Elsevier Ltd **60**, 93–99.

Feakins, S. J., Wu, M. S., Ponton, C., Galy, V. & West, A. J. (2018). Dual isotope evidence for sedimentary integration of plant wax biomarkers across an Andes-Amazon elevation transect. *Geochimica et Cosmochimica Acta*. Elsevier Ltd **242**, 64–81.

France-Lanord, C. & Derry, L. A. (1997). Organic carbon burial forcing of the carbon cycle from Himalayan erosion. *Nature* **390**, 65–67.

Freymond, C. V., Lupker, M., Peterse, F., Haghipour, N., Wacker, L., Filip, F., Giosan, L. & Eglinton, T. I. (2018). Constraining Instantaneous Fluxes and Integrated Compositions of Fluvially Discharged Organic Matter. *Geochemistry, Geophysics, Geosystems* **19**, 2453–2462.

Freymond, C. V., Peterse, F., Fischer, L. V., Filip, F., Giosan, L. & Eglinton, T. I. (2017). Branched GDGT signals in fluvial sediments of the Danube River basin: Method comparison and longitudinal evolution. *Organic Geochemistry*. Elsevier Ltd **105**, 37–38.

Fu, S., Liu, B., Liu, H. & Xu, L. (2011). The effect of slope on interrill erosion at short slopes. *Catena* **84**, 29–34.

Gabet, E. J., Burbank, D. W., Pratt-Sitaula, B., Putkonen, J. & Bookhagen, B. (2008). Modern erosion rates in the High Himalayas of Nepal. *Earth and Planetary Science Letters* **267**, 482–494.

Galy, V., France-Lanord, C. & Lartiges, B. (2008). Loading and fate of particulate organic carbon from the Himalaya to the Ganga-Brahmaputra delta. *Geochimica et Cosmochimica Acta* **72**, 1767–1787.

Galy, V., Peucker-Ehrenbrink, B. & Eglinton, T. (2015). Global carbon export from the terrestrial biosphere controlled by erosion. *Nature* **521**, 204–207.

Gardner, R. A. M. & Gerrard, A. J. (2003). Runoff and soil erosion on cultivated rainfed terraces in the Middle Hills of Nepal. *Applied Geography* **23**, 23–45.

Heimsath, A. M., DiBiase, R. A. & Whipple, K. X. (2012). Soil production limits and the transition to bedrock-dominated landscapes. *Nature Geoscience*. Nature Publishing Group **5**, 210–214.

HMG (1995). His Majesty's Government of Nepal. *Climatolgical records of Nepal 1987-1990, Dept. of Hydrol. and Meteorol.* **Kathmandu**.

Hoffmann, B., Feakins, S. J., Bookhagen, B., Olen, S. M., Adhikari, D. P., Mainali, J. & Sachse, D. (2016). Climatic and geomorphic drivers of plant organic matter transport in the Arun River, E Nepal. *Earth and Planetary Science Letters*. Elsevier B.V. **452**, 104–114.

Hopmans, E. C., Schouten, S. & Sinninghe Damsté, J. S. (2016). The effect of improved chromatography on GDGT-based palaeoproxies. *Organic Geochemistry*. Elsevier Ltd **93**, 1–6.

Huguet, C., Hopmans, E. C., Febo-Ayala, W., Thompson, D. H., Sinninghe Damsté, J. S. & Schouten, S. (2006). An improved method to determine the absolute abundance of glycerol dibiphytanyl glycerol tetraether lipids. *Organic Geochemistry* **37**, 1036–1041.

Jacinthe, P. A. & Lal, R. (2001). A mass balance approach to assess carbon dioxide evolution during erosional events. *Land Degradation and Development* **12**, 329–339.

Jobbagy, E. G. & Jackson, R. B. (2000). The vertical distribution of soil organic carbon and its relation to climate and vegetation. *Ecological Applications* **10**, 423–436.

Jun, C., Ban, Y. & Li, S. (2014). Open access to Earth land-cover map. *Nature* **514**, 434.

Kirkels, F. M. S. A., Ponton, C., Galy, V., West, A. J., Feakins, S. J. & Peterse, F. (2020). From Andes to Amazon : Assessing Branched Tetraether Lipids as Tracers for Soil Organic Carbon in the Madre de Dios River System. *Journal of Geophysical Research: Biogeosciences* **125**, 1–18.

Li, Z., Peterse, F., Wu, Y., Bao, H., Eglinton, T. I. & Zhang, J. (2015). Sources of organic matter in Changjiang (Yangtze River) bed sediments: Preliminary insights from organic geochemical proxies. *Organic Geochemistry*. Elsevier Ltd **85**, 11–21.

Ludwig, W., Probst, J. L. & Kempe, S. (1996). Predicting the oceanic input of organic carbon by continental erosion. *Global Biogeochemical Cycles* **10**, 23–41.

Marc, O., Behling, R., Andermann, C., Turowski, J. M., Illien, L., Roessner, S. & Hovius, N. (2019). Long-term erosion of the Nepal Himalayas by bedrock landsliding: The role of monsoons, earthquakes and giant landslides. *Earth Surface Dynamics* **7**, 107–128.

Montgomery, D. R. (2007). Soil erosion and agricultural sustainability. *Proceedings of the National Academy of Sciences* **104**, 13268–13272.

Morin, G. P., Lavé, J., France-Lanord, C., Rigaudier, T., Gajurel, A. P. & Sinha, R. (2018). Annual Sediment Transport Dynamics in the Narayani Basin, Central Nepal: Assessing the Impacts of Erosion Processes in the Annual Sediment Budget. *Journal of Geophysical Research: Earth Surface* **123**, 2341–2376.

Patton, N. R., Lohse, K. A., Seyfried, M. S., Godsey, S. E. & Parsons, S. B. (2019). Topographic controls of soil organic carbon on soil-mantled landscapes. *Scientific Reports*. Springer US **9**, 1–15.

Peterse, F., Kim, J. H., Schouten, S., Kristensen, D. K., Koç, N. & Sinninghe Damsté, J. S. (2009). Constraints on the application of the MBT/CBT palaeothermometer at high latitude environments (Svalbard, Norway). *Organic Geochemistry*. Elsevier Ltd **40**, 692–699.

Putkonen, J. K. (2004). Continuous snow and rain data at 500 to 4400 m altitude near Annapurna, Nepal, 1999-2001. *Arctic, Antarctic, and Alpine Research* **36**, 244–248.

Roback, K., Clark, M. K., West, A. J., Zekkos, D., Li, G., Gallen, S. F., Chamlagain, D. & Godt, J. W. (2018). The size, distribution, and mobility of landslides caused by the 2015 Mw7.8 Gorkha earthquake, Nepal. *Geomorphology*. The Authors **301**, 121–138.

Scharlemann, J. P. W., Tanner, E. V. J., Hiederer, R., Kapos, V., Pw, J., Tanner, E. V. J., Hiederer, R. & Kapos, V. (2014). Global soil carbon : understanding and managing the largest terrestrial carbon pool Global soil carbon : understanding and managing the largest terrestrial carbon pool. *Carbon Management* **5**, 81–91.

Scheingross, J. S., Hovius, N., Dellinger, M., Hilton, R. G., Repasch, M., Sachse, D., Gröcke, D. R., Vieth-Hillebrand, A. & Turowski, J. M. (2019). Preservation of organic carbon during active fluvial transport and particle abrasion. *Geology* **47**, 958–962.

Schlesinger, W. H. (1995). Soil respiration and changes in soil carbon stocks. *Biotic feedbacks in the global climatic system: will the warming feed the warming, Oxford Univ. Press* 159–168.

Schouten, S., Hopmans, E. C. & Sinninghe Damsté, J. S. (2013). The organic geochemistry of glycerol dialkyl glycerol tetraether lipids: A review. *Organic Geochemistry*. Elsevier Ltd **54**, 19–61.

Semwal, R. L., Nautiyal, S., Sen, K. K., Rana, U., Maikhuri, R. K., Rao, K. S. & Saxena, K. G. (2004). Patterns and ecological implications of agricultural land-use changes : a case study from central Himalaya , India. *Agriculture, Ecosystems and Environment* **102**, 81–92.

Sinninghe Damasté, J. S., Ossebaar, J., Schouten, S. & Verschuren, D. (2012). Distribution of tetraether lipids in the 25-ka sedimentary record of Lake Challa : extracting reliable TEX 86 and MBT / CBT palaeotemperatures from an equatorial African lake. *Quaternary Science Reviews*. Elsevier Ltd **50**, 43–54.

Smith, S. V., Renwick, W. H., Buddemeier, R. W. & Crossland, C. J. (2001). Budgets of soil erosion and deposition for sediments and sedimentary organic carbon across the posited across the United States. *Global Biogeochemical Cycles* **15**, 697–707.

Stallard, R. F. (1998). Terrestrial sedimentation and the carbon cycle : Coupling weathering and erosion to carbon burial. *Water Resources* **12**, 231–257.

Stockmann, U. *et al.* (2013). The knowns, known unknowns and unknowns of sequestration of soil organic carbon. *Agriculture, Ecosystems and Environment*. Elsevier B.V. **164**, 80–99.

Tarolli, P. & Sofia, G. (2016). Human topographic signatures and derived geomorphic processes across landscapes. *Geomorphology* **255**, 140–161.

Uddin, K., Shrestha, H. L., Murthy, M. S. R., Bajracharya, B., Shrestha, B., Gilani, H., Pradhan, S. & Dangol, B. (2015). Development of 2010 national land cover database for the Nepal. *Journal of Environmental Management*. Elsevier Ltd **148**, 82–90.

Upadhayay, H. R., Smith, H. G., Griepentrog, M., Bodé, S., Man, R., Blake, W., Cornelis, W. & Boeckx, P. (2018). Community managed forests dominate the catchment sediment cascade in the mid-hills of Nepal : A compound-specific stable isotope analysis. *Science of the Total Environment*. Elsevier B.V. **637**–**638**, 306–317.

Wang, Z., Hoffmann, T., Six, J., Kaplan, J. O., Govers, G., Doetterl, S. & Van Oost, K. (2017). Human-induced erosion has offset one-third of carbon emissions from land cover change. *Nature Climate Change* **7**, 345–349.

Wasson, R. J., Juyal, N., Jaiswal, M., McCulloch, M., Sarin, M. M., Jain, V., Srivastava, P. & Singhvi, A. K. (2008). The mountain-lowland debate: Deforestation and sediment transport in the upper Ganga catchment. *Journal of Environmental Management* **88**, 53–61.

Weijers, J. W. H., Schefuß, E., Schouten, S. & Damsté, J. S. S. (2007a). Evolution of Tropical Africa over the Last Deglaciation. *Science* **315**, 1701–1705.

Weijers, J. W. H., Schouten, S., van den Donker, J. C., Hopmans, E. C. & Sinninghe Damsté, J. S. (2007b). Environmental controls on bacterial tetraether membrane lipid distribution in soils. *Geochimica et Cosmochimica Acta* **71**, 703–713.

West, A. J., Arnold, M., Aumaître, G., Bourlès, D. L., Keddadouche, K., Bickle, M. & Ojha, T. (2015). High natural erosion rates are the backdrop for present-day soil erosion in the agricultural Middle Hills of Nepal. *Earth Surface Dynamics* **3**, 363–387.

Yoo, K., Amundson, R., Heimsath, A. M. & Dietrich, W. E. (2006). Spatial patterns of soil organic carbon on hillslopes: Integrating geomorphic processes and the biological C cycle. *Geoderma* **130**, 47–65.

Yue, Y. *et al.* (2016). Lateral transport of soil carbon and land-atmosphere CO2 flux induced by water erosion in China. *Proceedings of the National Academy of Sciences of the United States of America* **113**, 6617–6622.

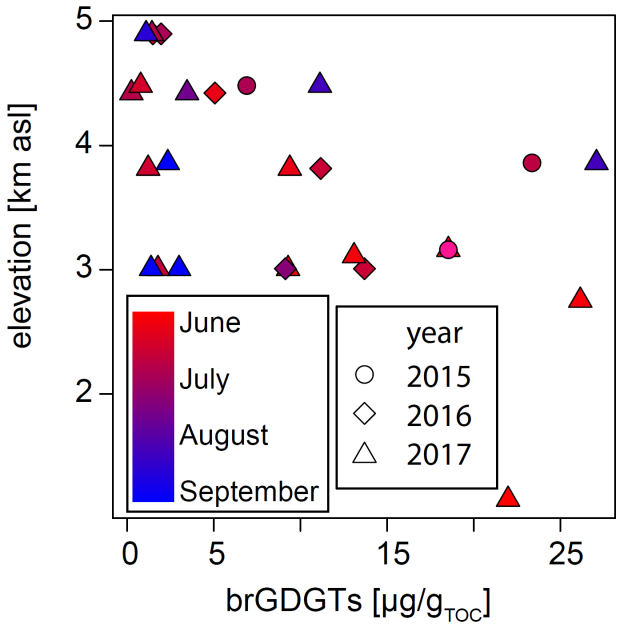

Figure S3: *Concentration of brGDGTs normalized to the TOC content of river sediments plotted against the mean catchment elevation. Shapes of symbols correspond to the sampling year and they are colored in function of the season of sampling.*

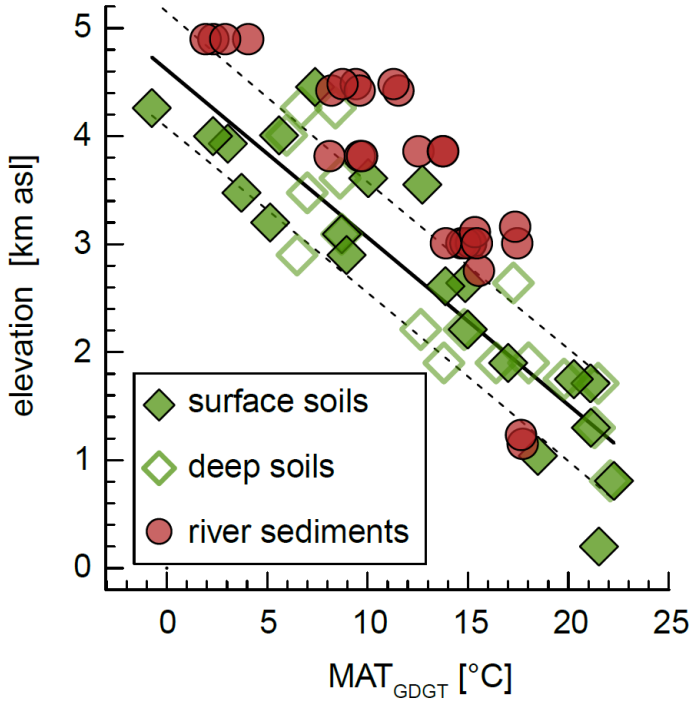

Figure S3: *MAT of brGDGTs in soils (diamonds) and river sediments (circles). The linear regression was fitted through the MATGDGT of soil brGDGTs and the one-sigma confidence interval is shown. The elevation of river sediments corresponds to the mean catchment elevation (note that Figure 2 in the main text shows mean elevation of soil-covered catchment).*

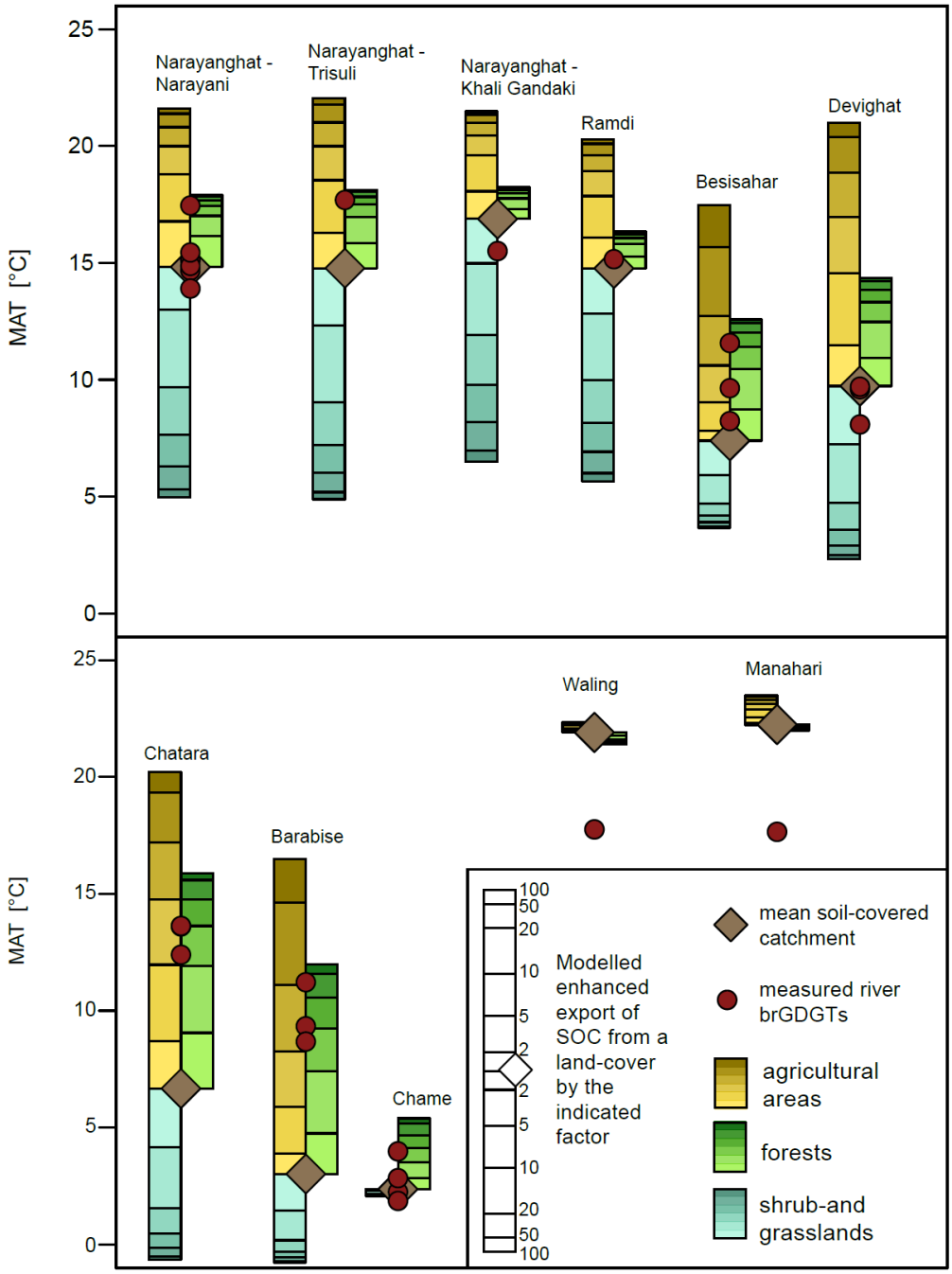

Figure S4: *Results of sensitivity analysis: Red circles show the MAT_{GDGT} of measured brGDGTs in river sediments and brown diamonds illustrate the theoretical MAT_{GDGT} signal assuming that SOC yield from all the land-covers is equal. Colored bars show the modelled MAT_{GDGT} expected in river sediments if SOC export from a single land-cover type (shrub- and grassland, forest, agricultural area) in the respective catchment is enhanced by different factors (2, 5, 10, 20, 50, 100) while all else is kept constant. Note that reduced SOC export from one land-cover type would have the opposite effect and reverse the direction of its color bar. The MAT_{GDGT} signals in Chatara and Barabise are most likely associated to lower SOC yields from grass- and shrublands on the Tibetan Plateau (see main text).*

Data from His Majesty's Government of Nepal (HMG, 1995)

Station	Lat. [°N]	Long. [°E]	Elevation [m asl]	MAT 1987 [°C]	MAT 1988 [°C]	MAT 1989 [°C]
Jomsom	28'47	83'43	2744	11.7	12	11.2
Thakmarpha	28'45	83'42	2566	-	11.7	10.8
Baglung	28'16	83'36	984	21.8	22.5	21.9
Beni Bazar	28'21	83'34	835	-	-	-
Lomangthang	29'11	83'58	3705	6	7.2	5.1
Kushma	28'13	83'42	891	-	-	-
Tansen	27'52	83'32	1067	19.7	20.6	-
Bhairahawa	27'31	83'26	109	25	24.8	-
Dumkauli	27'41	84'13	154	24.8	25.1	24.6
Bhairahawa	27'32	83'28	120	25.1	25.1	24.2
Khanchikot	27'56	83'09	1760	16.4	16.5	16
Taulihawa	27'33	83'04	94	25.9	25.5	24.5
Tamghas	28'04	83'15	1530	17.5	17.5	16.6
Simari	27'32	83'45	154	25.5	25.6	24.6
Khudi Bazar	28'17	84'22	823	-	21.4	-
Pokhara	28'13	84'00	827	21	21.3	20.5
Syangja	28'06	83'53	868	21	21.3	20.8
Gorkha	28'00	84'37	1097	20.9	21.3	20.7
Chapkot	27'53	83'49	460	23.1	23.4	22.8
Malepatan	28'07	84'07	856	-	-	20.4
Lumle	28'18	83'48	1740	16	16.3	15.8
Khairinitar	28'02	84'06	500	22.8	23.2	22.8
Chame	28'33	84'14	2680	-	-	-
Rampur	27'37	84'25	256	24	-	23.9
Daman	27'36	85'05	2314	13.7	13.5	12.8
Hetaunda	27'25	85'03	474	23.3	23.2	22.5
Simara	27'10	84'59	130	24.4	24.4	23.7
Parwanipur	27'04	84'58	115	24.9	24.9	24.1
Gaur	26'46	85'18	90	-	-	-
Nuwakot	27'55	85'10	1003	-	-	-
Kakani	27'48	85'15	2064	15	-	14.9
Godavari	27'35	85'24	1400	16	16.7	16.4
Khumaltar	27'40	85'20	1350	17.6	18	17.7
Kathmandu	27'42	85'22	1337	18.4	18.9	18.6

from Puktonen (2004)

Station	Lat. [°N]	Long. [°E]	Elevation [m als]	MAT (1999-2001) [°C]
Ganpokhara	28'17.142	84'18.218	2120	13.9
Khudi	28'16.931	84'21.285	820	20.1
Koprung	28'22.863	84'21.047	3133	6.7
Purano	28'18.248	84'21.107	1787	15.5
Purkot	28'3.662	84'28.161	528	21.4
Rambrong	28'24.54	84'14.342	4435	-0.5
Sundar	28'25.07	84'19.694	3823	3.2
Tal	28'28.002	84'22.446	1600	14.9

Table S1: *MAT data from HMG (1995) and Putkonen (2004).*

Table S2: *Data of soil samples*

Soil samples

Sample	Lat [°N]	Long [°E]	Elevation [m asl]	Sampling depth [cm]	TOC [%]	brGDGTs [µg/g soil]	brGDGTs [µg/g TOC]	MBT'_{5Me}	CBT'	Measured pH	Calculated pH	$MAT_{est.}$ [°C][1]	MAT_{GDGT} [°C]	Mean precipitation [mm/yr][2]
CA-904	28.2935	84.3323	1040	10 - 20	1.66	0.704	42.432	0.86	-0.89	5	5.7	19.9	18.5	3758
CA-913A	28.2959	84.301	2210	0 - 15	3.47	8.961	258.541	0.75	-1.73	4.1	4.4	13.1	15	3832
CA-913B	28.2959	84.301	2210	30 - 50	1.43	0.172	12.037	0.74	-1.28	4.2	5.1	13.1	14.8	3832
CA-913C	28.2959	84.301	2210	85 - 115	0.19	0.018	9.626	0.67	-0.94	4.1	5.7	13.1	12.6	3832
CA-924	28.3556	84.2753	3200	0 - 10	8.11	13.894	171.317	0.44	-1.18	3.9	5.3	7.3	5.1	4555
CA-927	28.4001	84.2473	4000	0 - 10	4.06	2.823	69.53	0.35	-1.43	3.7	4.9	2.6	2.3	3902
CA-929	28.4037	84.2568	3930	0 - 5	7.63	17.881	234.347	0.37	-1.35	3.6	5	3	3	3902
NEQ-175-01A	27.5669	85.2329	1711	2 - 15	0.61	0.14	22.928	0.94	-1.33	4.4	5	16	21.1	2611
NEQ-175-01B	27.5669	85.2329	1711	30 - 40	0.24	0.043	17.992	0.96	-1.24	4.5	5.2	16	21.5	2611
NEQ-175-02A	27.5731	85.1956	1300	2 - 15	4.65	2.374	51.098	0.94	-0.77	5	5.9	18.4	21.1	2748
NEQ-175-02B	27.5731	85.1956	1300	30 - 40	1.96	1.404	71.729	0.95	-0.78	4.8	5.9	18.4	21.3	2748
NEQ-175-03A	27.5278	85.0874	808	2 - 15	0.75	0.1	13.297	0.98	-1.49	4.1	4.8	21.3	22.3	3872
NEQ-175-03B	27.5278	85.0874	808	30 - 40	0.47	0.046	9.853	0.97	-1.13	4.9	5.4	21.3	22.1	3872
NEQ-175-09A	27.7256	84.4275	200	2 - 15	2.16	0.45	20.855	0.96	-1.09	5.2	5.4	24.8	21.5	1735
NEQ-175-42A	28.5455	84.2352	2899	2 - 15	20.15	16.321	81.006	0.56	-0.47	5.6	6.4	9	9	1604
NEQ-175-42B	28.5455	84.2352	2899	30 - 40	1.63	0.763	46.695	0.48	0.11	6.9	7.3	9	6.5	1604
NEQ-175-45A	28.5349	84.2196	3475	2 - 15	11.59	15.401	132.88	0.39	-0.57	4.7	6.2	5.7	3.7	2176
NEQ-175-45B	28.5349	84.2196	3475	20 - 30	-	0.094	-	0.5	-0.44	4.7	6.5	5.7	7	2176
NEQ-175-48A	28.5485	84.2294	3092	2 - 15	15.28	7.436	48.675	0.55	-0.79	4.7	5.9	7.9	8.7	1604
NEQ-175-48B	28.5485	84.2294	3092	25 - 35	2.23	1.749	78.606	0.55	-0.43	5.4	6.5	7.9	8.7	1604
NEQ-175-55A	28.6491	84.0184	4007	2 - 15	16.24	10.159	62.553	0.45	-0.14	5.8	6.9	2.6	5.6	562
NEQ-175-55B	28.6491	84.0184	4007	35 - 45	5.43	2.609	48.097	0.46	-0.32	5.7	6.6	2.6	6	562
NEQ-175-58	28.6639	84.0201	3551	2 - 15	0.4	0.029	7.164	0.68	0.6	7.9	8.1	5.2	12.7	343
NEQ-175-61A	28.6758	84.0454	4260	2 - 15	6.33	2.402	37.947	0.25	0.3	6.3	7.6	1.1	-0.7	343
NEQ-175-61B	28.6758	84.0454	4260	30 - 35	3.74	1.859	49.703	0.49	-0.07	6.8	7	1.1	6.7	343
NEQ-175-61C	28.6758	84.0454	4260	60 - 70	1.94	0.706	36.378	0.54	-0.13	6.7	6.9	1.1	8.4	343
NEQ-175-63.2	28.7766	83.972	4455	2 - 15	-	2.806	-	0.51	0.28	6.8	7.6	0	7.4	398
CA-10-155A	28.1611	85.4096	2640	0 - 5	6.62	1.473	22.249	0.75	-0.96	4.2	5.6	10.6	14.9	1767

Continuation of Table S2

Soil samples

Sample	Lat [°N]	Long [°E]	Elevation [m asl]	Sampling depth [cm]	TOC [%]	brGDGTs [µg/g soil]	brGDGTs [µg/g TOC]	MBT'_{5Me}	CBT'	Measured pH	Calculated pH	$MAT_{est.}$ [°C][1]	MAT_{GDGT} [°C]	Mean precipitation [mm/yr][2]
CA-10-155B	28.1611	85.4096	2640	10 - 20	2.1	0.24	11.405	0.82	-1.3	4.3	5.1	10.6	17.3	1767
CA-10-157A	28.167	85.3632	2610	5 - 7	3.67	1.995	54.346	0.71	-1.19	3.8	5.3	10.7	13.9	2564
CA-10-158A	28.1502	85.3543	1900	0 - 3	9.49	4.426	46.634	0.81	-0.57	4.8	6.2	14.9	17	2564
CA-10-158B	28.1502	85.3543	1900	10 - 20	6.57	5.248	79.881	0.79	-0.66	4.8	6.1	14.9	16.4	2564
CA-10-158C	28.1502	85.3543	1900	40	0.39	0.014	3.625	0.85	-0.94	4.3	5.7	14.9	18	2564
CA-10-158D	28.1502	85.3543	1900	80 - 85	0.24	0.005	2.084	0.71	-1.12	4.3	5.4	14.9	13.8	2564
MO-52A	28.2995	84.636	3610	10 - 20	2.77	0.594	21.454	0.59	-1.2	3.8	5.2	4.9	10	3575
MO-52B	28.2995	84.636	3610	20 - 30	1.66	0.453	27.333	0.55	-1.22	3.9	5.2	4.9	8.6	3575
MO-87A	28.1592	84.6508	1750	10 - 20	1.23	0.14	11.461	0.92	-1.32	4.1	5.1	15.8	20.3	2584
MO-87B	28.1592	84.6508	1750	20 - 30	0.89	0.063	7.094	0.9	-1.15	4.1	5.3	15.8	19.8	2584

[1]Estimated MAT with data from the HMG (1995) and Putkonen (2004).

[2]Data from NASA's GIOVANNI

Table S3: *Data of river suspended sediment samples*

River sediment samples

Sample	Location	River	Date	Sample type[1]	Lat [°N]	Long [°E]	Elevation [m asl]	TOC [%]	brGDGTs [µg/g sediment]	brGDGTs [µg/g TOC]	MBT'_{5Me}	CBT'	Calculated pH	MAT_{GDGT} [°C]	Mean catchment elev. [m asl]	Mean soil-covered catchment elev. [m asl][2]	Mean catchment elev. with NDVI > 0.08 [m asl][3]
NEQ-16-d	Narayanghat	Narayani	02.07.-15.07.2016	dis.	27.7255	84.4277	200	-	0.031	-	0.745	-0.359	6.6	14.9	3008	2314	2475
NEQ-D-NA1603	Narayanghat	Narayani	02.07.-15.07.2016	int.	27.7255	84.4277	200	0.28	0.039	13.975	0.715	-0.407	6.5	13.9	3008	2314	2475
NEQ-D-NA1604	Narayanghat	Narayani	16.07.-29.07.2016	int.	27.7255	84.4277	200	0.2	0.018	9.305	0.764	-0.392	6.5	15.3	3008	2314	2475
NEQ-D-NA1704	Narayanghat	Narayani	04.07.-11.07.2017	int.	27.7255	84.4277	200	0.35	0.006	1.808	0.739	-0.487	6.4	14.7	3008	2314	2475
NEQ-D-NA1707	Narayanghat	Narayani	15.08.-28.08.2017	int.	27.7255	84.4277	200	0.26	0.008	3.045	0.754	-0.577	6.2	15.1	3008	2314	2475
NEQ-D-NA1707-dup	Narayanghat	Narayani	15.08.-28.08.2017	int.	27.7255	84.4277	200	0.26	0.004	1.402	0.754	-0.574	6.2	15.2	3008	2314	2475
NEQ-172-13	Narayanghat	Narayani	29.06.2017	dis.	27.7255	84.4277	200	0.64	0.061	9.423	0.827	-0.566	6.2	17.5	3008	2314	2475
NEQ-172-29	Narayanghat	Trisuli	30.06.2017	dis.	27.7419	84.4288	200	0.36	0.069	18.869	0.824	-0.363	6.6	17.3	3161	2361	2506
NEQ-172-25	Narayanghat	Khali Gandaki	30.06.2017	dis.	27.7546	84.4196	200	0.51	0.135	26.663	0.767	-0.359	6.6	15.5	2753	1988	2184
NEQ-172-35	Ramdi	Khali Gandaki	01.07.2017	dis.	27.902	83.6322	380	0.37	0.049	13.375	0.76	-0.341	6.6	15.3	3111	2299	2475
NEQ-D-MA1612	Besisahar	Marshiangdy	26.06.-09.07.2016	int.	28.2313	84.3838	700	0.25	0.013	5.184	0.639	-0.189	6.9	11.5	4422	3473	3847
NEQ-D-MA1713	Besisahar	Marshiangdy	07.07.-21.07.2017	int.	28.2313	84.3838	700	0.22	0.001	0.249	0.533	-0.069	7	8.2	4422	3473	3847
NEQ-D-MA1714	Besisahar	Marshiangdy	22.07-05.08.2017	int.	28.2313	84.3838	700	0.22	0.008	3.523	0.578	0.002	7.2	9.6	4422	3473	3847
NEQ-D-TR1632	Devighat	Trisuli	02.07.-15.07.2016	int.	27.8059	85.0081	400	0.2	0.023	11.396	0.578	-0.576	6.2	9.6	3815	3101	3368
NEQ-D-TR1729	Devighat	Trisuli	02.07.-15.07.2017	int.	27.8059	85.0018	400	0.18	0.002	1.23	0.53	-0.381	6.5	8.1	3815	3101	3368
NEQ-172-51	Devighat	Trisuli	03.07.2017	dis.	27.8059	85.0081	400	0.4	0.038	9.527	0.582	-0.499	6.4	9.7	3815	3101	3368
NEQ-D-BK1519	Barabise	Bhote Khosi	09.07.-23.07.2015	int.	27.7968	85.8961	890	0.37	0.026	7.104	0.632	-0.376	6.6	11.3	4482	4135	4034
NEQ-D-BK1737	Barabise	Bhote Khosi	01.07.-16.07.2017	int.	27.7968	85.8961	890	0.34	0.003	0.801	0.572	-0.361	6.6	9.4	4482	4135	4034
NEQ-D-BK1739	Barabise	Bhote Khosi	01.08.-15.08.2017	int.	27.7968	85.8961	890	0.28	0.032	11.389	0.551	-0.188	6.9	8.8	4482	4135	4034
NEQ-D-KH1525	Chatara	Khosi	06.07.-20.07.2015	int.	26.8561	87.1508	130	0.25	0.059	23.739	0.71	-0.647	6.1	13.7	3860	3558	3525
NEQ-D-KH1746	Chatara	Khosi	01.08.-15.08.2017	int.	26.8561	87.1508	130	0.26	0.072	27.59	0.71	-0.397	6.5	13.8	3860	3558	3525
NEQ-D-KH1747	Chatara	Khosi	16.08.-31.08.2017	int.	26.8561	87.1508	130	0.25	0.006	2.396	0.671	-0.425	6.5	12.5	3860	3558	3525
NEQ-D-MA1621	Chame	Marshiangdy	26.06.-09.07.2016	int.	28.5523	84.2407	2660	0.21	0.003	1.659	0.346	0.33	7.7	2.3	4898	4236	4499
NEQ-D-MA1622	Chame	Marshiangdy	09.07.-22.07.2016	int.	28.5523	84.2407	2660	0.17	0.004	2.066	0.334	0.197	7.5	1.9	4898	4236	4499
NEQ-D-MA1722	Chame	Marshiangdy	07.07.-22.07.2017	int.	28.5523	84.2407	2660	0.16	0.002	1.481	0.401	0.393	7.8	4.1	4898	4236	4499
NEQ-D-MA1724	Chame	Marshiangdy	06.08.-21.08.2017	int.	28.5523	84.2407	2660	0.2	0.002	1.143	0.365	0.31	7.6	2.9	4898	4236	4499
NEQ-172-39	Waling	Dadi Khola	01.07.2017	dis.	27.9858	83.7657	720	-	0.171	-	0.833	-0.44	6.5	17.6	1233	1233	-
NEQ-172-01	Manahari	Manahari Khola	28.06.2017	dis.	27.54	84.81	150	0.73	0.164	22.417	0.836	-0.212	6.8	17.7	1151	1151	-

[1] Sample types: dis. = discrete filtered suspended sediment sample; int. = integrated suspended sediment sample over two weeks.

[2]Calculated with land-cover maps from Uddin et al. (2015) and Jun et al. (2014).

[3]NDVI data from Didan (2015).

4

Structural diversity of petrogenic organic carbon exported in a trans-Himalayan river

Lena Märki[1], Matthieu E. Galvez[1], Maarten Lupker[1], Jérôme Lavé[2], Ananta P. Gajurel[3], Negar Haghipour[1,4], Timothy Eglinton[1]

[1] Geological Institute, ETH Zürich, Switzerland
[2] CRPG, CNRS – Université de Lorraine, France
[3] Department of Geology, Tribhuvan University, Nepal
[4] Ion Beam Physics, ETH Zürich, Switzerland

Abstract

The oxidation of rock-derived, or petrogenic, organic carbon (OC_{petro}), is an essential component of the global carbon cycle. An important part of this oxidation likely happens during floodplain transit of OC_{petro} entrained in riverine sediments. The molecular structure of the OC_{petro} material plays a key role in determining its oxidation rates. However, the structural composition of OC_{petro} in fluvial sediments and its fate during riverine transport remain largely unknown. Here, we characterize the structural diversity of OC_{petro} in suspended sediments of a trans-Himalayan river with Raman spectroscopy. Our results reveal that riverine sediments of the Central Himalaya export a large diversity of OC_{petro} material, ranging from relatively low-grade carbonaceous material to highly graphitic grains. We show that the upstream region, where the mildly metamorphosed metasediments of the Tethyan Sedimentary Sequence, outcrops, is the main source of OC_{petro} in the Marshyandi-Narayani river system. The wide diversity of OC_{petro} material exported in a trans-Himalayan river further highlights the importance of a systematic study of OC_{petro} for constraining its fate during riverine transport.

Introduction

The oxidative weathering of rock-derived, or petrogenic organic carbon (OC_{petro}), transfers carbon from the Earth's crust to Earth's surface reservoirs, including the biosphere, the atmosphere and the ocean and thus influences global climate on geological timescales (Berner, 1989; Hilton *et al.*, 2014; Petsch, 2014; Galvez *et al.*, 2020). It has been estimated that on timescales $>10^5$ years the oxidation of OC_{petro} releases 40-100 Mt C/year globally (Petsch, 2014). This carbon flux opposes the net CO_2 sinks associated with export and burial of biospheric OC (OC_{bio}, soil or plant debris-derived OC) and silicate weathering coupled to carbonate precipitation (Berner and Canfield, 1989).

Through erosion, OC_{petro} gets entrained in riverine sediments and exported to the ocean (Sackett *et al.*, 1974) where it is buried in marine sediments. An important fraction of the exported OC_{petro}, however, does not reach the ocean, as it gets lost to oxidation during transit. While the carbon flux associated with OC_{petro} weathering has been estimated in various mountain ranges (Hilton *et al.*, 2014; Horan *et al.*, 2019; Hilton and West, 2020), little is known about the processes controlling OC_{petro} oxidation. The oxidation of rock-derived OC can take place through abiotic or biotic weathering in the bedrock and in soils (Petsch *et al.*, 2000, 2001; Hemingway *et al.*, 2018). Another part of the oxidation probably happens during the transit of OC_{petro} in river sediments through large floodplains (Galy *et al.*, 2008; Bouchez *et al.*, 2010). Flume experiences suggest minimal OC loss during fluvial transport itself (Scheingross *et al.*, 2019) implying that the OC_{petro} oxidation is likely to occur during temporary sediment storage in floodplains and valley fills.

The efficiency of riverine OC_{petro} export probably depends on multiple factors. Climatic and geomorphic settings, such as the glacial coverage of a mountain range or the transfer distance between sediment source and sink, have been suggested to play an important role in the OC_{petro} oxidation rates (Hilton *et al.*,

2011; Horan *et al.*, 2017; Hemingway *et al.*, 2018). Similarly, OC_{petro} oxidation rates have been shown to be more important in mountain ranges with high runoff and erosion rates, which suggests a link between physical erosion and OC_{petro} oxidation (Hilton *et al.*, 2014). In addition, mineral protection during riverine transport or sediment storage could prevent OC_{petro} grains from oxidation (Blattmann *et al.*, 2019; Hemingway *et al.*, 2019). A largely unexplored factor is the inherent structural and reactive diversity of the OC_{petro} material that plays a crucial role for the oxidation rate (Galvez *et al.*, 2020).

The pool of OC_{petro} is heterogeneous, displaying materials with a large chemical and structural diversity, as well as multiple abiotic and biogenic sources. Those materials range from highly reactive light hydrocarbons and bitumen (Vandenbroucke and Largeau, 2007; Galvez *et al.*, 2020) to recalcitrant graphite (Galvez *et al.*, 2020). The degree of structural ordering, or graphitization, of the OC_{petro} increases with the peak metamorphic temperature reached by the rock. This process renders the OC_{petro} more resilient to oxidative weathering (Galvez *et al.*, 2020). Galy *et al.* (2008) suggested that the proportion of low-temperature OC_{petro} relative to graphitic material decreases during transport through the Gangetic floodplain. The authors estimated that only around 30-50% of the exported OC_{petro} by Himalayan rivers is buried in the Bay of Bengal due to oxidation of the less graphitic material. In the Amazon basin the OC_{petro} oxidation rate in fluvial sediments has been suggested to be even higher, which may be linked to the high abundance of low-grade metamorphic rocks in the catchment area (Bouchez *et al.*, 2010). Although the above mentioned studies are lacking statistically robust analysis, they reveal a relationship between the OC_{petro} oxidation and the degree of structural ordering of the material (Galy *et al.*, 2008; Bouchez *et al.*, 2014).

While the oxidation of refractory low-grade metamorphic OC_{petro} constitutes an important carbon source to the Earth's surface, the process of graphitization can stabilize OC in the Earth's crust at time-scales of $>10^6$ years (Galvez *et al.*, 2020; Sparkes *et al.*, 2020). As such, graphitic OC_{petro} in river sediments of Taiwan has been shown to persist through at least three cycles of uplift and erosion (Sparkes *et al.*, 2020). The process of graphitization with progressive metamorphism contributes therefore to reduce the intrinsic reactivity of OC_{petro} and stabilize it in the Earth's crust (Galvez *et al.*, 2020).

When referring to riverine OC_{petro} export and its potential impact on the carbon cycle, it is thus essential to define the degree of graphitization of the exported OC_{petro} material. While the differentiation between OC_{bio} and OC_{petro} in suspended sediments with radiocarbon measurements has been applied to various regions (e.g., Galy *et al.*, 2008), the OC_{petro} is rarely further characterized (Nibourel *et al.*, 2015; Sparkes *et al.*, 2020). In this study, we aim to characterize the OC_{petro} and its structural diversity in suspended sediments of a trans-Himalayan river with Raman spectroscopy. A set of bedrock samples are measured to define the upstream source region additionally to the downstream lithologies that have been characterized by Beyssac *et al.* (2004). We define the concentration of OC_{petro} in riverine sediments with radiocarbon and OC concentration measurements and identify its main source regions.

The Central Himalaya

With its high erosion rates (Gabet *et al.*, 2008) and its important proportion of metasedimentary lithologies, the Central Himalaya provides an ideal environment for relatively high OC_{petro} oxidation rates. Here, we study suspended sediments from three sampling stations along the Marshyandi-Narayani river system. The Narayani River drains around a third of the Nepalese Himalayan area and is an important confluent of the Ganga (Figure 1). It discharges around 100 Mt of sediments and around 138 kt of OC_{petro} annually to the Gangetic floodplain (Andermann *et al.,* 2012; Märki *et al.* (submitted)). The Ganga transits through an extensive floodplain before delivering its sediments to the Bay of Bengal which is characterized by high OC burial rates (Galy *et al.*, 2007).

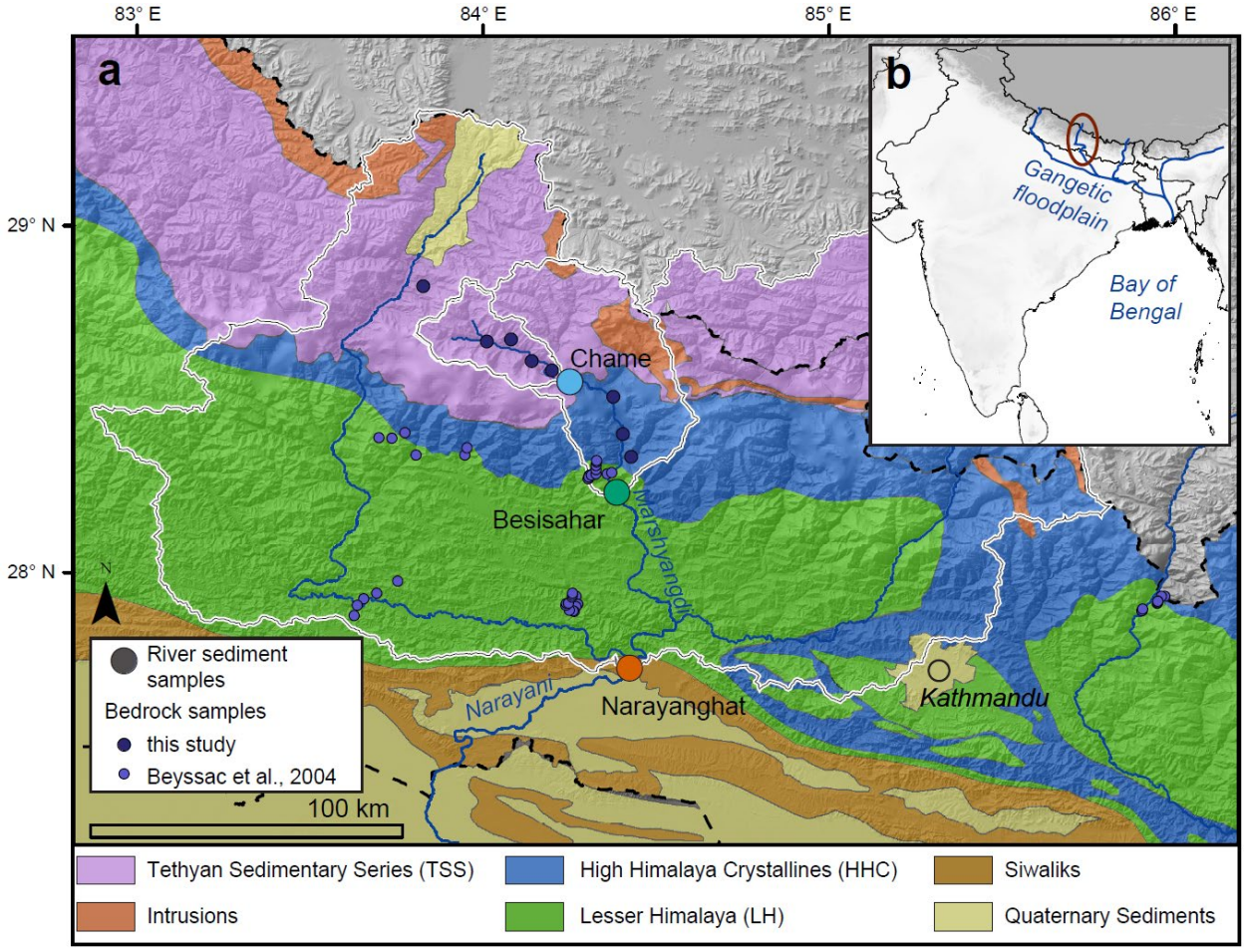

Figure 1: a*.Tectonic map of the Central Himalaya. Sampling stations and their respective catchment areas are illustrated. Locations of bedrock sampling of this study and of Beyssac et al. (2004) are shown. Dashed line indicates the national borders.* ***b.*** *Overview of the study area.*

In its Himalayan segment, the Narayani River crosses four major tectonic units which are from north to south (Figure 1): The Tethyan Sedimentary Series (TSS) represent a sequenece of metasediments from the Cambrian to Eocene evolution of the Neo-Tethys ocean (Le Fort, 1975; Garzanti, 1999). The low to middle metamorphic grade of the TSS increases structurally downwards which corresponds to an around north-south gradient (e.g., Le Fort, 1975; Schneider & Masch, 1993). The Total Organic Carbon (TOC) concentration in the heterogeneous sequence of the TSS varies in a large range between 0.09 and 2.03% (Aucour *et al.*, 2006; Menges *et al.*, 2020). The TSS are underlain by the High Himalayan Crystalline (HHC) sequence. The latter consists of Precambrian metasediments and orthogneiss that underwent high-grade metamorphism (Molnar, 1984). The HHC displays an inverted metamorphic gradient and is locally cut by leucogranitic intrusions (Le Fort, 1975; Molnar, 1984). The TOC content in the HHC is very low (~0.04%) (France-Lanord and Derry, 1997; Aucour *et al.*, 2006; Menges *et al.*, 2020). The tectonic unit of the Lesser Himalaya (LH) to the south of the HHC is composed of Precambrian metasedimentary and igneous rocks displaying mid-to low-grade metamorphism (Molnar, 1984). The metamorphic peak temperatures in the LH have among other techniques been defined by Raman spectroscopy and are decreasing structurally downwards (Beyssac *et al.*, 2004). Black shales outcropping in the LH have high TOC contents (7-11 %) but are relatively sparse (Aucour *et al.*, 2006). The mean TOC concentration in the LH has been estimated to < 0.18% (Aucour *et al.*, 2006). To the south, the Siwaliks form the Central Himalayan foothills and are composed of molassic sediments from the erosion of the Himalaya (Le Fort, 1975; Molnar, 1984).

Methods

Sampling

Suspended sediment samples were collected at the three stations in Chame, Besisahar and Narayanghat, along the Marshyandi-Narayani river system in the Nepalese Himalaya (Figure 1). For sampling, 3L of surface water was collected daily from the middle of the river during the four months of monsoon seasons (June-September) in the years 2015-2017. The sampled river water was stored in a barrel. After two weeks the settled-down sediment was collected by a tap at the bottom of the barrel and air-dried. The sediments were stored in a dark and cool place. They were frozen and freeze-dried upon arrival at ETH Zurich. 10 sediment samples were prepared for Raman spectroscopy and radiocarbon analysis (Table 1). Table 2 displays the location of the 8 bedrock samples from the TSS and the HHC in Central Nepal.

Suspended sediments

location	sampling date	lat (°N)	long (°E)	TOC (%)	fraction modern
Chame	09.07. - 22.07.2016	28.5524	84.2408	0.17	0.23
Chame	22.06. - 07.07.2017	28.5524	84.2408	-	-
Chame	06.08. - 21.08.2017	28.5524	84.2408	-	-
Besisahar	31.05. - 14.06.2015	28.2377	84.3806	0.38	0.17
Besisahar	15.06. - 29.06.2015	28.2377	84.3806	0.27	0.43
Besisahar	22.07. - 05.08.2017	28.2377	84.3806	0.22	0.30
Narayanghat	30.05 - 14.06.2015	27.7255	84.4277	0.51	0.48
Narayanghat	15.06 - 30.06.2015	27.7255	84.4277	0.61	0.77
Narayanghat	28.08 - 10.09.2015	27.7255	84.4277	0.25	0.73
Narayanghat	01.08. - 14.08.2017	27.7255	84.4277	-	-

location	$\delta^{13}C$ (‰)	OC_{petro} (%)	OC_{petro} error (%)	OC_{bio} (%)	OC_{bio} error (%)
Chame	-21.83	0.13	0.01	0.07	0.01
Chame	-	-	-	-	-
Chame	-	-	-	-	-
Besisahar	-25.25	0.31	0.01	0.06	0.01
Besisahar	-25.8	0.15	0.01	0.12	0.01
Besisahar	-22.76	0.15	0.01	0.07	0.01
Narayanghat	-24.25	0.27	0.02	0.24	0.02
Narayanghat	-24.8	0.14	0.03	0.47	0.03
Narayanghat	-27.3	0.07	0.01	0.18	0.01
Narayanghat	-	-	-	-	-

Table 1: *Suspended sediment samples, measured TOC, $\delta^{13}C$ and fraction modern (radiocarbon isotopic composition) and calculated OC_{petro} and OC_{bio} concentrations with their respective errors from the applied mixing model.*

Raman spectroscopy

Raman Spectroscopy on Carbonaceous Material (RSCM) is a useful tool for defining the structural ordering and thus peak metamorphic temperatures (Beyssac *et al.*, 2002a). The degree of graphitization of carbonaceous material increases irreversibly with temperature until 650 °C where graphite reaches its final structural ordering (Beyssac *et al.*, 2002a). RSCM on detrital material has been used to trace the provenance of OC_{petro} in riverine and marine sediments (Nibourel *et al.*, 2015; Sparkes *et al.*, 2018, 2020). Weathering of OC_{petro} has been shown not to affect the temperature calibration of RSCM (Chazhengina and Kovalevski, 2017).

Bedrock samples

sample	geological unit	lat (°N)	long (°E)	age (Myr)[1]	rock type
MK-R-30	TSS	28.819	83.834	145-100	schist
UM-18-24	TSS	28.670	84.004	360-300	black schist
UM-18-15	TSS	28.667	84.084	360	marly schist
UM-18-12	TSS	28.611	84.151	480-440	marly schist
UM-18-4	TSS	28.576	84.187	540-485	marble
MK-R-19	HHC	-	-	-	gneiss
MK-R-15	HHC	-	-	-	gneiss
MK-R-13	HHC	-	-	-	gneiss

sample	nr of RSCM analaysis	mean R2	mean T_{R2} (°C)	standard deviation (°C)
MK-R-30	15	0.59	378	9
UM-18-24	17	0.58	381	9
UM-18-15	4	0.52	411	9
UM-18-12	15	0.36	481	50
UM-18-4	12	0.50 [2]	432 [2]	76
MK-R-19	-		-	-
MK-R-15	-		-	-
MK-R-13	-		-	-

[1] estimated from the stratigraphic map of Parsons et al. (2015)
[2] sample is going to be remeasured

Table 2: *Locations of bedrock samples from the TSS (Tethyan Sedimentary Series) and the HHC (High Himalayan Crystalline), corresponding ages are estimated from the stratigraphic map of Parsons et al. (2014) and results of RSCM.*

An aliquot of the dried sediment samples was milled in a zirconium ball mill. The milling has been shown to not affect the Raman spectra of OC_{petro} (Sparkes *et al.*, 2013). A modified protocol after (Beyssac *et al.*, 2002b) was followed for concentrating the OC in the sediment samples. Briefly, HCl (36%) was added to the samples for removal of inorganic carbon. The samples were subsequently centrifuged four times and the supernatant was pipetted out between each run. The sediments were then left in HF (48%) on a hotplate (80 °C) during three days for dissolution of the silicate phases. After pipetting out the supernatant the samples were first rinsed with HCl and then with water. They were centrifuged four times before being dried on a hotplate.

Raman spectra were obtained using a DILOR LabRam spectrometer coupled to an Olympus BX 40 microscope at ETH Zurich. HCl-HF dissolved sediment samples were distributed on a glass slice for analysis. The OC_{petro} in the rock samples was characterized using polished thin sections of the bedrock samples. Before each session, the Raman spectrometer was calibrated with a silicone standard. A filter with an attenuation factor of 10^{-1} was applied to the green 532 nm laser (0.26 mW on the sample) to avoid the

destruction of the OC_{petro}. The acquisition time was set to 30 s for 5 times for each spectrum. The Raman shift was measured in the range between 1000 and 2000 cm^{-1}. 50 spectra were obtained in each sediment sample, and around 10 points in each thin section in which carbonaceous material was found. The spectra were manually fitted using the software PeakFit 3.0 and the bands of the spectra were computed. The R2 ratio (ratio of areas of different bands defined in the Raman spectra) was calculated as described in Beyssac *et al.* (2002a) and the respective band areas were used to compute a structural parameter (R2) that varies in inverse proportion to the structural order of the material. The R2 ratio is inversely proportional to the structural ordering, such that low R2 ratios characterize carbonaceous material with great crystalline ordering. We converted the R2 ratio to an apparent metamorphic peak temperature (T_{R2}) using the linear calibration of Beyssac *et al.* (2002a) (T_{R2} [°C] = -445 * R2 + 641). This conversion of the R2 ratio to the metamorphic peak temperature, however, presumes knowledge about the metamorphic conditions and the host rock. Technically, this calibration is applicable in a temperature range of around 330 – 650 °C, for OC of biological origin subjected to slow, regional metamorphism, and its typical uncertainty is ± 50 °C (Beyssac *et al.*, 2004). The translation of R2 to temperature may be perturbed if it is applied in regions flushed by metamorphic fluids, as in shear zones, and should therefore be used with caution (Galvez *et al.*, 2013). As the OC_{petro} in river sediments come from a wide range of bedrock material of which we do not have exact information about their metamorphic history, we use the R2 ratio for characterizing the riverine OC_{petro}. Figure 2 shows examples of obtained OC_{petro} spectra from sediments in Narayanghat, R2 ratios and corresponding apparent T_{R2}.

Radiocarbon and Total Organic Carbon content measurements

For determination of the Total Organic Carbon (TOC) content and the isotopic signatures of the bulk suspended sediments, ~50 mg of the milled samples were weighed into combusted silver capsules. Samples were fumigated in HCl vapor for removal of inorganic carbon (3 days at 60 °C), and neutralized with NaOH (4 days at 60 °C). The capsules were subsequently wrapped in tin boats and TOC and its isotopic compositions were measured on a coupled online EA-IRMS-AMS system (McIntyre *et al.*, 2017) at the Ion Beam Physics Institute of the ETH Zurich. $^{13}C/^{12}C$ ratios are reported in $\delta^{13}C$ notation relative to the Vienna Pee Dee Belemnite (VPDB) standard and the ^{14}C content is reported as fraction modern (Fm). For the typical error on the measurements and in addition to routine standards (McIntyre *et al.*, 2017), a river sediment sample was used as internal standard and measured 7 times in different batches as described in Märki et al. (submitted).

We used a binary mixing model to distinguish the petrogenic and biospheric OC fractions of the sediments based on TOC concentration and radiocarbon signature as described in Märki et al. (submitted). For the model, a modern biospheric and a petrogenic end-member with known TOC and radiocarbon signatures were used and a Monte Carlo simulation ($n=10^5$) sampled randomly within the end-member composition and the errors of the measurement (Märki et al. (submitted)). The surface sediment samples are taken as

representative of the whole water column as in large and turbulent Himalayan rivers hydrodynamic sorting of OC has been shown to be minor (Menges et al., 2020; Märki et al. (submitted)).

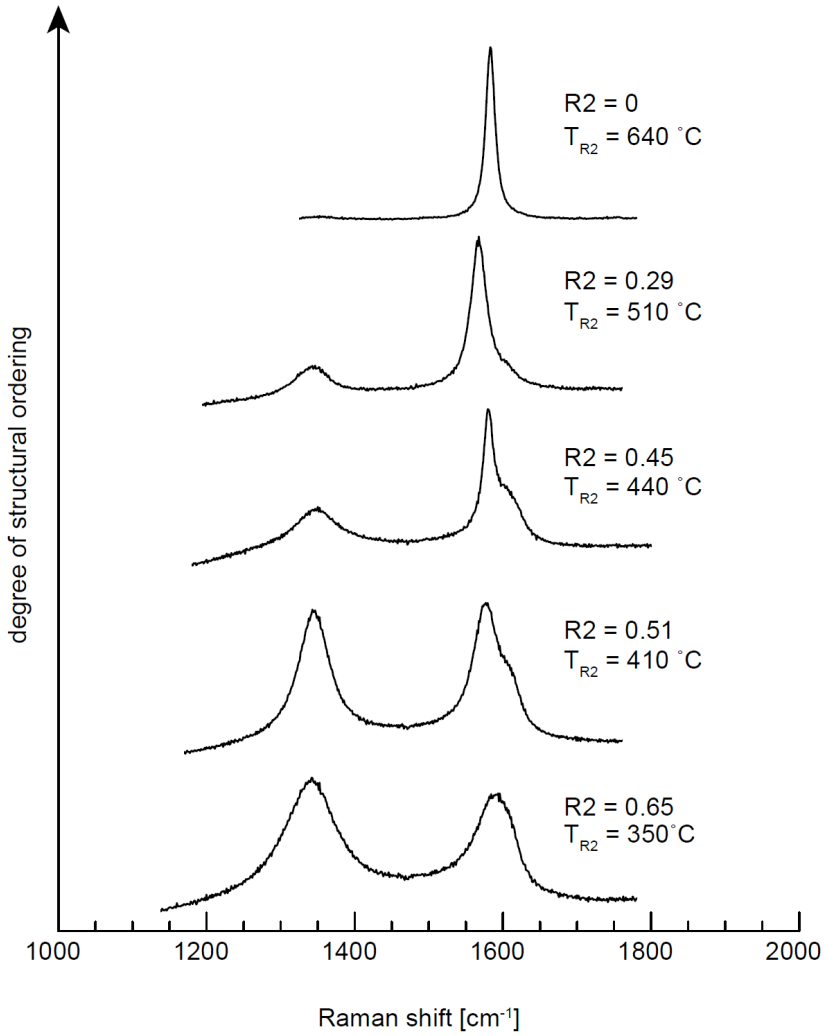

Figure 2: *Diversity of Raman spectra of OC_{petro} in riverine sediment samples from Narayanghat. The R2 ratio and corresponding metamorphic peak temperature (T_{R2}) obtained by Raman spectroscopy (RSCM) are indicated for each spectra.*

Results

The R2 ratio of the three samples at the upstream station in Chame vary in a narrow range between 0.42 and 0.66 with a mean of 0.58. The R2 of OC_{petro} displays a relatively low variability between the three samples of this station (Figure 3a). River sediments from Besisahar, around 50 km downstream of Chame, contain OC_{petro} with slightly lower R2 (0 – 0.65) with a mean of 0.52. Especially one sample includes OC_{petro}

with lower R2 ratios (and thus higher crystalline ordering) (Figure 3a). This particular sample therefore displays a higher standard deviation of R2. A greater variability in sediments of Besisahar has been observed compared to samples from the upstream station in Chame (Figure 3b). The downstream sampling station in Narayanghat contains OC_{petro} with R2 ratios ranging from 0 – 0.73 with a mean of 0.47. We observe a large diversity of the degree of structural ordering of OC_{petro} in sediment samples from Narayanghat (Figures 2 and 3).

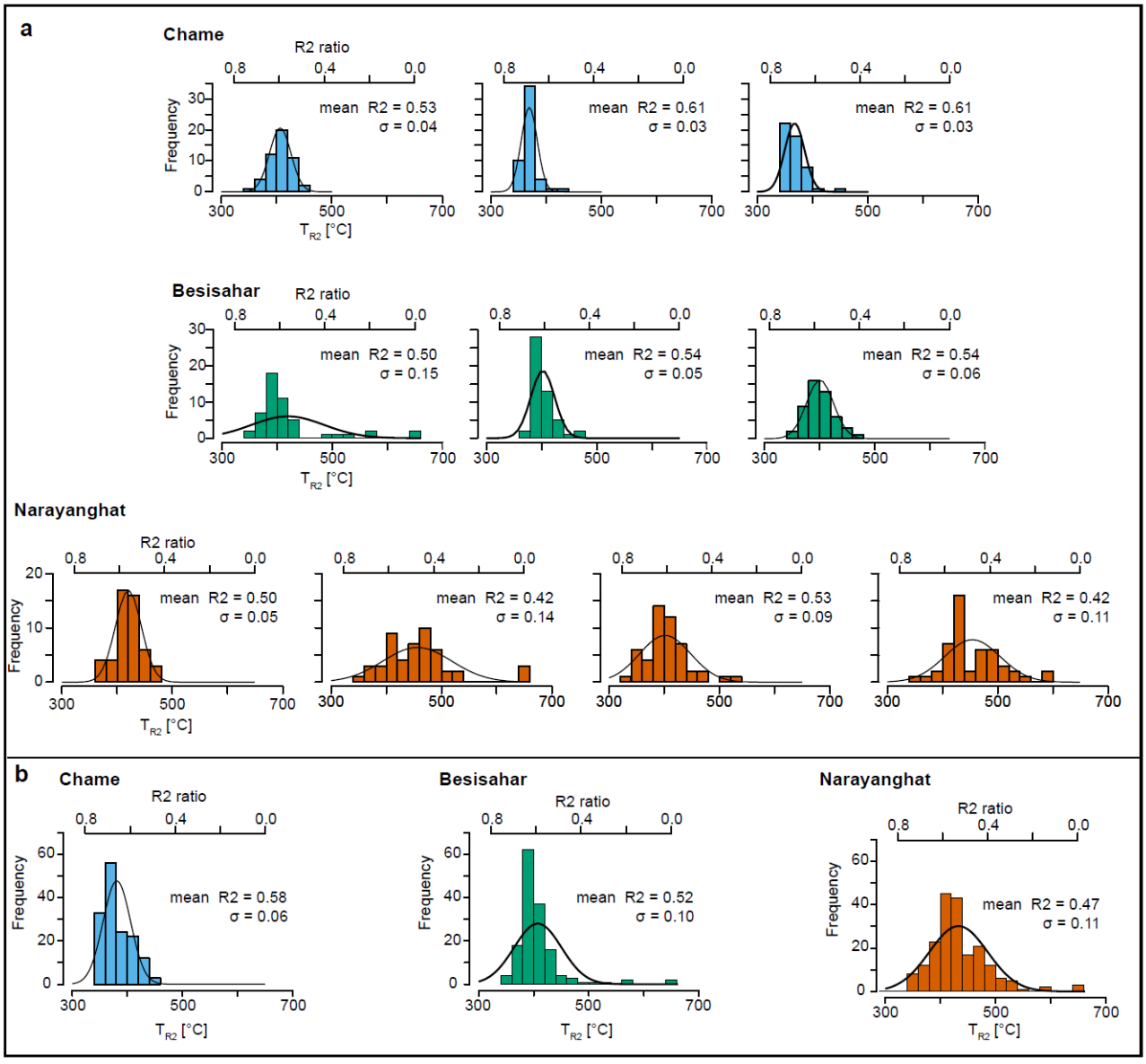

Figure 3: a. *Histograms of R2 ratios and corresponding temperatures (T_{R2}) of the OC_{petro} in ten sediment samples measured with RSCM. The mean R2 and the standard deviation (σ) for each sample are indicates. Black lines represent the best fit of a normal distribution.* ***b.*** *Mean R2 and T_{R2} values of the three sampling stations.*

Bulk suspended sediments contain between 0.17 and 0.61% of TOC with an average radiocarbon signature of Fm 0.44 (Table 2). A general trend of increasing TOC concentrations and fraction modern is visible from up-to downstream (Figure 4). The results of the mixing model suggest that in Chame and in Besisahar 77% and 52-87% respectively of the TOC is of petrogenic origin whereas in Narayanghat the proportion of OC_{petro} in the TOC lies between 23-52%.

The R2 ratios and corresponding temperatures of OC_{petro} grains in thin sections of the TSS are reported in Table 2. The errors on the T_{R2} correspond to the standard deviation of the temperature of the different grains within one sample. For comparison with metamorphic temperatures obtained from petrological studies in the same area, the results are shown in temperatures calculated from the R2 ratio. The temperatures estimated by Raman spectroscopy of the TSS lie between 378-481 °C and show a clear gradient with increasing temperatures towards the south (structurally downwards). The gneiss samples from the HHC do not contain any identifiable OC_{petro} and no estimation of the metamorphic peak temperatures could be made for these samples.

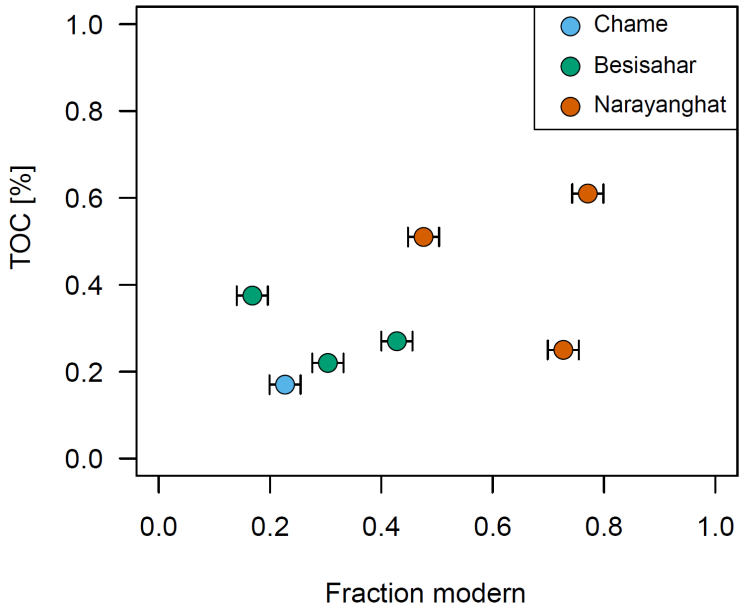

Figure 4: *Radiocarbon signatures (fraction modern) of bulk riverine sediment samples plotted against their total organic carbon (TOC) concentration. Typical errors of the fraction modern are shown; errors of the TOC measurements are smaller than symbol size.*

Discussion

Metamorphic gradient in the Tethyan Sedimentary Sequence determined by RSCM

Figure 5 shows a geological map of the TSS in the Central Himalaya (Parsons *et al.*, 2015) with the T_{R2} calculated in this study and peak metamorphic temperatures inferred by carbonate solvus thermometry

by Schneider and Masch (1993). Taking into account the typical error of ± 50 °C, the temperatures estimated by RSCM are consistent with the previously reported metamorphic gradient in the TSS displaying increasing temperatures structurally downwards (e.g., Le Fort, 1975; Schneider and Masch, 1993). The general metamorphic gradient can be slightly disturbed by folding linked to the uplift in this region. For a more detailed study about the metamorphic history of the TSS by RSCM, a larger number of bedrock samples would be needed which is out of the scope of this study. One sample shows significantly lower temperatures (in red on Figure 5), which can be attributed to the Raman measurement on the mineral surface in a thin section. Through polishing the Raman signal of OC_{petro} can get altered, and therefore RSCM should be performed in a OC_{petro} grain. This sample is going to be measured carefully a second time.

Metamorphic temperatures obtained by Raman spectroscopy on bedrock samples from the TSS confirm that multiple formations contain an important amount of OC_{petro} which can potentially be found in river sediments draining this geological unit. As expected from previous studies, the metamorphic temperatures of the TSS (378-530 °C (Schneider and Masch, 1993; this study)) are in a similar range as temperatures in the LH (330-560 °C (Beyssac *et al.*, 2004)) which makes the source tracing of OC_{petro} in trans-Himalayan river sediments on the basis of RSCM challenging.

Samples from the HHC contain no OC_{petro}, that could be found by visually Raman. This is consistent with previous TOC analysis (France-Lanord and Derry, 1997; Aucour *et al.*, 2006; Menges *et al.*, 2020). Therefore, we expect a minor contribution of OC_{petro} from the HHC in the river sediments of the Marshyandi-Narayani river system.

RSCM signal of OC_{petro} in Himalayan river sediments

OC_{petro} exported in river sediments of the Central Himalaya covers a wide range of degrees of structural ordering ranging from highly graphitized grains (R2=0; T_{R2} ca. 640 °C) to relatively disordered material (R2=0.73; T_{R2} ca. 300 °C) (Figure 2 and 3). Despite this variability and the different lithologies outcropping between the sampling stations, the average R2 signal shows only modest variations from up- to downstream. This suggests that the OC_{petro} composition of a river sediment not only depends on the metamorphic grade of the upstream bedrock, but also on other factors such as TOC concentrations of the different lithologies as well as local erosion rates as it has been shown in sediments of the Southern Alps (Nibourel *et al.*, 2015). The R2 variability generally increases proportionally with the catchment area reflecting the larger diversity of bedrocks in the drainage basin (Figure 2b).

While the R2 variability changes between stations, the average is relatively stable and reflects minor temporal variability in the source of OC_{petro} of the samples integrating a two week-period. Our sampling strategy is therefore adequate to smooth out daily variabilities in riverine OC_{petro} export. The large diversity of R2 ratios within one sample highlights the importance of a high number of RSCM analysis on suspended sediments of large rivers in order to display the whole range of structural ordering.

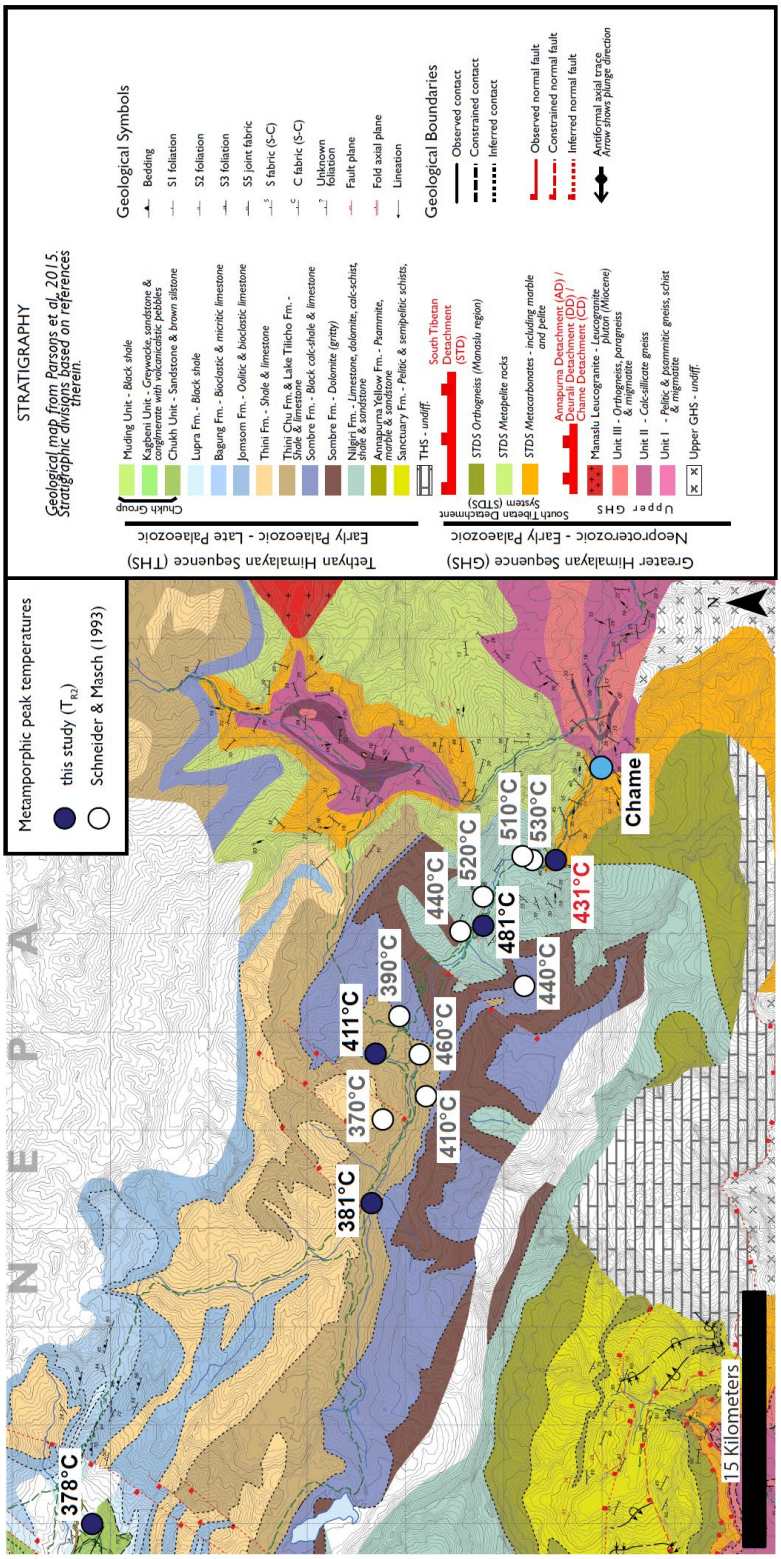

Figure 5: *Geological map of the Chame region from Parsons et al. (2015). Bedrock samples and their calculated T_{R2} are indicated in dark blue; white symbols and corresponding metamorphic temperatures are from Schneider and Masch (1993). The sample in red is going to be measured a second time.*

OC_{petro} concentrations in suspended sediments

While the TOC content increases with the catchment size (Figure 4), the concentration of OC_{petro} in the suspended sediments does not show any significant evolution from up- to downstream (Figure 6). The suspended sediment of the Narayani River therefore likely gets loaded with biospheric OC between Chame and Narayanghat while the addition of OC_{petro} is minor. These results support the findings of Menges et al. (2020) who proposed that the biospheric OC loading in a trans-Himalayan river increases during its transit through the High Himalayas.

The OC_{petro} content of the river sediments shows a weak correlation to the mean value of the R2 ratio of a sample (r^2= 0.38) (Figure 6). This correlation suggests a relatively high-concentration OC_{petro} source of mildly graphitized material (i.e. high R2 ratios), and a source of highly ordered OC_{petro} (i.e. low R2 ratios) with lower concentrations. The latter seems mainly important for the OC_{petro} of sediments from the downstream sampling station in Narayanghat. The erosion and riverine export of OC_{petro} in the Central Himalaya can, however, not be explained by a binary mixing given the large range of R2 in each sample and the relatively weak correlation between mean R2 values and the OC_{petro} concentration. The total OC_{petro} concentration in suspended sediments of the Marshyandi-Narayani river system is thus controlled by the OC_{petro} input of various source regions. This complexity of riverine OC_{petro} export is expected in a system with a large variety of lithologies and locally varying erosion rates (Garzanti *et al.*, 2007; Gabet *et al.*, 2008; Struck *et al.*, 2015).

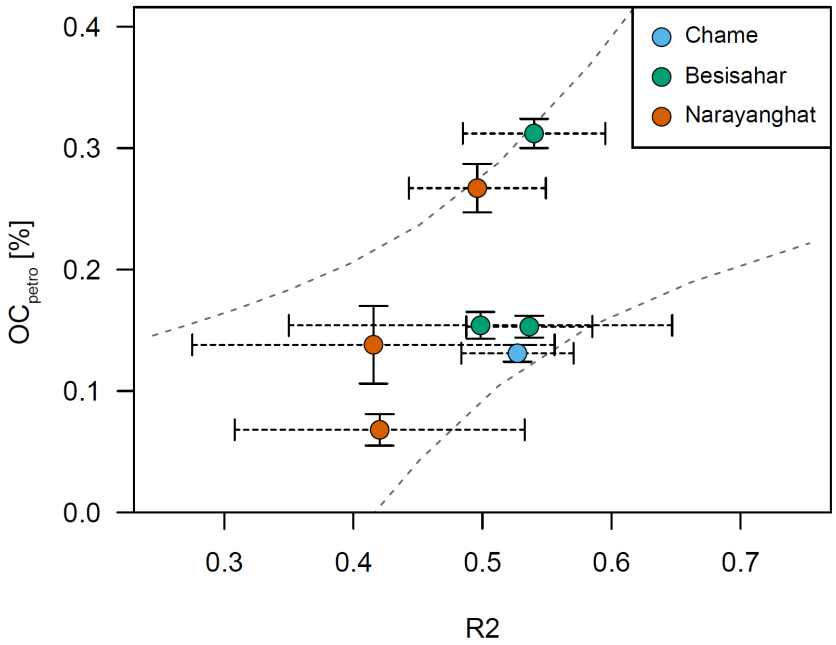

Figure 6: *Mean R2 values in riverine sediments plotted against the concentration of OC_{petro} in a sample. Vertical error bars show the error of the mixing model, which was used to deduce OC_{petro} concentrations from the total organic carbon content. Horizontal error bars show the range of the R2 ratio measured in a sample. Grey dashed lines illustrate the 0.68 confidence interval of the linear regression between the mean R2 and the OC_{petro} concentrations (r^2= 0.38).*

The source of OC_{petro} in a trans-Himalayan river

As mentioned above, in the Central Himalaya the TSS and the LH low- to mid-grade metamorphic rocks are found structurally below and above high-grade HHC formations (e.g., Le Fort, 1975; Kohn, 2014), which makes the sediment source tracing with RSCM challenging. The temperatures between 350-500 °C that are present in all of the samples, can be found in both the TSS and the LH units. Combining OC_{petro} concentrations and RSCM signals of the Marshyandi-Narayani river, we can however get some information about the main source region of the OC_{petro} in this trans-Himalayan river.

We can take the structural diversity of the OC_{petro} in sediments from the upstream sampling station as representative of the TSS as this is the only tectonic unit drained in Chame (Figures 1 and 7). We observe that the R2 ratio of OC_{petro} in sediments from Chame does not fall below 0.4 (Figure 7) which is characteristic for low- to mid-grade metamorphic rocks. Compared to Chame, we notice a slight decrease of the mean R2 ratio in sediments from the sampling station in Besisahar and one sample with some OC_{petro} grains of clearly higher metamorphic temperatures (Figures 3 and 7). This suggests that the OC_{petro} in Besisahar mainly derives from the same source as in Chame, with a minor input of OC_{petro} of higher structural ordering. While the distribution of RSCM signals is wider in sediments from Narayanghat, the mean R2 ratio is only slightly lower than in samples from upstream stations (Figure 3). Around 23% of the OC_{petro} in Narayanghat seems to derive from a source region with higher metamorphic temperatures than found in Chame (Figure 7).

These observations suggest that the main OC_{petro} input of low-to mid-grade metamorphic bedrock does not significantly change from up-to downstream. We therefore propose that the TSS provides the major part of OC_{petro} exported in sediments of the Marshyandi-Narayani river system. The minor input of OC_{petro} from the HHC can be explained by the low TOC concentrations in this geological unit (France-Lanord and Derry, 1997; Aucour *et al.*, 2006; Menges *et al.*, 2020). This input from a source with OC_{petro} of higher structural ordering and lower TOC concentrations could also be responsible for the correlation between the OC_{petro} content and the mean R2 (Figure 6). A minor OC_{petro} contribution from the Lesser Himalaya could be attributed to thick soil covers and shallow landsliding in this region, which mobilize a limited amount of bedrock material (Menges *et al.*, 2020). The contribution of the Siwaliks to the OC_{petro} in the suspended sediments in Narayanghat cannot be defined here. The Siwaliks hills are composed of Himalayan sediments and they can therefore contain OC_{petro} in the whole variability present in the Himalayan bedrocks. However, the Siwaliks probably play a minor role in the total OC_{petro} content of samples from the Narayani, as the river drains only a small part of the Siwaliks before Narayanghat.

We observe a minor decrease of OC_{petro} concentrations from up-to downstream (Figure 6). On the contrary, the sediment input from the HHC segment to the Marshyandi River between Chame and Narayanghat is important due to important landsliding rates in this region (Morin *et al.*, 2018; Marc *et al.*, 2019; Menges *et al.*, 2020). Therefore, a constant supply of OC_{petro} is required to maintain OC_{petro} concentration, and avoid dilution by low OC_{petro} concentrations of the HHC. One possibility is that this

supply of OC_{petro} is provided by the abrasion of bedload material during transport that would release OC_{petro} to the sediment suspended load.

The provenance of OC_{petro} in riverine sediments from Narayanghat can also be estimated with erosion rates data of the three main tectonic units and their relative area in the catchment. We use erosion rates estimated within the Narayani catchment (TSS: ca. 1 mm/yr; HHC: ca. 3.5 mm/yr; LH: ca. 1.6 mm/yr) (Garzanti *et al.*, 2007; Gabet *et al.*, 2008; Struck *et al.*, 2015) and mean TOC concentrations for each unit (TSS: ca. 1%; HHC: ca. 0.04%; LH: ca. 0.15%) (France-Lanord and Derry, 1997; Aucour *et al.*, 2006; Menges *et al.*, 2020). We find that ca. 80% of the OC_{petro} in Narayanghat derives from the TSS units; around 20% from the LH and <1% from the HHC. These results are similar to our estimates from RSCM and radiocarbon measurements. The use of two independent methods thus shows that RSCM on riverine sediments combined with TOC and radiocarbon measurements can be employed to semi-quantitatively trace the source region of OC_{petro}.

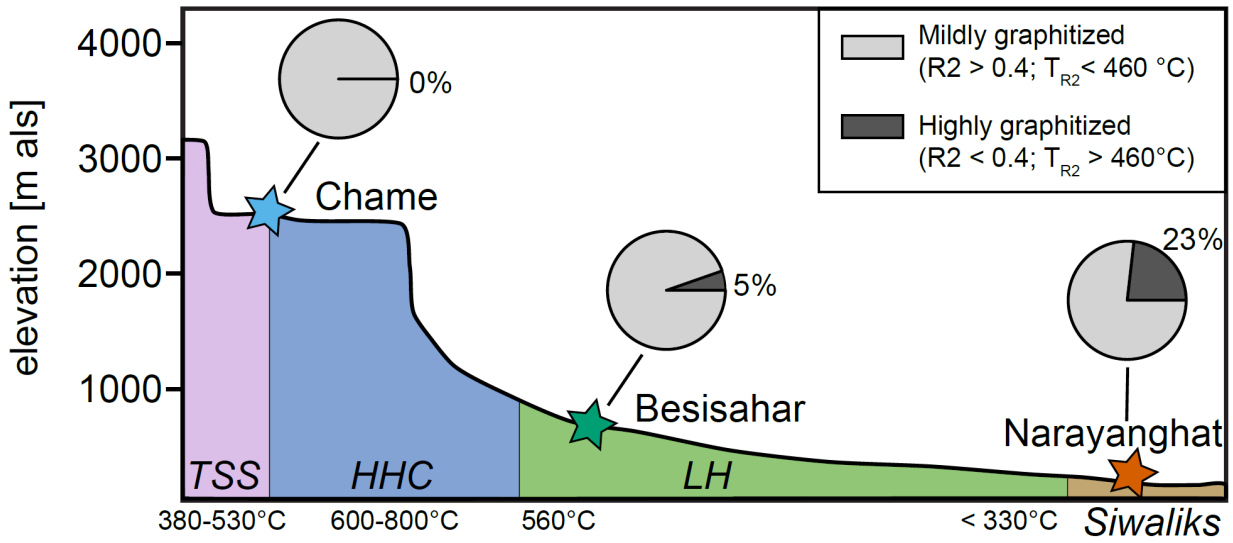

Figure 7: *Elevation profile of the Marshyandi-Narayani river system. The geological units of the bedrock illustrated by colors and their peak metamorphic temperatures are shown at the bottom (Beyssac et al., 2004; Kohn, 2014; Schneider and Masch, 1993; this study). The mean proportion of mildly (R2>0.4) and highly (R2<0.4) graphitized OC_{petro} is illustrated in a pie diagram for each sampling station. The mean proportion of highly graphitized OC_{petro} in the three to four samples per station is indicated.*

Implications for the carbon budget of the Central Himalaya

Due to relatively stable RSCM signals and OC_{petro} concentrations between the different sampling stations, we propose that oxidation of OC_{petro} during riverine transport in the Marshyandi-Narayani river system is negligible. This is supported by short transit times of suspended sediments through the Himalaya (Morin *et al.*, 2018) and by the erosive and turbulent nature of the trans-Himalayan river. Most of the OC_{petro}

oxidation in the Central Himalaya thus likely happens on hillslopes, while another important part of the total OC_{petro} oxidation is thought to happen in the floodplain of the Ganga (Galy *et al.*, 2008). The fate of OC_{petro} during the Gangetic floodplain transit is thus crucial for its role in the carbon cycle.

Galy *et al.* (2008) showed that the ranges of OC_{petro} graphitization in sediments of the Ganga and the Bay of Bengal are substantially narrower than in river sediments in at the Himalayan outlet. While high-grade metamorphic OC_{petro} particles can be traced until the Bay of Bengal, the structurally less ordered OC_{petro} is probably lost to oxidation in the Gangetic floodplain (Galy *et al.*, 2008). The latter study is, however, mostly based qualitative data analysis. A comparison between the Raman spectra from Galy et al. (2008) and the R2 calibration employed in our study (Beyssac *et al.*, 2002a) (Figure 2), shows that only OC_{petro} with ca. R2< 0.4 was found in marine sediments of the Bay of Bengal. With this value as a guideline, we classify the OC_{petro} of the Marshyandi-Narayani river system in mildly graphitized (R2> 0.4; 350-460 °C) and highly graphitized (R2< 0.4; >460 °C) groups, adopting a classification scheme similar to Sparkes et al. (2020) (Figure 7). We assume that the highly graphitized OC_{petro} is transported to the Bay of Bengal and buried in marine sediments without any significant loss as suggested by Galy *et al.* (2008) in the Ganga and by Sparkes *et al.* (2020) in Taiwan. On the other hand, an important part of the mildly graphitized OC_{petro} is expected to be lost to oxidation during floodplain transit. Figure 7 shows that for the carbon source through OC_{petro} oxidation in Himalayan sediments, the TSS plays a major role. While the TSS unit is the main source of the total OC_{petro} in suspended sediments of the Marshyandi-Narayani river system, it is also the main contributor to the carbon flux through OC_{petro} oxidation in Gangetic sediments as it provides low- to mid-grade OC_{petro} material to the sediments. In contrast, the OC_{petro} of the high-grade rocks in the HHC has the potential to survive multiple erosion and uplift cycles as found in Taiwan (Sparkes *et al.*, 2020).

Outlook: Systematic study of RSCM in riverine sediments of the Ganga

For a more detailed understanding and a more precise quantification of the OC_{petro} oxidation in riverine sediments, this RSCM study is going to be extended to sediments of the Ganga. The latter transits for several 1000 km through the Gangetic floodplain where low flow velocities and high sediment loads favor the intermittent sediment storage. Sediment transfer times through the Gangetic floodplain have been estimated to range in the order of 20 to several 100 kyr (Granet *et al.*, 2010), which contrasts to the sediment transit through the Central Himalaya in a few days (Morin *et al.*, 2018). Temporal storage is generally thought to be a major driver of chemical weathering of sediments and OC oxidation (e.g., Lupker *et al.*, 2012; Torres *et al.*, 2017). Himalayan rivers are the main sediment suppliers of the Ganga river which makes it possible to study the evolution of Himalayan sediments during floodplain transit (Lupker *et al.*, 2011). Galy *et al.* (2008) proposed that most of the low-to mid-grade Himalayan OC_{petro} gets oxidized in the Gangetic floodplain. With a systematic RSCM study of OC_{petro} in Gangetic sediments and its comparison to the signature of Himalayan rivers, this hypothesis of Galy *et al.* (2008) based on the qualitative analysis of a small number of Raman spectra could be verified in a semi-quantitative way. This

study would help to quantify the fraction of OC_{petro} that is oxidized during the transit through the Gangetic floodplain and would therefore give insights on its impact on the net carbon budget of the Central Himalayan erosion.

Further, the study of OC_{petro} in cores from marine sediments of the Bay of Bengal with RSCM could give insights about variations of OC_{petro} oxidation rates on time scales of glacial-interglacial cycles and/or the Neogene. While chemical weathering rates and OC_{bio} export fluxes have been shown to fluctuate on timescales of 10 kyr (Lupker *et al.*, 2013; Hein *et al.*, 2017), it has recently been suggested that erosion rates in the Himalaya stayed relatively constant on timescales of the late Cenozoic (Lenard *et al.*, 2020). A study about the fluctuations of OC_{petro} oxidation rates, would fill an important gap for reconstructing interactions between the erosion rates and carbon fluxes.

Conclusions

In this study, we show that the well-described metamorphic gradient in the Tethyan Sedimentary Series can be traced with RSCM technique. Furthermore, Raman spectroscopy on riverine sediments reveals a great diversity of structural OC_{petro} types in suspended sediments of a trans-Himalayan river.

While the variability of OC_{petro} material in the studied river system increases from up-to downstream, the mean structural ordering stays relatively constant. With RSCM data and OC_{petro} concentrations, we show that the TSS units are the main source area of OC_{petro} in riverine sediments from the Marshyandi-Narayani river system. This suggests that the structural diversity of OC_{petro} in suspended sediments is not only controlled by oxidation rates, but also by other factors such as local erosion rates, TOC concentrations in the bedrock, and replenishment along the stream. The large variability of OC_{petro} material also highlights the importance of a systematic and statistically robust investigation of OC_{petro} in sediments of the Ganga to examine the fate of OC_{petro} during transit of the Gangetic floodplain and to further investigate how the molecular structure of OC_{petro} controls its oxidation rates.

References

Andermann, C., Crave, A., Gloaguen, R. & Davy, P. (2012). Connecting source and transport : Suspended sediments in the Nepal Himalayas. *Earth and Planetary Science Letters* **352**, 158–170.

Aucour, A.-M., France-Lanord, C., Pedoja, K., Pierson-Wickmann, A.-C. & Sheppard, S. M. F. (2006). Fluxes and sources of particulate organic carbon in the Ganga-Brahmaputra river system. *Global Biogeochemical Cycles* **20**, 1–12.

Berner, R. A. (1989). Biogeochemical cycles of carbon and sulfur and their effect on atmospheric oxygen over Phanerozoic time. *Palaeogeography, Palaeoclimatology, Palaeoecology* **75**, 97–122.

Berner, R. A. & Canfield, D. E. (1989). A new model for atmospheric oxygen over Phanerozoic time. *American Journal of Science*, 333–361.

Beyssac, O., Bollinger, L., Avouac, J. P. & Goffé, B. (2004). Thermal metamorphism in the lesser Himalaya of Nepal determined from Raman spectroscopy of carbonaceous material. *Earth and Planetary Science Letters* **225**, 233–241.

Beyssac, O., Goffe, B., Chopin, C. & Rouzaud, J. N. (2002a). Raman spectra of carbonaceous material in metasediments: a new geothermometer. *Journal of Metamorphic Geology* **20**, 859–871.

Beyssac, O., Rouzaud, J.-N., Goffé, B., Brunet, F. & Chopin, C. (2002b). Graphitization in a high-pressure , low-temperature metamorphic gradient: a Raman microspectroscopy and HRTEM study. *Contrib. Mineral. Petrol* 19–31.

Blattmann, T. M., Liu, Z., Zhang, Y., Zhao, Y., Haghipour, N., Montluçon, D. B., Plötze, M. & Eglinton, T. I. (2019). Mineralogical control on the fate of continentally derived organic matter in the ocean. *Science* **366**, 742–745.

Bouchez, J., Beyssac, O., Galy, V., Gaillardet, J., France-Lanord, C., Maurice, L. & Moreira-Turcq, P. (2010). Oxidation of petrogenic organic carbon in the Amazon floodplain as a source of atmospheric CO2. *Geology* **38**, 255–258.

Bouchez, J., Galy, V., Hilton, R. G., Gaillardet, J., Moreira-Turcq, P., Perez, M. A., France-Lanord, C. & Maurice, L. (2014). Source , transport and fluxes of Amazon River particulate organic carbon : Insights from river sediment depth-profiles. *Geochimica et Cosmochimica Acta* **133**, 280–298.

Chazhengina, S. Y. & Kovalevski, V. V (2017). Raman spectroscopy of weathered shungites. *Journal of Raman Spectroscopy* 1590–1596.

France-Lanord, C. & Derry, L. A. (1997). Organic carbon burial forcing of the carbon cycle from Himalayan erosion. *Nature* **390**, 65–67.

Gabet, E. J., Burbank, D. W., Pratt-Sitaula, B., Putkonen, J. & Bookhagen, B. (2008). Modern erosion rates in the High Himalayas of Nepal. *Earth and Planetary Science Letters* **267**, 482–494.

Galvez, M. E., Beyssac, O., Martinez, I., Benzerara, K., Chaduteau, C., Malvoisin, B. & Malavieille, J. (2013). Graphite formation by carbonate reduction during subduction. *Nature Geoscience*. Nature Publishing Group **6**, 473–477.

Galvez, M. E., Fischer, W. W., Jaccard, S. L. & Eglinton, T. I. (2020). Materials and pathways of the organic carbon cycle through time. *Nature Geoscience*. Springer US **13**, 535–546.

Galy, V., Beyssac, O., France-Lanord, C. & Eglinton, T. (2008). Recycling of graphite during Himalayan erosion: a geological stabilization of carbon in the crust. *Science* **322**, 943–945.

Galy, V., France-Lanord, C., Beyssac, O., Faure, P., Kudrass, H. & Palhol, F. (2007). Efficient organic carbon burial in the Bengal fan sustained by the Himalayan erosional system. *Natural Hazards and Earth System Science* 407–

411.

Garzanti, E. (1999). Stratigraphy and sedimentary history of the Nepal Tethys Himalaya passive margin. *Journal of Asian Earth Sciences* **17**, 805–827.

Garzanti, E., Vezzoli, G., Andò, S., Lavé, J., Attal, M., France-Lanord, C. & DeCelles, P. (2007). Quantifying sand provenance and erosion (Marsyandi River, Nepal Himalaya). *Earth and Planetary Science Letters* **258**, 500–515.

Granet, M., Chabaux, F., Stille, P., Dosseto, A., France-lanord, C. & Blaes, E. (2010). U-series disequilibria in suspended river sediments and implication for sediment transfer time in alluvial plains : The case of the Himalayan rivers. *Geochimica et Cosmochimica Acta*. Elsevier Ltd **74**, 2851–2865.

Hein, C. J., Galy, V., Galy, A., France-Lanord, C., Kudrass, H. & Schwenk, T. (2017). Post-glacial climate forcing of surface processes in the Ganges – Brahmaputra river basin and implications for carbon sequestration. *Earth and Planetary Science Letters*. Elsevier B.V. **478**, 89–101.

Hemingway, J. D., Hilton, R. G., Hovius, N., Eglinton, T. I., Haghipour, N., Wacker, L., Chen, M. & Galy, V. V (2018). Microbial oxidation of lithospheric organic carbon in rapidly eroding tropical mountain soils. *Science* **360**, 209–212.

Hemingway, J. D., Rothman, D. H., Grant, K. E., Rosengard, S. Z., Eglinton, T. I., Derry, L. A. & Galy, V. V. (2019). Mineral protection regulates long-term global preservation of natural organic carbon. *Nature*. Springer US **570**, 228–231.

Hilton, R. G., Gaillardet, J., Calmels, D. & Birck, J. L. (2014). Geological respiration of a mountain belt revealed by the trace element rhenium. *Earth and Planetary Science Letters*. Elsevier B.V. **403**, 27–36.

Hilton, R. G., Galy, A., Hovius, N., Horng, M. J. & Chen, H. (2011). Efficient transport of fossil organic carbon to the ocean by steep mountain rivers: An orogenic carbon sequestration mechanism. *Geology* **39**, 71–74.

Hilton, R. G. & West, A. J. (2020). Mountains, erosion and the carbon cycle. *Nature Reviews Earth & Environment*. Springer US **1**, 284–299.

Horan, K. *et al.* (2019). Carbon dioxide emissions by rock organic carbon oxidation and the net geochemical carbon budget of the Mackenzie River Basin. *American Journal of Science* **319**, 473–499.

Horan, K., Hilton, R. G., Selby, D., Ottley, C. J., Gröcke, D. R., Hicks, M. & Burton, K. W. (2017). Mountain glaciation drives rapid oxidation of rock-bound organic carbon. *Science Advances* **3**, 1–9.

Kohn, M. J. (2014). *Himalayan metamorphism and its tectonic implications*. *Annual Review of Earth and Planetary Sciences*.

Le Fort, P. (1975). Himalayas: the collided range. Present knowledge of the continental arc. *American Journal of Science*, 1–44.

Lenard, S. J. P., Lavé, J., France-Lanord, C., Aumaître, G., Bourlès, D. L. & Keddadouche, K. (2020). Steady erosion rates in the Himalayas through late Cenozoic climatic changes. *Nature Geoscience*. Springer US **13**, 448–452.

Lupker, M. *et al.* (2012). Predominant floodplain over mountain weathering of Himalayan sediments (Ganga basin). *Geochimica et Cosmochimica Acta* **84**, 410–432.

Lupker, M., France-Lanord, C., Galy, V., Lavé, J. & Kudrass, H. (2013). Increasing chemical weathering in the Himalayan system since the Last Glacial Maximum. *Earth and Planetary Science Letters* **365**, 243–252.

Lupker, M., France-Lanord, C., Lavé, J., Bouchez, J., Galy, V., Métivier, F., Gaillardet, J., Lartiges, B. & Mugnier, J. L. (2011). A Rouse-based method to integrate the chemical composition of river sediments: Application to the Ganga basin. *Journal of Geophysical Research: Earth Surface* **116**, 1–24.

Marc, O., Behling, R., Andermann, C., Turowski, J. M., Illien, L., Roessner, S. & Hovius, N. (2019). Long-term erosion of the Nepal Himalayas by bedrock landsliding: The role of monsoons, earthquakes and giant landslides. *Earth Surface Dynamics* **7**, 107–128.

McIntyre, C. P., Wacker, L., Haghipour, N., Blattmann, T. M., Fahrni, S., Usman, M., Eglinton, T. I. & Synal, H.-A. (2017). Online 13C and 14C Gas Measurements by EA-IRMS–AMS at ETH Zürich. *Radiocarbon* **59**, 893–903.

Menges, J., Hovius, N., Andermann, C., Lupker, M., Haghipour, N., Märki, L. & Sachse, D. (2020). Variations in organic carbon sourcing along a trans-Himalayan river determined by a Bayesian mixing approach. *Geochimica et Cosmochimica Acta* **286**, 159–176.

Molnar, P. (1984). STRUCTURE AND TECTONICS OF THE HIMALAYA : Constraints and Implications of Geophysical Data. *Annual Review of Earth and Planetary Sciences* 489–518.

Morin, G. P., Lavé, J., France-Lanord, C., Rigaudier, T., Gajurel, A. P. & Sinha, R. (2018). Annual Sediment Transport Dynamics in the Narayani Basin, Central Nepal: Assessing the Impacts of Erosion Processes in the Annual Sediment Budget. *Journal of Geophysical Research: Earth Surface* **123**, 2341–2376.

Nibourel, L., Herman, F., Cox, S. C., Beyssac, O. & Lavé, J. (2015). Provenance analysis using Raman spectroscopy of carbonaceous material: A case study in the Southern Alps of New Zealand. *Journal of Geophysical Research: Earth Surface* **120**, 2056–2079.

Parsons, A. J., Law, R. D., Searle, M. P., Phillips, R. J. & Llyold, G. E. (2015). Geology of the Dhaulagiri-Annapurna-Manaslu Himalaya, Western Region. *Taylor & Francis*.

Petsch, S. T. (2014). Weathering of organic carbon. *Treatise on Geochemistry* **12**, 217–238.

Petsch, S. T., Berner, R. A. & Eglinton, T. I. (2000). A field study of the chemical weathering of ancient sedimentary organic matter. *Organic Geochemistry* **31**, 475–487.

Petsch, S. T., Eglinton, T. I. & Edwards, K. J. (2001). 14C-dead living biomass: Evidence for microbial assimilation of ancient organic carbon during shale weathering. *Science* **292**, 1127–1131.

Sackett, W. M., Poag, C. W. & Eadie, B. J. (1974). Kerogen recycling in the Ross Sea, Antarctica. *Science* **185**, 1045–1047.

Scheingross, J. S., Hovius, N., Dellinger, M., Hilton, R. G., Repasch, M., Sachse, D., Gröcke, D. R., Vieth-Hillebrand, A. & Turowski, J. M. (2019). Preservation of organic carbon during active fluvial transport and particle abrasion. *Geology* **47**, 958–962.

Schneider, C. & Masch, L. (1993). The metamorphism of the Tibetan Series from the Manang area, Marsyandi Valley, Central Nepal. *Geological Society Special Publication* **74**, 357–374.

Sparkes, R., Hovius, N., Galy, A. & Liu, J. T. (2020). Survival of graphitized petrogenic organic carbon through multiple erosional cycles. *Earth and Planetary Science Letters*. Elsevier B.V. **531**, 115992.

Sparkes, R., Hovius, N., Galy, A., Vasant Kumar, R. & Liud, J. T. (2013). Automated analysis of carbon in powdered geological and environmental samples by Raman spectroscopy. *Applied Spectroscopy* **67**, 779–788.

Sparkes, R., Maher, M., Blewett, J., Selver, A. O., Gustafsson, O., Semiletov, I. P. & Van Dongen, B. E. (2018). Carbonaceous material export from Siberian permafrost tracked across the Arctic Shelf using Raman spectroscopy. *Cryosphere* **12**, 3293–3309.

Struck, M., Andermann, C., Hovius, N., Korup, O., Turowski, J. M., Bista, R., Pandit, H. P. & Dahal, R. K. (2015). Monsoonal hillslope processes determine grain size-specific suspended sediment fluxes in a trans-Himalayan river. *Geophysical Research Letters* 2302–2308.

Torres, M. A., Limaye, A. B., Ganti, V., Lamb, M. P., Joshua West, A. & Fischer, W. W. (2017). Model predictions of

long-lived storage of organic carbon in river deposits. *Earth Surface Dynamics* **5**, 711–730.

Vandenbroucke, M. & Largeau, C. (2007). Kerogen origin , evolution and structure. *Organic Geochemistry* **38**, 719–833.

5

Chemical weathering pathways constrained by $DI^{14}C$, $DI^{13}C$ and $\delta^{34}S$ signatures in Central Himalayan river waters

Lena Märki[1], Maarten Lupker[1], Guillaume Paris[2], Negar Haghipour[1,3], Thomas Blattmann[4], Timothy Eglinton[1]

[1] Geological Institute, ETH Zürich, Switzerland
[2]CRPG, CNRS – Université de Lorraine, France
[3] Ion Beam Physics, ETH Zürich, Switzerland
[4]Biogeochemistry Research Center, JAMSTEC, Japan

Abstract

The partitioning of chemical weathering between the different weathered lithologies (carbonates, silicates or evaporites) and between the acids (H_2CO_3 and H_2SO_4) involved in the reaction, is crucial for understanding its effect on the carbon budget of the Earth's surface. Previous studies have shown that disentangling the chemical weathering pathways in the Central Himalaya remains challenging. Here, we test an inversion modeling approach using the cosmogenic and the stable isotopic composition of Dissolved Inorganic Carbon (DIC) and the stable sulfur isotopic compositions of dissolved sulfate together with major ion concentrations of 43 river water samples from the Nepalese Himalaya. This method gives a holistic view of chemical weathering processes in the Himalaya. We show that chemical weathering pathways are best constrained by the $DI^{14}C$ signature and the ion concentrations of river water. Our results suggest that the sulfuric acid-driven weathering of carbonates and silicates is a major weathering process in the Central Himalaya. We further observe an important lithological control on the proportion of weathering driven by sulfuric acid. The mean slope of a catchment, a first-order proxy for erosion rates, does not significantly influence the relative proportions of chemical weathering pathways in this system.

1. Introduction

The chemical disintegration of rocks at the Earth's surface exerts a key control on atmospheric CO_2 concentration over timescales of $>10^5$ years (Ebelmen, 1845; Walker *et al.*, 1981; Berner, 1989). Defining the impact of chemical weathering on the carbon cycle is, however, complicated by different weathering pathways influencing the carbon budget of the Earth's surface in opposing directions. Depending on the bedrock lithology and the acid involved in the reaction, chemical weathering acts as either a carbon source or carbon sink relative to Earth's surface carbon reservoirs (the atmosphere, biosphere, and oceans). The two major acids involved in chemical weathering (H_2CO_3 and H_2SO_4) in streams and on hillslopes originate from different sources. Carbonic acid is provided to rivers and groundwater through dissolution of atmospheric CO_2 and through microbial respiration of organic matter (e.g., Telmer and Veizer, 1999). Sulfuric acid, on the other hand, results from the dissolution of sulfide minerals, such as pyrite. The dissolution of silicate minerals by carbonic acid (Sil_{H2CO3}, reaction 1) coupled to carbonate precipitation in the oceans (reaction 5) constitutes a major carbon sink transferring carbon from the Earth's surface to the geological record (Walker *et al.*, 1981; Raymo and Ruddiman, 1992). On the contrary, carbonate weathering with carbonic acid ($Carb_{H2CO3}$, reaction 2) is neutralized through carbonate precipitation (reaction 5) and therefore does not affect the carbon budget of the Earth's surface on geological timescales. Similarly, the reaction of sulfuric acid with silicate minerals (Sil_{H2SO4}, reaction 3) does not involve carbon. Sulfuric acid-mediated weathering of carbonate minerals ($Carb_{H2SO4}$, reaction 4), however, releases CO_2 stored in the crust to the Earth's surface when coupled to carbonate precipitation (reaction 5) (Calmels *et al.*, 2007; Torres *et al.*, 2014, 2016). The weathering pathway of $Carb_{H2SO4}$ has only recently

been recognized to constitute an essential part of the global carbon cycle (Torres *et al.*, 2014; Burke *et al.*, 2018). The partitioning of the weathered lithology and the acid involved in the reaction is thus crucial for understanding the impact of chemical weathering on the carbon cycle.

$$CaSiO_3 + 2H_2CO_3 + H_2O \rightarrow Ca^{2+} + H_4SiO_4 + 2HCO_3^- \quad (1)$$

$$CaCO_3 + H_2CO_3 \rightarrow Ca^{2+} + 2HCO_3^- \quad (2)$$

$$CaSiO_3 + H_2SO_4 + H_2O \rightarrow Ca^{2+} + H_4SiO_4 + SO_4^{2-} \quad (3)$$

$$CaCO_3 + 0.5\ H_2SO_4 \rightarrow Ca^{2+} + HCO_3^- + 0.5\ SO_4^{2-} \quad (4)$$

$$Ca^{2+} + 2HCO_3^- \rightarrow CaCO_3 + CO_2 + H_2O \quad (5)$$

$$CaSO_4{\cdot}2H_2O \rightarrow Ca^{2+} + SO_4^{2-} + 2H_2O \quad (6)$$

Despite its importance for a complete understanding of the carbon cycle, the differentiation of chemical weathering pathways remains a challenging task. Weathering reactions are most commonly inferred from the dissolved ionic load and Sr isotopic compositions carried by rivers (e.g., Gaillardet *et al.*, 1999). This approach uses the elemental and Sr isotopic compositions of the endmember lithologies for defining their relative input to the total weathering budget. It, however, does not allow the distinction between the carbonic and the sulfuric acid involved in weathering reactions. Other studies have tried to account for this difference by using the dissolved $\delta^{13}C$ isotopic composition (e.g., Galy and France-Lanord, 1999). The quantification of sulfuric acid-mediated weathering rates is yet further complicated by the dissolution of evaporitic minerals (mainly gypsum and anhydrite). The latter reaction produces sulfate ions (reaction 6) which need to be distinguished from the sulfide-derived SO_4^{2-} as they do not imply any weathering reactions (Calmels *et al.*, 2007). Studies defining the relative proportions of weathered silicates and carbonates thus have to estimate the proportion of sulfide derived from evaporite dissolution (e.g., Galy and France-Lanord, 1999). $\delta^{34}S$ in combination with oxygen isotopes has been used as a tool for disentangling evaporitic and sulfide sources of dissolved sulfate (Karim and Veizer, 2000; Calmels *et al.*, 2007). Evaporites are enriched in ^{34}S (Longinelli and Edmond, 1983), while pyrite is generally characterized by a light sulfur isotopic signature. While the use of $\delta^{34}S$, dissolved ionic load and Sr isotopic compositions can be used to disentangle chemical weathering pathways in the Amazon (Torres *et al.*, 2016), the sulfur isotopic composition of dissolved sulfate in Himalayan rivers remains complicated to explain (Turchyn *et al.*, 2013; Hemingway *et al.*, 2019).

The pathways of chemical weathering and associated weathering rates are controlled by various factors such as bedrock lithology, runoff, climate and erosion rates, and can therefore vary locally (e.g., Galy and France-Lanord, 1999; Hartmann *et al.*, 2009; Larsen *et al.*, 2014; Torres *et al.*, 2016; West *et al.*, 2005). Chemical weathering rates are generally enhanced in highly erosive environments through the constant supply of fresh minerals prone to weathering (Gaillardet *et al.*, 1999; West, 2012). As such, fresh landslide scars favor chemical weathering through carbonic and sulfuric acid by exposing unweathered bedrock surfaces (Emberson *et al.*, 2016, 2018). The proportion of chemical weathering reactions taking place on exposed bedrock surfaces relative to weathering in soils increases in regions characterized by high denudation rates (West, 2012). The locus and reaction kinetics of chemical weathering are additionally controlled by intrinsic properties of the weathering agents. Sulfuric acid reacts readily after its formation and has therefore proposed to be mainly important in mountainous source regions with high denudation rates (Galy and France-Lanord, 1999; Torres *et al.*, 2016, 2017). On the other hand, carbonic acid weathering is slower and its relative importance thus increases with a longer residence time of sediments in the weathering zone (West, 2012; Torres *et al.*, 2016). Furthermore, bedrock lithology also influences the weathering kinetics, with carbonate minerals generally reacting faster than silicates (Tipper *et al.*, 2006a).

Since the proposition that silicate weathering in the Himalaya has substantially influenced the global climate over the past 40 Myrs (Raymo and Ruddiman, 1992), different studies have attempted to define the carbon fluxes associated with silicate weathering in this mountain range. Galy and France-Lanord (1999) proposed that chemical weathering fluxes of the Central Himalaya are dominated by carbonate dissolution and that dissolved sulfate in Himalayan rivers originates 70 – 100% from sulfide oxidation. Various studies have used different approaches to define chemical weathering pathways in the Himalaya through dissolved ion concentrations (e.g., Bhatt *et al.*, 2018; Bickle *et al.*, 2018; Dalai and Sarin, 2002; France-Lanord *et al.*, 2003; Kumar *et al.*, 2019; Tsering *et al.*, 2019; Wolff-Boenisch *et al.*, 2009), Sr isotopes (Jacobson *et al.*, 2002; Bickle *et al.*, 2005; Tipper *et al.*, 2006a) and other isotopic systems such as Ca and Mg isotopes (Tipper *et al.*, 2006b). The accuracy of chemical weathering estimates as well as the source of sulfate in Himalayan rivers, however, remain uncertain. Turchyn *et al.* (2013) used $\delta^{34}S$ and $\delta^{18}O$ of dissolved sulfate to disentangle inputs from evaporites and sulfide minerals in the Central Himalaya. They showed that dissolved $\delta^{34}S$ signature of trans-Himalayan rivers systematically increase downstream, while an important evaporitic input is not supported by major ion concentrations (Turchyn *et al.*, 2013; Hemingway *et al.*, 2020). This trend has been attributed to bacterial reduction of dissolved sulfate and subsequent secondary sulfide precipitation (Turchyn *et al.*, 2013; Hemingway *et al.*, 2020).

Recently, Blattmann *et al.* (2019) proposed a novel approach for defining chemical weathering pathways using the radiocarbon (^{14}C) signature of DIC coupled to major ion concentrations. DIC compromises all species of dissolved inorganic carbon (CO_2, CO_3^{2-}, HCO_3^- and H_2CO_3). Their relative abundance depends on the pH of a solution, but in the pH range of most natural rivers (pH 6.5-8) HCO_3^- is the most abundant species. The radiocarbon composition of DIC ($DI^{14}C$) is a useful tracer of the carbon source involved in

chemical weathering as each abovementioned reaction involves its unique signature (Raymond *et al.*, 2000; Marwick *et al.*, 2015; Blattmann *et al.*, 2019).

Here, we aim to test the application of $DI^{14}C$, $DI^{13}C$ ($\delta^{13}C$ of DIC) and $\delta^{34}S$ of dissolved sulfate to constrain the relative importance of weathered carbonate and silicate minerals as well as the proportion of carbonic and sulfuric acid involved in chemical weathering reactions across the Nepalese Himalaya. This approach allows a holistic view of chemical weathering processes in the Central Himalaya.

2. Study area and methods

2.1. Geology of the Central Himalaya

The Central Himalaya is characterized by four main tectonic units (Figure 1b). The Tethyan Sedimentary Series (TSS) in the northern part represents a sequence of Cambrian to Eocene metasediments ranging from limestones overlaying pelites to sandstones (Le Fort, 1975; Garzanti, 1999). The TSS are underlain by the High Himalayan Crystalline (HHC) sequence. The latter consists of Precambrian metasediments and orthogneiss that underwent high-grade metamorphism (Molnar, 1984). The HHC are locally cut by leucogranitic intrusions (Le Fort, 1975; France-Lanord and Le Fort, 1988). The tectonic unit of the Lesser Himalaya (LH) to the south of the HHC is composed of Precambrian metasedimentary and igneous rocks displaying mid-to low-grade metamorphism (Molnar, 1984). The Siwaliks, the foreland hills of the Central Himalaya, consist of mollassic sediments from the Himalayan erosion (Le Fort, 1975; Molnar, 1984).

2.2. Sampling and analytical methods

43 river water and 2 hot spring samples were collected in different field campaigns from 2015 to 2018 during the dry season and the monsoon (Table 1). The locations of the 28 rivers and the two hot springs sampled for this study are indicated on Figure 1. Water samples were directly passed through 0.2 µm PES filters. DIC samples were subsequently filled in poisoned ($HgCl_2$) 12 ml exetainer vials without headspace. Samples for $\delta^{34}S$ and major ion concentrations, were stored in acid-washed (HCl) 60 ml HDPE bottles.

For the measurement of the isotopic compositions of the DIC, water samples were purged with He and acidified with H_3PO_4 (85%). The $^{12}C/^{13}C$ ratio was measured on a gasbench connected to an IRMS (Breitenbach and Bernasconi, 2011) and results are reported as $\delta^{13}C$ (normalized to the Vienna Pee Dee Belemnite standard). The radiocarbon content was measured using an online AMS system (Wacker *et al.*, 2013). The radiocarbon signature is reported as fraction modern (Fm). The sulfur isotopic composition was measured on aliquots of non-acidified water samples by multicollector inductively coupled plasma mass spectrometry (MC-ICP-MS) at the CRPG Nancy (Paris *et al.*, 2013). Concentrations of major cations and anions were measured by ion chromatography at ETH Zürich. The concentration of DIC was determined by charge balance of the measured ions. With this conservative method we only consider the

DIC that is in equilibrium and therefore less prone to degas to the atmosphere (Galy and France-Lanord, 1999).

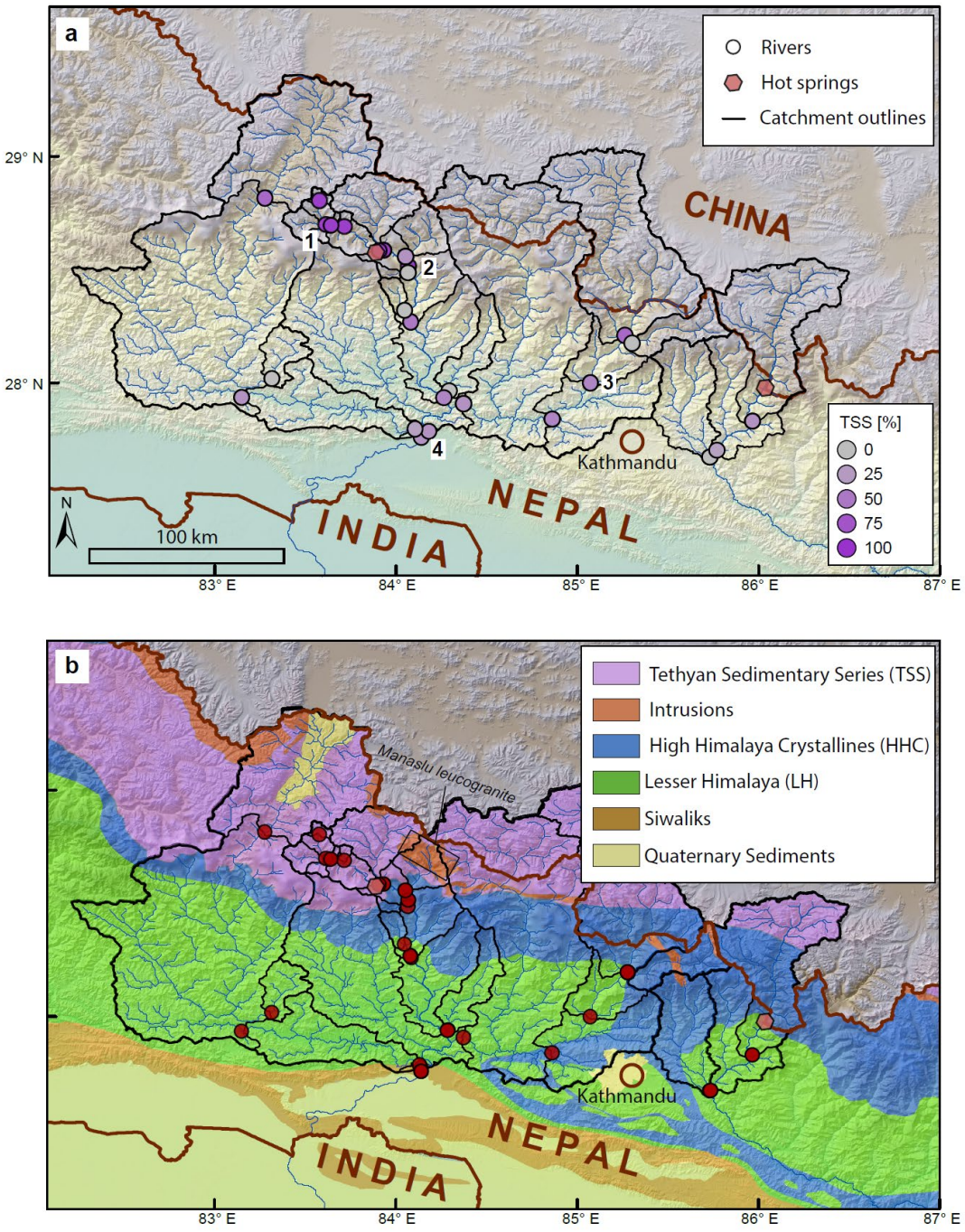

Figure 1: a. *Map of the Central Himalaya with river and hot spring sample locations. The river samples are colored in function of the proportion of Tethyan Sedimentary Series outcropping in their catchment. Numbers correspond to the following sampling locations: 1 – Manang, Marsyangy; 2 – tributary Marsyangdi; 3 – Devighat, Trisuli; 4 –Narayanghat, Narayani* ***b.*** *Tectonic map of the Central Himalaya with sampling locations. The location of the outcropping Manaslu leucogranite is schematically shown.*

Sample	River	Location	lat [°N]	long [°E]	Na [µmoles/L]	Ca [µmoles/L]	Mg [µmoles/L]	K [µmoles/L]	Cl [µmoles/L]
NEQ-17564	Marsyangdi	Thorung Phedi	28.775	83.975	181	1727	976	25	3
NEQ-18103	Marsyangdi	Manang	28.668	84.005	130	1056	748	48	25
NEQ-17551	Marsyangdi	Manang	28.664	84.021	164	1110	747	37	11
NEQ-17537	Marsyangdi	Chame	28.552	84.241	167	1064	707	41	34
NEQ-16223	Marsyangdi	Chame	28.552	84.241	139	719	558	40	40
NEQ-16213	Marsyangdi	Tal	28.484	84.37	206	778	380	58	168
NEQ-17522	Marsyangdi	Tal	28.484	84.37	249	954	425	46	192
NEQ-16234	Marsyangdi	Besisahar	28.238	84.381	252	707	293	63	232
NEQ-17512	Marsyangdi	Besisahar	28.238	84.38	328	780	312	101	378
NEQ-17245	Marsyangdi	Besisahar	28.231	84.384	123	601	163	47	100
NEQ-16242	Marsyangdi	confluence Darundi	27.906	84.544	214	597	263	60	155
NEQ-17202	Narayani	Devghat	27.726	84.428	102	499	186	57	48
NEQ-17206	Narayani	Devghat	27.726	84.428	104	522	195	60	44
NEQ-17232	Narayani	Devghat	27.726	84.428	101	554	231	56	46
NEQ-17506	Narayani	Devghat	27.726	84.428	183	629	321	55	88
NEQ-16208	Narayani	Devghat	27.726	84.428	155	419	315	144	134
NEQ-17568	Khali Gandaki	Jomsom	28.786	83.735	964	1531	901	92	804
NEQ-17237	Khali Gandaki	Ramdi	27.902	83.632	71	532	236	73	43
NEQ-17223	Khali Gandaki	Devghat	27.742	84.429	94	619	336	63	43
NEQ-16248	Langtang Khola	Syabru Beshi	28.163	85.344	122	264	97	31	14
NEQ-18109	Langtang Khola	Syabru Beshi	28.163	85.344	134	301	72	41	21
NEQ-16219	Dudh Khola	Dharapani	28.527	84.357	121	487	107	23	54
NEQ-17527	Dudh Khola	Dharapani	28.527	84.357	120	578	74	22	64
NEQ-17518	tributary Marsyangdi	-	28.454	84.369	47	385	47	29	4
NEQ-16226	Nar Khola	Chame	28.554	84.259	194	1559	922	43	28
NEQ-17532	Nar Khola	Chame	28.554	84.259	241	1613	1028	44	27
NEQ-18102	Humde	Julu	28.659	84.086	214	2192	1271	51	96
NEQ-18104	Ghatte Khola	Manang	28.665	84.028	347	1767	887	38	23
NEQ-16275	Bhote Khosi	Dolalghat	27.639	85.706	224	357	158	46	44
NEQ-16296	Bhote Khosi	Barabise	27.797	85.896	114	344	215	39	18
NEQ-18112	Bhote Khosi	Barabise	27.93	85.938	175	513	137	44	23
NEQ-17253	Bhote Khosi	Barabise	27.797	85.896	73	363	125	51	19
NEQ-162102	Bhote Khosi	Dolalghat	27.641	85.709	137	320	225	51	23
NEQ-18115	Bhote Khosi	Dolalghat	27.641	85.71	140	494	207	57	29
NEQ-18107	Trisuli	Betrawati	27.967	85.178	182	528	178	57	51
NEQ-18110	Trisuli	Syabru Beshi	28.166	85.343	217	687	231	44	65
NEQ-16253	Trisuli	Syabru Beshi	28.166	85.343	197	473	199	42	53
NEQ-17248	Trisuli	Devighat	27.806	85.008	63	380	74	41	12
NEQ-18105	Trisuli	Riverside Resort	27.875	84.614	241	789	276	65	85
NEQ-17228	Trisuli	Devghat	27.755	84.42	110	531	191	57	50
NEQ-17241	Dadi Khola	Mirdi	27.986	83.766	56	271	198	32	34
NEQ-16239	Darundi	confluence Marsyangdi	27.909	84.546	185	563	346	97	44
NEQ-17515	Khudi	Khudi Bazar	28.288	84.354	90	338	151	80	46
NEQ-18111	Tatopani (hot spring)	Tatopani	27.947	85.952	4981	1166	667	592	685
NEQ-1801	Tatopani (hot spring)	Chame	28.552	84.243	15463	4152	221	1227	17565

Table 1: *River and hot spring sample locations, measured major ion concentrations, $DI^{14}C$, $DI^{13}C$ and $\delta^{34}S$ of dissolved sulfate.*

Sample	River	Location	SO_4 [µmoles/L]	HCO_3 [µmoles/L]	NO_3 [µmoles/L]	F [µmoles/L]	$DI^{14}C$ [Fm]	$\delta^{13}C$ [‰]	$\delta^{34}S$ [‰]
NEQ-17564	Marsyangdi	Thorung Phedi	2002	1605	0	0	0.4	1.5	-17.9
NEQ-18103	Marsyangdi	Manang	947	1867	0	0	0.46	-0.4	-3.6
NEQ-17551	Marsyangdi	Manang	1041	1822	0	0	0.49	-1.1	-12
NEQ-17537	Marsyangdi	Chame	982	1752	0	0	0.61	-1.5	-8.5
NEQ-16223	Marsyangdi	Chame	861	960	9	0	0.61	-	-9
NEQ-16213	Marsyangdi	Tal	554	1282	12	8	0.73	-	-10
NEQ-17522	Marsyangdi	Tal	680	1499	0	0	0.71	-1.4	-10
NEQ-16234	Marsyangdi	Besisahar	340	1391	4	7	0.77	-	-8.4
NEQ-17512	Marsyangdi	Besisahar	440	1355	0	0	0.75	-3.4	-8.7
NEQ-17245	Marsyangdi	Besisahar	227	1145	0	0	0.72	-3.1	-7.6
NEQ-16242	Marsyangdi	confluence Darundi	235	1351	12	6	0.81	-	-6.9
NEQ-17202	Narayani	Devghat	136	1210	0	0	0.76	-5.3	-1.3
NEQ-17206	Narayani	Devghat	139	1275	0	0	0.78	-5.6	-1
NEQ-17232	Narayani	Devghat	160	1351	10	0	0.79	-6.3	-1.1
NEQ-17506	Narayani	Devghat	229	1590	0	0	0.78	-4.8	-2.6
NEQ-16208	Narayani	Devghat	166	1283	14	4	0.78	-	-2.2
NEQ-17568	Khali Gandaki	Jomsom	1448	2222	0	0	0.4	1.7	-12.7
NEQ-17237	Khali Gandaki	Ramdi	129	1367	11	0	0.8	-6.7	0.4
NEQ-17223	Khali Gandaki	Devghat	195	1632	0	0	0.82	-7.1	1.5
NEQ-16248	Langtang Khola	Syabru Beshi	73	695	11	10	0.95	-	7.4
NEQ-18109	Langtang Khola	Syabru Beshi	102	697	0	0	0.95	0.4	7.5
NEQ-16219	Dudh Khola	Dharapani	72	1101	15	18	0.8	-	2.3
NEQ-17527	Dudh Khola	Dharapani	101	1181	0	0	0.82	-3.2	2.2
NEQ-17518	tributary Marsyangdi	-	77	780	0	0	0.9	-1.8	10.1
NEQ-16226	Nar Khola	Chame	1916	1323	10	9	0.63	-	-12.8
NEQ-17532	Nar Khola	Chame	1753	2034	0	0	0.63	-0.3	-13.2
NEQ-18102	Humde	Julu	1534	4027	0	0	0.37	0.1	-7
NEQ-18104	Ghatte Khola	Manang	1416	2837	0	0	0.52	-1	-15.4
NEQ-16275	Bhote Khosi	Dolalghat	39	1166	7	6	0.8	-	7.3
NEQ-16296	Bhote Khosi	Barabise	86	1064	9	6	0.88	-	2
NEQ-18112	Bhote Khosi	Barabise	171	1154	0	0	0.72	0.5	-3
NEQ-17253	Bhote Khosi	Barabise	69	941	0	0	0.8	-4.6	4.3
NEQ-162102	Bhote Khosi	Dolalghat	88	1065	14	0	0.85	-	4.1
NEQ-18115	Bhote Khosi	Dolalghat	120	1331	0	0	0.83	-2.7	3.1
NEQ-18107	Trisuli	Betrawati	198	1204	0	0	0.82	0	-1.2
NEQ-18110	Trisuli	Syabru Beshi	289	1455	0	0	0.72	-0.1	-2.6
NEQ-16253	Trisuli	Syabru Beshi	171	1165	14	8	0.72	-	-1.9
NEQ-17248	Trisuli	Devighat	62	861	15	0	0.77	-3.9	1.2
NEQ-18105	Trisuli	Riverside Resort	244	1863	0	0	0.77	-5	-3.4
NEQ-17228	Trisuli	Devghat	155	1251	0	0	0.76	-6.9	-1.8
NEQ-17241	Dadi Khola	Mirdi	16	949	11	0	0.89	-10	6.9
NEQ-16239	Darundi	confluence Marsyangdi	78	1890	7	4	0.83	-	6.2
NEQ-17515	Khudi	Khudi Bazar	101	901	0	0	0.82	-5.7	6.9
NEQ-18111	Tatopani (hot spring)	Tatopani	881	6792	0	0	0.01	1.8	9.6
NEQ-1801	Tatopani (hot spring)	Chame	683	6507	0	0	0.15	-2.6	18.2

2.3. Endmember definition and linear inverse modeling

For the inversion the following five endmembers were defined: Sil_{H2CO3}, $Carb_{H2CO3}$, Sil_{H2SO4}, $Carb_{H2SO4}$ and evaporites (table 2). The chemical composition of silicate lithologies was determined using the range of 16^{th}-64^{th} quartiles from a database with 246 bedrock samples from the HHC and the LH of the Central Himalaya (Lupker *et al.*, 2011). The elemental ratios of carbonates were defined with known ratios of calcite to dolomite of a large Himalayan river (Morin *et al.*, 2018). The evaporitic composition was modified from Lerman *et al.* (2007). In the model we use elemental endmember compositions and ion data as concentrations normalized to the sum of cations (e.g., Ca / Σ^{+}).

The $DI^{14}C$ endmembers are defined as in Blattmann *et al.* (2019): Silicates weathered by carbonic acid originating from the atmosphere or from organic matter (reaction 1), both imply a modern radiocarbon source with a Fraction modern (Fm) between 0.9-1.1. In the weathering reaction of carbonic acid with carbonates (reaction 2) this modern $DI^{14}C$ signature is mixed with ^{14}C-free (Fm=0) carbonate minerals. The $DI^{14}C$ signature of this reaction is thus around Fm=0.5. The sulfuric acid-mediated weathering of carbonates is characterized by the pure radiocarbon-free signal of carbonates (Fm=0). For the $DI^{13}C$ endmember definition, we assume that carbonic acid is derived from the dissolution of atmospheric CO_2 (-5‰) and from the oxidation of organic matter. The latter DIC source is characterized by an isotopically light $\delta^{13}C$ signature and can vary over a relatively large range (-20 to -13‰) (e.g., Spence and Telmer, 2005). The carbonates were assigned a $DI^{13}C$ of -1 - +1‰ (Lupker *et al.*, 2012). For sulfur isotopes, we use traditional endmember compositions, with $\delta^{34}S$ signatures varying between -10 - +1‰ for sulfide minerals and an evaporitic $\delta^{34}S$ signature of +10 - +19‰ (Longinelli and Edmond, 1983; Burke *et al.*, 2018) (Table 2).

Measured ion concentrations as well as isotopic compositions were corrected for rainwater input before applying the inversion model. For the correction of major ion concentrations, values of measured rainwater of the Central Himalaya from Wolff-Boenisch *et al.* (2009) were subtracted from the measured river water. Rainwater input was assigned a modern radiocarbon signature of Fm 1.1 and a $\delta^{13}C$ of -5‰. The $\delta^{34}S$ composition of rainwater was randomly sampled between -5 and +9‰ (Longinelli and Edmond, 1983) before each iteration of the inverse model ($n = 5 \times 10^4$; see below).

A linear inverse model approach was applied to estimate the relative contributions of the five chemical weathering endmembers (Sil_{H2CO3}, $Carb_{H2CO3}$, Sil_{H2SO4}, $Carb_{H2SO4}$ and evaporties) in each sampled catchment similar to the method applied in Blattmann *et al.* (2019). The relative contributions of the weathering endmembers in the 43 river samples and two hot spring samples were solved with the following equation:

$$\min ||A*x - b||^2$$

Where the matrix A contains the elemental and isotopic compositions of the five endmembers (table 2) and b is a vector containing the measured compositions of the river and hot spring samples corrected for rainwater input. X is the vector with the relative contributions to be determined. This linear inverse problem was solved with the lsei function in Rstudio. A Monte Carlo simulation ($n = 5 \times 10^4$) was applied

allowing the model to randomly sample within a uniform distribution of the defined endmember compositional ranges (Table 2). For the evaporitic endmember, Na and Cl, as well as SO_4 and Ca are expected to be correlated and thus set to similar concentrations. Each iteration was forced to respect the charge balance and to generate positive endmember contributions. The results were sorted according to their best fit of the calculated $DI^{14}C$ range for the modelled endmember proportions to the measured $DI^{14}C$. The results were only kept if this $DI^{14}C$ error and the difference between the modelled and the measured sum of cations were <15%. 1% of the best fitting inversions were accepted and used to determine the mean and the 5th and 95th percentiles of the relative endmember contributions.

endmember	Na / Σ^+	Ca / Σ^+	Mg / Σ^+	K / Σ^+	Cl / Σ^+
Sil_{H2CO3}	0.04 - 0.26	0 - 0.12	0.16 - 0.46	0.15 - 0.36	0
Sil_{H2SO4}	0.04 - 0.26	0 - 0.12	0.16 - 0.46	0.15 - 0.36	0
$Carb_{H2CO3}$	-	0.7 - 0.9	0.1 - 0.3	-	0
$Carb_{H2SO4}$	-	0.7 - 0.9	0.1 - 0.3	-	0
evaporites	0.1 - 0.5	0 - 0.5	-	-	0.1 - 0.5

endmember	SO_4 / Σ^+	HCO_3 / Σ^+	$DI^{14}C$ [Fm]	$\delta^{13}C$ [‰]	$\delta^{34}S$ [‰]
Sil_{H2CO3}	0	1	0.90 - 1.10	-20 - -5	-
Sil_{H2SO4}	1	0	-	-	-10 - +1
$Carb_{H2CO3}$	0	1	0.50 - 0.55	-6 - -1	-
$Carb_{H2SO4}$	0.5	0.5	0	-3 - +3	-10 - +1
evaporites	0 - 0.5	-	-	-	+10 - +19

Table 1: *Endmember compositions used in for the inversion. Major ions are normalized to the sum of cations. The elemental composition of evaporites is modified from Lerman et al. (2007) and its $\delta^{34}S$ is from Longinelli & Edmond (1983). Elemental compositions for silicates are from a database used in Lupker et al. (2011).*

3. Results

3.1. Measurements

All results of major ion concentrations and isotopic compositions are reported in Table 1. As expected from previous studies, we observe lower ion concentrations during the monsoon season due to dilution (e.g., Bhatt *et al.*, 2018). The concentrations lie in a similar range as major ion concentrations published in Galy and France-Lanord (1999). The $DI^{14}C$ signature of the studied Himalayan rivers lies in a large range between Fm 0.37 and 0.95 and the two hot springs show significantly lower $DI^{14}C$ values (Fm 0.01 and 0.15) (Figures 2a, b). We observe a weak negative correlation between the $DI^{14}C$ and the HCO_3^-/Σ^+ (concentration of HCO_3^- normalized to the sum of cations). This implies that samples with a lower $DI^{14}C$ concentrations generally contain more SO_4^{2-} (Figure 2b). Additionally, the proportion of the catchment lying in the metasedimentary units of the TSS shows a negative correlation to the $DI^{14}C$ signature and the

relative HCO_3^- content (Figure 1a). The $DI^{13}C$ varies between -10 and +1.7‰. Samples with higher HCO_3^- concentrations show slightly lower $\delta^{13}C$ values (Figure 2c). The $\delta^{34}S$ signature of dissolved sulfate in the Himalayan rivers and hot springs ranges between -17.9 and +10.1‰. The $\delta^{34}S$ shows a clear gradient towards lower values in samples with a large area of the catchment lying in the TSS region (Figure 2d). This corresponds to a north-south gradient of $\delta^{34}S$ signatures that has been described earlier in Himalayan rivers (Turchyn *et al.*, 2013). As shown in Turchyn *et al.* (2013) we observe higher SO_4^{2-} concentrations in samples with isotopically lighter $\delta^{34}S$ signatures (Figure 2d).

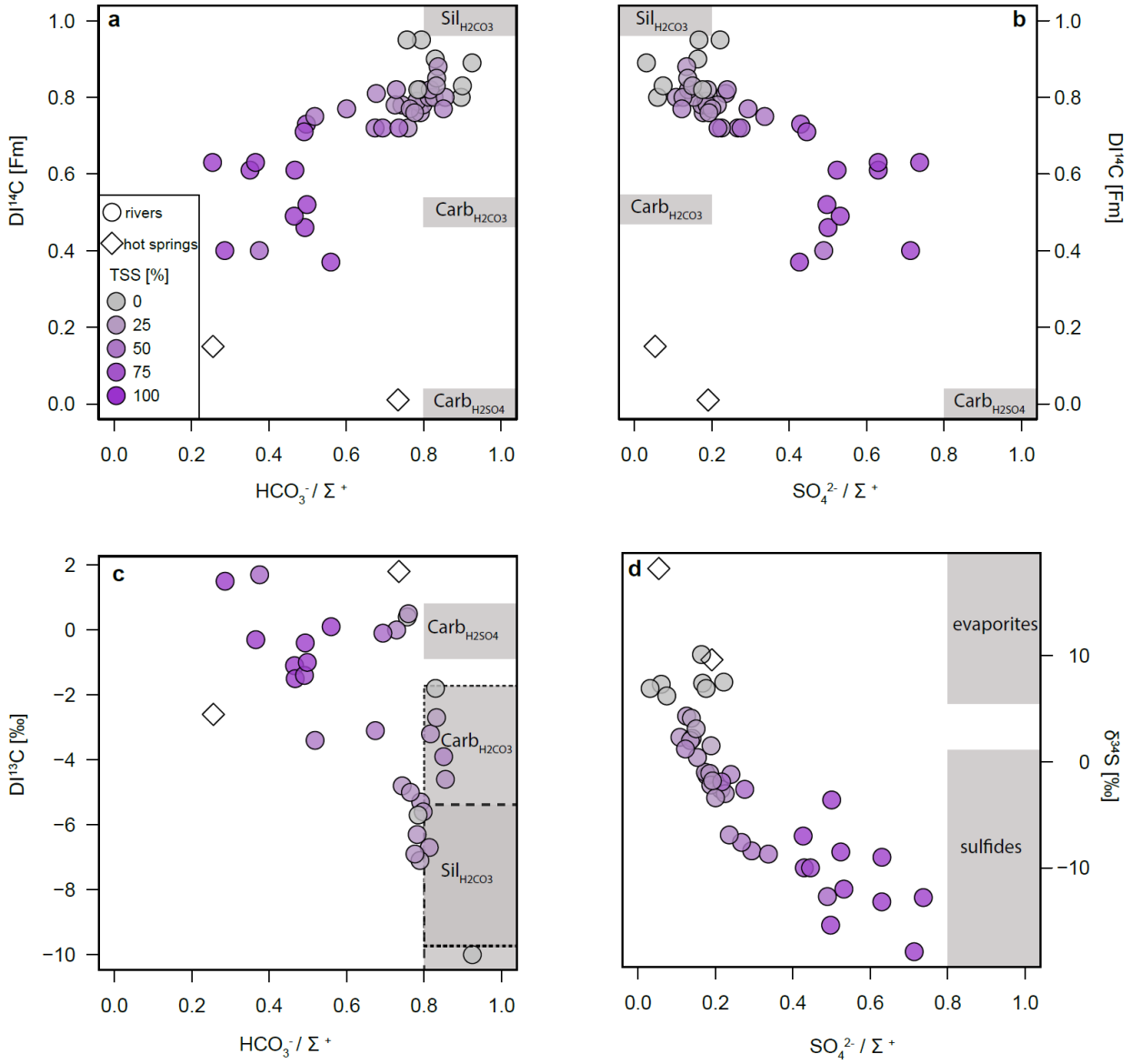

***Figure 2**: Concentration of HCO_3^- normalized to the sum of cations as a function of the $DI^{14}C$ (**a**) and as a function of the $DI^{13}C$ (**c**). SO_4^{2-} normalized to the sum of cations as a function of $DI^{14}C$ (**b**) and as a function of the dissolved $\delta^{34}S$ (**d**). River samples are colored in function of the proportion of outcropping TSS in their catchments. Endmember compositions are schematically shown in grey boxes.*

3.2. Modeling results

The linear inverse model using major ion concentrations and $DI^{14}C$ signatures shows a relatively small residual error (mean: 0.06) for the rivers and higher errors for the two hot spring samples (0.19). For most of the rivers the modelled $DI^{14}C$ and sum of cations fit the measured values with an error of less than 15% (mean: 4%). Four rivers and one hot spring sample displayed errors between the modelled and the measured $DI^{14}C$ that are larger than 15%. These four river samples are not considered for further discussions as the large observed misfit implies that the defined endmembers are not able to explain the data satisfactorily. Also the two hot spring samples are excluded for further interpretations because they are likely to include different weathering processes than rivers (see also section 4.1).

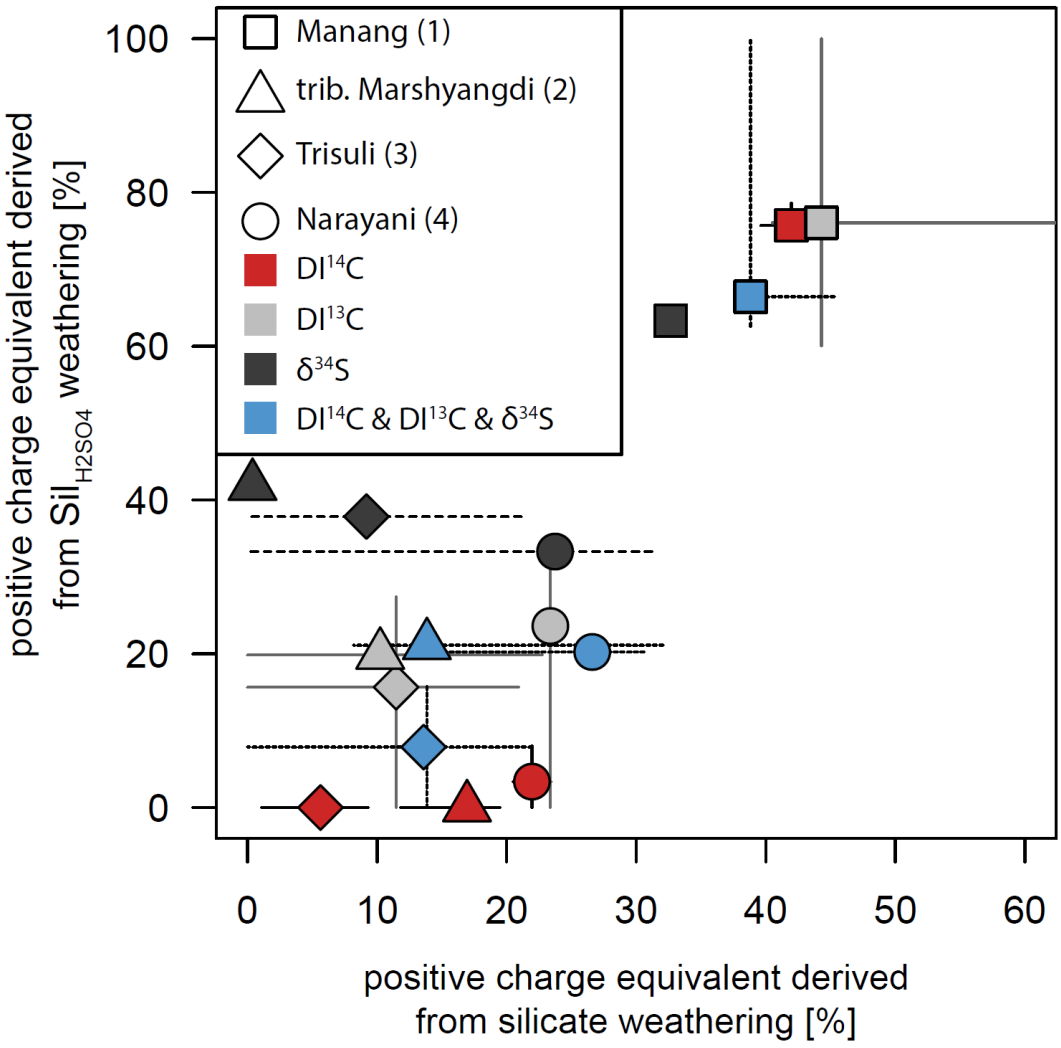

Figure 3: *Results of four inversion models: A model using major ion concentrations and $DI^{14}C$ (red), one with major ions and $DI^{13}C$ (light grey), one with major ions and $\delta^{34}S$ (dark grey) and one using ions and all the three isotopic systems (blue). The proportion of positive charge equivalent derived from silicate weathering is plotted against the positive charge equivalent issued from sulfuric acid-mediated silicate weathering and the error bars show the 5^{th}-95^{th} percentiles of the accepted results. The numbers correspond to the sample locations on Figure 1a. Values for the Narayani River are the mean results of 5 samples.*

In a second model we use the major ion concentrations together with the $DI^{13}C$ signatures of the samples. The results of this inversion were sorted according to the best fit of the modelled $DI^{13}C$ to its measured values and if the error was <15%, the first 1% of the output was accepted as described in the methods section. The errors between the measured and the modelled $DI^{13}C$ are minimal for all the samples (0%) and the residual fit of the inversion lies at 0.06. Figure 3 compares the results of the different inversion models on four rivers in different lithologies and of distinct catchment sizes (Figure 1a, numbers 1-4). The results displayed for the Narayani River are taken from the mean of five samples. The comparison of these results with the inversion using $DI^{14}C$ reveals that the $DI^{13}C$ leads to larger ranges of 5^{th} – 95^{th} percentiles on the samples and pulls the results towards higher contributions of Sil_{H2SO4} (Figure 3). The relative proportion of total silicate weathering, however, is similar between the two models.

For a third inversion we add the dissolved $\delta^{34}S$ compositions to major ion concentrations. The residual fit of this inversion is slightly higher (0.16) and the errors between the modelled and the measured $\delta^{34}S$ were relatively high, with ten samples showing errors between 29-82%. As expected from the endmember compositions, this inversion suggests a higher input of evaporites in downstream rivers with isotopically heavy $\delta^{34}S$ signatures. The calculated evaporite contributions, however, remained relatively low with values <22%. The 5^{th} – 95^{th} range of some samples are relatively large and compared to previous models, the proportion of cations derived from silicate weathering through sulfuric acid is increased (Figure 3).

Finally, we employed an inversion model with all the measured isotopic systems ($DI^{14}C$, $DI^{13}C$ and $\delta^{34}S$) and the major ion concentrations. The results show a higher residual fit of 0.6. The errors between the modelled and the measured values stay low for $DI^{14}C$ (mean: 1%) and for $DI^{13}C$ (mean: 1%), but are significantly higher for $\delta^{34}S$ (mean: 23%). We observe that the proportion of silicate weathering is similar to previous inversions using $DI^{14}C$ and $DI^{13}C$ and that the 5^{th} – 95^{th} range is large compared to the inversion with only $DI^{14}C$ values (Figure 3).

4. Discussion

In this section we discuss the challenges of constraining chemical weathering pathways in general and the differences between the above mentioned inversions using distinct isotopic systems. We chose the best fitting model for further interpretations and highlight the implications of its results for chemical weathering pathways in the Himalaya.

4.1. Challenges in understanding the partitioning of chemical weathering pathways

Complications in the use of elemental ratios for endmember definitions

Our inversion models were able to accurately reconstruct measured $DI^{14}C$ and $DI^{13}C$ values, as well as the sum of cations, but reaching a difference of <15% between the modelled and the measured concentrations of each ion was not possible. Some ion concentrations such as Cl are difficult to reconstruct

due to their small concentration and therefore the errors easily exceed 15%. However, we also observe important errors in some rivers for concentrations of major ions as Ca. This discrepancy between major ion concentrations and isotopic compositions of DIC can have different reasons as our inversion assumes conservative behavior of the elemental as well as the isotopic composition of rivers.

Previous studies have shown that ion concentrations of some Himalayan rivers remain difficult to explain by the bedrock lithology alone (Bickle *et al.*, 2005, 2015; Tipper *et al.*, 2006a; Wolff-Boenisch *et al.*, 2009). Secondary calcite precipitation has been identified as a major process of non-conservative behavior of ions in Himalayan rivers *(*e.g., Bickle *et al.,* 2005; Galy and France-Lanord, 1999; Jacobson *et al.*, 2002). The precipitation of calcite decreases the Ca and HCO_3^- concentrations in the stream water and could therefore lead to an underestimation of carbonate weathering and of the fraction of carbonic acid weathering.

The elemental ratios defining our endmembers are based on a database of 246 bedrock samples from the HHC and the LH units in the Central Himalaya. Despite this large number of rock samples, we are probably not able to integrate the whole spectrum of lithologies in the large studied area. Bedrock with different elemental ratios could induce uncertainty in the model results. The database used here does not, for example, include samples from leucogranitic intrusions which mainly outcrop in the Manaslu region in the studied catchments (Figure 1b). We therefore tested the addition of a leucogranitic endmember with compositions from Vidal *et al.* (1982) in the inversion model with $DI^{14}C$. The results of this inversion were very similar to the original model. Rivers draining the Manaslu leucogranite mainly point towards carbonate weathering (~75% of cations derived from carbonates) and therefore suggest that the proportion of chemical weathering of the leucogranitic intrusion is minor. This could be attributed to the presence of marbles in the catchments (Le Fort, 1975). In a further test, we evaluate the compositional differences between lithologies from the HHC and the LH. For this inversion we computed distinct silicate endmembers for each of the three main tectonic units (TSS, HHC and LH). The composition of the TSS silicate endmembers was defined using the combination of HHC and LH elemental ratios due to the lack of more detailed constraints. This model again showed similar results as the original inversion, with slightly higher errors on modeled $DI^{14}C$ (4.4%) and six samples that could not fit the measured $DI^{14}C$ with an error <15%. We therefore decided to continue the study with the original model, allowing the ion concentrations to vary in a larger range and therefore better accounting for local differences in lithologies.

A yet largely unknown question, is the problem of representability of bedrock chemistry for chemical weathering products. Incongruent weathering can cause differences between the elemental ratios of the bedrock and the weathering product (Herczeg and Edmunds, 2000). Furthermore, part of the chemically weathered minerals can intermediately precipitate as clay minerals and thus change the ratio of dissolved ions as weathering product (e.g., Chamley, 1989).

As mentioned above, four of the 43 river samples could not be fitted to the measured $DI^{14}C$ with errors <15%. We notice that three of these samples are from smaller streams mainly draining the LH. It is thus

possible that either the elemental ratios used here are not entirely representative of the LH or other that weathering processes are substantially different in the warm and soil-covered Lesser Himalaya than in upstream catchments.

Unknowns about DIC

The modelled $Carb_{H2SO4}$ rates with $DI^{14}C$ and $DI^{13}C$ could additionally be underestimated due to direct CO_2 degassing. The weathering of carbonates with sulfuric acid can result in direct degassing of CO_2 instead of dissolved HCO_3^- formation (Torres *et al.*, 2014). This reaction is thus not visible in the $DI^{14}C$ and $DI^{13}C$ signatures of rivers. We added an endmember of $Carb_{H2SO4}$ with direct degassing of CO_2 to the inversion using $DI^{14}C$ to account for this process. This endmember was assigned the same chemical composition as $Carb_{H2SO4}$, but without any resulting HCO_3^-. The inversion with this additional endmember displays larger ranges of the 5^{th}-95^{th} percentiles of modelled endmember contributions (Figure 4) and for eight of the 43 rivers the error of modelled $DI^{14}C$ value was larger than 15%. The results suggest that most of the sulfuric-acid derived weathering of carbonates forms gaseous CO_2 (Figure 4). While little is known about this CO_2 degassing, we assume that the proportion relative to the carbonate weathering forming HCO_3^- (Figure 4) of the modeling output are likely overestimated if this is an important process.

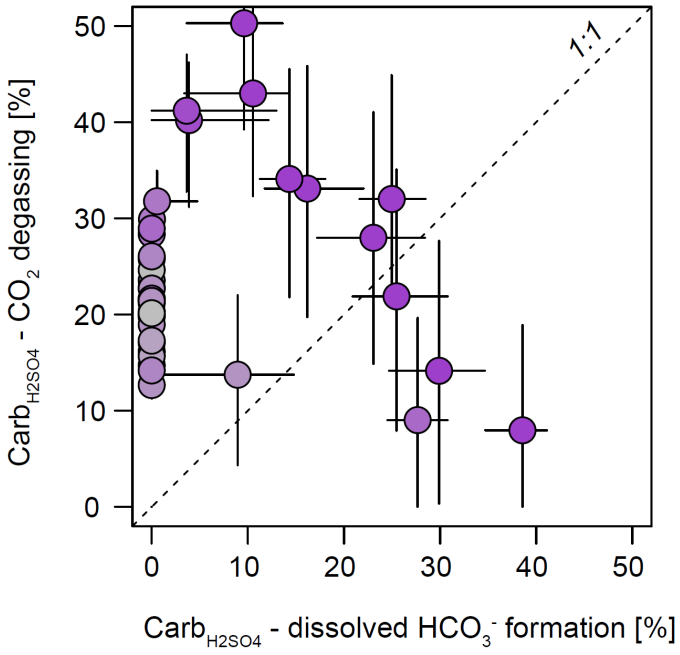

Figure 4: *Proportion of positive charge equivalent derived from carbonate weathering with sulfuric acid divided in reactions that form dissolved HCO_3^- and in reactions that degas CO_2. Error bars show the range from the 5^{th} – 95^{th} percentile of accepted results.*

The two hot spring samples display large errors of the modelled relative contribution of weathering endmembers in all of the models. This can likely be attributed to the contribution of metamorphic CO_2 to the alkalinity of groundwater. The HCO_3^- in hot springs along the active Main Central Thrust in the Central Himalaya has been shown to originate mainly from metamorphic degassing (Evans *et al.*, 2004, 2008). The nearly radiocarbon-dead signature of the hot springs (Fm 0.01 and 0.15) and their relatively low SO_4^{2-} concentrations suggest that weathering through carbonic acid provided by metamorphic reactions is the dominate weathering process (Evans *et al.*, 2004). The addition of silicate and carbonate endmembers weathered through metamorphic CO_2 would thus have to be added to the inversion model for defining the weathering pathways in Himalayan hot springs. We have not added these additional endmembers to the model as the hot spring contribution to the total alkalinity of Central Himalayan rivers remains relatively low (~10% in large Himalayan rivers) (Evans *et al.*, 2004).

For our inversion models, we assume that organic matter decay produces carbonic acid that is prone to react with minerals. In some environments, DIC can additionally derive from heterotrophic consumption of particulate or dissolved organic carbon within rivers (Raymond *et al.*, 2000, 2004). The DIC produced through in-river respiration has a modern $DI^{14}C$ signature and a negative $DI^{13}C$ composition of around -27‰ (Telmer and Veizer, 1999; Raymond *et al.*, 2004). Our $\delta^{13}C$ measurements of DIC show a relatively heavy isotopic signature (mean $\delta^{13}C$: -2.8‰) which suggests that the process of internally added DIC is minor. In addition, short transit times in the mountainous rivers of the Himalaya are likely not favorable for in-river degradation of organic matter.

4.2. Chemical weathering pathways constrained with $DI^{14}C$ and major ions

The relatively small errors of each sample and the good fit between the modelled and the measured $DI^{14}C$, suggest that the radiocarbon signature of DIC combined with major ion concentrations is a useful proxy for tracing chemical weathering pathways as shown by Blattmann *et al.* (2019). The inversion model was able to reconstruct measured $DI^{14}C$ values and the sum of cations for most of the studied rivers. Despite important heterogeneities of bedrock lithology, geomorphology, climate and catchment size of the sampled rivers, we could estimate the proportion of the major chemical weathering processes in the Central Himalaya. The results of the partitioning between silicates and carbonates are mostly similar to previous studies in which different methods for defining chemical weathering pathways were applied (e.g., Bhatt *et al.*, 2018; Bickle *et al.*, 2005, 2015; Galy and France-Lanord, 1999; Tipper *et al.*, 2006; Wolff-Boenisch *et al.*, 2009). With our available data, we are additionally able to calculate the proportion of sulfate derived from evaporites.

The $DI^{14}C$ signature as a proxy for constraining chemical weathering pathways has the advantage of well-defined endmembers varying in a relatively small range. Furthermore, $DI^{14}C$ is not affected by fractionation processes, as the unit Fm is corrected for the isotopic fractionation between ^{14}C and ^{12}C. $DI^{13}C$ on the other hand, is influenced by the isotopic fractionation during riverine CO_2 degassing or the

precipitation of secondary minerals. The use of $DI^{14}C$ for chemical weathering modeling does also not require any bedrock constraints, while complicated $\delta^{34}S$ signatures of Himalayan rivers call for sulfur isotope measurements on bedrock samples (Turchyn *et al.*, 2013; Hemingway *et al.*, 2020).

A major unknown in this modeling approach using $DI^{14}C$ signatures is the isotopic equilibration of river water with the atmosphere. In our model, we assume that the radiocarbon signature of riverine DIC behaves conservatively. Isotopic equilibration between the riverine DIC and the atmosphere has, however, been shown to affect $DI^{14}C$ signatures (Broecker and Walton, 1959; Hendy and Hall, 2006; Bourke *et al.*, 2014). As rivers are generally depleted in radiocarbon relative to the atmosphere (Fm 1.1), rivers are gaining radiocarbon through isotopic exchange in order to approach isotopic equilibrium. Relatively little is known about the rates of DIC isotopic equilibration with the atmosphere. The process depends on various environmental factors such as mixing in the water column, the surface roughness and the travel time of the DIC in the river (Craig, 1957; Broecker and Walton, 1959). Laboratory experiments have shown that the isotopic exchange between the surface layer of a water table and the atmosphere is quicker, if the isotopic composition of DIC is further from the atmospheric equilibrium (Abongwa and Atekwana, 2013; Bourke *et al.*, 2014). The number of unknown factors controlling the isotopic exchange of DIC in Himalayan rivers with the atmosphere make its importance difficult to quantify. We thus cannot exclude that the $DI^{14}C$ signature of Himalayan rivers is affected by isotopic exchange with the atmosphere. This process would preferentially affect downstream samples with longer travel distances and would increase the $DI^{14}C$ signature. The shift towards higher $DI^{14}C$ values through isotopic equilibration of DIC could thus be a reason for the higher proportion of silicate weathering in our results compared to previous studies. The large range of measured $DI^{14}C$ and the absence of a significant gradient from up-to downstream, however, suggest that the radiocarbon signal of DIC in the Central Himalaya is mainly controlled by the carbon source.

4.3. Inversion model using the stable isotopic signature of DIC

The inversion with $DI^{13}C$ values pulls the results towards higher proportions of silicates weathered by sulfuric acid (Figure 3). If the $\delta^{13}C$ is assigned an increased weight in the inversion, the results show higher silicate weathering concentrations. We thus interpret the larger Sil_{H2SO4} contributions in this inversion as resulting from an important discrepancy between $DI^{13}C$ and major ion concentrations. This could be linked to the fact that $DI^{13}C$ does not completely allow us to distinguish between the different endmembers as their signatures overlap (Table 2). The $DI^{13}C$ signature is additionally sensitive to the difference between atmospheric CO_2 (-5 ‰) and degraded organic matter as carbonic acid source (-20 to -13‰) (e.g., Spence and Telmer, 2005).

Additionally, as mentioned above, the discrepancy between the isotopic composition of DIC and major ion concentrations could also be linked to isotopic exchange between the river and the atmosphere. Similar to the radiocarbon exchange, $DI^{13}C$ is pulled towards isotopically heavier values through isotopic

exchange with the atmosphere (e.g., Abongwa and Atekwana, 2013; Telmer and Veizer, 1999). The $DI^{13}C$ is additionally complicated by gas exchange between river and atmosphere. Rivers are generally supersaturated in carbon with respect to the atmosphere and therefore degas CO_2 (Richey *et al.*, 2002; Mayorga *et al.*, 2005). The degassing induces an isotopic fractionation which can shift the DIC signature towards isotopically heavier $\delta^{13}C$ signatures (Abongwa and Atekwana, 2013). Similarly, the precipitation of secondary calcite within the river induces a fraction and can thus alter the $\delta^{13}C$ signature of DIC (Emberson *et al.*, 2018). The minimal error between the measured and the reconstructed $DI^{13}C$ can be attributed to the large compositional ranges of the endmembers (Table 2).

The use of $DI^{13}C$ as a proxy for chemical weathering pathways is thus complicated through different processes which fractionate the stable isotopic composition of DIC and through relatively large ranges defining the $\delta^{13}C$ signature of the different endmembers.

4.4. Chemical weathering pathways constrained by the $\delta^{34}S$ signature of dissolved sulfate

The large errors on the modelled $\delta^{34}S$ (0-82%) suggest an important discrepancy between the major ion concentrations and the sulfur isotopic composition of the endmembers. This confirms that the dissolved sulfur isotopic composition in Central Himalayan rivers cannot be explained using the above mentioned endmember definitions (Table 2) (Turchyn *et al.*, 2013; Hemingway *et al.*, 2020). The increasing $\delta^{34}S$ towards the south would point to an increase in evaporite contributions in the southern part of the Nepalese Himalaya. In studied area of the Central Himalaya no outcrops of evaporites have been described. Deposits of evaporitic minerals could, however, occur at the bottom of the TSS close to the contact with the HHC as they have been described in equivalent formations in the western Himalayas (Strauss, 1993) or in the metasedimentary sequence of the LH. However, major ion compositions do not fit an important source of evaporites. The increasing $\delta^{34}S$ signature towards downstream in Himalayan rivers has previously been explained by bacterial reduction of sulfate (Turchyn *et al.*, 2013; Hemingway *et al.*, 2020). Bacterial sulfate reduction in soils or groundwater leads to sulfide precipitation during which the $\delta^{34}S$ is fractionated by the biotic uptake of sulfate. This shifts the remaining dissolved sulfate to isotopically heavier signatures. We would expect bacterial reduction to be more important in the warmer rivers of the foreland hills. However, our data shows that, for example, a steep stream draining the HHC at elevations >1700 m asl is characterized by a $\delta^{34}S$ of +10.1‰. We therefore suggest that the $\delta^{34}S$ in Himalayan rivers is controlled by the weathered lithology. A bedrock endmember with sulfides minerals characterized by heavier sulfur isotopic compositions than classically proposed (~ 0 to +10‰) would be necessary to explain the gradient of dissolved $\delta^{34}S$ in trans-Himalayan rivers. This is similar to new findings by P. Kemeny (personal communication) and also agrees with preliminary EA-IRMS $\delta^{34}S$ data of Himalayan bedrock samples.

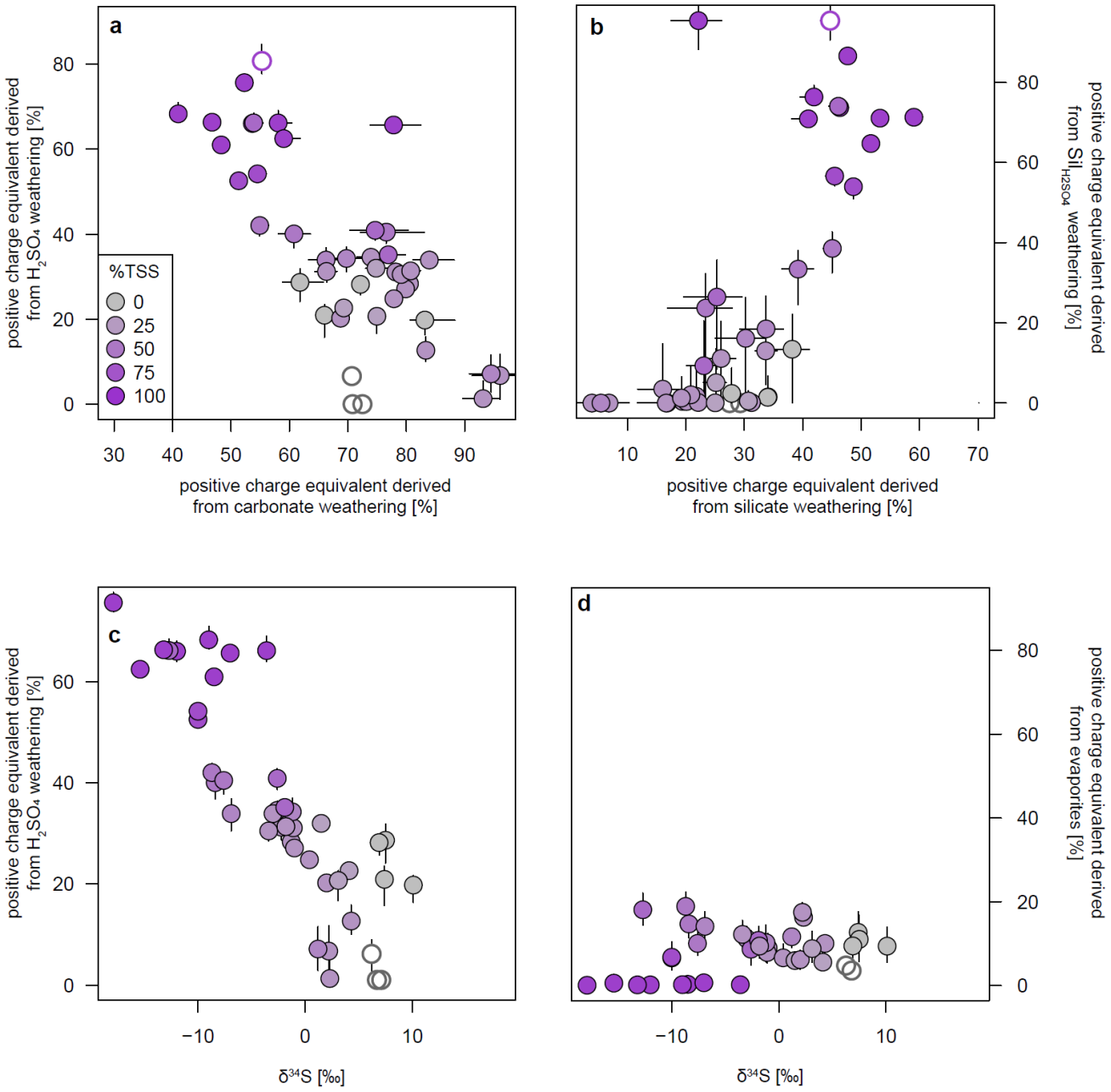

Figure 5: *Output of the inversion model with DI^{14}C and major ion concentrations: (**a**) Proportion of positive charge equivalent sourced from carbonate weathering as a function of cations sourced from sulfuric acid-mediated weathering. (**b**) Positive charge equivalent derived from silicate weathering plotted against the cations issued from silicate weathering through sulfuric acid. Measured $\delta^{34}S$ of dissolved sulfate as a function of (**c**) the proportion positive charge equivalent derived from sulfuric acid weathering and (**d**) positive charge equivalent derived from the dissolution of evaporites. All river samples are colored in function of the proportion of TSS in their catchments. Open symbols show rivers with an error on the modelled DI^{14}C >15%. Error bars illustrate the range from the 5th – 95th percentile of accepted results.*

4.5. Differences between the tested inversions

Despite a large scatter, different chemical weathering regimes between the samples are visible (Figure 2). The stream draining only the metasedimentary units of the TSS (Manang) shows significantly higher inputs from silicate weathering in general and also from sulfuric acid-derived silicate weathering. We further observe that the relative proportion of silicate weathering remains relatively stable between the different models, suggesting that they are mainly controlled by major ion concentrations in the inversion model.

Due to the above discussed complications in using $DI^{13}C$ and $\delta^{34}S$ and due to larger errors on the results of these models, we use the inversion model only including $DI^{14}C$ and major ion concentrations for further interpretations.

4.6. Implications for chemical weathering pathways in the Central Himalaya

The results from all the rivers calculated with the inversion using $DI^{14}C$ and major ions are illustrated on Figure 5. They suggest that the weathering regime in the Central Himalaya is dominated by carbonates as has been proposed previously (e.g., Bhatt *et al.*, 2018; Bickle *et al.*, 2005, 2015; Galy and France-Lanord, 1999; Tipper *et al.*, 2006; Wolff-Boenisch *et al.*, 2009). Figure 5a shows that the proportion of carbonate weathering decreases in weathering regimes dominated by sulfuric acid. In contrast, the proportion of silicate weathering by sulfuric acid increases with the relative importance of silicate weathering (Figure 5b). Sulfuric acid mediated weathering of silicates seems to dominate in catchments draining mainly the lithologies of the TSS (Figure 5a, b and c). Furthermore, sulfuric acid-driven weathering is more important in rivers with isotopically lighter $\delta^{34}S$ compositions (Figure 5c) as expected from the higher sulfate concentration in these rivers (Figure 2d). The modelled ion input from evaporites is low for all the studied rivers and lies in a similar range as previously proposed (0-30%; Galy and France-Lanord, 1999) (Figure 5d). We observe that rivers draining only TSS bedrock mostly display no evaporitic contribution.

The inversion results suggest a lithological control on the sulfuric acid weathering rates (Figures 5a, b and c). Geomorphological factors, such as the mean slope of a catchment (serving as a first order proxy for erosion) do not seem to influence the relative importance of sulfuric acid weathering (Figure 6a). The weak correlation of the mean annual precipitation rate of a catchment to the proportion of sulfuric acid weathering can likely be attributed to the strong north-south precipitation gradient which is sub-parallel to the lithological boundaries (Figure 6b). These results are consistent with previous studies which have identified the TSS as major sulfate source to Himalayan rivers (Galy and France-Lanord, 1999; Wolff-Boenisch *et al.*, 2009; Turchyn *et al.*, 2013). On the other hand, in the HHC and the LH, the main weathering agent seems to be carbonic acid. While it has classically been suggested that the acidity resulted from sulfide mineral oxidation gets mainly neutralized through the dissolution of carbonates (e.g., Galy and France-Lanord, 1999; Wolff-Boenisch *et al.*, 2009), our results suggest that sulfuric acid reaction with silicate minerals is also an important weathering process with relative contributions between 0 and 41% of the positive charge equivalent (Figure 5a and b).

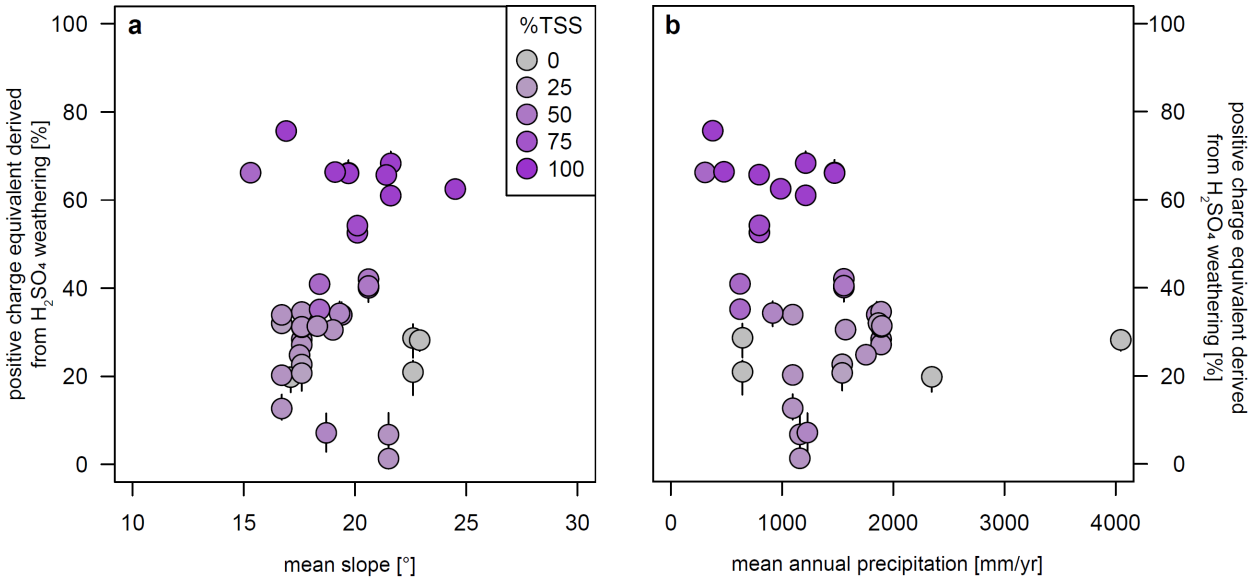

Figure 6: *Modelled proportion of cations derived from sulfuric acid weathering plotted against (**a**) the mean slope in sampled river catchments and (**b**) the mean annual precipitation of each catchment.*

The proportion of silicate weathering in our inversion results are generally slightly higher than previously suggested by forward modeling. Galy and France-Lanord (1999) and Bhatt *et al.* (2018) proposed that in Narayanghat (station number 4 on Figure 1a), only around 10% of the dissolved solids derive from silicate weathering, while our results point to around 22% of silicate weathering in the catchment of Narayanghat. A possible explanation for this discrepancy could be the above discussed isotopic equilibration with the atmosphere.

The minor evaporitic input constrained by $DI^{14}C$ and major ions (Figure 3d) cannot explain the shift from light to heavier sulfur isotopic compositions towards downstream which similar to findings of Turchyn *et al*. (2013) and Hemingway *et al*. (2020).

5. Outlook

MC- ICP-MS $\delta^{34}S$ measurements of gravels from Nepalese rivers through multiple geological units are pending. This additional data will provide a better constrain on the variability of the $\delta^{34}S$ signature of sulfides across lithological units and will improve our understanding of the dissolved sulfur isotopic composition in Himalayan rivers. The $\delta^{34}S$ of the sulfide endmember can then possibly be redefined based on these measurements. This would allow us to include dissolved $\delta^{34}S$ in the inversion along with $DI^{14}C$ and reduce the uncertainties around end-member contributions.

Further work is required to better understand riverine $DI^{14}C$ signatures. While DIC appears to be a useful proxy for constraining chemical weathering pathways, something that cannot be reliably estimated from major ion chemistry alone, a number of assumptions still need to be made for this calculation. An estimation of the isotopic exchange rate between rivers and the atmosphere would allow to correct $DI^{14}C$ values for atmospheric equilibration if needed.

6. Conclusions

We test the application of $DI^{14}C$, $DI^{13}C$ and $\delta^{34}S$ coupled to major ion concentrations for defining chemical weathering pathways in the Central Himalaya. The measured values are best reconstructed with the inversion model including $DI^{14}C$ and ion concentrations and this model is thus used for further interpretation. This approach allows us for the first time to define the proportions of the weathered lithologies as well as the acid involved in chemical weathering in the Central Himalaya.

Our results suggest that chemical weathering in the Central Himalaya is dominated by carbonates which agrees with previous studies (e.g., Galy and France-Lanord, 1999). The minor input of evaporites to the total weathering regime is not able to explain the previously described shift of $\delta^{34}S$ along trans-Himalayan rivers (Turchyn *et al.*, 2013; Hemingway *et al.*, 2020) and therefore requires $\delta^{34}S$ measurements on bedrock samples for further understanding of sulfur isotopic compositions in Himalayan rivers. Additionally, we show that chemical weathering pathways in the Himalaya are mainly controlled by the lithology and can therefore vary on a local scale. Geomorphological factors, such as the mean slope of a catchment, do not significantly influence the partitioning between the different agents of weathering. This suggests that extrapolations of chemical weathering rates in large catchments have to be made carefully, as chemical weathering pathways can vary on a local scale.

References

Abongwa, P. T. & Atekwana, E. A. (2013). Assessing the temporal evolution of dissolved inorganic carbon in waters exposed to atmospheric CO2(g): A laboratory approach. *Journal of Hydrology*. Elsevier B.V. **505**, 250–265.

Berner, R. A. (1989). Biogeochemical cycles of carbon and sulfur and their effect on atmospheric oxygen over Phanerozoic time. *Palaeogeography, Palaeoclimatology, Palaeoecology* **75**, 97–122.

Bhatt, M. P., Hartmann, J. & Acevedo, M. F. (2018). Seasonal variations of biogeochemical matter export along the Langtang-Narayani river system in central Himalaya. *Geochimica et Cosmochimica Acta*. The Authors **238**, 208–234.

Bickle, M. J., Chapman, H. J., Bunbury, J., Harris, N. B. W., Fairchild, I. J., Ahmad, T. & Pomiès, C. (2005). Relative contributions of silicate and carbonate rocks to riverine Sr fluxes in the headwaters of the Ganges. *Geochimica et Cosmochimica Acta* **69**, 2221–2240.

Bickle, M. J., Chapman, H. J., Tipper, E., Galy, A., De La Rocha, C. L. & Ahmad, T. (2018). Chemical weathering outputs from the flood plain of the Ganga. *Geochimica et Cosmochimica Acta*. The Authors **225**, 146–175.

Bickle, M. J., Tipper, E., Galy, A., Chapman, H. & Harris, N. (2015). On discrimination between carbonate and silicate inputs to Himalayan rivers. *American Journal of Science* **315**, 120–166.

Blattmann, T. M., Wang, S., Lupker, M., Märki, L., Haghipour, N. & Wacker, L. (2019). Sulphuric acid-mediated weathering on Taiwan buffers geological atmospheric carbon sinks. *Scientific Reports* **9**, 3–10.

Bourke, S. A., Harrington, G. A., Cook, P. G., Post, V. E. & Dogramaci, S. (2014). Carbon-14 in streams as a tracer of discharging groundwater. *Journal of Hydrology*. Elsevier B.V. **519**, 117–130.

Breitenbach, S. F. M. & Bernasconi, S. M. (2011). Carbon and oxygen isotope analysis of small carbonate samples (20 to 100 µg) with a GasBench II preparation device. *Rapid Communications in Mass Spectrometry* **25**, 1910–1914.

Broecker, W. S. & Walton, A. (1959). The geochemistry of 14C in fresh-water systems. *Geochimica et Cosmochimica Acta* **16**, 15–38.

Burke, A. *et al.* (2018). Sulfur isotopes in rivers : Insights into global weathering budgets, pyrite oxidation, and the modern sulfur cycle. *Earth and Planetary Science Letters*. Elsevier B.V. **496**, 168–177.

Calmels, D., Gaillardet, J., Brenot, A. & France-Lanord, C. (2007). Sustained sulfide oxidation by physical erosion processes in the Mackenzie River basin: Climatic perspectives. *Geology* **35**, 1003–1006.

Chamley, H. (1989). Clay Formation Through Weathering. *Clay Sedimentology*. Berlin, Heidelberg: Springer Berlin Heidelberg, 21–50.

Craig, H. (1957). The natural distribution of radiocarbon and the exchange time of carbon dioxide between atmosphere and sea. *Tellus* **9**, 1–17.

Dalai, T. K. & Sarin, M. M. (2002). Major ion chemistry in the headwaters of the Yamuna river system: Chemical weathering, its temperature dependence and CO2 consumption in the Himalaya. *Geochimica et Cosmochimica Acta* **66**, 3397–3416.

Ebelmen, J. (1845). Sur les produits de la décomposition des especes minérales de la famille des silicates. *Annal des Mines* **7**, 3–66.

Emberson, R., Galy, A. & Hovius, N. (2018). Weathering of Reactive Mineral Phases in Landslides Acts as a Source of Carbon Dioxide in Mountain Belts. *Journal of Geophysical Research: Earth Surface* **123**, 2695–2713.

Emberson, R., Hovius, N., Galy, A. & Marc, O. (2016). Chemical weathering in active mountain belts controlled by stochastic bedrock landsliding. *Nature Geoscience* **9**, 42–45.

Evans, M. J., Deny, L. A. & France-Lanord, C. (2004). Geothermal fluxes of alkalinity in the Narayani river system of central Nepal. *Geochemistry, Geophysics, Geosystems* **5**.

Evans, M. J., Derry, L. A. & France-Lanord, C. (2008). Degassing of metamorphic carbon dioxide from the Nepal Himalaya. *Geochemistry, Geophysics, Geosystems* **9**.

France-Lanord, C., Evans, M., Hurtrez, J. E. & Riotte, J. (2003). Annual dissolved fluxes from Central Nepal rivers: Budget of chemical erosion in the Himalayas. *Comptes Rendus - Geoscience* **335**, 1131–1140.

France-Lanord, C. & Le Fort, P. (1988). Crustal melting and granite genesis during the Himalayan collision orogenesis. *Transactions of the Royal Society of Edinburgh: Earth Sciences* **79**, 183–195.

Gaillardet, J., Dupré, B., Louvat, P. & Allègre, C. J. (1999). Global silicate weathering and CO2 consumption rates deduced from the chemistry of large rivers. *Chemical Geology* **159**, 3–30.

Galy, A. & France-Lanord, C. (1999). Weathering processes in the Ganges-Brahmaputra basin and the riverine alkalinity budget. *Chemical Geology* **159**, 31–60.

Garzanti, E. (1999). Stratigraphy and sedimentary history of the Nepal Tethys Himalaya passive margin. *Journal of Asian Earth Sciences* **17**, 805–827.

Hartmann, J., Jansen, N., Dürr, H. H., Kempe, S. & Köhler, P. (2009). Global CO2 -consumption by chemical weathering: What is the contribution of highly active weathering regions ? *Global and Planetary Change*. Elsevier B.V. **69**, 185–194.

Hemingway, J. D., Olson, H., Turchyn, A. V, Tipper, E. T. & Bickle, M. J. (2020). Triple oxygen isotope insight into terrestrial pyrite oxidation. *PNAS* 1–8.

Hemingway, J. D., Rothman, D. H., Grant, K. E., Rosengard, S. Z., Eglinton, T. I., Derry, L. A. & Galy, V. V. (2019). Mineral protection regulates long-term global preservation of natural organic carbon. *Nature*. Springer US **570**, 228–231.

Hendy, C. H. & Hall, B. L. (2006). The radiocarbon reservoir effect in proglacial lakes: Examples from Antarctica. *Earth and Planetary Science Letters* **241**, 413–421.

Herczeg, A. L. & Edmunds, W. M. (2000). Inorganic Ions as Tracers. In: Cook, P. G. & Herczeg, A. L. (eds) *Environmental Tracers in Subsurface Hydrology*. Boston, MA: Springer US, 31–77.

Jacobson, A. D., Blum, J. D. & Walter, L. M. (2002). Reconciling the elemental and Sr isotope composition of Himalayan weathering fluxes: Insights from the carbonate geochemistry of stream waters. *Geochimica et Cosmochimica Acta* **66**, 3417–3429.

Karim, A. & Veizer, J. (2000). Weathering processes in the Indus River Basin : implications from riverine carbon , sulfur , oxygen , and strontium isotopes. *Chemical Geology* **170**, 153–177.

Kumar, P., Meena, N. K. & Mahajan, A. K. (2019). Major ion chemistry , catchment weathering and water quality of Renuka Lake , north - west Himalaya , India. *Environmental Earth Sciences*. Springer Berlin Heidelberg **78**, 1–16.

Larsen, I. J., Montgomery, D. R. & Greenberg, H. M. (2014). The contribution of mountains to global denudation. *Geology* **42**, 527–530.

Le Fort, P. (1975). Himalayas: the collided range. Present knowledge of the continental arc. *American Journal of Science*, 1–44.

Lerman, A., Wu, L. & Mackenzie, F. T. (2007). CO2 and H2SO4 consumption in weathering and material transport to the ocean , and their role in the global carbon balance. *Marine Chemistry* **106**, 326–350.

Longinelli, A. & Edmond, J. M. (1983). Isotope Geochemistry of the Amazon Basin ' A Reconnaissance. *Journal of*

Geophysical Research **88**, 3703–3717.

Lupker, M. *et al.* (2012). Predominant floodplain over mountain weathering of Himalayan sediments (Ganga basin). *Geochimica et Cosmochimica Acta* **84**, 410–432.

Lupker, M., France-Lanord, C., Lavé, J., Bouchez, J., Galy, V., Métivier, F., Gaillardet, J., Lartiges, B. & Mugnier, J. L. (2011). A Rouse-based method to integrate the chemical composition of river sediments: Application to the Ganga basin. *Journal of Geophysical Research: Earth Surface* **116**, 1–24.

Marwick, T. R., Tamooh, F., Teodoru, C. R., Borges, A. V., Darchambeau, F. & Boillon, S. (2015). The age of river-transported carcon: A global perspective. *Global Biogeochemical Cycles* **29**, 122–137.

Mayorga, E., Aufdenkampe, A. K., Masiello, C. A., Krusche, A. V., Hedges, J. I., Quay, P. D., Richey, J. E. & Brown, T. A. (2005). Young organic matter as a source of carbon dioxide outgassing from Amazonian rivers. *Nature* **436**, 538–541.

Molnar, P. (1984). STRUCTURE AND TECTONICS OF THE HIMALAYA : Constraints and Implications of Geophysical Data. *Annual Review of Earth and Planetary Sciences* 489–518.

Morin, G. P., Lavé, J., France-Lanord, C., Rigaudier, T., Gajurel, A. P. & Sinha, R. (2018). Annual Sediment Transport Dynamics in the Narayani Basin, Central Nepal: Assessing the Impacts of Erosion Processes in the Annual Sediment Budget. *Journal of Geophysical Research: Earth Surface* **123**, 2341–2376.

Paris, G., Sessions, A. L., Subhas, A. V. & Adkins, J. F. (2013). MC-ICP-MS measurement of δ34S and Δ33S in small amounts of dissolved sulfate. *Chemical Geology*. Elsevier B.V. **345**, 50–61.

Raymo, M. E. & Ruddiman, W. F. (1992). Tectonic forcing of late Cenozoic climate. *Nature* **357**, 57–59.

Raymond, P. A., Bauer, J. E., Caraco, N. F., Cole, J. J., Longworth, B. & Petsch, S. T. (2004). Controls on the variability of organic matter and dissolved inorganic carbon ages in northeast US rivers. *Marine Chemistry* **92**, 353–366.

Raymond, P. A., Bauer, J. E. & Cole, J. J. (2000). Atmospheric CO2 evasion, dissolved inorganic carbon production, and net heterotrophy in the York River estuary. *Limnology and Oceanography* **45**, 1707–1717.

Richey, J. E., Melack, J. M., Aufdenkampe, A. K., Ballester, V. M. & Hess, L. L. (2002). Outgassing from Amazonian rivers and wetlands as a large tropical source of atmospheric CO 2. *Nature* **416**, 617–620.

Spence, J. & Telmer, K. (2005). The role of sulfur in chemical weathering and atmospheric CO2 fluxes: Evidence from major ions, δ13CDIC, and δ34SSO4 in rivers of the Canadian Cordillera. *Geochimica et Cosmochimica Acta* **69**, 5441–5458.

Strauss, H. (1993). The sulfur isotopic record of Precambrian sulfates : new data and a critical evaluation of the existing record. *Precambrian Research* **63**, 225–246.

Telmer, K. & Veizer, J. (1999). Carbon fluxes , pCO2 and substrate weathering in a large northern river basin, Canada : carbon isotope perspectives. *Chemical Geology* **159**, 61–86.

Tipper, E. T., Bickle, M. J., Galy, A., West, A. J., Pomiès, C. & Chapman, H. J. (2006a). The short term climatic sensitivity of carbonate and silicate weathering fluxes: Insight from seasonal variations in river chemistry. *Geochimica et Cosmochimica Acta* **70**, 2737–2754.

Tipper, E. T., Galy, A. & Bickle, M. J. (2006b). Riverine evidence for a fractionated reservoir of Ca and Mg on the continents : Implications for the oceanic Ca cycle. *Earth and Planetary Science Letters* **247**, 267–279.

Torres, M. A., Limaye, A. B., Ganti, V., Lamb, M. P., Joshua West, A. & Fischer, W. W. (2017). Model predictions of long-lived storage of organic carbon in river deposits. *Earth Surface Dynamics* **5**, 711–730.

Torres, M. A., West, A. J., Clark, K. E., Paris, G., Bouchez, J., Ponton, C., Feakins, S. J., Galy, V. & Adkins, J. F. (2016). The acid and alkalinity budgets of weathering in the Andes–Amazon system: Insights into the erosional

control of global biogeochemical cycles. *Earth and Planetary Science Letters*. Elsevier B.V. **450**, 381–391.

Torres, M. A., West, A. J. & Li, G. (2014). Sulphide oxidation and carbonate dissolution as a source of CO2 over geological timescales. *Nature*. Nature Publishing Group **507**, 346–349.

Tsering, T., Abdel, M. S. M., Iftekhar, S. & Sillanpää, M. (2019). Journal of Hydrology : Regional Studies Major ion chemistry of the Teesta River in Sikkim Himalaya , India : Chemical weathering and assessment of water quality. *Journal of Hydrology: Regional Studies*. Elsevier **24**, 100612.

Turchyn, A. V., Tipper, E. T., Galy, A., Lo, J. K. & Bickle, M. J. (2013). Isotope evidence for secondary sulfide precipitation along the Marsyandi River, Nepal, Himalayas. *Earth and Planetary Science Letters*. Elsevier **374**, 36–46.

Vidal, P., Cocherie, A. & Le Fort, P. (1982). Geochemical investigations of the origin of the Manaslu leucogranite (Himalaya, Nepal). *Geochimica et Cosmochimica Acta* **46**, 2279–2292.

Wacker, L., Fahrni, S. M., Hajdas, I., Molnar, M., Synal, H. A., Szidat, S. & Zhang, Y. L. (2013). A versatile gas interface for routine radiocarbon analysis with a gas ion source. *Nuclear Instruments and Methods in Physics Research, Section B: Beam Interactions with Materials and Atoms*. Elsevier B.V. **294**, 315–319.

Walker, J. C. G., Hays, P. B. & Kasting, J. F. (1981). A negative feedback mechanism for the long-term stabilization of Earth's surface temperature. *Journal of Geophysical Research: Oceans* **86**, 9776–9782.

West, A. J. (2012). Thickness of the chemical weathering zone and implications for erosional and climatic drivers of weathering and for carbon-cycle feedbacks. *Geology* **40**, 811–814.

West, A. J., Galy, A. & Bickle, M. (2005). Tectonic and climatic controls on silicate weathering. *Earth and Planetary Science Letters* **235**, 211–228.

Wolff-Boenisch, D., Gabet, E. J., Burbank, D. W., Langner, H. & Putkonen, J. (2009). Spatial variations in chemical weathering and CO2 consumption in Nepalese High Himalayan catchments during the monsoon season. *Geochimica et Cosmochimica Acta*. Elsevier Ltd **73**, 3148–3170.

6

Conclusions and further directions

Synthesis

In this thesis, we studied different aspects of the carbon fluxes driven by Central Himalayan erosion. We showed that the Central Himalaya acts as a net carbon sink to the Earth's surface, mainly due to the mobilization and riverine export of biospheric Organic Carbon (OC). The 2015 Gorkha earthquake (Mw 7.8) did not significantly perturb large-scale Himalayan carbon fluxes. These findings suggest that the influence of extreme events on the carbon fluxes in some environments (Wang *et al.*, 2016; Frith *et al.*, 2018) cannot be simply extrapolated for other regions. In mountain ranges with high background erosion rates, such as the Himalaya, sediment and carbon fluxes may not be significantly impacted by external perturbations. Additionally, due to the absence of any important earthquake signal we propose that the calculated carbon budget for the Central Himalayan erosion is representative on timescales of at least interglacials. This finding is important for our further understanding of the feedbacks between erosion and the global climate as erosional carbon budget until know have often been snapshots of a short time (Horan *et al.*, 2019; Hilton and West, 2020).

We further showed that isomer distributions of brGDGTs (branched Glycerol Dialkyl Glycerol Tetraethers) in Himalayan river sediments can be used to trace the main source regions of soil OC inputs in large catchments. Our results suggest that soil organic matter mobilization in the Himalaya occurs pervasively across the soil-covered catchments. This implies that enhanced soil erosion due to anthropogenic activities at lower elevations is either negligible in comparison to background soil erosion processes or is balanced out by OC inputs through naturally enhanced soil erosion in the Upper Himalaya (Montgomery, 2007; West *et al.*, 2015; Tarolli and Sofia, 2016). This study thus sheds new light on large-scale soil OC mobilization processes in mountainous environments.

We demonstrated a wide structural diversity of petrogenic OC material in suspended sediments of a trans-Himalayan river. This large diversity highlights the importance of a systematic study of petrogenic OC in riverine sediments and thus questions previous studies about petrogenic OC oxidation in floodplains (Galy *et al.*, 2008a; Bouchez *et al.*, 2010). Our results further show that petrogenic OC in Himalayan sediments is mainly sourced from the upstream region's metasedimentary units illustrating the lithological control of petrogenic OC export. In-river degradation of petrogenic OC seems to be negligible in this mountainous system which is similar to findings of experimental studies (Scheingross *et al.*, 2019).

Chemical weathering pathways across the Central Himalaya were disentangled applying a novel approach of inverse modelling with radiocarbon signatures of Dissolved Inorganic Carbon (DIC) and major ion concentrations (Blattmann *et al.*, 2019). This method gives for the first time a compete view on chemical weathering pathways in the Himalaya, quantifying the relative importance of the weathered lithologies and the acids (carbonic and sulfuric acids) involved in the reactions as well as the sulfide-derived dissolved sulfate. Our results suggest that chemical weathering pathways vary on a local scale mainly controlled by the lithology. This further implies that large-scale extrapolations of weathering rates have to take into account local variations linked to the bedrock lithology.

Further directions

Having solved some unknowns about carbon fluxes linked to erosion, this study also raises new questions. Some possible directions for future studies are listed below.

Daily variations of riverine OC export in the Narayani River

In Chapter 2, we show that the Total Organic Carbon (TOC) concentration as well as the radiocarbon signature of OC in suspended sediments from Narayanghat vary on a daily scale. This short-term variations are surprising especially considering the large catchment area of the Narayani River. We did not find any first-order correlation of the bulk radiocarbon signature to the water discharge, the total sediment load or the TOC concentration of the sediment (see also Appendix A). A further study of the riverine OC export dynamics in the Narayani River is necessary to unravel this unsolved question. One approach could be the use of meteorological data for searching for any relationship between rainfall in the catchment and the concentration and isotopic signature of OC in sediments from Narayanghat. If larger samples are taken in the future, a biomarker study (fatty acids, alkanes and GDGTs) could give insights in the sources of biospheric OC and their daily variations. The mineral surface area measurement of the river sediments could be interesting information for testing if the OC content is varying synchronously with the total surface area of the sediment as proposed earlier (Blair and Aller, 2012). The daily variations of OC exported in sediments of the Narayani could, however, also simply be linked to the stochastic nature of erosional process, particularly landsliding, governing the petrogenic and biospheric OC export. If the Narayani catchment is not large enough to smooth out these variabilities, further studies of sediment export in mountainous rivers have to take into account important daily variations by time-series sampling.

Dynamics of riverine OC export across the Central Himalaya

In Appendix A, a large dataset of TOC concentrations as well as radiogenic and stable isotopic compositions of riverine sediments from six sampling stations across Nepal can be found. Due to time constraints, this dataset remains to be studied in detail. The time-series over three monsoon seasons (2015-2017) could be used for a detailed study about the controls on OC export in trans-Himalayan rivers. It has been shown on a trans-Himalayan river that suspended sediments get mostly loaded in petrogenic OC in the upstream region and the biospheric OC is added during the transit through the Higher and Lesser Himalaya (Menges *et al.*, 2020). It would be interesting to study these up-to downstream variations in more detail and on a larger sample set. Geomorphological, lithological and climatic parameters can be tested for their controls on riverine OC export. The time-series could give information about the temporal evolution of OC export during the monsoon and between different years. Further, the sample set could be used to test if the signal of coseismic landslides of the Gorkha earthquake is visible on a smaller scale than the Narayani catchment. The large size of the samples would allow biomarker studies (fatty acids,

alkanes and GDGTs) as well as mineral surface area measurements. The latter could be used to further investigate if sediments with large surface areas get loaded with OC along the river.

Petrogenic OC oxidation processes and controls

In Chapter 2, we have defined the erosional carbon budget of the Central Himalaya. For defining the carbon fluxes linked to petrogenic OC (OC_{petro}) oxidation, we had to assume that dissolved Re concentrations effectively trace the oxidation rates. While dissolved Re probably gives a reliable estimation (Dalai *et al.*, 2002; Hilton *et al.*, 2014), it would be interesting to define OC_{petro} oxidation rates more precisely. We could show in Chapter 4 by Raman spectroscopy that in-river oxidation rates in the Himalaya are minor, which implies that hillslopes probably act as major locus for oxidation (Hemingway *et al.*, 2018). A study about the OC_{petro} oxidation in Himalayan soils and bedrock would be interesting for a better understanding of these processes. This could be done by direct measurement of CO_2 fluxes or with biomarkers similar to the method employed in Hemingway et al. (2018). While landslide scars have been identified as reactors for chemical weathering (Emberson *et al.*, 2016, 2018), it should be tested if OC_{petro} oxidation is also enhanced on these sites.

The study of the structural diversity of OC_{petro} in river sediments (Chapter 4) could be extended to the Gangetic floodplain and the Bay of Bengal. A systematic approach for characterizing the OC_{petro} material would allow new insights in the role of floodplains for OC_{petro} oxidation. For more quantitative results, the OC_{petro} in riverine sediments could additionally be characterized by ramped pyrolysis or Rock-Eval pyrolysis.

Improving the distinction of chemical weathering pathways

The results of Chapter 5 show that $\delta^{34}S$ coupled to major ion concentrations cannot be explained by traditional endmember compositions. The measurement of $\delta^{34}S$ on gravels will probably allow us to redefine the sulfur isotopic compositions of Himalayan silicates.

The slightly higher silicate inputs constrained with the radiocarbon signature of DIC ($DI^{14}C$) than calculated by previous studies with major ion concentrations (e.g., Bickle *et al.*, 2015; A. Galy and France-Lanord, 1999) raises questions about the in-river processes that could affect $DI^{14}C$ values. Particularly, studies about the isotopic exchange rate between DIC and the atmosphere would allow a correction of $DI^{14}C$ values. This would probably need some experimental studies and systematic $DI^{14}C$ measurements along rivers. Additionally, the direct CO_2 degassing during sulfuric acid-mediated weathering requires further process-based work.

Global carbon fluxes

The net carbon budget of chapter 2 demonstrates that Central Himalayan erosion acts as a carbon sink to the Earth's surface. This sink is, however, lower than previously thought (Raymo and Ruddiman, 1992; France-Lanord and Derry, 1997; Galy *et al.*, 2008b) due to the efficient carbon sources associated with sulfuric acid-driven weathering and OC_{petro} oxidation. More work about global carbon fluxes is thus required to understand if the important CO_2 sources through volcanism and metamorphism are balanced out by the weathering of mountain ranges. Particularly the erosional carbon budget in volcanic settings could act as more efficient carbon sinks than metasedimentary mountain ranges as the Himalaya, due to the absence of additional carbon sources (OC_{petro} oxidation and sulfuric acid-driven weathering of carbonates).

Paleo-fluxes of carbon from the Himalaya

Our hypothesis that carbon fluxes of Himalayan erosion are representative on timescales of at least interglacials should be tested. Sediment cores from terraces of the Narayani River could be analyzed for OC content and weathering proxies for reconstructing fluxes of carbon on relatively short timescales. This would allow a comparison to studies having showed fluctuations in chemical weathering rates and OC export on timescales of 10 kyrs (Lupker *et al.*, 2013; Hein *et al.*, 2017). Lenard *et al*. (2020) recently showed that erosion rates in the Himalaya on longer timescales (Myrs) stayed relatively constant. Sediment cores from the Bay of Bengal could give information about carbon fluxes since the late Cenozoic.

References

Bickle, M. J., Tipper, E., Galy, A., Chapman, H. & Harris, N. (2015). On discrimination between carbonate and silicate inputs to Himalayan rivers. *American Journal of Science* **315**, 120–166.

Blair, N. & Aller, R. (2012). The fate of terrestrial organic carbon in the marine environment. *Annual Review of Marine Science* **4**, 401–423.

Blattmann, T. M., Wang, S., Lupker, M., Märki, L., Haghipour, N. & Wacker, L. (2019). Sulphuric acid-mediated weathering on Taiwan buffers geological atmospheric carbon sinks. *Scientific Reports* **9**, 3–10.

Bouchez, J., Beyssac, O., Galy, V., Gaillardet, J., France-Lanord, C., Maurice, L. & Moreira-Turcq, P. (2010). Oxidation of petrogenic organic carbon in the Amazon floodplain as a source of atmospheric CO2. *Geology* **38**, 255–258.

Dalai, T. K., Singh, S. K., Trivedi, J. R. & Krishnaswami, S. (2002). Dissolved rhenium in the Yamuna River System and the Ganga in the Himalaya: Role of black shale weathering on the budgets of Re, Os, and U in rivers and CO2 in the atmosphere. *Geochimica et Cosmochimica Acta* **66**, 29–43.

Emberson, R., Galy, A. & Hovius, N. (2018). Weathering of Reactive Mineral Phases in Landslides Acts as a Source of Carbon Dioxide in Mountain Belts. *Journal of Geophysical Research: Earth Surface* **123**, 2695–2713.

Emberson, R., Hovius, N., Galy, A. & Marc, O. (2016). Chemical weathering in active mountain belts controlled by stochastic bedrock landsliding. *Nature Geoscience* **9**, 42–45.

France-Lanord, C. & Derry, L. A. (1997). Organic carbon burial forcing of the carbon cycle from Himalayan erosion. *Nature* **390**, 65–67.

Frith, N. V *et al.* (2018). Carbon export from mountain forests enhanced by earthquake-triggered landslides over millennia. *Nature Geoscience* **11**, 772–776.

Galy, A. & France-Lanord, C. (1999). Weathering processes in the Ganges-Brahmaputra basin and the riverine alkalinity budget. *Chemical Geology* **159**, 31–60.

Galy, V., Beyssac, O., France-Lanord, C. & Eglinton, T. (2008a). Recycling of graphite during Himalayan erosion: a geological stabilization of carbon in the crust. *Science* **322**, 943–945.

Galy, V., France-Lanord, C. & Lartiges, B. (2008b). Loading and fate of particulate organic carbon from the Himalaya to the Ganga-Brahmaputra delta. *Geochimica et Cosmochimica Acta* **72**, 1767–1787.

Hein, C. J., Galy, V., Galy, A., France-Lanord, C., Kudrass, H. & Schwenk, T. (2017). Post-glacial climate forcing of surface processes in the Ganges – Brahmaputra river basin and implications for carbon sequestration. *Earth and Planetary Science Letters*. Elsevier B.V. **478**, 89–101.

Hemingway, J. D., Hilton, R. G., Hovius, N., Eglinton, T. I., Haghipour, N., Wacker, L., Chen, M. & Galy, V. V (2018). Microbial oxidation of lithospheric organic carbon in rapidly eroding tropical mountain soils. *Science* **360**, 209–212.

Hilton, R. G., Gaillardet, J., Calmels, D. & Birck, J. L. (2014). Geological respiration of a mountain belt revealed by the trace element rhenium. *Earth and Planetary Science Letters*. Elsevier B.V. **403**, 27–36.

Hilton, R. G. & West, A. J. (2020). Mountains, erosion and the carbon cycle. *Nature Reviews Earth & Environment*. Springer US **1**, 284–299.

Horan, K. *et al.* (2019). Carbon dioxide emissions by rock organic carbon oxidation and the net geochemical carbon budget of the Mackenzie River Basin. *American Journal of Science* **319**, 473–499.

Lenard, S. J. P., Lavé, J., France-Lanord, C., Aumaître, G., Bourlès, D. L. & Keddadouche, K. (2020). Steady erosion rates in the Himalayas through late Cenozoic climatic changes. *Nature Geoscience*. Springer US **13**, 448–452.

Lupker, M., France-Lanord, C., Galy, V., Lavé, J. & Kudrass, H. (2013). Increasing chemical weathering in the Himalayan system since the Last Glacial Maximum. *Earth and Planetary Science Letters* **365**, 243–252.

Menges, J., Hovius, N., Andermann, C., Lupker, M., Haghipour, N., Märki, L. & Sachse, D. (2020). Variations in organic carbon sourcing along a trans-Himalayan river determined by a Bayesian mixing approach. *Geochimica et Cosmochimica Acta* **286**, 159–176.

Montgomery, D. R. (2007). Soil erosion and agricultural sustainability. *Proceedings of the National Academy of Sciences* **104**, 13268–13272.

Raymo, M. E. & Ruddiman, W. F. (1992). Tectonic forcing of late Cenozoic climate. *Nature* **357**, 57–59.

Scheingross, J. S., Hovius, N., Dellinger, M., Hilton, R. G., Repasch, M., Sachse, D., Gröcke, D. R., Vieth-Hillebrand, A. & Turowski, J. M. (2019). Preservation of organic carbon during active fluvial transport and particle abrasion. *Geology* **47**, 958–962.

Tarolli, P. & Sofia, G. (2016). Human topographic signatures and derived geomorphic processes across landscapes. *Geomorphology* **255**, 140–161.

Wang, J., Jin, Z., Hilton, R. G., Zhang, F., Li, G., Densmore, A. L., Gröcke, D. R., Xu, X. & Joshua West, A. (2016). Earthquake-triggered increase in biospheric carbon export from a mountain belt. *Geology* **44**, 471–474.

West, A. J., Arnold, M., Aumaître, G., Bourlès, D. L., Keddadouche, K., Bickle, M. & Ojha, T. (2015). High natural erosion rates are the backdrop for present-day soil erosion in the agricultural Middle Hills of Nepal. *Earth Surface Dynamics* **3**, 363–387.

Acknowledgments

First, I want to thank Maarten Lupker, for having initiated this whole study and for having provided me the opportunity to work on this project. Thank you, Maarten, for sharing your passion for science and guiding me through these four years of research. Our uncountable interesting discussions inspired me and your optimism always gave me the motivation to accept new challenges. Thank you for your confidence in me, for always leaving your door open for all my questions and for your incredible speed in email answering.
Further, I would like to thank Tim Eglinton for offering me the opportunity to work in the Biogeoscience group. Thank you for your interesting inputs and your trust in me. I appreciate the friendly and warm atmosphere you are creating in our group.
Thank you, Matthieu Galvez, for having introduced me to the world of Raman spectroscopy and to the petrological part of the carbon cycle. Our captivating discussions and your critical inputs made me look at my data from a different point of view. I am grateful to Christian France-Lanord for his geochemical advises and for being part of my committee. I would also like to thank Josh West for having agreed to join the thesis committee.

I am very grateful to work on a unique set of time-series samples from the Himalaya. A special thank goes to our collaborators in Nepal who probably made the hardest part of this work: daily sampling of river water in the monsoonal rain. I also want to thank Christian, Jérôme, Maarten, Sean and Ananta for having installed and organized the sampling stations.
I had the great opportunity to join several fieldtrips to the Himalaya and want to thank the “Nepal-team”, Ananta, Akash, Maarten, Hannah, Katie, Sean, Marius and Dorran for help during sampling and for the wonderful time in Nepal. I particularly would like to thank Ananta who is a great guide during fieldwork and always knows where to drink the best chai.

Thank you, Negar, for having measured an incredible amount of samples for me; without them this study would not have been possible. I would also like to thank Daniel for help and interesting discussions in the lab and Fanny for assistance with the IC measurements and confidence in my lab-skills. Madalina Jäggi is thanked for $\delta^{13}C$ measurements and Guillaume Paris for $\delta^{34}S$ measurements. I am grateful to Nadine Keller and Anna van Brummen for their efficient help with labwork.
Further, I would like to thank Jérôme for all his critical comments on my manuscripts; they made me think twice about everything I wrote. I also thank Sean for the interesting collaboration and for having shown so much interest in my geochemistry work.

I am very lucky to be able to share the ups and downs of a PhD life with Hannah. Thank you, Hannah, for the great time, you made conferences feel like holidays and lunch breaks feel like weekends. I also want to thank Julia, Elena, Negar, Lisa, Julie, Fatemeh, Nora, Kathrin, Cindy and the whole Biogeoscience group for good vibes in the lab, at lunch and around a beer. Special thanks go to my friends from the geophysical institute: Jana for your contagious positive energy during our uncountable coffee breaks and Jessica for

all the philosophical discussions during lunch breaks in person or on zoom during lockdown, and for even bringing me delicious food when I am too stressed for cooking. I further thank my officemates Yanyan, Richard and Melissa for having shared our beautiful office. Yanyan also became the perfect remote-officemate.

I warmly thank my parents, Irene and Walter, and my sister, Flora, for all your support and love, which are my sources of energy.

Thomas became my officemate for the last seven months and made out of the lockdown an adventure to experience together. Thomas, there are so many things I am grateful to you for. You are the sun in my life.

Appendix A

Riverine organic carbon export across the Central Himalaya

In this appendix, preliminary data of riverine Organic Carbon (OC) on a set of time-series samples from six stations in the Nepalese Himalaya are presented. The Total Organic Carbon (TOC) concentration and the isotopic compositions of OC (radiocarbon signature and $\delta^{13}C$) were measured on suspended sediments. The results of daily samples from Narayanghat are presented in Chapter 2 of this thesis.

Sampling

The location of the six sampling stations in the Nepalese Himalaya are shown on Figure 1. Samples consist of two types: daily samples (from Chame, Besisahar and Narayanghat) and drum samples (from all the stations). For the daily samples, 3L of surface water was taken from the middle of the rivers in Chame, Besisahar and Narayanghat every day during the four months of monsoon season. The water was filtered with a pressure filtration unit through 0.2 µm PES membranes. Drum samples integrate the suspended sediment load over a two-week period. For the sampling of the later, local collaborators collected 20 to 40 L of river water, which was added to a 120 L opaque container and left to settle overnight before removing the supernatant by a water tap. This procedure was repeated daily for two weeks. After this period, the resulting sediment was collected by a water tap at the bottom of the container and air-dired. Both sample types were stored in a cool and dark place.

Analytical methods

Upon arrival at ETH, the sediment samples were frozen, freeze-dried and weighed. The suspended sediment load was calculated with the sample weight. A sample from every second to third day from the daily sample set and all the drum samples were prepared for analysis. The sample preparation and measurement of the radiocarbon signature (Fraction modern, Fm) and the $\delta^{13}C$ of OC as well as the TOC is described in further details in Chapter 2 of this thesis.

For the determination of the relative proportions of biospheric OC (OC_{bio}) and petrogenic OC (OC_{petro}), we applied a binary mixing model with a petrogenic (Fm=0) and a biospheric endmember (Fm = 0.9 – 1.1). Details about the mixing model are given in Chapter 2 of this thesis.

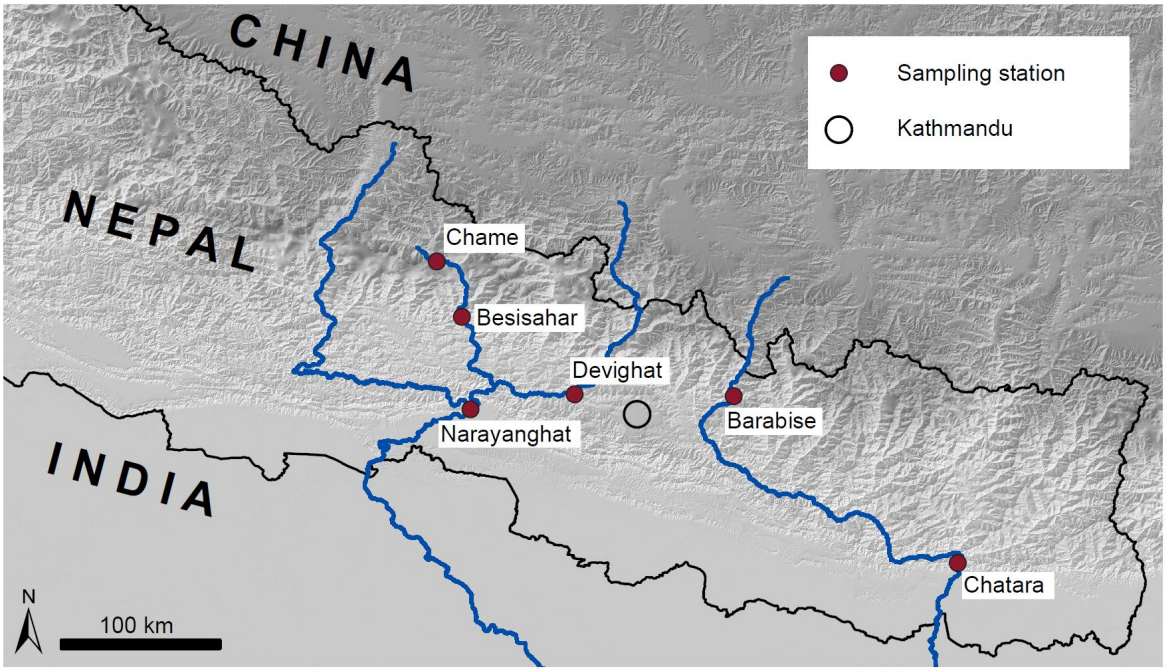

Figure 1: *Locations of sampling stations and major rivers of the Central Himalaya.*

Results

Results are listed in Tables 1-5 with the exception of daily samples from Narayanghat, which can be found in the appendix of Chapter 2. Daily samples from Narayanghat, Besisahar and Chame show a large variability of TOC concentrations, Fm and $\delta^{13}C$ signatures at a daily scale. Figure 2 shows no first-order correlation between the isotopic signature of OC, its concentration and the total sediment load. Additionally, daily samples do not reveal any temporal trends during a monsoon season (Figure 2). We observe an increase in the variability of the radiocarbon signature and TOC, and a shift towards higher Fm values from up- (Chame) to downstream (Narayanghat).

The measured values of drum samples lie a large range of TOC (0.1 - 0.8 %) and of radiocarbon signatures (Fm: 0.17 – 0.94), while the $\delta^{13}C$ values vary between -30 and -19 ‰. Figure 3 illustrates the signatures of drum samples from the monsoon season 2015. The monsoon 2015 is shown because it is the most complete dataset of the three studied years. Figure 3a reveals that the radiocarbon concentration of upstream rivers (Chame and Barabise) is generally lower than the Fm of large rivers of the Himalayan Middle Hills (Narayanghat and Chatara). The variability of Fm and TOC is also slightly lower in these two large rivers (Figure 3a and b). In most rivers (Besisahar, Devighat, Chatara and Narayanghat), the TOC concentration drops with the onset of the monsoon and increases towards the end of the monsoon season.

Daily variability

While the OC signatures in Chame are relatively stable, the daily variability of TOC concentrations and radiocarbon signatures in sediments from Narayanghat and Besisahar suggest a heterogeneous OC input on short timescales (Figure 2). The large catchment area of the Narayani River in Narayanghat (32'000 km^2) is not able to smooth out these variabilities. The respective sediment loads in Narayanghat and Besisahar show a similar pattern during the monsoon 2015 (Figure 2), pointing at the important role of the Besisahar-catchment for the sediment input to the Narayani River in Naryanghat. Stochastic landsliding has been shown to be the major process of erosion and sediment supply in the Narayani catchment (Marc et al., 2019; Morin et al., 2018) and could also be responsible for the variability in OC export. While further work is required to understand the short-term variability in OC export of Himalayan rivers, these results highlight the importance of time-series sampling.

Figure 4 compares the radiocarbon signature of daily and drum samples from Narayanghat of the monsoon 2015. The mean radiocarbon signatures of daily samples from a two-week period show similar values as drum samples from the same time interval. We can therefore, confidently assume that drum samples represent the mean OC signature of a two-week period and are not affected by potential in-situ production in the barrel where samples are stored. The latter would shift the radiocarbon signature of drum samples to significantly higher values. Figure 4 further suggests that the two-week period smooths out daily heterogeneities of OC export in the large Narayani River.

Riverine organic carbon export across the Central Himalaya

The general trend to higher radiocarbon signatures of OC from up-to downstream suggests that trans-Himalayan river sediments get loaded in OC_{bio} during fluvial export if we assume that in-river OC loss is minimal. The results of the mixing model (Figure 5) demonstrate a similar trend, with a higher proportion of OC_{bio} in the large rivers of the Himalayan Middle Hills.

The relatively low Fm signature of OC in river sediments from Chame can be attributed to an important input of OC_{petro} (figures 2 and 5). The Marshyandi River in Chame drains the Tethyan Sedimentary Series (TSS). In this metasedimentary series, the OC concentration varies between 0.09 and 2.03% (Aucour et al., 2006; Menges et al., 2020). Menges et al. (2020), as well the Chapter 4 of this thesis, suggest that the TSS are the main source region of OC_{petro} exported in Central Himalayan rivers. This is in line with Figure 4 showing that around 80% of the OC from Chame is of petrogenic origin, while the input of OC_{bio} in this high mountain catchment is minor.

The difference of the Fm signature and the proportion of OC_{bio} between samples from Chame and Besisahar proposes the addition of OC_{bio} during the riverine transit through the High Himalaya assuming a minimal loss of OC during fluvial transport. This could be linked to the high frequency of landsliding in

the High Himalaya which probably exports a significant amount of OC_{bio} (Menges et al., 2020; Morin et al., 2018).

Drum samples from Barabise display an important variability of TOC concentrations and radiocarbon signatures (Figure 5). The sampling station of Barabise lies downstream of a steep valley, which was heavily affected by coseismic landsiliding during the 2015 Gorkha earthquake (Mw 7.8) (Roback et al., 2018). Material of the coseismic landslides or frequent mass wasting during 2016 could cause the important variability of the TOC and Fm signals in sediments from Barabise.

The most important part of the OC_{bio} however seems to be added to trans-Himalayan rivers during their transit through the Lesser Himalaya (e.g., between Besisahar and Narayanghat). Thick soil covers and important landsliding rates could be the triggers for OC_{bio} mobilization in this region.

These preliminary results highlight the complexity of riverine OC export in the Central Himalaya and the importance of time-series sampling of river sediments.

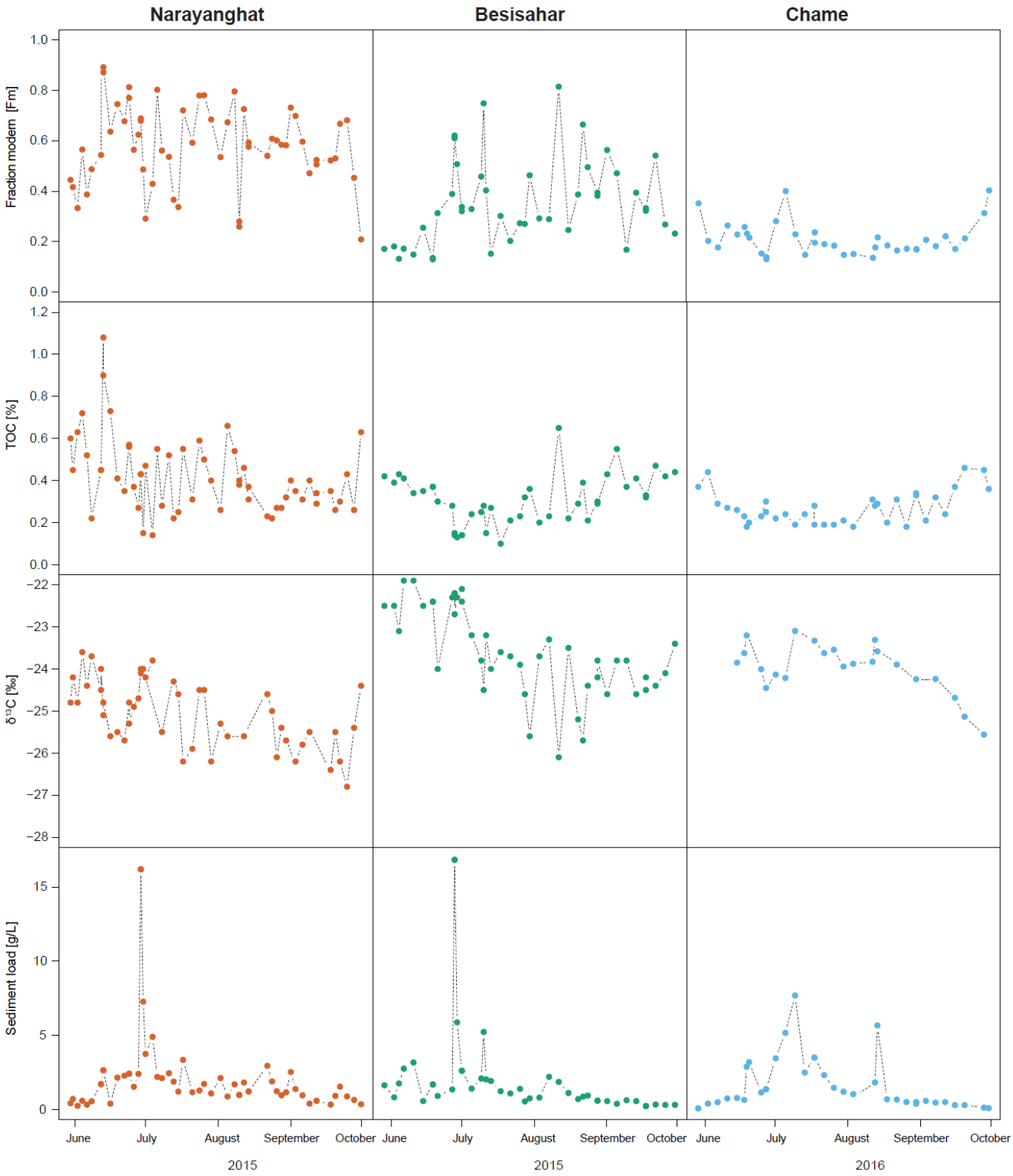

Figure 2: *Radiocarbon signature (Fm), total OC concentration (TOC), stable isotopic composition of OC ($\delta^{13}C$) and the sediment load measured on daily samples of the monsoon season 2015 (Narayanghat and Besisahr) and 2016 (Chame).*

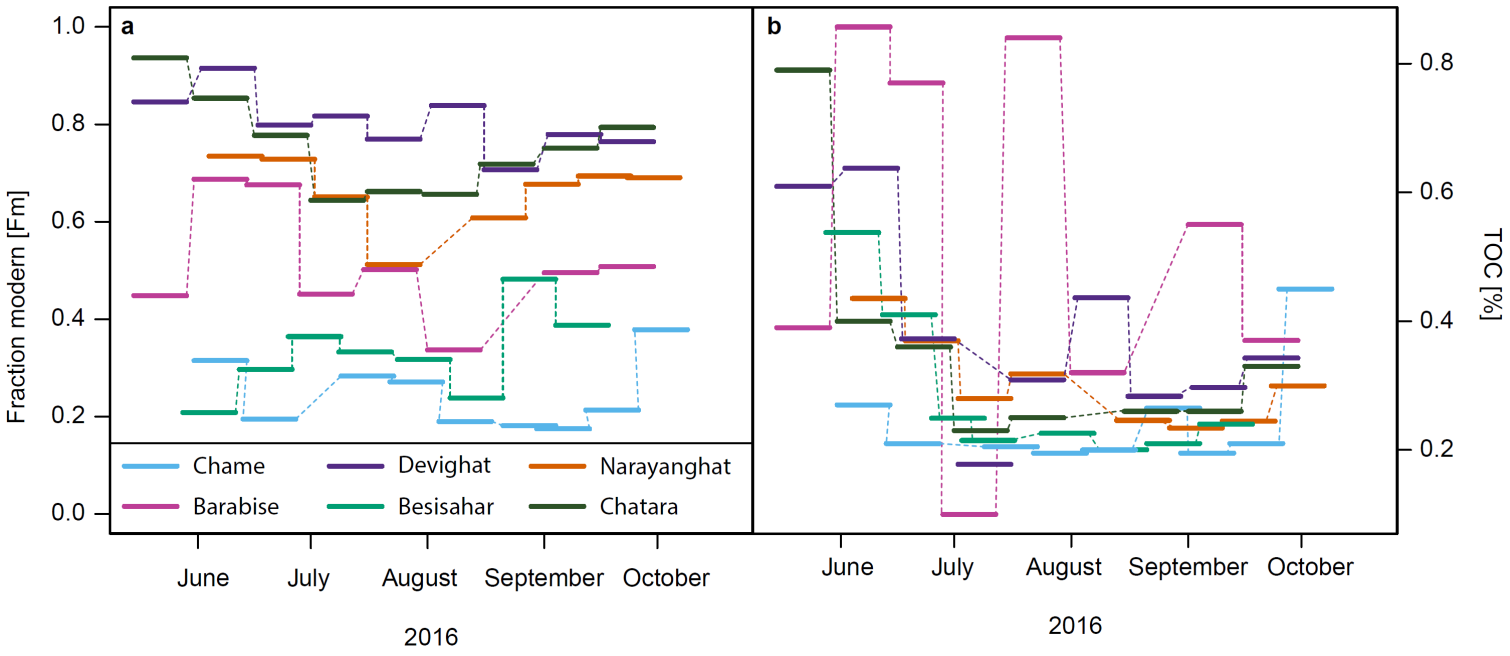

Figure 3: *Results from drums samples of the monsoon 2016 from all the sampling stations. Temporal evolution of* ***a.*** *the radiocarbon signature of OC and* ***b.*** *the TOC concentrations.*

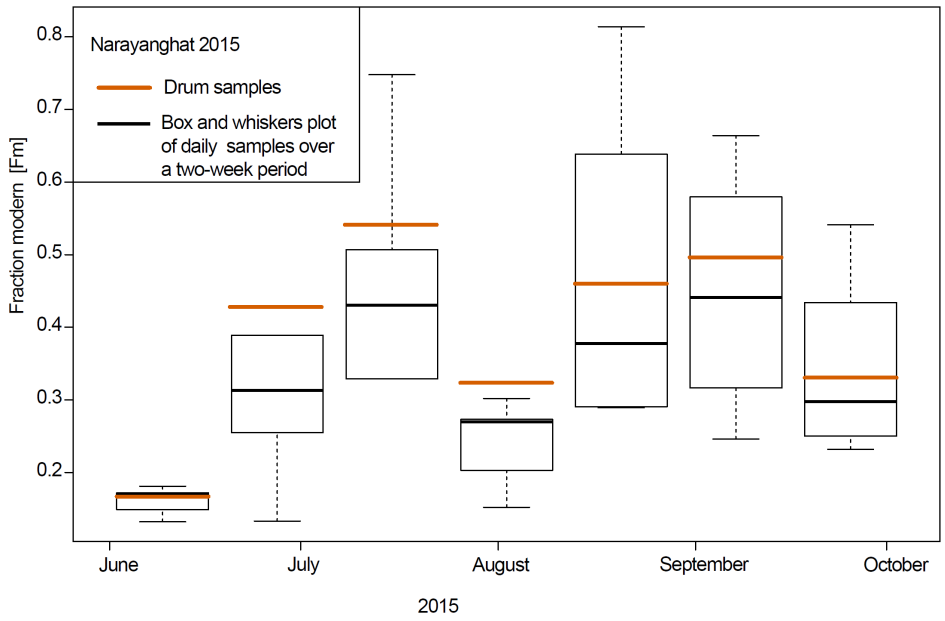

Figure 4: *Radiocarbon signature of OC in drum samples from Narayanghat during the monsoon 2015 (orange lines) compared to box and whiskers plot of the daily Fm during a two-week period.*

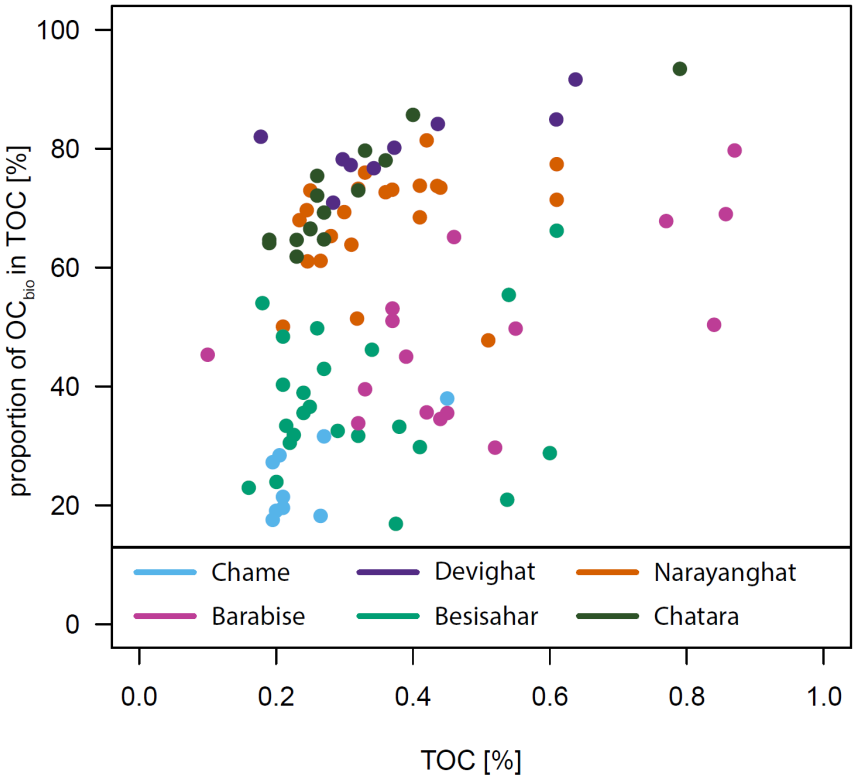

Figure 5: *TOC concentration of all drum samples (monsoon seasons 2015-2017) plotted against the calculated proportion of biospheric OC.*

Daily samples from Besisahar 2015

location	name	date	TOC (%)	$\delta^{13}C$ (‰)	Fraction modern	sediment load (g/L)
Besisahar	MA15-31-05	31.05.2015	0.42	-24.36	0.17	1.64
Besisahar	MA15-04-06	04.06.2015	0.39	-26.48	0.18	0.84
Besisahar	MA15-06-06	06.06.2015	0.43	-24.00	0.13	1.77
Besisahar	MA15-08-06	08.06.2015	0.41	-25.11	0.17	2.77
Besisahar	MA15-12-06	12.06.2015	0.34	-23.93	0.15	3.18
Besisahar	MA15-16-06	16.06.2015	0.35	-26.74	0.26	0.59
Besisahar	MA15-20-06	20.06.2015	0.37	-24.90	0.13	1.70
Besisahar	MA15-22-06	22.06.2015	0.30	-21.85	0.31	0.93
Besisahar	MA15-28-06	28.06.2015	0.28	-24.93	0.39	1.37
Besisahar	MA15-29-06	29.06.2015	0.15	-22.05	0.62	16.84
Besisahar	MA15-30-06	30.06.2015	0.13	-16.19	0.51	5.89
Besisahar	MA15-02-07	02.07.2015	0.14	-20.38	0.33	2.62
Besisahar	MA15-06-07	06.07.2015	0.24	-21.10	0.33	1.42
Besisahar	MA15-10-07	10.07.2015	0.25	-21.41	0.46	2.10
Besisahar	MA15-11-07	11.07.2015	0.28	-22.51	0.75	5.24
Besisahar	MA15-12-07	12.07.2015	0.15	-19.45	0.40	2.04
Besisahar	MA15-14-07	14.07.2015	0.27	-22.30	0.15	1.94
Besisahar	MA15-18-07	18.07.2015	0.10	-23.84	0.30	1.25
Besisahar	MA15-22-07	22.07.2015	0.21	-23.03	0.20	1.10
Besisahar	MA15-26-07	26.07.2015	0.23	-21.84	0.27	1.40
Besisahar	MA15-28-07	28.07.2015	0.32	-25.44	0.27	0.56
Besisahar	MA15-30-07	30.07.2015	0.36	-20.30	0.46	0.76
Besisahar	MA15-03-08	03.08.2015	0.20	-19.58	0.29	0.82
Besisahar	MA15-07-08	07.08.2015	0.23	-19.37	0.29	2.21
Besisahar	MA15-11-08	11.08.2015	0.65	-22.26	0.81	1.87
Besisahar	MA15-15-08	15.08.2015	0.22	-21.75	0.25	1.13
Besisahar	MA15-19-08	19.08.2015	0.29	-24.38	0.39	0.72
Besisahar	MA15-21-08	21.08.2015	0.39	-27.63	0.66	0.88
Besisahar	MA15-23-08	23.08.2015	0.21	-22.34	0.50	0.95
Besisahar	MA15-27-08	27.08.2015	0.29	-21.86	0.39	0.61
Besisahar	MA15-31-08	31.08.2015	0.43	-20.16	0.56	0.58
Besisahar	MA15-04-09	04.09.2015	0.55	-22.51	0.47	0.40
Besisahar	MA15-08-09	08.09.2015	0.37	-21.70	0.17	0.64
Besisahar	MA15-12-09	12.09.2015	0.41	-20.52	0.39	0.58
Besisahar	MA15-16-09	16.09.2015	0.32	-23.56	0.33	0.25
Besisahar	MA15-20-09	20.09.2015	0.47	-20.31	0.54	0.35
Besisahar	MA15-24-09	24.09.2015	0.42	-21.08	0.27	0.33
Besisahar	MA15-28-09	28.09.2015	0.44	-20.82	0.23	0.33

Table 1: *Daily samples of the monsoon season 2015 from Besisahar.*

Daily samples from Chame 2016

location	name	date	TOC (%)	$\delta^{13}C$ (‰)	Fraction modern	sediment load (g/L)
Chame	MA16-C-01-06	01.06.2016	0.37	NA	0.35	0.09
Chame	MA16-C-05-06	05.06.2016	0.44	NA	0.20	0.41
Chame	MA16-C-09-06	09.06.2016	0.29	NA	0.18	0.51
Chame	MA16-C-13-06	13.06.2016	0.27	NA	0.26	0.76
Chame	MA16-C-17-06	17.06.2016	0.26	-21.41	0.23	0.79
Chame	MA16-C-20-06	20.06.2016	0.23	-22.70	0.26	0.66
Chame	MA16-C-21-06	21.06.2016	0.18	-23.39	0.23	2.90
Chame	MA16-C-22-06	22.06.2016	0.20	NA	0.22	3.20
Chame	MA16-C-27-06	27.06.2016	0.23	-22.73	0.15	1.16
Chame	MA16-C-29-06	29.06.2016	0.28	-26.42	0.13	1.38
Chame	MA16-C-03-07	03.07.2016	0.22	-21.95	0.28	3.47
Chame	MA16-C-07-07	07.07.2016	0.24	-25.61	0.40	5.18
Chame	MA16-C-11-07	11.07.2016	0.19	-20.50	0.23	7.69
Chame	MA16-C-15-07	15.07.2016	0.24	NA	0.15	2.51
Chame	MA16-C-19-07	19.07.2016	0.24	-20.74	0.22	3.51
Chame	MA16-C-23-07	23.07.2016	0.19	-24.84	0.19	2.33
Chame	MA16-C-27-07	27.07.2016	0.19	-23.47	0.18	1.48
Chame	MA16-C-31-07	31.07.2016	0.21	-25.96	0.15	1.21
Chame	MA16-C-04-08	04.08.2016	0.18	-20.50	0.15	1.05
Chame	MA16-C-12-08	12.08.2016	0.31	-24.78	0.14	NA
Chame	MA16-C-13-08	13.08.2016	0.28	-24.10	0.18	1.84
Chame	MA16-C-14-08	14.08.2016	0.29	-23.63	0.22	5.68
Chame	MA16-C-18-08	18.08.2016	0.20	NA	0.19	0.71
Chame	MA16-C-22-08	22.08.2016	0.31	-25.67	0.16	0.69
Chame	MA16-C-26-08	26.08.2016	0.18	NA	0.17	0.52
Chame	MA16-C-30-08	30.08.2016	0.33	-24.48	0.17	0.46
Chame	MA16-C-03-09	03.09.2016	0.21	NA	0.21	0.60
Chame	MA16-C-07-09	07.09.2016	0.32	-25.95	0.18	0.48
Chame	MA16-C-11-09	11.09.2016	0.24	NA	0.22	0.52
Chame	MA16-C-15-09	15.09.2016	0.37	-25.96	0.17	0.31
Chame	MA16-C-19-09	19.09.2016	0.46	-26.94	0.21	0.31
Chame	MA16-C-27-09	27.09.2016	0.45	-28.00	0.31	0.14
Chame	MA16-C-29-09	29.09.2016	0.36	NA	0.40	0.11

Table 2: *Daily samples of the monsoon season 2016 from Chame.*

Drum samples 2015

location	river	name	date	TOC (%)	$\delta^{13}C$ (‰)	Fraction modern
Narayanghat	Narayani	D-NA1501	31.05. - 14.06.2015	0.51	-23.31	0.48
Narayanghat	Narayani	D-NA1502	15.06. - 30.06.2015	0.61	-27.05	0.77
Narayanghat	Narayani	D-NA1503	01.07. - 15.07.2015	0.36	-24.26	0.72
Narayanghat	Narayani	D-NA1504	15.07. - 30.07.2015	0.42	-27.77	0.81
Narayanghat	Narayani	D-NA1505	31.07. - 13.08.2015	0.41	-24.26	0.68
Narayanghat	Narayani	D-NA1506	14.08. - 27.08.2015	0.33	-25.74	0.76
Narayanghat	Narayani	D-NA1507	28.08. - 10.09.2015	0.25	-24.45	0.73
Narayanghat	Narayani	D-NA1508	11.09. - 24.09.2015	0.32	-25.89	0.73
Besisahar	Marsyangdi	D-MA1509	31.05. - 14.06.2015	0.38	-25.15	0.17
Besisahar	Marsyangdi	D-MA1510	15.06. - 29.06.2015	0.27	-26.08	0.43
Besisahar	Marsyangdi	D-MA1511	30.06 - 13.07.2015	0.18	-25.83	0.54
Besisahar	Marsyangdi	D-MA1512	14.07. - 28.07.2015	0.29	-25.55	0.32
Besisahar	Marsyangdi	D-MA1513	28.07. - 11.08.2015	0.34	-25.65	0.46
Besisahar	Marsyangdi	D-MA1514	11.08. - 26.08.2015	0.26	-25.02	0.50
Besisahar	Marsyangdi	D-MA1515	13.09. - 30.09.2015	0.54	-25.80	0.55
Besisahar	Marsyangdi	D-MA1516	27.09. - 10.10.2015	0.38	-24.40	0.33
Barabise	Bhote Khosi	D-BK1517	08.06. - 23.06.2015	0.87	-23.77	0.79
Barabise	Bhote Khosi	D-BK1518	23.06. - 09.07.2015	0.46	-23.71	0.65
Barabise	Bhote Khosi	D-BK1519	09.07. - 23.07.2015	0.37	-25.50	0.53
Barabise	Bhote Khosi	D-BK1520	24.07. - 07.08.2015	0.33	-24.34	0.39
Barabise	Bhote Khosi	D-BK1521	08.08. - 23.08.2015	0.52	-26.56	0.30
Barabise	Bhote Khosi	D-BK1522	24.08. - 08.09.2015	0.45	-24.53	0.35
Barabise	Bhote Khosi	D-BK1523	09.09. - 23.09.2015	0.44	-23.37	0.34
Barabise	Bhote Khosi	D-BK1524	24.09. - 08.10.2015	0.42	-23.79	0.36
Chatara	Khosi	D-KH1525	06.07. - 20.07.2015	0.25	NA	0.66
Chatara	Khosi	D-KH1526	21.07. - 07.08.2015	0.23	NA	0.62
Chatara	Khosi	D-KH1527	08.08. - 22.08.2015	0.27	NA	0.65
Chatara	Khosi	D-KH1528	23.08. - 06.09.2015	0.19	NA	0.64
Chatara	Khosi	D-KH1529	07.09. - 21.09.2015	0.19	NA	0.64
Chatara	Khosi	D-KH1530	22.09. - 03.10.2015	0.27	NA	0.69
Chatara	Khosi	D-KH1531	04.10. - 12.10.2015	0.32	NA	0.73

Table 3: *Drum samples of the monsoon 2015 from four sampling stations.*

Drum samples 2016

location	river	name	date	TOC (%)	$\delta^{13}C$ (‰)	Fraction modern
Narayanghat	Narayani	D-NA1601	04.06. - 17.06.2016	0.44	NA	0.73
Narayanghat	Narayani	D-NA1602	18.06. - 01.07.2016	0.37	NA	0.73
Narayanghat	Narayani	D-NA1603	02.07. - 15.07.2016	0.28	NA	0.65
Narayanghat	Narayani	D-NA1604	16.07. - 29.07.2016	0.20	NA	0.61
Narayanghat	Narayani	D-NA1605	30.07. - 12.08.2016	0.24	-24.02	0.51
Narayanghat	Narayani	D-NA1606	13.08. - 26.08.2016	0.25	NA	0.61
Narayanghat	Narayani	D-NA1607	27.08. - 09.09.2016	0.23	NA	0.68
Narayanghat	Narayani	D-NA1608	10.09. - 23.09.2016	0.24	NA	0.69
Narayanghat	Narayani	D-NA1609	24.09. - 04.10.2016	0.30	NA	0.69
Besisahar	Marsyangdi	D-MA1610-B	29.05. - 11.06.2016	0.54	NA	0.21
Besisahar	Marsyangdi	D-MA1611-B	12.06. - 25.06.2016	0.41	NA	0.30
Besisahar	Marsyangdi	D-MA1612-B	26.06. - 09.07.2016	0.25	NA	0.36
Besisahar	Marsyangdi	D-MA1613-B	10.07. - 23.07.2016	0.21	NA	0.33
Besisahar	Marsyangdi	D-MA1614-B	24.07. - 06.08.2016	0.23	NA	0.32
Besisahar	Marsyangdi	D-MA1615-B	07.08. - 20.08.2016	0.20	NA	0.24
Besisahar	Marsyangdi	D-MA1616-B	21.08. - 03.09.2016	0.21	NA	0.48
Besisahar	Marsyangdi	D-MA1617-B	04.09. - 17.09.2016	0.24	NA	0.39
Besisahar	Marsyangdi	D-MA1618-B	18.09. - 30.09.2016	NA	NA	NA
Chame	Marsyangdi	D-MA-1619-C	31.05. - 13.06.2016	0.27	-25.43	0.31
Chame	Marsyangdi	D-MA-1620-C	13.06. - 23.06.2016	0.21	-17.95	0.19
Chame	Marsyangdi	D-MA-1621-C	26.06. - 09.07.2016	0.21	-19.78	0.27
Chame	Marsyangdi	D-MA-1622-C	09.07. - 22.09.2016	0.20	-23.76	0.28
Chame	Marsyangdi	D-MA-1623-C	22.07. - 04.08.2016	0.20	-27.93	0.27
Chame	Marsyangdi	D-MA-1624-C	04.08. - 17.08.2016	0.20	-22.31	0.19
Chame	Marsyangdi	D-MA-1625-C	17.08. - 30.08.2016	0.26	-22.73	0.18
Chame	Marsyangdi	D-MA-1626-C	30.08. - 12.09.2016	0.20	-25.33	0.17
Chame	Marsyangdi	D-MA-1627-C	12.09. - 25.09.2016	0.21	-22.95	0.21
Chame	Marsyangdi	D-MA-1628-C	25.09. - 04.10.2016	0.45	-28.55	0.38
Devighat	Trisuli	D-TR1629	15.05. - 01.06.2016	0.61	NA	0.85
Devighat	Trisuli	D-TR1630	02.06. - 16.06.2016	0.64	NA	0.92
Devighat	Trisuli	D-TR1631	17.06. - 01.07.2016	0.37	NA	0.80
Devighat	Trisuli	D-TR1632	02.07. - 15.07.2016	0.18	NA	0.82
Devighat	Trisuli	D-TR1633	16.07. - 01.08.2016	0.31	NA	0.77
Devighat	Trisuli	D-TR1634	02.08. - 15.08.2016	0.44	NA	0.84
Devighat	Trisuli	D-TR1635	16.08. - 01.09.2016	0.28	NA	0.71
Devighat	Trisuli	D-TR1636	02.09. - 15.09.2016	0.30	NA	0.78
Devighat	Trisuli	D-TR1637	16.09. - 01.10.2016	0.34	NA	0.76
Barabise	Bhote Khosi	D-BK1638	15.07. - 30.07.2016	0.84	NA	0.50
Barabise	Bhote Khosi	D-BK1639	01.08. - 15.08.2016	0.32	NA	0.34
Barabise	Bhote Khosi	D-BK1640	16.08. - 31.08.2016	NA	NA	NA
Barabise	Bhote Khosi	D-BK1641	01.09. - 15.09.2016	0.55	NA	0.50
Barabise	Bhote Khosi	D-BK1642	16.09. - 30.09.2016	0.37	NA	0.51
Barabise	Bhote Khosi	D-BK1643	15.05. - 30.05.2016	0.39	NA	0.45
Barabise	Bhote Khosi	D-BK1644	31.05. - 14.06.2016	0.86	NA	0.69
Barabise	Bhote Khosi	D-BK1645	14.06. - 29.06.2016	0.77	NA	0.68
Barabise	Bhote Khosi	D-BK1646	29.06. - 14.07.2016	0.10	NA	0.45

location	river	name	date	TOC (%)	$\delta^{13}C$ (‰)	Fraction modern
Chatara	Khosi	D-KH1647	15.05. - 14.06.2016	0.79	NA	0.94
Chatara	Khosi	D-KH1648	16.06. - 30.06.2016	0.40	NA	0.85
Chatara	Khosi	D-KH1649	16.06. - 30.06.2016	0.36	NA	0.78
Chatara	Khosi	D-KH1650	01.07. - 15.07.2016	0.23	NA	0.64
Chatara	Khosi	D-KH1651	16.07. - 30.07.2016	0.25	NA	0.66
Chatara	Khosi	D-KH1652	31.07. - 14.08.2016	NA	NA	0.66
Chatara	Khosi	D-KH1653	15.08. - 31.08.2016	0.26	NA	0.72
Chatara	Khosi	D-KH1654	01.09. - 15.09.2016	0.26	NA	0.75
Chatara	Khosi	D-KH1655	16.09. - 30.09.2016	0.33	NA	0.79

Table 4: *Drum samples of the monsoon 2016 from the six sampling stations.*

Drum samples 2017

location	river	name	date	TOC (%)	$\delta^{13}C$ (‰)	Fraction modern
Narayanghat	Narayani	NEQ-D-NA1701	23.05. - 05.06.2017	0.44	NA	0.73
Narayanghat	Narayani	NEQ-D-NA1702	06.06. - 19.06.2017	0.61	NA	0.71
Narayanghat	Narayani	NEQ-D-NA1703	20.06. - 03.07.2017	0.41	NA	0.74
Narayanghat	Narayani	NEQ-D-NA1704	04.07. - 17.07.2017	0.48	NA	0.76
Narayanghat	Narayani	NEQ-D-NA1705	18.07. - 31.07.2017	0.31	NA	0.64
Narayanghat	Narayani	NEQ-D-NA1706	01.08. - 14.08.2017	NA	NA	NA
Narayanghat	Narayani	NEQ-D-NA1707	15.08. - 28.08.2017	0.27	NA	0.61
Narayanghat	Narayani	NEQ-D-NA1708	29.08. - 11.09.2017	0.21	NA	0.50
Narayanghat	Narayani	NEQ-D-NA1709	12.09. - 25.09.2017	NA	NA	NA
Besisahar	Marsyangdi	NEQ-D-MA1710-B	23.05. - 06.06.2017	0.61	NA	0.66
Besisahar	Marsyangdi	NEQ-D-MA1711-B	07.06. - 21.06.2017	0.60	NA	0.29
Besisahar	Marsyangdi	NEQ-D-MA1712-B	22.06. - 06.07.2017	0.32	NA	0.32
Besisahar	Marsyangdi	NEQ-D-MA1713-B	07.07. - 21.07.2017	0.24	NA	0.35
Besisahar	Marsyangdi	NEQ-D-MA1714-B	22.07. - 05.08.2017	0.22	NA	0.30
Besisahar	Marsyangdi	NEQ-D-MA1715-B	06.08. - 20.08.2017	0.16	NA	0.23
Besisahar	Marsyangdi	NEQ-D-MA1716-B	21.08. - 04.09.2017	0.21	NA	0.40
Besisahar	Marsyangdi	NEQ-D-MA1717-B	05.09. - 19.09.2017	NA	NA	0.47
Besisahar	Marsyangdi	NEQ-D-MA1718-B	20.09. - 30.09.2017	NA	NA	0.54
Chame	Marsyangdi	NEQ-D-MA1719-C	24.05. - 07.06.2017	NA	NA	NA
Chame	Marsyangdi	NEQ-D-MA1720-C	07.06. - 22.06.2017	NA	NA	NA
Chame	Marsyangdi	NEQ-D-MA1721-C	22.06. - 07.07.2017	NA	NA	NA
Chame	Marsyangdi	NEQ-D-MA1722-C	07.07. - 22.07.2017	0.16	NA	0.18
Chame	Marsyangdi	NEQ-D-MA1723-C	22.07. - 06.08.2017	NA	NA	NA
Chame	Marsyangdi	NEQ-D-MA1724-C	06.08. - 21.08.2017	0.20	NA	0.19
Chame	Marsyangdi	NEQ-D-MA1725-C	21.08. - 05.09.2017	NA	NA	0.27
Chame	Marsyangdi	NEQ-D-MA1726-C	05.09. - 20.09.2017	NA	NA	NA
Devighat	Trisuli	NEQ-D-TR1727	01.06. - 15.06.2017	NA	NA	NA
Devighat	Trisuli	NEQ-D-TR1728	16.06. - 01.07.2017	NA	NA	NA
Devighat	Trisuli	NEQ-D-TR1729	02.07. - 15.07.2017	0.18	NA	NA
Devighat	Trisuli	NEQ-D-TR1730	16.07. - 01.08.2017	NA	NA	NA
Devighat	Trisuli	NEQ-D-TR1731	02.08. - 15.08.2017	NA	NA	NA
Devighat	Trisuli	NEQ-D-TR1732	16.08. - 01.09.2017	NA	NA	NA
Devighat	Trisuli	NEQ-D-TR1733	02.09. - 15.09.2017	NA	NA	NA
Devighat	Trisuli	NEQ-D-TR1734	16.09. - 30.09.2017	NA	NA	NA
Barabise	Bhote Khosi	NEQ-D-BK1735	01.06. - 15.06.2017	NA	NA	NA
Barabise	Bhote Khosi	NEQ-D-BK1736	16.06. - 30.06.2017	NA	NA	NA
Barabise	Bhote Khosi	NEQ-D-BK1737	01.07. - 16.07.2017	0.34	NA	NA
Barabise	Bhote Khosi	NEQ-D-BK1738	16.07. - 31.07.2017	NA	NA	NA
Barabise	Bhote Khosi	NEQ-D-BK1739	01.08. - 15.08.2017	0.28	NA	NA
Barabise	Bhote Khosi	NEQ-D-BK1740	16.08. - 31.08.2017	NA	NA	NA
Barabise	Bhote Khosi	NEQ-D-BK1741	16.09. - 30.09.2017	NA	NA	NA

location	river	name	date	TOC (%)	$\delta^{13}C$ (‰)	Fraction modern
Chatara	Khosi	NEQ-D-KH1742	01.06. - 15.06.2017	NA	NA	NA
Chatara	Khosi	NEQ-D-KH1743	16.06. - 30.06.2017	NA	NA	NA
Chatara	Khosi	NEQ-D-KH1744	01.07. - 15.07.2017	NA	NA	NA
Chatara	Khosi	NEQ-D-KH1745	16.07. - 31.07.2017	NA	NA	NA
Chatara	Khosi	NEQ-D-KH1746	01.08. - 15.08.2017	0.26	NA	NA
Chatara	Khosi	NEQ-D-KH1747	16.08. - 31.08.2017	0.25	NA	NA
Chatara	Khosi	NEQ-D-KH1748	01.09. - 15.09.2017	NA	NA	0.89
Chatara	Khosi	NEQ-D-KH1749	16.09. - 30.09.2017	NA	NA	0.78

Table 5: *Drum samples of the monsoon 2017 from the six sampling stations.*

Appendix B

Fluorescence signal of the Narayani River before and after a major earthquake

Different techniques have been proposed to predict earthquakes with non-seismic signals, however they remain challenging. A yet largely unexplored method to consists in measuring the fluorescence signal of groundwater and streams (e.g., Freund et al., 2006; Freund & Freund, 2015; Grant et al., 2011). This technique is based on peroxy defects, i.e. the change of an oxygen anion from the valence state O^{2-} to O^{-}, which build up in igneous and metamorphic rocks. Laboratory experiments have shown that a mechanical stress moving through the rocks can cause the breakage of these peroxy defects (Grant et al., 2011). The stress released by earthquakes is therefore thought to significantly reduce the number of peroxy defects in the bedrock (Freund et al., 2006). The valence state of O- in a bedrock transmits a charge to the groundwater circulating through the rock and can therefore be detected in the fluorescence signal of water (Grant et al., 2011). A limited number of studies have monitored the fluorescence signal in groundwater or streams before and after an earthquake, and have observed an increase of the signal intensity before the earthquake (Fidani et al., 2017; Grant et al., 2011; Mäder et al., 2018).

We measured the fluorescence signal of the Narayani River in Narayanghat, Central Himalaya, on water samples from different seasons. A sample set from shortly before the Gorkha earthquake (Mw 7.8), that hit Central Nepal in April 2015, and from the post-seismic period allows us to test the effect of a major seismic event on the fluorescence signal of the Narayani River.

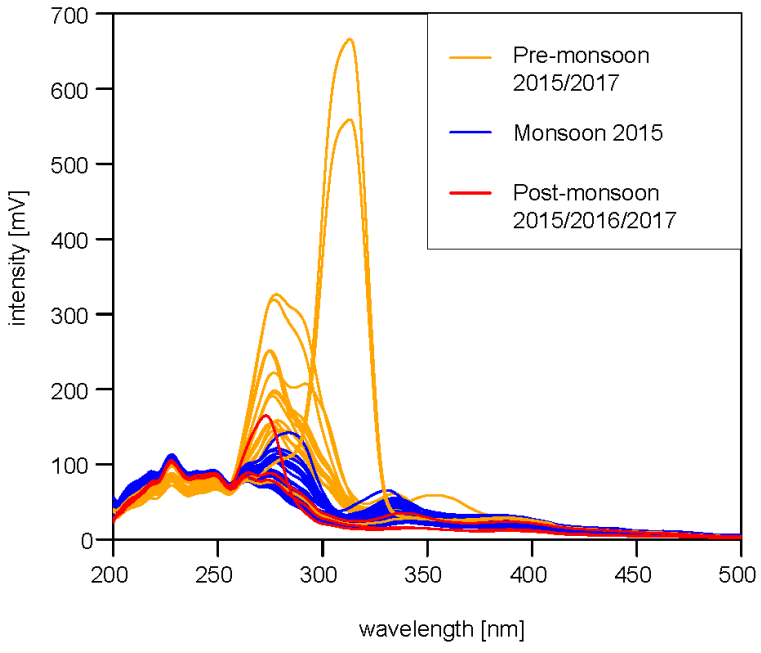

Figure 1: *Fluorescence signal of the Narayani River during different season: Pre-monsoon (January-May); monsoon (June-September) and post-monsoon (October-December).*

The fluorescence signal of the Narayani River shows a significant dependence on the season (Figure 1). As such, the fluorescence signals of the dry season prior to the monsoon (Figure 1, January-April) are of higher intensities than the signals measured on samples from the monsoon (June-September) and post-monsoon season (Figure 1; October). Figure 2 illustrates the fluorescence signal of the Narayani from the pre-earthquake and post-earthquake samples. The signal of the pre-earthquake days show, as expected in the dry season, a relatively high signal. The last pre-earthquake sample has been taken four days before the Gorkha earthquake and does not show any significant difference to earlier samples in January and March (Figure 2). We observe that the samples from after the seismic event, reveal significantly lower intensity of the fluorescence signal in the Narayani (Figure 2). The post-earthquake period, however, also correlates to the onset of the monsoon season.

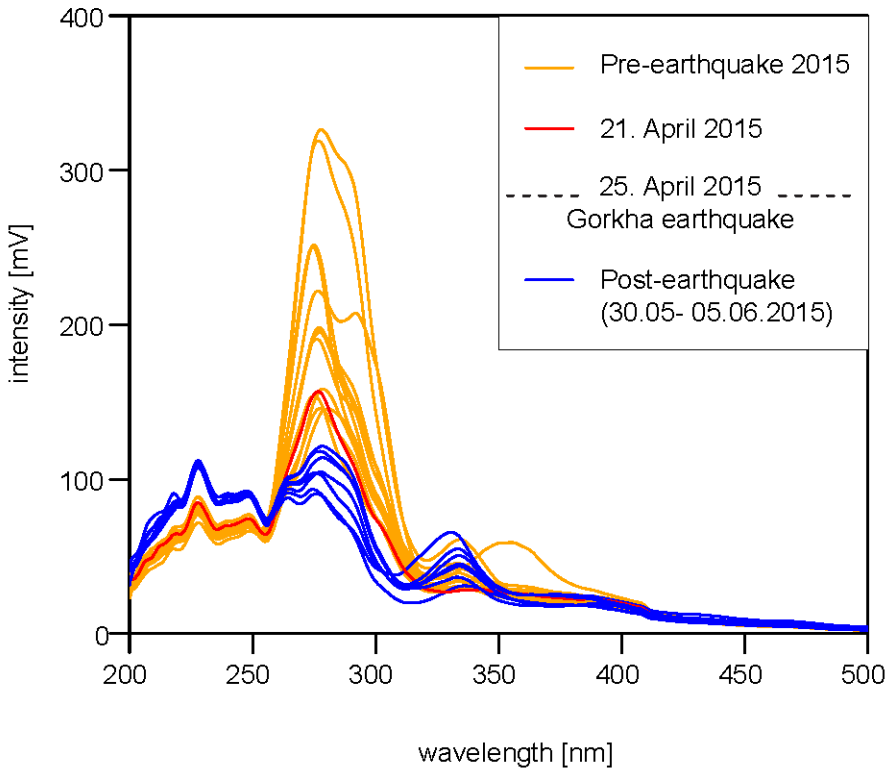

Figure 2: *Fluorescence signal of the Narayani River before and after the Gorkha earthquake (25. April 2015). The sample taken shortly before the earthquake is colored in red. The post-earthquake period overlaps with the onset of the monsoon season.*

The season seems to be the first order control of the fluorescence signal in the Narayani River. The higher intensities can be explained by the Narayani River that is mostly fed by groundwater during the dry season

(Morin et al., 2018; Tipper et al., 2006). The latter has circulated through fractured bedrocks where it gets charged with the peroxy defect signal. On the other hand, during the monsoon season, most of the water in Himalayan rivers is directly provided by precipitation with a minor part of the runoff coming from the groundwater (Morin et al., 2018; Tipper et al., 2006). After the monsoon the freshly filled groundwater table probably has not have time to get significantly charged with the peroxy defects signals.

No significant change of the fluorescence signals during the days shortly before the 2015 Gorkha earthquake has been found. The fluorescence signal of large Himalayan rivers can therefore likely not be used for prediction of major earthquakes. The absence of a pre-earthquake signal is likely linked to the size of the Narayani River which contrasts to the groundwater samples used in previous studies (Fidani et al., 2017; Grant et al., 2011; Mäder et al., 2018). Any potential pre-earthquake fluorescence signal probably gets diluted in the large Narayani River.

We thus conclude that the fluorescence signal as earthquake predictor has to be tested on springs or streams, as the signal can get diluted in large rivers. In addition, the seasonality as the pronounced monsoon season in central Nepal can complicate the interpretation of the riverine fluorescence signal.

References

Fidani, C., Balderer, W., & Leuenberger, F. (2017). The Possible Influences of the 2012 Modena Earthquakes on the Fluorescence Spectra of Bottled Mineral Water. *Hydrology Current Research*, *8*(3). https://doi.org/10.4172/2157-7587.1000288

Freund, F. T., & Freund, M. M. (2015). Paradox of peroxy defects and positive holes in rocks . Part I : Effect of temperature. *Journal of Asian Earth Sciences*, *114*, 373–383. https://doi.org/10.1016/j.jseaes.2015.04.047

Freund, F. T., Takeuchi, A., & Lau, B. W. S. (2006). Electric currents streaming out of stressed igneous rocks – A step towards understanding pre-earthquake low frequency EM emissions. *Physics and Chemistry of the Earth*, *31*, 389–396. https://doi.org/10.1016/j.pce.2006.02.027

Grant, R. A., Halliday, T., Balderer, W. P., Leuenberger, F., Newcomer, M., Cyr, G., & Freund, F. T. (2011). Ground Water Chemistry Changes before Major Earthquakes and Possible Effects on Animals. *International Journal of Environmental Research and Public Health*, *8*, 1936–1956. https://doi.org/10.3390/ijerph8061936

Mäder, M., Leuenberger, F., & Balderer, W. (2018). Effects of seismic activity on the fluorescence signal of groundwater.

Morin, G. P., Lavé, J., France-Lanord, C., Rigaudier, T., Gajurel, A. P., & Sinha, R. (2018). Annual Sediment Transport Dynamics in the Narayani Basin, Central Nepal: Assessing the Impacts of Erosion Processes in the Annual Sediment Budget. *Journal of Geophysical Research: Earth Surface*, *123*, 2341–2376. https://doi.org/10.1029/2017JF004460

Tipper, E. T., Bickle, M. J., Galy, A., West, A. J., Pomiès, C., & Chapman, H. J. (2006). The short term climatic sensitivity of carbonate and silicate weathering fluxes: Insight from seasonal variations in river chemistry. *Geochimica et Cosmochimica Acta*, *70*(11), 2737–2754. https://doi.org/10.1016/j.gca.2006.03.005

Appendix C

Carbon isotopes of dissolved organic carbon from Himalayan rivers

The radiogenic and the stable isotopic compositions of carbon were measured on 31 samples of Dissolved Organic Carbon (DOC) from Central Himalayan rivers. The results are listed in Table 1. The concentration of DOC could not be determined due to too low concentrations. Figure 1 shows that DOC of Himalayan rivers is generally characterized by modern Fm signatures (Fm 0.62 - 1.26). The radiocarbon signature of DOC is not directly linked to the size of the catchments or to the mean annual precipitation in the catchment.

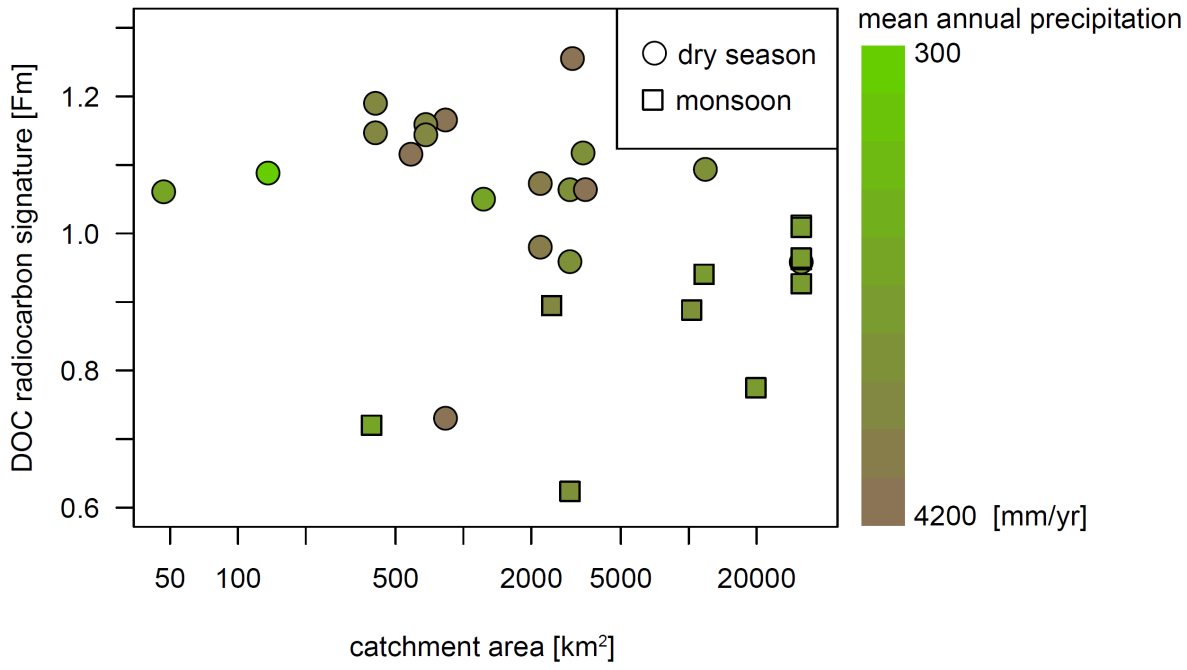

Figure 1: *Radiocarbon signature of DOC plotted against the size of the sampled river catchments. Symbols are colored in function of the mean annual precipitation in the catchment.*

Dissolved organic carbon

location	river	name	lat [°N]	long [°E]	Fraction modern	error Fraction modern (%)	$\delta^{13}C$ (‰)
Besisahar	Marsyangdi	NEQ-175-11	28.238	84.381	1.06	4.52	NA
Khudi Bazar	Khudi	NEQ-175-16	28.288	84.354	1.09	4.88	NA
-	trib. Marsyangdi	NEQ-175-19	28.454	84.369	1.06	4.87	NA
Tal	Marsyangdi	NEQ-175-23	28.484	84.37	1.07	7.00	NA
Dharapani	Dudh Khola	NEQ-175-28	28.527	84.357	1.19	8.03	NA
Koto	Naar Khola	NEQ-175-33	28.554	84.259	1.17	16.32	NA
Chame	Marsyangdi	NEQ-175-38	28.552	84.241	1.16	16.57	NA
Jomsom	Kali Gandaki	NEQ-175-69	28.786	83.735	1.26	22.49	NA
River Resort	Trisuli	NEQ-162-05	27.875	84.614	1.09	6.39	-27.63
Chame	Marsyangdi	NEQ-162-22	28.552	84.241	1.14	16.40	-28.75
Serfu Besi	Trisuli	NEQ-162-54	28.166	85.343	1.06	6.35	-28.44
Narayanghat	Narayani	NEQ-172-05	27.726	84.428	0.96	1.42	-27.64
Devghat	Khali Gandaki	NEQ-172-23	27.742	84.429	0.94	3.48	-27.57
Mirdi	Dadi Khola	NEQ-172-40	27.986	83.766	0.72	1.73	-28.75
Besisahar	Marsyangdi	NEQ-172-46	28.238	84.381	0.62	1.61	-29.67
Narayanghat	Narayani	NEQ-162-07	27.726	84.428	0.96	5.73	-28.32
Dolalghat	Indrawati	NEQ-162-74	27.639	85.706	1.05	4.23	-26.88
Hindi	Bhote Khosi	NEQ-162-95	27.909	85.922	0.98	6.31	-28.92
Barabise	Bhote Khosi	NEQ-172-54	27.797	85.896	0.89	2.03	-28.45
Tal	Marsyangdi	NEQ-162-12	28.484	84.37	0.98	6.22	-28.00
Dharapani	Dudh Khola	NEQ-162-17	28.527	84.357	1.15	9.15	-28.27
Koto	Naar Khola	NEQ-162-27	28.554	84.259	0.73	8.50	-28.34
Besisahar	Marsyangdi	NEQ-162-33	28.238	84.381	0.96	8.86	-27.80
Serfu Besi	Langtang	NEQ-162-49	28.163	85.344	1.12	12.90	-28.29
Dolalghat	Sunkoshi	NEQ-162-101	27.639	85.706	1.12	10.85	-28.52
Narayanghat	Narayani	NEQ-172-07	27.726	84.428	1.01	2.68	-27.77
Narayanghat	Narayani	NEQ-172-08	27.726	84.428	0.96	3.49	NA
Narayanghat	Narayani	NEQ-172-12	27.726	84.428	1.01	2.04	-27.37
Devghat	Trisuli	NEQ-172-27	27.806	85.008	0.77	1.89	-27.46
Narayanghat	Narayani	NEQ-172-31	27.726	84.428	0.93	3.15	-28.61
Ramdi	Khali Gandaki	NEQ-172-36	27.902	83.632	0.89	1.77	-27.80

Table 1: *Fraction modern and $\delta^{13}C$ of dissolved organic carbon*